2021

Carboxyalkylated cullulose nanocrystals for novel applications

Feizi, Zahra Hosseinpour

CARBOXYALKYLATED CELLULOSE NANOCRYSTALS FOR NOVEL APPLICATIONS

A Thesis Submitted to the
Faculty of Graduate Studies of
Lakehead University

by

Zahra Hosseinpour Feizi

Submitted in partial fulfillment of requirements for the degree of

Doctor of Philosophy in Biotechnology

January 2021

Dedication

To my parents and husband for all their encouragement, support, and endless love

Abstract

Cellulose nanocrystals (CNC), rigid rod-like nanoparticles, are derived from cellulose through acid hydrolysis and are considered as emerging nanomaterials according to their beneficial properties and commercial availability. In this thesis, the use of CNC derivatives in novel applications was explored. To make CNC more suitable for these applications, carboxyalkylation has been carried out to increase the charge density of CNC and induce hairy structure on the surface of CNC.

Since the dispersibility of kaolinite particles are very crucial in their end-use applications ranging from cosmetics to drilling, carboxymethylated CNC was used as a dispersant to increase the stability of such suspensions. In the meantime, CNC was produced in different sizes prior to carboxymethylation to analyze the effect of CNC size on its performance as a dispersant. It was observed that the larger the modified CNC, the higher the charge density, and thus, the more the CNC adsorption to kaolinite particles. Hence, with increasing the CNC size, a lower dosage of modified CNC was observed to be required for attaining better kaolinite stability, which would be industrially attractive. Another fundamental discovery of this research study was that the functional groups on the carboxymethylation of CNC was observed to play a more critical role in the settling affinity of the kaolinite particles than the CNC size.

To make CNC a potential candidate to be used in different industries, extensive modification and analysis may be required. In such cases, CNC is needed to be treated with solvents. To evaluate whether the CNC treatment in solvents would affect its characteristics, dimethyl sulfoxide (DMSO) and 4-Methylmorpholine N-oxide (NMMO), the two most extensively used cellulose solvents, were used for CNC treatment under different conditions. CNC properties, such as crystallinity, thermal stability, molecular chemical composition, dispersion stability, self-assembly as well as water-uptake and hydrophilicity/hydrophobicity of CNC were analyzed to track changes induced on CNC via solvent treatments. A polymorphism transition of cellulose I to II was observed in CNC under all conditions while treatment temperature was found to be the most effective factor compared to treatment time and CNC concentration. This transition was further affected the external hydrogen bonding, and thus, enhanced the water-uptake and hydrophilicity of CNC. It also increased the self-assembly of CNC and hence, the hydrodynamic size and instability of CNC suspension. Comparing the effect of DMSO and NMMO on CNC, DMSO was found to yield a more polymorphism transition. According to the findings in this research study, it

is critical to consider the alterations in the CNC structure via treating with solvents for analytical laboratory and industry uses.

Since the cellulose-surfactant interaction is very critical in the industry, this interaction is important to produce functional CNC with altered physicochemical properties for applications ranging from biomedical and personal care formulations to food. For this reason, different carboxyalkylation reactions of carboxymethylation, carboxybutylation, carboxyheptanation, and carboxypantadecanation were carried out on CNC to not only increase its surface negative charge density but also to induce a functional group with different alkyl chain length. Produced modified CNC samples then interacted with a cationic surfactant, MTAB, to investigate the effect of CNC chain length on its interaction with MTAB under different conditions of pH, salinity, and MTAB concentration. Results showed that the longer the CNC functional group chain length, the more MTAB adsorption was observed due to hydrophobic and electrostatic interactions, which could be beneficial in producing custom-designed CNC for different applications such as coating.

Although antibiotics are beneficial for human health, their liberation into the environment has been an enhanced global concern. In this study, CNC was used to adsorb some mostly used antibiotics of sulfamethoxazole (SMX), ciprofloxacin (CIP), and doxycycline (DOX). CNC was carboxyalkylated to carry different carbon chain lengths, but a similar negative charge density, on its surface. Among antibiotics, DOX showed higher and faster adsorption to the carboxyalkylated CNC derivatives. In the pH range studied (3.0 to 10.0), the highest DOX adsorption was observed on the CNC with the longest carbon chain (PCNC) at pH 6.0, which was due to the electrostatic and π interactions along with the hydrogen bonding. The contact angle and Quartz crystal microbalance (QCM) adsorption analyses implied a faster interaction and adsorption of DOX on PCNC. The obtained results also demonstrated the diffusion of DOX into the porous structure of CNC derivatives, especially for that of PCNC. In addition, a more compact adsorbed layer of DOX was generated on PCNC than other CNC surfaces. Carboxyalkylation was observed to slightly reduce the surface area of CNC, while the antibiotic adsorption boosted the surface area of CNC due to their adsorption on the surface. Results obtained through XPS analysis conveyed that carboxyalkylation remarkably increased C-C/C-H bonds, while antibiotic adsorption to PCNC enhanced C-C/C-H and C-N/C-O bonding ratio in the antibiotic-loaded CNC samples. Overall, carboxyalkylated CNC was detected to have an outstanding affinity to antibiotics, especially DOX,

which could pave the way for the use of CNC for applications in which the surface/antibiotic interactions are critical.

The CNC modification and its evaluation for different applications would not only reveal possibilities for widening the use of CNC but also would provide insights into the interaction mechanisms that unmodified or carboxyalkylated CNC would develop with different materials.

Acknowledgments

I would like to express my sincere gratitude to my Supervisor, Dr. Pedram Fatehi, for all his support, efforts and precious time that he dedicated to my Ph.D. studies. His endless guidance in discussing the research with me, as well as editing my manuscripts greatly aided me in every step of the way. I simply could not be luckier and prouder to land in Dr. Fatehi's research team with an advanced multi-disciplinary lab. I would also like to thank Dr. Fatehi for providing me with many opportunities such as attending conferences as well as conducting collaborative research with the Qilu University of Technology in China. I could go on and on here, but words are certainly not enough to express my endless gratitude to Dr. Fatehi.

I would also like to thank the external reviwer of this thesis, professor Hongbin Liu from Tianjin University of Science and Technology for his time and effort put on evaluating this thesis.

I would like to extend my sincere thanks to my committee members, Dr. Baoqiang Liao, and Dr. Wensheng Qin for their valuable input in writing this thesis. I truly was very lucky to have the two most supportive faculty members in the Biotechnology Department on my committee.

I would also like to appreciate my fellow lab-members for not only providing me with a great work environment but for their guidance and discussion from time to time regarding my research. I also would especially like to thank our lab manager, Dr. Weiju Gao, for her instant technical and supply support throughout my research. I would also like to thank Dr. Guoseheng Wu, and Mr. Michael Sorokopud at LUIL department of Lakehead University for their assistance and support. I also thank both the faculty and staff of the Department of Biotechnology for their assistance.

I would also like to thank my beloved parents for all their support and sacrifices they made such as sending me overseas for me to receive a better education while they themselves had to deal with me being apart for so many years. I also thank them for their full financial support of me throughout my master's and Ph.D. studies from day one.

Last but not least, I would like to express my appreciation to my lovely husband, Armin Eraghi Kazzaz, who has supported me throughout my studies and his constant encouragement when things seemed arduous. Studying a Ph.D. is not easy and having a dedicated partner like Armin has definitely helped me through all the ups and downs, and would have not been possible without him. There are certainly no words that can truthfully express the level of appreciation I have for you.

I would also like to acknowledge the financial assistance we received from FPInnovations and NSERC, Canada.

Table of Contents

List of Figures:

List of Tables:

Chapter 1: Introduction

1.1 Overview

The desire for green and sustainable materials has attracted attention to using biodegradable sources of polymers to replace oil-based ones (Chen et al., 2018). This has led to the expansion of research on the extraction and modification of bio-based polymers in recent decades. Nanocellulose has been a novel derivate of cellulose which is of interest to people in both academia and industry (Habibi et al., 2010). Cellulose nanocrystals (CNC) is one of the cellulose derivates that has gained tremendous attention due to its unique properties such as large surface area and abundant surface hydroxyl groups. These characteristics have made CNC a promising potential candidate for a wide variety of applications (Habibi et al., 2010; Tardy et al., 2017). While the current commercial utilization of CNC is limited, its vast commercial production in the last decade has paved the way to generate functionalized CNC suitable to be used in different applications.

In this thesis, novel applications for CNC such as dispersant or adsorbent have been introduced. Dispersants are substrates that are added to suspensions to prevent the agglomeration and/or settling of the particles. The environmental footprints of oil-based dispersants have resulted in a strong motivation to pursue the production of green dispersants i.e. CNC (Tang et al. 2017; Chen et al. 2018). Kaolinite suspensions are being utilized extensively as the raw material in various industries, including ceramics, cosmetics, and paints, as well as in paper making (Aras 2004; Cheng et al. 2010; Koci et al. 2011). Kaolinite particles aggregate through self-assembly in the concentrated suspensions. Since the stability and fluidity of these suspensions are important to generate adequate end-use products, using dispersants is required to promote kaolinite suspension stability (Sjöberg et al. 1999). Also, due to the involvement of electrostatic repulsion in the kaolinite suspension stability, the effect of pH on the performance of carboxymethylated CNC as a dispersant, as well as the strength of the suspension stability, is critical to be investigated.

In addition, CNC must undergo many modifications and analyses to make this nanocellulose more suitable for a wide range of applications. Some analyses, such as surface coatings or NMR, demand dispersion or dissolution of CNC in different solvents, in which 4-Methylmorpholine N-oxide (NMMO) and dimethyl sulfoxide (DMSO) have been applied substantially as effective CNC solvents for laboratory analyses (El-Wakil & Hassan, 2008; Dankovich & Gray, 2011; Yang et al., 2017). Further, the cellulose/NMMO complex is used in the commercial production of lyocell

fibers (Krysztof et al., 2018), while DMSO is known to be utilized along with other solvents in producing cellulose ethers (Casarano et al., 2014). The structure and characteristics of CNC recovered from these solutions require intensive study at a molecular level to explore the influence of solvent treatment on CNC used in different analyses and applications.

Surfactants are substrates comprised of hydrophilic and hydrophobic segments that have significant continuations to the industry acting as emulsifying, cleaning, and dispersing agents (Tardy et al., 2017), as well as playing a critical role in the day-to-day lives of people. (Because of their extensive use, the interaction of surfactants with polymers has been an important subject of study over recent decades because of their use in technological applications such as food and drug delivery, paint, coating fluids, cosmetics, and laundry products (Chakraborty et al., 2006). Thus, studying the interaction of CNC and surfactants to produce complexes with desired properties is beneficial for their use in different fields. Meanwhile, generating a functional CNC-surfactant complex requires analyzing the effect of pH and salt on their interaction and properties, since both significantly affect the electrostatic interactions of charged CNC and surfactant (Curtis et al., 2016). The effect of surfactant concentration is also vital to study because surfactant monomers adopt different conformations in varied concentrations, further affecting their interaction with functionalized CNC.

The extensive use of antibiotics in medicine and agriculture has resulted in their accumulation in wastewater plants, sludge, as well as underground and surface water in high concentrations (Yu et al., 2019). It is known that antibiotics pass the body mostly unchanged and are also not degraded in wastewater treatment plants (Lange et al., 2006). The liberation of antibiotics into the environment has detrimental effects including the generation of antibiotic-resistant bacteria and genes. This imposes a potential risk on the environment and human health (Suda et al., 2012; Yu et al., 2019; Hou et al., 2019). Thus, developing methods to remove antibiotics from wastewater and hinder their release into the environment is essential. Adsorption technology is a fast and efficient method widely used in wastewater treatment. While substrates such as silica and activated carbon have been studied as antibiotic adsorbents, the use of non-toxic bio-based polymers has had very little analysis. CNC is a good candidate for use as an antibiotic adsorbent due to CNC's large surface area, high aspect ratio, and abundant surface hydroxyl groups. Thus, carboxyalkylated CNC has been produced and used to adsorb some of the most common antibiotics of doxycycline, ciprofloxacin, and sulfamethoxazole from aqueous solution.

The aim of this thesis is to functionalize CNC and introduce new applications for this non-toxic, abundant, and renewable nanomaterial to further contribute to developing greener industrial materials and applications. In the first chapter of this thesis (**Chapter 1**), a summary of subsequent chapters, as well as the research motivation and objectives are presented.

Chapter 2 involves concepts and literature relevant to the field of nanocellulose, especially CNC, as well as a more detailed discussion of CNC functionalization and applications. The discussion related to various methods used in this thesis to analyze and evaluate the characteristics of pristine and modified CNC, as well as methods to study the efficiency of CNC for each application, are included.

Chapter 3 describes the production of CNC in various hydrodynamic sizes, CNC carboxymethylation, and finally, the performance of the produced functionalized CNC as a dispersant for enhancing the stability of kaolinite suspensions. The effect of the CNC size and surface functional groups on its dispersion performance is analyzed extensively and discussed in this chapter.

Chapter 4 includes an extensive study related to the polymorphism transition of CNC after the solvent treatment. For the treatment, CNC was dispersed/dissolved in two most common solvents of NMMO and DMSO under different time, temperature, and CNC concentration while being compared to CNC treated in the same condition in water. The wide treatment conditions analyzed in this study include harsh conditions that are used in the industry, as well as mild conditions that are followed for the sample preparation protocols of CNC analysis, e.g. H-NMR or surface coatings application of CNC. Analyzed CNC properties include crystallinity changes, molecular chemical composition, and binding energies, thermal stability, dispersion stability, self-assembly, hydrophilicity/hydrophobicity, and water-uptake ability. The effect of NMMO and DMSO on CNC properties were also compared for the first time in this chapter.

Chapter 5 reveals the interaction of carboxyalkylated CNC with a cationic surfactant. The CNC samples of similar charge densities but with varying alkyl chain lengths were generated, and the effect of alkyl chain length on the interaction of CNC and the cationic surfactant was examined. Also, different conditions of pH, salinity, and surfactant concentration were used to explore their effect on the interaction of functionalized CNC and the charged surfactant. Further discussion on the possible applications of the produced carboxyalkylated CNC samples has also been included

which also sheds light on the possible future applications of CNC derivatives associated with cationic surfactants.

Chapter 6 describes the use of carboxyalkylated CNC samples as adsorbents of the three antibioticsdoxycycline, ciprofloxacin, and sulfamethoxazole which are amongst the most used antibiotics and the frequently detected ones in wastewater plants. Carboxyalkylation reactions of carboxyheptanation and carboxypantadecanation were carried out on CNC to increase CNC functionality and also reveal the effect of carboxyl groups with different hydrocarbon length on the antibiotic adsorption. Antibiotic adsorption was analyzed using UV spectrometer and Quartz crystal microbalance with dissipation (QCM-D). Also, the hydrophilicity/hydrophobicity and diffusion study as well as zeta potential of CNC samples and antibiotics were investigated to further determine the driven adsorption force. BET and XPS analysis were also performed to understand the changes in the CNC properties before and after the antibiotic adsorption.

Chapter 7 concludes major contributions of this thesis and reveals future work recommendations.

1.2 Objectives

Objectives of this thesis are to:

1. perform CNC carboxyalkylation to alter surface properties for different applications.
2. study the performance of CNC as a kaolinite suspension dispersant
3. reveal the effect of CNC hydrodynamic size and functional groups on its dispersion performance.
4. report whether the mild or harsh treatment with DMSO and NMMO would lead to polymorphism transition in CNC which could further affect laboratory analyses such as NMR or coating, as well as industrial applications.
5. reveal the effect of chain length of the carboxyalkylated CNC on its interaction with a cationic surfactant.
6. investigate the effect of pH, salt, and surfactant concentration on the interaction of the surfactant with carboxyalkylated CNC.
7. analyze the performance of CNC as an antibiotic adsorbent.
8. reveal the effect of carboxyalkyl chain length of CNC on the antibiotic adsorption.

1.3 References

Aras, A. (2004). The change of phase composition in kaolinite-and illite-rich clay-based ceramic bodies. *Applied Clay Science*, *24*(3-4), 257-269.

Casarano, R., Pires, P. A., Borin, A. C., & El Seoud, O. A. (2014). Novel solvents for cellulose: Use of dibenzyldimethylammonium fluoride/dimethyl sulfoxide (DMSO) as solvent for the etherification of the biopolymer and comparison with tetra (1-butyl) ammonium fluoride/DMSO. *Industrial Crops and Products*, *54*, 185-191.

Chakraborty, T., Chakraborty, I., & Ghosh, S. (2006). Sodium carboxymethylcellulose− CTAB interaction: a detailed thermodynamic study of polymer− surfactant interaction with opposite charges. *Langmuir*, *22*(24), 9905-9913.

Chen, J., Eraghi Kazzaz, A., AlipoorMazandarani, N., Hosseinpour Feizi, Z., & Fatehi, P. (2018). Production of flocculants, adsorbents, and dispersants from lignin. *Molecules*, *23*(4), 868.

Cheng, H., Liu, Q., Zhang, J., Yang, J., & Frost, R. L. (2010). Delamination of kaolinite–potassium acetate intercalates by ball-milling. *Journal of colloid and interface science*, *348*(2), 355-359.

Curtis, K. A., Miller, D., Millard, P., Basu, S., Horkay, F., & Chandran, P. L. (2016). Unusual salt and pH induced changes in polyethylenimine solutions. *PLoS One*, *11*(9).

Dankovich, T. A., & Gray, D. G. (2011). Contact angle measurements on smooth nanocrystalline cellulose (I) thin films. *Journal of Adhesion Science and Technology*, 25(6-7), 699-708.

El-Wakil, N. A., & Hassan, M. L. (2008). Structural changes of regenerated cellulose dissolved in FeTNa, NaOH/thiourea, and NMMO systems. *Journal of Applied Polymer Science*, *109*(5), 2862-2871.

Habibi, Y., Lucia, L. A., & Rojas, O. J. (2010). Cellulose nanocrystals: chemistry, self-assembly, and applications. *Chemical reviews*, *110*(6), 3479-3500.

Hou, T., Du, H., Yang, Z., Tian, Z., Shen, S., Shi, Y., ... & Zhang, L. (2019). Flocculation of different types of combined contaminants of antibiotics and heavy metals by thermo-responsive flocculants with various architectures. *Separation and Purification Technology*, 223, 123-132.

Kočí, K., Matějka, V., Kovář, P., Lacný, Z., & Obalová, L. (2011). Comparison of the pure TiO2 and kaolinite/TiO2 composite as catalyst for CO_2 photocatalytic reduction. *Catalysis Today*, *161*(1), 105-109.

Krysztof, M., Olejnik, K., Kulpinski, P., Stanislawska, A., & Khadzhynova, S. (2018). Regenerated cellulose from N-methylmorpholine N-oxide solutions as a coating agent for paper materials. *Cellulose*, *25*(6), 3595-3607.

Lange, F., Cornelissen, S., Kubac, D., Sein, M. M., Von Sonntag, J., Hannich, C. B., ... & Von Sonntag, C. (2006). Degradation of macrolide antibiotics by ozone: a mechanistic case study with clarithromycin. *Chemosphere*, 65(1), 17-23.

Sjöberg, M., Bergström, L., Larsson, A., & Sjöström, E. (1999). The effect of polymer and surfactant adsorption on the colloidal stability and rheology of kaolin dispersions. *Colloids and Surfaces A: Physicochemical and Engineering Aspects*, *159*(1), 197-208.

Suda, T., Hata, T., Kawai, S., Okamura, H., & Nishida, T. (2012). Treatment of tetracycline antibiotics by laccase in the presence of 1-hydroxybenzotriazole. *Bioresource technology*, 103(1), 498-501.

Tang, J., Sisler, J., Grishkewich, N., & Tam, K. C. (2017). Functionalization of cellulose nanocrystals for advanced applications. *Journal of colloid and interface science*, *494*, 397-409.

Tardy, B. L., Yokota, S., Ago, M., Xiang, W., Kondo, T., Bordes, R., & Rojas, O. J. (2017). Nanocellulose–surfactant interactions. *Current opinion in colloid & interface science*, *29*, 57-67.

Yang, X., Wang, X., Liu, H., Zhao, Y., Jiang, S., & Liu, L. (2017). Impact of dimethyl sulfoxide treatment on morphology and characteristics of nanofibrillated cellulose isolated from corn husks. *BioResources*, *12*(1), 95-106.

Yu, K., Sun, C., Zhang, B., Hassan, M., & He, Y. (2019). Size-dependent adsorption of antibiotics onto nanoparticles in a field-scale wastewater treatment plant. *Environmental Pollution*, 248, 1079-1087.

Chapter 2: Background and literature review

2.1 Cellulose

Cellulose is the most abundant polymer on Earth, making it a truly renewable resource. This organic polymer contributes to about one-third of the total mass of plants and its annual production is estimated to be higher than 1.5×10^{12} tons. Although cellulose is mainly produced in tall plants such as trees, grasses, and cotton, there are other organisms, such as marine animals (e.g. tunicate), fungi, bacteria, and algae that contribute to the production of cellulose as well. Irrespective of its source, cellulose is composed of β-1,4-linked anhydro-D-glucopyranose units, AGU. Each glucose is rotated 180° concerning its neighbors, forming repeated units called cellobiose (Figure 2.1). Also, cellulose chains have directional asymmetry in which the terminal groups are unique and assumed as the reducing end, having a functional hemiacetal unit and nonreducing end, with a hydroxyl group attached to the C4 carbon. In cellulose, the β-1,4-linked AGU in the C1 position makes hydroxyl groups in an equatorial plane, allowing the development of intramolecular hydrogen bonding. This inter and intramolecular hydrogen bonding yields cellulose fiber with a high strength along its chains. Furthermore, the axial orientation of hydrogen atoms along the backbone of the polymer results in generally hydrophobic regions and raises the amphiphilic nature of cellulose. This property, followed by the high density of intramolecular hydrogen bonding and van der Waals forces, leads to the formation of a highly crystalline structure which, despite being hydrophilic and moisture responsive, is completely insoluble in water and most common solvents.

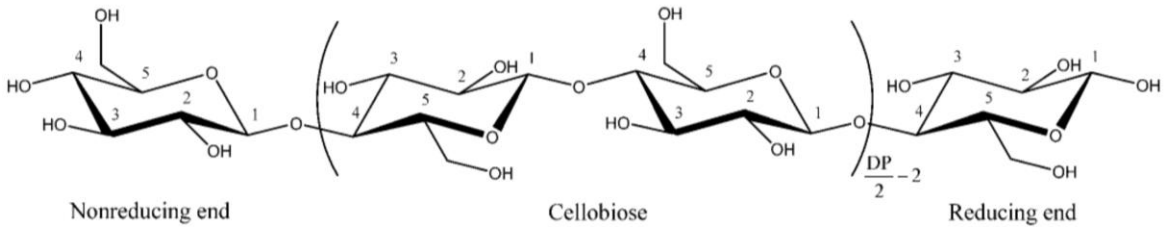

Figure 2.1. Cellulose chemical structure. Figure adopted from Habibi et al., (2012).

Depending on the source, cellulose chains have a degree of polymerization in the range of 500 to 15000. Cellulose elementary fibrils are composed of two distinct regions: highly crystalline, and amorphous. The internal strain resulting from the twisted and tilted structure of elementary fibril leads to chain dislocations and further formations of crystalline and amorphous regions along the length of the fibril. Cellulose exists in different polymorphs of I, II, III, and IV which are distinguished by their unique inter and intramolecular hydrogen bonds. Cellulose I is often referred

to as a native or natural cellulose and contains parallel chains of cellulose generated by plants, algae, tunicate, and bacteria. The mercerization (treating cellulose with aqueous sodium hydroxide) or regeneration (solubilization and recrystallization) could convert the metastable cellulose I to cellulose II. This polymorph of cellulose, which consists of antiparallel chains, is used extensively in many industrial applications and is utilized mainly as a raw material to produce Rayon and cellophane, amongother product. While cellulose II is more thermodynamically favorable and has found numerous applications in the industry, the cellulose I is found to have a higher elastic modulus due to its crystalline structure. Treating cellulose I or II with gas or liquified ammonia yields cellulose III_I and III_{II} respectively, while further thermal treatment of cellulose III_I and III_{II} at a very high temperature (around 260°C) in glycerol produces cellulose IV_I and IV_{II}, respectively. Overall, cellulose I, III_I, and IV_I have a parallel chain packing, and cellulose II, III_{II}, and IV_{II} have an antiparallel packing (Nelson, & O'Connor, 1964).

In cellulose I, two polymorphs are known to coexist in different proportions (Figure 2.2) contingent on the source of cellulose: Iα by having a triclinic structure (Figure 2.2a) is the predominant polymorph of cellulose I, produced by bacteria and algae, and Iβ by having a monoclinic structure (Figure 2.2b) is the dominant polymorph generated by plants and tunicates. In both polymorphs, cellulose chains hydrogen bond in the equatorial plane, also referred to as the hydrogen bonding plane, and are also organized in sheets that assemble through van der Waals and hydrophobic interactions, further forming elementary fibrils. In both polymorphs, cellulose chains are in parallel configurations, while the most remarkable difference is in their hydrogen bonding patterns. For the Iα polymorph, hydrogen bonding planes are placed by c/4 in the c axis of the cell, while in that of Iβ hydrogen bonding planes are dislocated between +c/4 and -c/4. This process leads to different crystalline structures. Overall, the intermolecular hydrogen bonding, along with van der Waals forces and hydrophobic interactions, stabilizes elementary fibrils and creates more rigid cellulose with good mechanical properties.

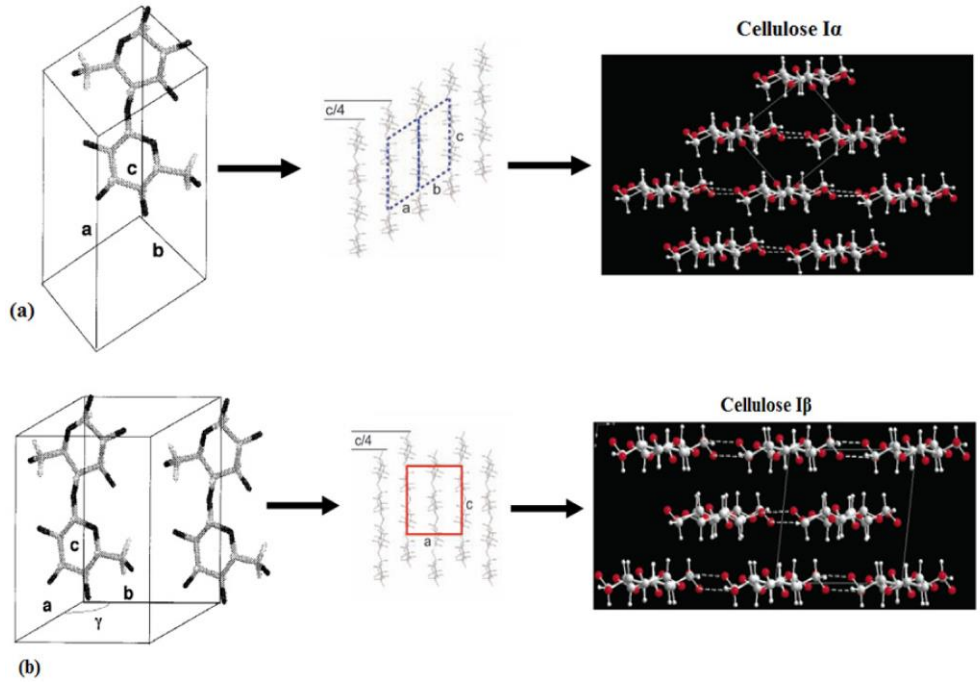

Figure 2.2. Schematic presentation of unit cells for cellulose a) Iα, and b) Iβ. Figure adopted from Poletto et al. (2013).

2.2 Nanocellulose

Nanocellulose is a cellulose derivative produced from nanostructures that exist within cellulose while having at least one nanoscale dimension. Nanocellulose inherits biocompatibility, renewability, and good mechanical properties from the cellulose fiber making it an attractive material for use in many applications ranging from composites to medical and personal care. Nanocellulose is produced via different methods of mechanical, chemical, and enzymatic treatments that yield nanocellulose with different properties. Nanofibrilated cellulose (NFC), bacterial nanocellulose (BC), and cellulose nanocrystals (CNC) are the three subcategories of nanocellulose.

2.2.1 Nanofibrilated cellulose

NFC, commonly produced by mechanically treating the cellulose fiber, possesses an entangled network with flexible, long and wide nanofibriles 20-100 nm in width and >10 µm in length The micron length of NFC significantly reduces the percolation threshold, which makes it ideal for use as a reinforcing agent. In addition, it provides CNF with unique viscoelastic and rheological properties, such as gelation and shear thinning, making it a promising candidate for medical, food,

and personal care applications. Moreover, NFC has both amorphous and crystalline parts which makes it very flexible and, therefore, yields remarkable molecular entanglement. This feature further allows CNF use in the production of robust physically entangled aerogels and hydrogels.

2.2.2 Bacterial nanocellulose

While cellulose is produced by plant cells to support them against osmotic pressure, bacteria produce cellulose to protect themselves under harsh chemical conditions or from UV radiation. With 20-50 nm in width and >1 μm in length, BC is known for its high crystallinity and chemical purity, biocompatibility, and extremely fine network architecture compared to other nanocellulose. Raised from its high purity and unique fine structure, BC has been substantially investigated for use in biomedical applications such as tissue scaffolding, and wound healing.

2.2.3 Cellulose nanocrystals

The possibility of producing colloidal suspensions from cellulose through a controlled sulfuric acid treatment was reported by Rånby in 1950 for the first time. His study was inspired by reports of Nickerson and Habrle (1947) who boiled cellulose fibers in acid and revealed that a degradation limit was reached after a certain treatment period (Habibi et al., 2010). Using transmission electron microscopy (TEM) and electron diffraction analyses, the images of dried suspension that were taken revealed the existence of needle-like particles that have the same crystalline structure as the cellulose fibers. Different names have been used over the last two decades to refer to these highly crystalline rod-like, including nanocrystalline cellulose, cellulose nanowhiskers, cellulose whiskers, nanorods, nanowires and cellulose crystallites. Although the name choice was that of each author, the term “cellulose nanocrystals (CNC)” has been the one most often used in publications.

CNC has been extracted from different sources such as wood, cotton, agricultural wastes, algae, and tunicate. While the dimensions of CNC are significantly dependant on its source and extraction method, CNC obtained from wood, cotton, and other higher order plants are generally in the length of 50-500 nm with a width of 3-20 nm (Figure 2.3). CNC production is usually performed with hydrochloric acid, which yields uncharged CNC with unstable colloidal suspension, and sulfuric acid, which generates negatively charged CNC. During sulfuric acid hydrolysis of cellulose fibers, sulfate half ester groups induce onto the CNC surface, leading to the production of a stable colloidal suspension. Since the latter hydrolysis method has been the one most often selected for

the commercial production of CNC, this method was used in our research to generate CNC samples as well. CNC is currently produced in large scales across North America by Celluforce, which has a capacity of 1 ton/year using sulfuric acid for hydrolyzing bleached kraft pulp. InnoTech Alberta produces CNC in the amount of one kg/day using different wood and cotton sources. The USDA Forest Products Lab also generates CNC in the capacity of tens of kg/day.

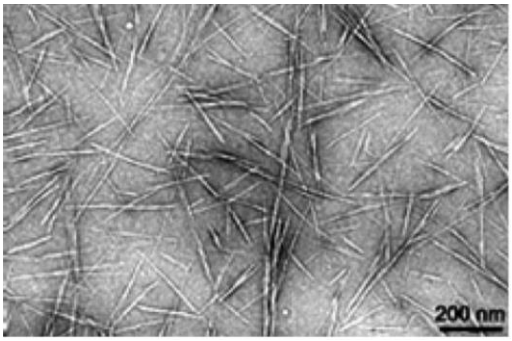

Figure 2.3. TEM image of plant-based CNC. Figure adopted from Habibi et al. (2010).

Producing CNC through sulfuric acid hydrolysis requires treating pulp with a highly concentrated acid (64%) at 45°C for about one hour. During hydrolysis, amorphous (disordered) regions of the cellulose elementary fibril which are more accessible for acid are hydrolyzed, leaving the highly crystalline regions behind with anionic sulfate half-ester groups (OSO_3^-) grafted on them (Figure 2.4).

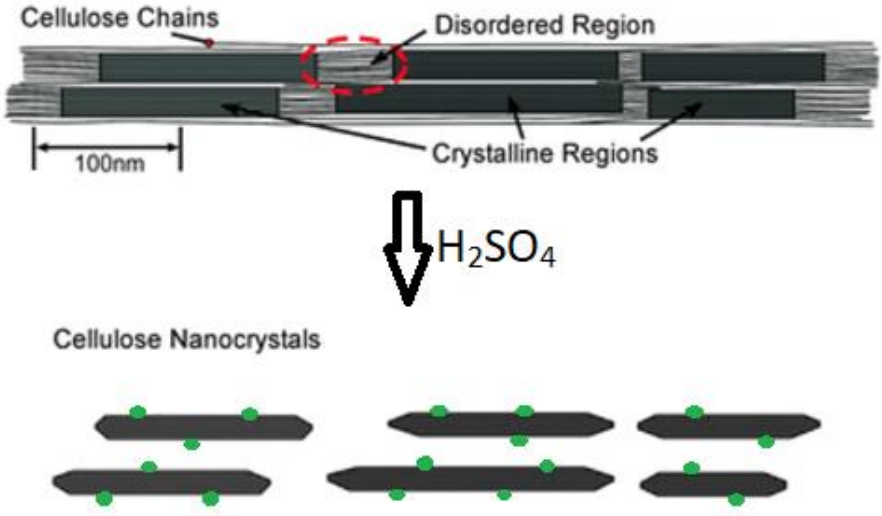

Figure 2.4. Schematic presentation of producing cellulose nanocrystals through sulfuric acid hydrolysis of cellulose elementary fibril. Green dots present OSO_3^- groups grafted onto CNC during hydrolysis. Figure reproduced from Moon et al. (2011).

2.3 Conclusions of the literature review and research gaps

Due to having abundant surface hydroxyl groups, cellulose derivatives have been used as dispersants in different suspensions. In one study, sodium carboxymethyl cellulose was utilized to stabilize a kaolin suspension (Sjöberg et al., 1999), while in another study, the impact of carboxylated nanofibrilated cellulose (CNF), on a kaolinite suspension stability was analyzed (Ming et al., 2016). However, the impact of carboxymethylated CNC on the stability of the kaolinite suspension has not been studied. Although CNF and CNC have similar chemical properties, they significantly vary from structural and morphological points of view. Thus, the dispersion performance of unmodified and anionic CNC was analyzed extensively to stabilize kaolinite suspensions for the first time, which is included in the third chapter of this thesis. The effect of CNC size and its functional groups on its dispersion performance was also investigated for the first time and included in this chapter.

Utilization of CNC in analytical studies, as well as industrial processes, require the treatment of CNC with different solvents among which DMSO and NMMO are the most used ones to treat cellulose derivates. Despite their extensive use, information on whether these solvents change the properties and thus the behavior of CNC after the treatment is limited. There is data available on the properties of the alcohol or NMMO or regenerated cellulose fibers (Biganska & Navard 2009), in which the porosity and phase separation of the cellulose fibers were mostly analyzed. There also have been several studies on the properties of the DMSO/NMMO/ionic liquid-recovered cellulose fibers (El-Wakil & Hassan, 2008; Hauru et al. 2012; Medronho & Lindman, 2014, Li et al. 2018). Nevertheless, studies on the effect of solvents on the structure of CNC is limited. In this case, most reports have discussed the solvents' effect on the production of CNF (Man et al. 2011; Laitinen et al. 2017) or the production of well-dispersed CNC suspension (Viet et al. 2007) without analyzing whether the structure of CNC was affected by such treatments. This research gap led us to analyze how the chemical properties of CNC would be affected by treating with NMMO and DMSO under different conditions in the fourth chapter of this thesis.

The CNC-surfactant complex is used in many industrial applications ranging from engineering to cosmetics and biomedical (Jackson et al, 2011; Dhar et al., 2012). Although the interaction of surfactants with varying alkyl chain lengths was analyzed with CNC (Brinatti et al., 2016), the effect of the physicochemical characteristics of CNC on its interaction with surfactants has not been evaluated in detail. This is critical to study since tailoring the chain length of a surfactant

could limit its use in some applications as it remarkably impacts the water solubility and critical micelle concentration (CMC) of the surfactant (Sharma et al., 2016). Instead, tuning the surface properties of CNC would expand the application of CNC-surfactant formulations, which is included in the fifth chapter of this dissertation.

The interaction of antibiotics with polymers is critical for many applications, such as drug delivery or separation of antibiotics from wastewater. While adsorbents such as thermal-responsive magnetic polymers (Xu et al., 2012), sewage/waste oil sludge-derived materials (Seredych & Bandosz, 2007), functionalized silica (Zhang et al., 2015), activated persulfate (Kang et al., 2016), activated carbon/graphene (Yu et al., 2016), or functionalized carbon nanotubes (Xiong et al., 2018) were developed as antibiotic adsorbents, these adsorbents either suffer from complicated generation pathways or could result in secondary pollution of the environment (Kakavandi et al., 2014). Thus, efforts have recently elevated for discovering bio-based and non-toxic adsorbents for antibiotics. Cellulose and its derivatives have been used as antibiotic adsorbents in the last decade. In one study ciprofloxacin was adsorbed onto anionic and cationic cellulose (Hu & Wang, 2016) while in another study, a graphene oxide/cellulose nanofibril aerogel was used for adsorbing antibiotics from aqueous media (Wang et al., 2017). A starch-based hydrogel has also been studied to adsorb Fluvastatin from water (Mohamed & Mahmoud, 2020). Nonetheless, CNC with abundant surface hydroxyl groups (i.e., an anchor for chemical modification) as well as a nano size (which contributes to a larger surface area) would be a better candidate for adsorbing antibiotics than other cellulose derivatives. In a research study, the composite of cellulose nanocrystals/graphene oxide was used as levofloxacin hydrochloride adsorbent (Tao et al., 2020). However, graphene oxide is not an eco-friendly material and could lead to cytotoxicity (Liao et al., 2011), which limits its applications in biomedical fields. Thus, the interaction of anionic CNC with antibiotics was studied in the last research chapter of this thesis.

2.4 Modification of CNC

The use of CNC in different applications requires tuning its surface characteristics through modification reactions. The abundance of hydroxyl functional groups on the CNC surface provides sites of reaction for functionalizing CNC. In the literature, various modifications have been carried out on CNC, such as oxidation, esterification, amidation, and etherification to produce functionalized CNC with the improved properties of higher charge density, better water

dispersibility, and better compatibility with non-polar media that can be used in applications such as cosmetics, food, nanocomposites, and biomedical (Grishkewich et al., 2017).

2.4.1 Carboxyalkylation of CNC

Carboxyalkylation is an etherification reaction performed to improve the surface chemistry of CNC for different applications. Carboxyalkylation is carried out under alkali condition in which sodium hydroxide (NaOH) reacts with the hydroxyl groups of CNC surface and generates strong nucleophiles. The alkoxide ions then attack the reagent resulting in the production of carboxyalkylated samples. The carboxyalkylation was carried out at 55°C for 3 hours in this work (Figure). Although carboxymethylation of CNC has been carried out in the literature (Ma et al., 2017; Ming et al., 2016), other carboxyalkylation reactions such as carboxybutylation, carboxyheptanation, and carboxypantadecanation, were performed on CNC to produce negatively charged CNC with different carboxyalkyl groups for the first time. Different reagents are used to introduce carboxylate groups to the CNC surface. In our studies, sodium chloroacetate (SCA), 5-chlorovaleric acid (CVA), 8-bromooctanoic acid (BOA), and 16-bromohexadecanoic acid (BHDA) were used as reagents for carboxymethylation, carboxtbutylation, carboxyheptanation, and carboxypantadecanation, respectively, to generate CNC with varied surface chemistry to use in different applications.

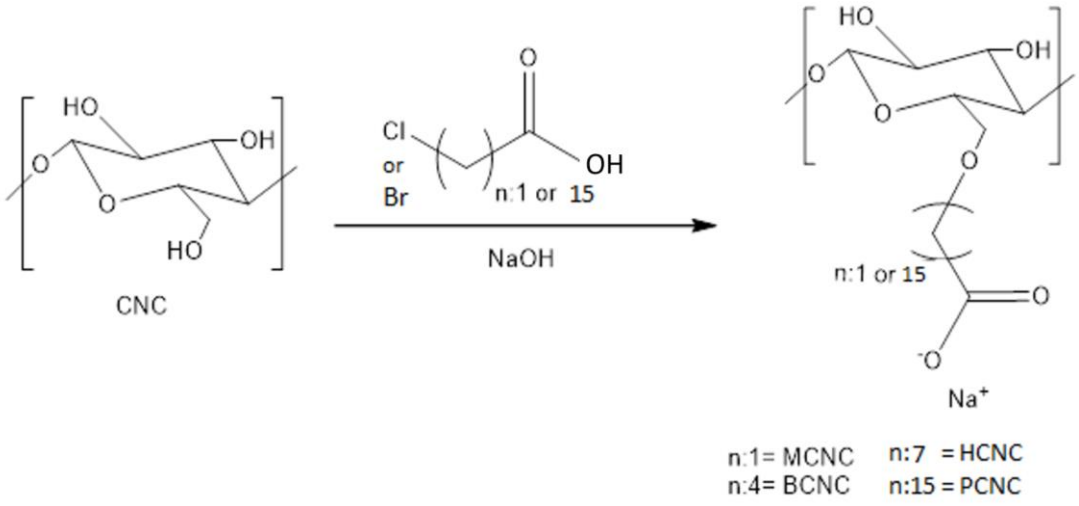

Figure 2.5. Carboxyalkylation of CNC conducted at 55°C for three hours.

2.5 Applications of CNC

Facile modification of CNC has made this material a potential candidate for use in various industrial applications. For instance, applications for CNC have been found in healable polymeric materials, in the papermaking and food industries, in the pharmaceutical industry for drug delivery and nanomedicine, as well as being used as a reinforcing filler for polymers. In our research, CNC has been used for different applications such as a dispersant for kaolinite suspension, interacted with surfactants to generate CNC-surfactant complexes, and used as an antibiotic adsorbent (Xie et al., 2018).

2.5.1 CNC as a dispersant for kaolinite suspensions

2.5.1.1 Dispersants

Dispersants are polymers that are widely utilized for suspending colloidal particles in paints, cosmetics, drilling mud, pharmaceuticals, cement, and ceramic applications. Many synthetic polymers are being used as dispersants such as hexametaphosphate or sodium polyacrylate. However, the toxic nature and non-biodegradability of these polymers limit their use in the industry. To address this challenge, semi-natural or natural polymers have been suggested for use as dispersants (Chen et al., 2018).

2.5.1.2 Kaolinite morphology and properties

Kaolinite suspensions are colloidal systems that are widely used in different industries of ceramics, cosmetics, papermaking, and drilling. Kaolinite is a 1:1 layered clay mineral. The layer is made of two different sheets of a silica tetrahedral (T face), and an alumina octahedral (O face) sheet. The siloxane surface of one layer is linked to the aluminol surface of another layer by large dipole-dipole interactions and a network of hydrogen bonds (Figure 2.6a) (Tombacz & Szekeres, 2006).

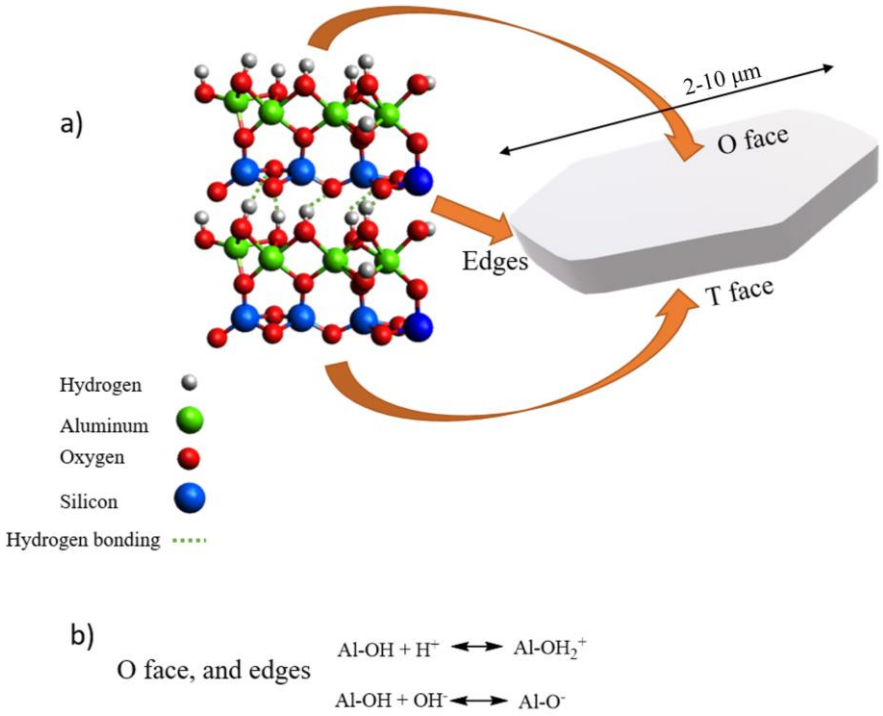

Figure 2.6. a) Kaolinite building blocks, and b) protonation and deprotonation of the free hydroxyl groups in O face and edges.

It is known that the silica basal plane (T face) of the kaolinite particle carries a negative charge permanently due to the isomorphous substitution of Al^{3+} for Si^{4+}. Meanwhile, the alumina octahedral sheet (O face) carries hydroxyl groups on the surface which begets the pH-dependency of this surface because of the protonation-deprotonation of exposed hydroxyl groups (Figure 2.6b). The edges T and O sheets also have highly reactive H^+ and OH^- ions and thus lead pH alterations to significantly affect the edge charges of kaolinite, as well (Kumar et al., 2-016; Kumar et al., 2017). In the meantime, kaolinite particles tend to self-aggregate in concentrated suspensions which further affects their stability. To address this problem, dispersants are used to stabilize these suspensions and enhance their fluidity to make these suspensions ideal for use in different industries. In our study, carboxymethylated CNC was used as a dispersant to hinder particle aggregations and to promote the stability of kaolinite suspensions. Modified CNC samples adsorb onto the O plane and edges of the kaolinite particles mostly through electrostatic adsorption and then enhance stabilization through developing a repulsive force among negatively charged kaolinite particles (Figure 2.7).

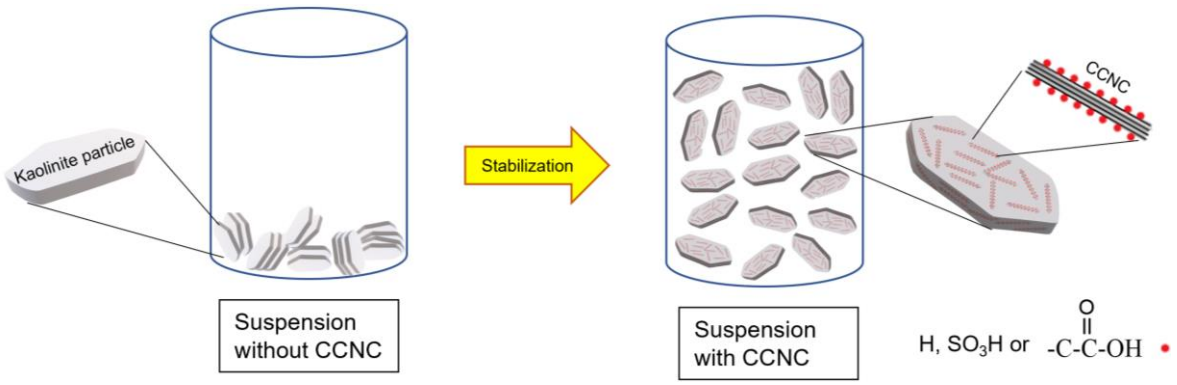

Figure 2.7. Schematic presentation of kaolinite suspension stabilized by carboxymethylated CNC (CCNC)

2.5.2 CNC and surfactants

Surfactants are compounds used extensively in the industry as cleaning, emulsifying, foaming, and dispersing agents. Surfactants contain hydrophilic and hydrophobic parts and are classified into different categories of anionic, cationic, amphoteric, and non-ionic (Figure 2.8) (Tardy et al., 2017). Cationic surfactants are used widely as cleaning, antimicrobial agents (Colomer et al., 2011), as well as in industries such as textiles (Tardy et al., 2017), Thus, a cationic surfactant, myristyltrimethylammonium bromide, was chosen to study its interaction with carboxyalkylated CNC in our study. Due to the importance of cellulose-surfactant interaction in the industry, this interaction is critical to producing functional CNC with altered physicochemical properties for applications ranging from biomedical (Jackson, et al., 2011) to food (Serpa et al., 2016) and personal care formulations (Dhar, Au, Berry, & Tam, 2012).

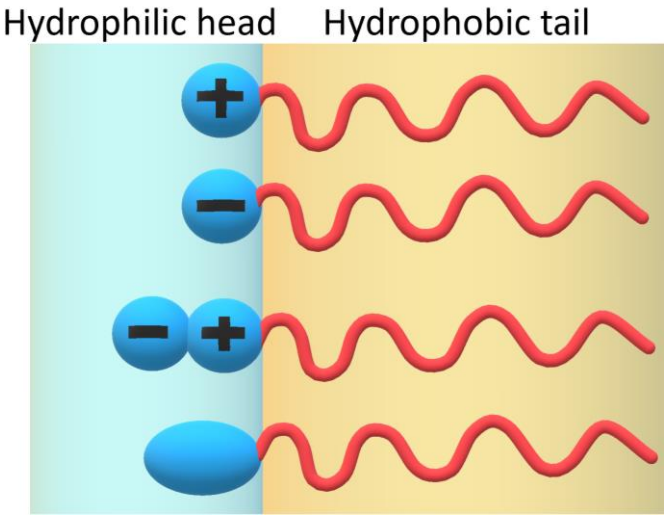

Figure 2.8. Schematic representation of surfactants

2.5.3 CNC as an antibiotic adsorbent

Antibiotics are substances that are used extensively against bacteria in different sectors of medicine and agriculture. They stop infections by killing bacteria or defecting their reproduction. Although antibiotics are advantageous to mammalian health to a point, their extensive use has led to their accumulation in wastewater plants, underground, sludge, and the surface water in high concentrations. Since antibiotics generally pass the body unchanged and are not degraded in the wastewater treatment plants (Lange et al., 2006), their release into the environment has had devastating effects comprising the generation of bacteria and genes that are antibiotic-resistant. This could subsequently impose a potential risk on the environment and, eventually, human health (Suda et al., 2012; Hou et al., 2019).

Since adsorption technology has been reported to be an efficient, fast, and cost-effective method, it has been used extensively in the wastewater treatment process (Yu et al., 2016). There are various adsorbents such as thermal-responsive magnetic polymers, sewage/waste oil sludge-derived materials, functionalized silica (Zhang et al., 2015), activated persulfate (Kang et al., 2016), activated carbon/graphene (Yu et al., 2016), or functionalized carbon nanotubes (Xiong et al., 2018) that have been developed to be used as antibiotic adsorbents. However, these adsorbents either suffer from complex production pathways or may result in secondary pollution and nanotoxicity. Using CNC as an antibiotic adsorbent would be beneficial due to its nontoxic nature, large surface area, and abundant surface hydroxyl groups. In our study, three commonly used antibiotics of sulfamethoxazole, doxycycline, ciprofloxacin (Figure 2.9)-all among the ten most consumed and frequently detected antibiotics in the aquatic environment (Carabineiro et al., 2011; Chen et al., 2014) were used to study their adsorption onto carboxyalkylated CNC samples.

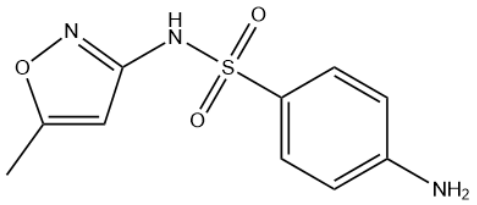

Sulfamethoxazole

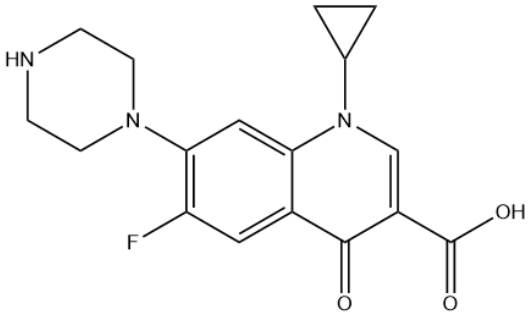

Ciprofloxacin

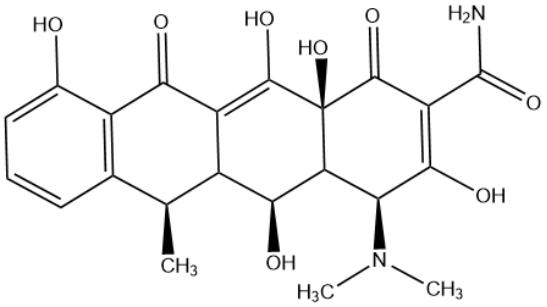

Doxycycline

Figure 2.9. Chemical structure of antibiotics

2.6 Methodology

Conductometric titration was used to measure the sulfate half-ester or carboxyalkyl group content of unmodified and modified CNC samples. For this analysis, acidic suspension of CNC is neutralized gradually with the addition of 0.1 M NaOH. By considering the amount of NaOH consumed to neutralize strong (OsO_3^-) or weak (COO^-) acids, the contents of functional groups are calculated according to equations of 2.1, and 2.2.

Equation 2.1.

$$Sulfate\ half\ ester\ group = \frac{V_i \times C_{NaOH}}{m_{CNC}}$$

Equation 2.2.

$$Carboxymethyl\ group = \frac{(V_{ii} - V_i) \times C_{NaOH}}{m_{CNC}}$$

where V_i and V_{ii} are the volume (mL) of NaOH which neutralized strong and weak acidic groups, respectively, C_{NaOH} is the NaOH concentration (mol/L) and m is the mass of dried weight (g) of CNC (Chen & van de Ven, 2016; Konduri & Fatehi, 2016).

Dynamic light scattering (DLS) was used to measure the hydrodynamic size of CNC in the suspension. This analysis uses a light beam and by analyzing the modulation intensity of the scattered light passed through the colloidal solution, it measures the hydrodynamic size of the nanoparticles or polymers in the colloidal suspensions. This analysis is based on the Brownian motion of particles which correlates with their hydrodynamic size. Smaller particles diffuse faster than large particles which lead the DLS instrument to mathematically correlate the motion to the size of the particles and their time-dependent scattering capacity (Stetefeld et al., 2016).

The zeta potential of particles/polymers as well as their isoelectric point are measured by the zeta potential analyzer. This method involves an electrophoresis concept. By submitting suspensions/solutions to the instrument, an electric field applies across the electrolyte solution and leads the charged particles/polymers to attract to the electrode of the opposite charges. Meanwhile, viscous forces acting on particles/polymers tend to prevent this movement. By these opposing forces reaching equilibrium, particles/polymers move with a constant velocity (Wang et al., 2016). This velocity, which is also referred to as the electrophoretic mobility, is used to calculate the zeta potential using equation 2.3.

Equation 2.3.

$$U_E = \frac{2\varepsilon z f(ka)}{3\eta}$$

in which z is the zeta potential in mV, U_E is the electrophoretic mobility in m/s, ε the dielectric constant, f(ka) is the Smoluchowski constant, and η is the viscosity of the suspension/solution in mPa.s.

Thermogravimetric analyzer (TGA) is used to analyze the thermal characteristics of the polymers by monitoring the mass of the substance respecting temperature and/or time as the substrate goes under a controlled temperature alteration in a controlled atmosphere. In this analysis, a mass loss reveals the degradation of the substrate at a particular temperature which is measured by a micro-

thermal balance (Mani et al., 2010). CNC samples were used in their freeze-dried form for this experiment.

Differential scanning calorimetry (DSC) is a technique that compares the amount of heat absorbed or released by the substrate with a reference as a function of temperature. DSC determines the thermal behavior of samples, such as heat capacity (C_p) and glass transition (T_g), as the sample is subjected to a gradual heat change. In detail, physical changes i.e. T_g happen in substrates upon an increase in the temperature which requires a higher heat to flow the substrate than the reference. The T_g happens when polymers transit from a glassy state to a rubbery state. Meanwhile, C_p is the amount of energy required to increase the temperature of the sample by 1°C and is measured in the unit of (J/g ºC) (Gill et al. 2010).

X-ray diffractometer is a tool to identify the phases in crystalline materials. For this analysis, CNC samples were freeze-dried and loaded onto silicon wafer pieces to be scanned for crystallographic characteristics. A blank run data was collected and subtracted from the experimental data of the CNC samples. Peak polarization and deconvolution were performed using the PeakFit software while using the Voit function for the crystalline peaks and the Fast Fourier transform (FFT) for the amorphous part (Yao et al. 2020; French 2020). The crystallinity index (CrI, %) was then calculated following equation 2.4 (Segal et al. 1959; Douard et al. 2020):

Equation 2.4.

$$CrI = \frac{Area_{crystalline} - area_{amorphous}}{I_{crystalline}} \times 100$$

The crystallite size (τ) was calculated using the X-ray diffraction patterns through the Scherrer equation (equation 2.5):

Equation 2.5.

$$\tau = \frac{K\lambda}{\beta cos\theta}$$

where K (0.94) is the Scherrer constant, λ (0.154 nm) is the X-ray radiation wavelength, β is the full width at half maximum of the (002) or (020) plane peak, and θ is the peak diffraction angle (Man et al. 2011). In addition, the plane spacing ($\frac{\Delta d}{d}$) fractional variation was calculated using equation 2.6, according to the literature (Aguayo et al. 2018):

Equation 2.6.

$$\left|\frac{\Delta d}{d}\right| = \frac{\beta}{2tan\theta}$$

X-ray photoelectron spectroscopy (XPS) is a quantitative technique that works based on the photoelectric effect. It identifies the elemental composition of substrates as well as their chemical bonding state by X-ray irradiation to the substrate, under a high vacuum (~10^{-6} Pa). For this analysis, freeze-dried samples are transferred onto a double-sided carbon tape and submitted for analysis (Kaboorani & Reidl, 2015; Fatona et al., 2018). The high-resolution XPS spectra of the samples are also analyzed using ESCApe software.

The specific surface area (S_{BET}) of the plain and antibiotic-loaded CNC samples were also determined following the Brunauer-Emmett-Teller (BET) method by NOVA 2200e (Quantachrome Instruments) in the N_2 adsorption isotherm relative pressure range of p/p_0 = 0.01-0.99. The average pore size (d_p) of the samples was determined ($d_p = 4V_p/S_{BET}$). The total pore volume (V_p) was also measured at p/p_0 = 0.99. The samples were degassed in a vacuum at 373 K for 12 h before performing the measurement (Kazzaz et al., 2018). To prepare the antibiotic-loaded CNC samples, CNC suspensions and antibiotics were prepared at neutral pH. CNC samples were then dosed into antibiotic samples to form the CNC concentration of 150 mg/L. Samples were then incubated at 25 °C for two hours at 150 rpm in a water bath shaker. Suspensions were then centrifuged at 2500 rpm for 10 min and then samples were collected from the bottom part of the glass vials and freeze-dried.

Scanning electron microscopy (SEM) is used to generate images of substrates by scanning surfaces with a focused electron beam. By analyzing various signals received from the surface of a sample upon electrons interacting with its atoms, an SEM image is produced. An SEM equipped with the energy dispersive X-ray spectroscopy (EDX) provides data not only about the surface topography of the sample, but also their chemical composition (Vie et al., 2007; Wu et al., 2012). SEM-EDX was used to analyze the surface coverage and composition of the CNC-coated sensors prior to adsorption analysis.

Tentiameter is used to analyze the hydrophobicity/hydrophilicity of substrates by measuring the water droplet on solid surfaces, or to identify the wettability of fibers using the Washburn capillary rise method. For contact angle analysis, the contact angle (θ) is the measure of the wetting of a solid by a liquid. The contact angle is the interior angle generated when a liquid droplet is placed

on a solid surface and the tangent to the interface of the droplet at the apparent intersection of all three interfaces. Figure 2.10 illustrates the contact angle of a liquid on a smooth surface. In detail, a contact angle below 90° indicates a hydrophilic surface with good wetting. Meanwhile, a contact angle above 90° is an indication of a hydrophobic surface and thus the liquid droplet tends to minimize its contact with the surface, further forming a compact droplet. A contact angle of 0°, in which the droplet is spread completely, is also an indication of an extremely hydrophilic surface with a perfect wetting (Yuan et al., 2013).

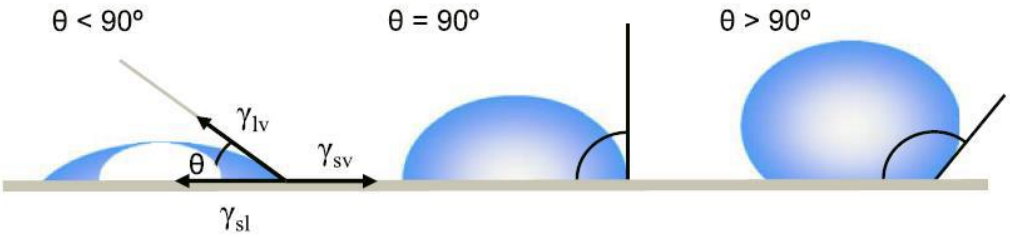

Figure 2.10. Schematic demonstration of contact angles generated by the sessile liquid droplets on a homogenous and smooth surface. Figure adapted from Yuan et al. (2013).

In this thesis, Theta Lite Contact Angle (Biolin Scientific, Finland) equipped with a camera was used for hydrophilicity/hydrophobicity analysis of CNC samples. A water droplet in the amount of 1.5 µL is located onto blank or CNC-coated surfaces, and the hydrophilicity/hydrophobicity of the samples was measured for 20 seconds following Young's equation (2.7) (Sriamornsak et al., 2008).

Equation 2.7.

$$\gamma_{sg} - \gamma_{sl} = \gamma_{gl} \cos\theta$$

where γ_{sg}, γ_{sl}, and γ_{gl} are interfacial tensions (mN/m) of solid-gas, solid-liquid, and gas-liquid, respectively. The θ (°) is the angle of water droplet when it is placed onto the CNC-coated surfaces. For measuring the powder wettability, the Washburn capillary rise method is used. For this analysis, samples in the form of powder are placed in a sample holder with a support bed. The holder is then gradually immersed into milli-Q water and the amount of water absorbed into the powder is then measured (Figure 2.11) (Meng et al., 2017). In this thesis, CNC samples were used in their freeze-dried form and were pressed inside the sample holder having small holes in its bottom.

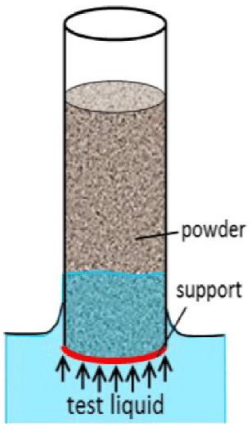

Figure 2.11. Powder wettability analysis using the Washburn capillary rise method. Figure adapted from Meng et a. (2017).

Dispersion of suspension is a critical factor in analyzing their stability or settling. The higher charge density on substrates leads to an increase in the suspension turbidity through developing repulsion forces, which leads to the suspension stabilization, while a reduction in the charge density leads to settling of the substances and thus reduction in the suspension turbidity. In this thesis, dispersion analysis of CNC and kaolinite suspensions were studied with the vertical scan analyzer as well as the LUMisizer dispersion analyzer.

For the vertical scan analyzer, kaolinite suspensions with or without CNC samples were prepared in desired concentration in aqueous media. Samples were then transferred to cylindrical glass vials and submitted to the instrument. The two sensors of this optical analyzer receive light transmitted through (180° from the incident light) and backscattered (45° from the incident radiation) by the suspension while scanning the entire height of the suspension. The more collected transmitted light, the less the stability of the suspension, while the more gathered backscattered light, the more the stability of the suspension (Konduri & Fatehi, 2018). The destabilization index is then calculated based on the transmitted and backscattering data using the turbisoft software through equation 2.8.

Equation 2.8.

$$DSI = \Sigma_i \frac{\Sigma_h |scan_i(h) - scan_{i-1}(h)|}{H}$$

in which $scan_i$ (h), and $scan_{i-1}$ (h) are the transmitted signals for the two successive time intervals at a given height, and H is the total height of the sample (Konduri & Fathi, 2018).

This analysis was carried out for two hours with scanning intervals of two min at 30°C for evaluating the performance of unmodified and carboxymethylated CNC samples as a dispersant for kaolinite suspensions.

LUMiSizer is an analytical centrifuge which utilizes the concept of centrifugal separation to evaluate suspension dispersion along with the particle size, and particle sedimentation/creaming velocity. This instrument is a combination of a centrifuge and an optic system (NIR or a blue light source and a linear detector) which monitors the concentration profile over the entire sample length under centrifugation. Figure 2.12 shows the principle of this instrument to analyze dispersion. To analyze samples, parallel NIR light beams with a wavelength of 880 nm pass through the sample cells lying on the rotor. Then, the local transmission distribution is recorded over the entire sample by a CCD-line detector. Eventually, the integral value obtained from the space and time resolved transmission profiles reveals the sedimentation progress with respect to time (Bharti et al. 2011; Chang & Liao, 2016). This instrument was used for analyzing the dispersion stability of CNC samples as well as kaolinite suspensions, along with their particle size and sedimentation velocity.

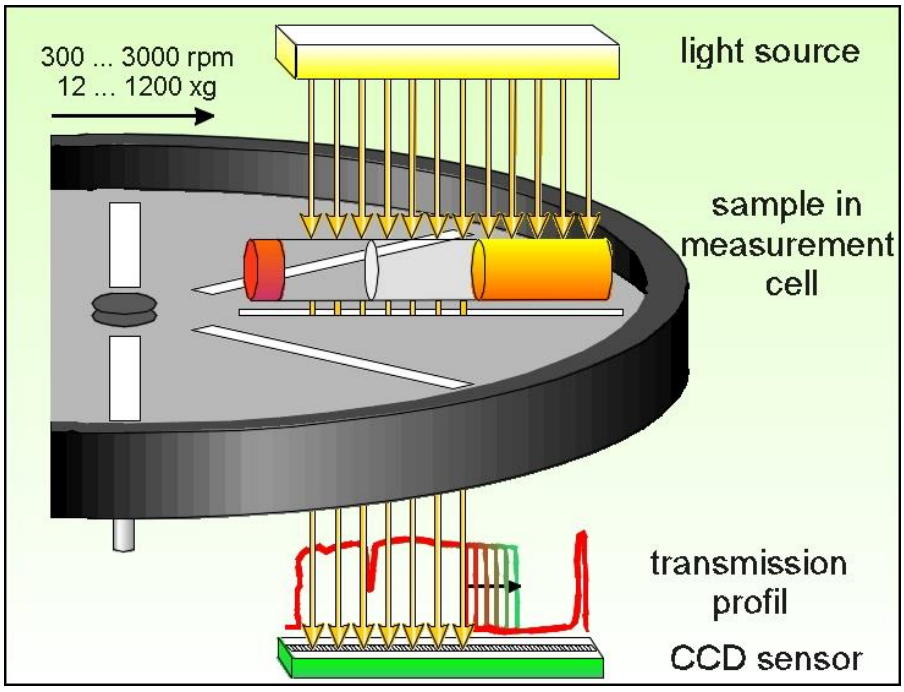

Figure 2.12. Principle of LUMiSizer dispersion analyzer. Figure adapted from Gross-Rother et al. (2018)

Quartz crystal microbalance with dissipation (QCM-D) is a surface sensitive technique that is applied widely to study adsorption in different fields of biology and chemical engineering. This

instrument is used mainly to measure the adsorption amount, film thickness, and viscoelastic properties of the formed layers on coated sensors in real-time by measuring changes in the bound mass per unit area monitored by the frequency shift of a resonating quartz crystal sensor. During the operation, an electric field induces a standing shear wave to the sensor which resonates between 5 and 20 MHz (Marx, 2003). Moreover, the sensor is driven at odd integer resonance overtones which leads to measurements that are sensitive to regions at and above the surface of the sensor. Substrate adsorption yields a reduction in the frequency or by an enhancement in the oscillation period (Niinivaara et al., 2015). The frequency shift magnitude is used to calculate the mass of adsorbed substrate using the Sauerbrey or Voigt viscoelastic models (Aulin et al., 2008). For the Sauerbrey model, the adsorbed mass is assumed to behave elastically, and is calculated through equation 2.9 in the order of ng/cm^2.

Equation 2.9.

$$\frac{\Delta f}{n} = \frac{-2\Gamma_s f^2}{A\sqrt{(\mu\rho_q)}} = -C\Gamma_s$$

in which Δf is the changes in the frequency, n is the overtone number (1, 3, 5, 7, 9, 11, and 13), f is the crystal frequency, Γ_s the mass change, A is the electrode area, ρ_q is the quartz's density, and μ is the shear modulus. Since constants A, f, ρ_q, and μ are the instrument-specific, they all typically reduce to the constant C (Marx, 2003) which is referred to as the sensor mass sensitivity constant value (17.7 ng/ Hz ×cm^2) for a 5 MHz quartz crystal sensor. In addition, changes in the dissipation (D) or energy loss per oscillation is also monitored by the QCM-D instrument using equation 2.10.

Equation 2.10.

$$D = \frac{E_L}{2\pi E_S}$$

Where E_L is the energy that is lost over an oscillation cycle and E_S is the total energy that is stored in the sensor. The time scale of the decay reveals the viscoelasticity or rigidity of the adsorbed layer.

In this thesis, QCM-D is used to monitor the adsorption of surfactants and antibiotics onto golden sensors coated with unmodified or carboxyalkylated CNC samples by revealing the adsorbed amount as well as the viscoelastic properties of the adsorbed layer.

2.7 References

Aguayo, M., Fernández Pérez, A., Reyes, G., Oviedo, C., Gacitúa, W., Gonzalez, R., & Uyarte, O. (2018). Isolation and Characterization of Cellulose Nanocrystals from Rejected Fibers Originated in the Kraft Pulping Process. *Polymers*, *10*(10), 1145.

Aulin, C., Varga, I., Claesson, P. M., Wågberg, L., & Lindström, T. (2008). Buildup of polyelectrolyte multilayers of polyethyleneimine and microfibrillated cellulose studied by in situ dual-polarization interferometry and quartz crystal microbalance with dissipation. *Langmuir*, *24*(6), 2509-2518.

Biganska, O., Navard, P. (2009). Morphology of cellulose objects regenerated from cellulose-N-methylmorpholine N-oxide-water solutions. *Cellulose*, 16(2):179-188.

Breite, D., Went, M., Prager, A., & Schulze, A. (2016). The critical zeta potential of polymer membranes: how electrolytes impact membrane fouling. *RSC Advances*, *6*(100), 98180-98189.

Brinatti, C., Huang, J., Berry, R. M., Tam, K. C., & Loh, W. (2016). Structural and energetic studies on the interaction of cationic surfactants and cellulose nanocrystals. *Langmuir, 32*(3), 689-698.

Carabineiro, S. A. C., Thavorn-Amornsri, T., Pereira, M. F. R., & Figueiredo, J. L. (2011). Adsorption of ciprofloxacin on surface-modified carbon materials. *Water research*, *45*(15), 4583-4591.

Chang, C. W., & Liao, Y. C. (2016). Accelerated sedimentation velocity assessment for nanowires stabilized in a non-Newtonian fluid. *Langmuir*, *32*(51), 13620-13626.

Chen, D., & van de Ven, T. G. (2016). Flocculation kinetics of precipitated calcium carbonate induced by electrosterically stabilized nanocrystalline cellulose. *Colloids and Surfaces A: Physicochemical and Engineering Aspects*, *504*, 11-17.

Chen, J., Eraghi Kazzaz, A., AlipoorMazandarani, N., Hosseinpour Feizi, Z., & Fatehi, P. (2018). Production of flocculants, adsorbents, and dispersants from lignin. *Molecules*, *23*(4), 868.

Dhar, N., Au, D., Berry, R. C., & Tam, K. C. (2012). Interactions of nanocrystalline cellulose with an oppositely charged surfactant in aqueous medium. *Colloids and Surfaces A: Physicochemical and Engineering Aspects*, *415*, 310-319.

Douard, L., Bras, J., Encinas, T. & Belgacem, N. (2020). Natural acidic deep eutectic solvent to obtain cellulose nanocrystals using the design of experience approach. *Carbohydrate Polymers*, 117136-117145.

El-Wakil, N. A., & Hassan, M. L. (2008). Structural changes of regenerated cellulose dissolved in FeTNa, NaOH/thiourea, and NMMO systems. *Journal of Applied Polymer Science*, *109*(5), 2862-2871.

Fatona, A., Berry, R. M., Brook, M. A., & Moran-Mirabal, J. M. (2018). Versatile surface modification of cellulose fibers and cellulose nanocrystals through modular triazinyl chemistry. *Chemistry of Materials*, *30*(7), 2424-2435.

French. A.D. (2020). Increment in evolution of cellulose crystallinity analysis. *Cellulose*, *27*, 5445-5448.

Gill, P., Moghadam, T. T., & Ranjbar, B. (2010). Differential scanning calorimetry techniques: applications in biology and nanoscience. *Journal of biomolecular techniques: JBT*, *21*(4), 167.

Grishkewich, N., Mohammed, N., Tang, J., & Tam, K. C. (2017). Recent advances in the application of cellulose nanocrystals. *Current Opinion in Colloid & Interface Science*, *29*, 32-45.

Gross-Rother, J., Herrmann, N., Blech, M., Pinnapireddy, S. R., Garidel, P., & Bakowsky, U. (2018). The application of STEP-technology® for particle and protein dispersion detection studies in biopharmaceutical research. *International journal of pharmaceutics*, *543*(1-2), 257-268.

Habibi, Y., Lucia, L. A., & Rojas, O. J. (2010). Cellulose nanocrystals: chemistry, self-assembly, and applications. *Chemical reviews*, *110*(6), 3479-3500.

Hauru, L. K., Hummel, M., King, A. W., Kilpelainen, I., & Sixta, H. (2012). Role of solvent parameters in the regeneration of cellulose from ionic liquid solutions. *Biomacromolecules*, *13*(9), 2896-2905.

Hou, T., Du, H., Yang, Z., Tian, Z., Shen, S., Shi, Y., & Zhang, L. (2019). Flocculation of different types of combined contaminants of antibiotics and heavy metals by thermo-responsive flocculants with various architectures. *Separation and Purification Technology*, 223, 123-132.

Hu, D., & Wang, L. (2016). Adsorption of ciprofloxacin from aqueous solutions onto cationic and anionic flax noil cellulose. *Desalination and Water Treatment*, *57*(58), 28436-28449.

in Surface Sciences 51, DOI 10.1007/978-3-642-34243-1-1.

Jackson, J. K., Letchford, K., Wasserman, B. Z., Ye, L., Hamad, W. Y., & Burt, H. M. (2011). The use of nanocrystalline cellulose for the binding and controlled release of drugs. *International journal of nanomedicine*, *6*, 321.

Kaboorani, A., & Riedl, B. (2015). Surface modification of cellulose nanocrystals (CNC) by a cationic surfactant. *Industrial Crops and Products*, *65*, 45-55.

Kakavandi, B., Esrafili, A., Mohseni-Bandpi, A., Jonidi Jafari, A., & Rezaei Kalantary, R. (2014). Magnetic Fe3O4@ C nanoparticles as adsorbents for removal of amoxicillin from aqueous solution. *Water science and technology*, *69*(1), 147-155.

Kang, J., Duan, X., Zhou, L., Sun, H., Tadé, M. O., & Wang, S. (2016). Carbocatalytic activation of persulfate for removal of antibiotics in water solutions. Chemical Engineering Journal, 288, 399-405.

Kazzaz, A. E., Feizi, Z. H., & Fatehi, P. (2018). Interaction of sulfomethylated lignin and aluminum oxide. *Colloid and Polymer Science*, *296*(11), 1867-1878.

Konduri, M. K., & Fatehi, P. (2016). Synthesis and characterization of carboxymethylated xylan and its application as a dispersant. *Carbohydrate polymers*, *146*, 26-35.

Konduri, M. K., & Fatehi, P. (2018). Designing anionic lignin based dispersant for kaolin suspensions. *Colloids and Surfaces A: Physicochemical and Engineering Aspects*, *538*, 639-650.

Chen, H., Gao, B., & Li, H. (2014). Functionalization, pH, and ionic strength influenced sorption of sulfamethoxazole on graphene. Journal of Environmental Chemical Engineering, 2(1), 310-315.

Kumar, N., Andersson, M.P., Van den Ende, D., Mugele, F. & Sîretanu, I. (2017). Probing the surface charge on the basal planes of kaolinite particles with high-resolution atomic force microscopy. *Langmuir* 33(50),14226-14237.

Kumar, N., Zhao, C., Klaassen, A., van den Ende, D., Mugele, F. & Siretanu, I. (2016). Characterization of the surface charge distribution on kaolinite particles using high resolution atomic force microscopy. *Geochim Cosmochim Acta*, 175,100-112.

Laitinen, O., Ojala, J., Sirviö, J. A., & Liimatainen, H. (2017). Sustainable stabilization of oil in water emulsions by cellulose nanocrystals synthesized from deep eutectic solvents. *Cellulose*, *24*(4), 1679-1689.

Lange, F., Cornelissen, S., Kubac, D., Sein, M. M., Von Sonntag, J., Hannich, C. B., & Von Sonntag, C. (2006). Degradation of macrolide antibiotics by ozone: a mechanistic case study with clarithromycin. *Chemosphere*, 65(1), 17-23.

Li, Y., Wang, J., Liu, X., & Zhang, S. (2018). Towards a molecular understanding of cellulose dissolution in ionic liquids: anion/cation effect, synergistic mechanism and physicochemical aspects. *Chemical science*, *9*(17), 4027-4043.

Liao, K. H., Lin, Y. S., Macosko, C. W., & Haynes, C. L. (2011). Cytotoxicity of graphene oxide and graphene in human erythrocytes and skin fibroblasts. *ACS applied materials & interfaces*, *3*(7), 2607-2615.

Ma, X., Cheng, Y., Qin, X., Guo, T., Deng, J., & Liu, X. (2017). Hydrophilic modification of cellulose nanocrystals improves the physicochemical properties of cassava starch-based nanocomposite films. *LWT*, *86*, 318-326.

Man, Z., Muhammad, N., Sarwono, A., Bustam, M. A., Kumar, M. V., & Rafiq, S. (2011). Preparation of cellulose nanocrystals using an ionic liquid. *Journal of Polymers and the Environment*, *19*(3), 726-731.

Mani, T., Murugan, P., Abedi, J., & Mahinpey, N. (2010). Pyrolysis of wheat straw in a thermogravimetric analyzer: effect of particle size and heating rate on devolatilization and estimation of global kinetics. *Chemical engineering research and design*, *88*(8), 952-958.

Marx, K. A. (2003). Quartz crystal microbalance: a useful tool for studying thin polymer films and complex biomolecular systems at the solution− surface interface. *Biomacromolecules*, *4*(5), 1099-1120.

Medronho, B., & Lindman, B. (2014). Competing forces during cellulose dissolution: from solvents to mechanisms. *Current Opinion in Colloid & Interface Science*, *19*(1), 32-40.

Meng, X., Ning, P., Xu, G., & Cao, H. (2017). Removal of coke powder from coking wastewater by extraction technology. *Separation and Purification Technology*, *175*, 506-511.

Ming, S., Chen, G., Wu, Z., Su, L., He, J., Kuang, Y., & Fang, Z. (2016). Effective dispersion of aqueous clay suspension using carboxylated nanofibrillated cellulose as dispersant. *Rsc Advances*, *6*(44), 37330-37336.

Mohamed, A. K., & Mahmoud, M. E. (2020). Encapsulation of Starch Hydrogel and Doping Nanomagnetite onto Metal-Organic Frameworks for Efficient Removal of Fluvastatin Antibiotic from Water. *Carbohydrate Polymers*, 116438.

Moon, R. J., Martini, A., Nairn, J., Simonsen, J., & Youngblood, J. (2011). Cellulose nanomaterials review: structure, properties and nanocomposites. *Chemical Society Reviews*, *40*(7), 3941-3994.

Nelson, M. L., & O'Connor, R. T. (1964). Relation of certain infrared bands to cellulose crystallinity and crystal latticed type. Part I. Spectra of lattice types I, II, III and of amorphous cellulose. *Journal of applied polymer science*, *8*(3), 1311-1324.

Niinivaara, E., Faustini, M., Tammelin, T., & Kontturi, E. (2015). Water vapor uptake of ultrathin films of biologically derived nanocrystals: quantitative assessment with quartz crystal microbalance and spectroscopic ellipsometry. *Langmuir*, *31*(44), 12170-12176.

Poletto, M., Pistor, V., & Zattera, A. J. (2013). Structural characteristics and thermal properties of native cellulose. *Cellulose-fundamental aspects*, *2*, 45-68.

Segal. L., Creely, J. J., Martin, A.E. & Conrad, C.M. (1959). An empirical method for estimating the degree of crystallinity of native cellulose using the X-ray diffractometer. *Textile Research Journal*, *29*(10), 786-794.

Seredych, M., & Bandosz, T. J. (2007). Removal of cationic and ionic dyes on industrial− municipal sludge based composite adsorbents. *Industrial & engineering chemistry research*, *46*(6), 1786-1793.

Serpa, A., Velásquez-Cock, J., Gañán, P., Castro, C., Vélez, L., & Zuluaga, R. (2016). Vegetable nanocellulose in food science: A review. *Food Hydrocolloids*, *57*, 178-186.

Sharma, N. K., Singh, M., & Bhattarai, A. (2016). Hydrophobic study of increasing alkyl chain length of platinum surfactant complexes: synthesis, characterization, micellization, thermodynamics, thermogravimetrics and surface morphology. *RSC Advances*, *6*(93), 90607-90623.

Sjöberg, M., Bergström, L., Larsson, A., & Sjöström, E. (1999). The effect of polymer and surfactant adsorption on the colloidal stability and rheology of kaolin dispersions. *Colloids and Surfaces A: Physicochemical and Engineering Aspects*, *159*(1), 197-208.

Sriamornsak, P., Wattanakorn, N., Nunthanid, J., & Puttipipatkhachorn, S. (2008). Mucoadhesion of pectin as evidence by wettability and chain interpenetration. *Carbohydrate Polymers*, *74*(3), 458-467.

Stetefeld, J., McKenna, S. A., & Patel, T. R. (2016). Dynamic light scattering: a practical guide and applications in biomedical sciences. *Biophysical reviews*, *8*(4), 409-427.

Suda, T., Hata, T., Kawai, S., Okamura, H., & Nishida, T. (2012). Treatment of tetracycline antibiotics by laccase in the presence of 1-hydroxybenzotriazole. *Bioresource technology*, 103(1), 498-501.

Tao, J., Yang, J., Ma, C., Li, J., Du, K., Wei, Z., ... & Deng, X. (2020). Cellulose nanocrystals/graphene oxide composite for the adsorption and removal of levofloxacin hydrochloride antibiotic from aqueous solution. *Royal Society Open Science*, *7*(10), 200857.

Tardy, B. L., Yokota, S., sAgo, M., Xiang, W., Kondo, T., Bordes, R., & Rojas, O. J. (2017). Nanocellulose–surfactant interactions. *Current opinion in colloid & interface science*, *29*, 57-67.

Tombacz E, Szekeres M (2006) Surface charge heterogeneity of kaolinite in aqueous suspension in comparison with montmorillonite. Appl Clay Sci 34(1-4):105-124

Vie, R., Azema, N., Quantin, J. C., Touraud, E., & Fouletier, M. (2007). Study of suspension settling: A approach to determine suspension classification and particle interactions. *Colloids and Surfaces A: Physicochemical and Engineering Aspects*, *298*(3), 192-200.

Viet, D., Beck-Candanedo, S., & Gray, D. G. (2007). Dispersion of cellulose nanocrystals in polar organic solvents. *Cellulose*, *14*(2), 109-113.

Wang, J., Yao, Q., Sheng, C., Jin, C., & Sun, Q. (2017). One-step preparation of graphene oxide/cellulose nanofibril hybrid aerogel for adsorptive removal of four kinds of antibiotics. *Journal of Nanomaterials*, *2017*. https://doi.org/10.1155/2017/5150613

Wang, S., Konduri, M. K., Hou, Q., & Fatehi, P. (2016). Cationic xylan–METAC copolymer as a flocculant for clay suspensions. *RSC advances*, *6*(46), 40258-40269.

Wu, H., Chen, F., Feng, Q., & Yue, X. (2012). Oxidation and sulfomethylation of alkali-extracted lignin from corn stalk. BioResources, 7(3), 2742-2751.

Xie, S., Zhang, X., Walcott, M. P., & Lin, H. (2018). Applications of cellulose nanocrystals: a review. *Engineered Science*, *2*(14), 4-16.

Xiong, W., Zeng, Z., Li, X., Zeng, G., Xiao, R., Yang, Z., ... & Zhou, C. (2018). Multi-walled carbon nanotube/amino-functionalized MIL-53 (Fe) composites: remarkable adsorptive removal of antibiotics from aqueous solutions. *Chemosphere*, *210*, 1061-1069.

Xu, L., Pan, J., Dai, J., Li, X., Hang, H., Cao, Z., & Yan, Y. (2012). Preparation of thermal-responsive magnetic molecularly imprinted polymers for selective removal of antibiotics from aqueous solution. *Journal of hazardous materials*, *233*, 48-56.

Yao, W., Weng, Y. & Catchmark, J.M. (2020). Improved cellulose X-ray diffraction analysis using Fourier series modeling. *Cellulose*, 5563-5579.

Yu, F., Li, Y., Han, S., & Ma, J. (2016). Adsorptive removal of antibiotics from aqueous solution using carbon materials. *Chemosphere*, *153*, 365-385.

Yuan, Y., Lee, T.R., Bracco, G. 2013. Holst (eds.), Surface Science Techniques, Springer Series

Zhang, Z., Lan, H., Liu, H., & Qu, J. (2015). Removal of tetracycline antibiotics from aqueous solution by amino-Fe (III) functionalized SBA15. *Colloids and Surfaces A: Physicochemical and Engineering Aspects*, *471*, 133-138.

Chapter 3: Carboxymethylated cellulose nanocrystals as clay suspension dispersants: effect of size and surface functional groups

Adapted from: Zahra Hosseinpour Feizi, Pedram Fatehi*

Cellulose, (2020) 27:3759-3772.

Department of Chemical Engineering,
Lakehead University,
955 Oliver Road,
Thunder Bay, Ontario P7B 5E1, Canada

*Corresponding author

3.1 Abstract

In this study, cellulose nanocrystals (CNC) were produced with different sizes; they were then carboxymethylated to generate carboxymethylated CNC (CCNC) to be used as dispersants for a kaolinite suspension at different pH. It was observed that larger CNC rendered CCNC with a higher surface charge. The largest CCNC (CCNC3) adsorbed more on kaolinite particles and impacted the surface charge density of the particles more dramatically than did other CCNCs. Furthermore, CCNC3 stabilized the kaolinite suspension at a lower dosage and to a higher degree than other CCNCs, and the strength of stability was greater for CCNC3 compared to the other ones. Also, CCNC was a much better dispersant than CNC as it impacted the level and strength of kaolinite system's stability more pronouncedly. Furthermore, a larger CCNC, which can be produced under milder hydrolysis reactions of pulp, can respond to carboxymethylation more effectively and make a more efficient dispersant for the kaolinite suspension, which is advantageous for industrial applications.

Keywords: Carboxymethylation, Cellulose nanocrystals, Clay suspension, Colloid

3.2 Introduction

Kaolinite suspensions are used widely in different industries, e.g., paper, ceramic, cosmetic, and paint (Murray &Lyons, 1956; Aras, 2004; Cheng et al., 2010; Koci et al., 2011). The stabilization and fluidity of these suspensions are crucial in producing acceptable end-use products. Kaolinite particles aggregate through self-assembly in concentrated suspensions, which raises the need for using dispersants or surfactants to promote their stability (Sjöberg et al., 1999).

Despite their extensive uses, the environmental footprints of petroleum-derived surfactants and dispersants have generated a strong motivation to exploit the production of green dispersants (He et al., 2017; Tang et al., 2017; Chen et al., 2018). Cellulose derivatives have been introduced as dispersants for various suspensions. In one study, sodium carboxymethyl cellulose was used to stabilize a kaolin suspension (Sjöberg et al., 1999). In a more recent study, the impact of carboxylated nanofibrilated cellulose, CNF, on the stability of a kaolinite suspension was compared with that of sodium polyacrylate (Ming et al., 2016). Although CNF and cellulose nanocrystal (CNC) have similar chemical properties, they are structurally and morphologically

very different. In this work, the dispersion performance of CNC, an attractive derivative of cellulose with prominent properties, has been investigated fundamentally for kaolinite suspensions, for the first time.

To produce CNC with different properties, the acid hydrolysis of cellulose fibers was proved to be a suitable option (Beck-Candanedo et al., 2005). This treatment expands the possible applications of CNC while giving it excellent properties, such as a high aspect ratio, large surface area, chemical functionality and stability (Yang et al., 2016). In the past, CNC has been produced in various sizes following different hydrolysis routes, such as sulfuric acid or hydrochloric acid or TEMPO oxidation, leading to CNCs with different features (Beck Candanedo et al., 2005; Montanary et al., 2005; Hanif et al., 2014). CNC has proven to have an amphiphilic nature resulting from its hydrophobic pyranose rings as well as surface functional (hydroxyl/sulfate/carboxylate) groups (Olivier et al., 2012; Hamedi et al., 2014; Malaspina & Faraudo, 2019). In this work, CNC was produced in different sizes and the fate of size of CNC on its dispersion performance in clay suspensions was evaluated.

In addition, the charged groups associated with the surface of CNC may play a crucial role in improving its performance (Singh et al., 2012; Chen et al., 2018; Lee et al., 2019). In this work, carboxymethyl groups were introduced to CNC's surface for a better particle repulsion. As CCNC would have negative charges originating from its carboxylate groups, its charge interaction with suspension particles would be significantly different from uncharged CNC. Moreover, CCNC adsorption on particles is significantly affected by its surface charges and it critically impacts the suspension of particles as it facilitates the repulsion of the particles (Rubio- Hernández et al., 2016; Chen et al., 2018; Gharanjig et al., 2019). Currently, there is no data available on how the size and surface charges of CCNC would impact its interaction with particles in a suspension and its performance as a dispersant.

Herein, CNC was produced in varied sizes, then it was carboxymethylated and used as a dispersant for a kaolinite suspension. This study would clarify the effect of size and surface charge of highly charged CNC on CNC's interaction with kaolinite particles and finally on its dispersion performance in the kaolinite suspension.

3.3 Experimental

3.3.1 Materials

Softwood bleached pulp was supplied by a pulp mill in northern Ontario, Canada. Sodium hydroxide (≥97%), sodium chloroacetate (SCA) (98%), isopropyl alcohol, and kaolinite clay were obtained from Sigma Aldrich and used as received. Sulfuric acid (98%) was obtained from Sigma Aldrich and diluted to 64 wt.% or 1 M prior to use. Cellulosic dialysis membrane (with 1000 g/mol molecular weight cut off) was obtained from Spectrum Labs. Inc., USA. Polydiallyldimethylammoniumchloride (PDADMAC) (20% in water) and poly (vinyl sulfate) potassium (PVSK) were purchased from Sigma-Aldrich and diluted to 0.005 M prior to use.

3.3.2 CNC production

Cellulose nanocrystals (CNC) were prepared in a laboratory scale according to the method described in the literature (Beck-Candanedo et al., 2005) with a minor modification. The pulp was fragmented and hydrolyzed using 64 wt % sulfuric acid with the pulpto- acid ratio of 1/17 wt./wt. at 45 °C. CNC samples with varied sizes were produced by running hydrolysis process in three different time periods of 45, 60, and 75 min. Upon completion, the mixtures were diluted ten folds to stop the acid hydrolysis. The suspensions were then centrifuged to remove excess acid, washed with water, and centrifuged again. The washing and centrifuging steps were repeated twice for each sample. The pH of the residues was adjusted to 7 using 0.1 M NaOH and dialyzed against deionized water for 2 days using cellulosic dialysis membranes for further purification. Eventually, CNC suspensions were freeze-dried using a 1L benchtop freeze drier, Labconco Co., USA) and stored for further use.

3.3.3. Carboxymethylation of produced CNC

The carboxymethylation of CNC samples was performed as described by Ma et al. (2017) with a minor modification. In this work, 0.5 g of CNC was dispersed in 50 mL of isopropyl alcohol by stirring at 250 rpm and ambient temperature for 30 min. Afterward, the suspension pH was adjusted to 12 using 0.1 M NaOH and stirred for 20 min in order to deprotonate the hydroxyl groups of CNCs. Then, 0.75 g of SCA was dissolved in isopropyl alcohol and added to the mixture dropwise for 15 min. The suspension was left for the reaction at 55 °C for 3 h under constant stirring (250 rpm). After the reaction completion, the mixture was cooled to room temperature and left for the phase separation of CNC and the isopropyl alcohol. The isopropyl alcohol was then

discarded from the top, and the modified CNC was dispersed in ethanol/water at the ratio of 80/20 vol/vol, respectively. Mixtures were centrifuged, and the purified modified CNC samples were collected from the bottom. Distilled water was then added, and the pH was adjusted to 7 using 1 M sulfuric acid and transferred to dialysis membranes for dialysis for 48 h while changing the water every 12 h. Afterward, the samples were freeze-dried and stored for further analyses. These samples were denoted as CCNCs.

3.3.4. Carboxymethylate and sulfate half-ester group analyses

The conductometric titration was used for measuring the sulfate half-ester and carboxymethylate group contents of unmodified and modified CNC samples using an automatic conductometer (Metrohm 856 Titrado, Switzerland) according to the literature (Chen & van de Ven, 2016). Briefly, 0.03 g of dried CNC and CCNC samples were mixed with 2 mL of NaCl (0.02 mol/L). Then, 150 mL of Milli-Q water was added to the system, and samples were left for stirring until homogenized. Afterward, the pH of the suspension was set to 3.5 using 0.1 M HCl and titrated with 0.01 mol/L NaOH solution. The sulfate half-ester and carboxymethylate group contents were calculated following the literature (Chen & van de Ven, 2016).

Degree of substitution (DS) was calculated using equation 3.1:

Equation 3.1

$$\text{Degree of Substitution (DS)} = \frac{M \times A}{1 - (0.059 \times A)}$$

where A is the total carboxymethylate group content (mmol/g), 0.059 is the mass of attached carboxymethylated group (g/mmol), and M is the primary unit mass of CNC or CCNC (anhydroglucose unit) (0.162 g/mmol). The methodology for sulfate half-ester and carboxymethylate group analysis was described in the supplementary material.

3.3.5. Dynamic light scattering

The hydrodynamic size of CNC samples, as well as that of kaolinite particles, was measured using a 90Plus PALS Zeta Analyzer (Nano Brook, Brookhaven, USA) at the wavelength of 632 nm, scattering angle of 90° and 25 °C using 1 mM KCl (prefiltered with a 0.2 lm nylon filter), following the literature report (Reid et al., 2017; Feizi et al., 2019). Each sample was tested triplicates, and the mean particle size was reported in this work.

3.3.6. Isoelectric point (IEP) and zeta potential analyses

NanoBrook Zeta PALS (Brookhaven Instruments Corp, USA) was used to assess the isoelectric point (IEP) and zeta potential of CNC and CCNC as well as that of kaolinite particles in suspensions. For IEP analysis, 2 g/L suspensions of CNC and CCNC, and 100 g/L suspension of kaolinite were prepared and stirred overnight, separately. Afterward, the pH of the samples was adjusted to the values ranging from 3 to 11. Each sample was dispersed by ultrasonication for 1 min, and then 400 lL of the samples were transferred into 10 mL of 1 mM KCl solution (prefiltered with a 0.2 lmnylon filter) and submitted to the instrument. For the zeta potential analysis, CCNC samples were added to the kaolinite suspension in different dosages ranging from 9.95 to 104.27 mg/L at different pH under stirring (150 rpm) for 1 h at 30 °C. Then, each sample was dispersed by ultrasonication for 1 min, and then 400 µL of the samples were transferred into 10 mL of 1 mM KCl solution (prefiltered with a 0.2 µm nylon filter) and submitted to the instrument. The analysis was conducted three times for each sample, and the average values were reported in this work (Kazzaz et al., 2018a; Kazzaz & Fatehi, 2020).

3.3.7. Additional characterizations

The FTIR (Bruker Tensor 37, Germany, ATR accessory) analysis was conducted on CNC and CCNC samples to confirm the carboxymethylation reaction (details available in supplementary material). The charge density analysis was also performed on kaolinite particles, and the detailed information could be found in the supplementary data file.

3.3.8. Adsorption analysis

The adsorption of CNC and CCNC samples onto kaolinite particles was analyzed as a function of CNC and CCNC dosages at three pH of 3, 5.5, and 10, according to the literature (Wei & Gao, 2016). In this experiment, CNC and CCNC samples with 9.95-104.27 mg/L concentrations were added to 50 mL of a kaolinite suspension (100 g/L) and incubated for 1 h at 30 °C and 150 rpm. Then, the samples were collected via filtration using a 0.45 µm pore-sized filter to separate unadsorbed CNC and CCNC from kaolinite particles. Collected kaolinite particles were then dried at 60 °C for 2 days to eliminate moisture. The organic and inorganic contents of the samples were determined using the combustion method (Santi et al., 2006; Wang et al., 2011). After drying, samples were put in the furnace to burn their CNC/CCNC (organic compound) at 400 °C for 2 h (Ferek et al., 1998). According to the TGA analysis performed using a thermogravimetric analyzer,

i-1000 series, Instrument Specialist Inc. (Figure S3.1 in supplementary material), kaolinite and CNC started to lose weight at the temperatures of around 500 and 230 °C, respectively, which is supported by the literature (Cao et al., 2009; Klosek-Wawrzyn et al., 2013; Tan et al., 2015; Mariano et al., 2015). All samples were weighed before and after the burning process, and the mass balance was exploited for the adsorption analysis of CNC and CCNC on the kaolinite particles. Untreated CNC/CCNC and kaolinite samples were also combusted separately, and the ash content of control samples was considered in the adsorption analysis.

The Surface coverage (%) of the kaolinite particles by adsorbed CNC/CCNC on kaolinite particles was determined based on the CNC/CCNC adsorption amounts, considering the density and the projected surface area of CNC/CCNC nanoparticles (via considering their hydrodynamic sizes) on kaolinite.

3.3.9. Stability analysis under atmospheric condition

A vertical scan analyzer, Turbiscan (Lab Expert, Formulaction, France) instrument, was used to monitor the stability of kaolinite particles in suspensions in the absence and presence of CNC and CCNC samples. Since the stability of kaolinite particles is highly affected by the pH (Tombacz & Szekeres, 2006), this analysis was performed at pH 3, 5.5, and 10. In short, CNC/CCNC samples (9.95-104.27 mg/L) were added to the kaolinite suspension and incubated (1 h, 30 °C, 150 rpm). The prepared samples were submitted to the instrument, and the CNC' and CCNC's performance was evaluated in 2 h with scanning intervals of 2 min at 30 °C (Konduri & Fatehi, 2018a). Turbiscan Stability Index (TSI) was calculated based on the literature reports (Qin et al., 2016; Gharehkhani et al., 2018).

3.3.10. Stability analysis under centrifugal force

LUMiSizer analytical photocentrifuge (LUM GmbH, Germany) was used to quantitatively evaluate the CNC's and CCNC's dispersion performance in the kaolinite suspension at three different pH of 3, 5.5, and 10. A parallel NIR light with k = 865 nm passed through the cells, and the transmission signal was collected every 2 s interval (Bharti et al., 2011). In this set of experiments, CCNC samples were added to the kaolinite suspensions (at three different pH) and mixed for 1 h at 30 °C and then submitted to the instrument. Suspensions without CNC/CCNC addition was used as a blank. Samples were subjected to different centrifugal forces in the range

of 200 and 2500 rpm to generate different ratios of the centrifugal force to earth acceleration in this analysis (Kazzaz et al., 2018b).

3.4. Results and discussion

3.4.1. Carboxymethylation of CNC

In this study, CNC was produced via sulfuric acid hydrolysis in three different time durations of 45, 60, and 75 min to produce CNC with varied sizes. The properties of CNC and CCNC samples are presented in Table 3.1. As seen, the CNC1 (with 90 nm size), CNC2 (with 144 nm size) and CNC3 (with 185 nm size) (monomodal size distribution for the hydrodynamic size analysis is available in Figure S3.2) have the sulfate half-ester group content of 0.25, 0.21 and 0.19 mmol/g, respectively. Generally, prolonging the acid hydrolysis time reduces the size of CNC while introducing more sulfate half-ester groups to its surface (Singh et al., 2012). The produced CNC1, CNC2, and CNC3 had a negative charge density of 0.24, 0.20, and 0.17 mmol/g, respectively. Although the produced CNCs had sulfate half-ester groups grafted on them, the addition of more anionic charges to CNCs was expected to improve their performance as dispersants. Thus, the carboxymethylation of CNC was conducted using sodium chloroacetate (SCA), as the carboxymethylate group donor, through the SN_2 reaction mechanism (Figure S3.3) (Kazzaz et al., 2019). Mixing CNC with NaOH before adding the donor led to the deprotonation of hydroxyl groups. With adding SCA, the primary alkyl halide is attacked by the nucleophile, while the Cl leaves to form chloride (Figure S3.3a). SCA may also react with NaOH and produce sodium glycolate salt in a side reaction (Figure S3.3b), which can be separated during the purification process (Dodi et al., 2011; Konduri &Fatehi 2016; Ma et al., 2017).

FTIR analysis confirmed similar chemical structures for CNCs (Figure S3.4) and CCNCs (Figure S3.5). The smaller CNC (CNC1) was produced under harsher acidic condition, which hydrolyzed more sugars (Chang et al., 2018) and possibly functional OH from the pulp (Lee et al., 2014). In the carboxymethylation process under an alkaline condition, the sulfate half-ester content of CNC dropped slightly (Table 3.1), while introducing 1.27, 1.91 and 2.55 mmol/g of carboxymethylated group to CNC1, CNC2, and CNC3, respectively. The carboxymethylation led to a degree of substitution (DS) of 0.22, 0.34 and 0.48 mol/mol for CCNC1, CCNC2, and CCNC3, respectively. After acidic hydrolysis and carboxymethylation reaction, the charge density of CCNC1, CCNC2, and CCNC3 were - 1.45, 2.00 and 2.65 mmol/g, respectively. The higher carboxymethylate group

content and charge density of the CCNC3 than other CCNCs might be due to its higher efficiency (DS in Table 3.1) in carboxymethylation reaction originating probably from the presence of more OH on CNC3. A wide range of DS from 0.087 to 1.34 was reported in the literature for carboxymethylation of microfibrilated and nanofibrilated cellulose (with the size of equal or more than 1 lm), as well as that of cellulose nanocrystals (with the size of 50 nm) (Wågberg et al., 2008; Naderi et al., 2014; Ma et al., 2017). Table 3.1 also lists the size of the CCNC samples (monomodal size distribution for the hydrodynamic size analysis of the samples is available in Figure S3.2) as well as the properties of kaolinite particles used in this study. Kaolinite particles are composed of two different sheets which beget the pH dependency of these particles (details on the physiochemical properties of kaolinite particles is presented in the supplementary information). Kaolinite particles used in this study had a net negative charge density of 0.024 ± 0.01 meq/g and a hydrodynamic size of 4.78 μm.

Table 3.1. Properties of CNCs, CCNCs, and kaolinite particles.

Properties	Unmodified nanocrystals			Carboxymethylated nanocrystals			Kaolinite
	CNC1	CNC2	CNC3	CCNC1	CCNC2	CCNC3	
Sulfate half-ester group content, mmol/g	0.25 ± 0.03	0.21 ± 0.02	0.19 ± 0.02	0.16 ± 0.02	0.14 ± 0.01	0.11 ± 0.01	-
Carboxymethyl group content, mmol/g	-	-	-	1.27 ± 0.06	1.91 ± 0.04	2.55 ± 0.03	-
Degree of substitution, mol/mol	-	-	-	0.22	0.34	0.48	-
Charge density, mmol/g	-	-	-	-	-	-	-0.024± 0.01
Hydrodynamic diameter, nm	90	144	185	-	-	-	4780

3.4.2. Adsorption and surface coverage analysis

Adsorption of particles onto different surfaces depends on the functional groups present on particles' surface as well as their size (Ostolska and Wiśniewska, 2014). In this work, the adsorption isotherms of CNC and CCNC on kaolinite particles (shown in Figure S3.6a and S3.6b) were used to determine correlations between surface coverage and dosage of CNC/CCNC in Figure 3.1. Since CCNCs used in this study were varied in size, they would occupy the surface of kaolinite particle differently upon their adsorption. Figure 3.1a shows the surface coverage of the kaolinite particles by CCNC, which were calculated based on the adsorption of CCNC (Figure S3.6b), as a function of CCNC dosage. As seen, CCNC1, CCNC2, and CCNC3 covered 10, 11, and 13% of kaolinite particles' surface, respectively. Owing to its larger size, a smaller dosage of CCNC3 (39.22 mg/L) than other CCNCs was needed to cover the same proportion of the kaolinite particles' surface. The adsorption of CCNC on kaolinite would be hindered by the electrostatic repulsion between the negative sites of kaolinite and CCNC or repulsion development between the already adsorbed CCNC and approaching CCNC for adsorption. The surface coverage of kaolinite by CCNC might be due to the fact that there would still be some positive sites on kaolinite's surface at pH 5.5 that they would capture CCNC nanoparticles through electrostatic adsorption and hydrogen bonding (Moayedi et al., 2011a).

In Figure 3.1b, the effect of CCNC's adsorbed mass on altering kaolinite's theoretical charge density is illustrated. The theoretical charge density of kaolinite particles originates from the original charge of the kaolinite particles and the induced charge density upon CCNC adsorption. As seen, CCNC3 could significantly increase the kaolinite's surface charge density to -4.2 mmol/g at 1.6 mg/g adsorption (compared to CCNC1, which could increase the surface charge to -1.29 mmol/g at 0.92 mg/g adsorption). These results depict that although CCNC3 was larger, its higher adsorption (due to its higher carboxymethylate group content) impacted the surface charges of CNC more significantly than other CCNCs. The effect of carboxymethylate groups on CCNC adsorption is further illustrated in Figure 3.1c. CCNC3 and its corresponding CNC3 were chosen to be shown in this graph due to CCNC3's predominant adsorption. Since CCNC1 and CCNC2 followed the same trend, their graphs were depicted in Figure S3.7 in the supplementary information. As seen in Figure 3.1c, the induction of carboxymethylate group onto CNC surface not only significantly fortified its adsorption onto kaolinite, but also increased the kaolinite's surface charge density more significantly.

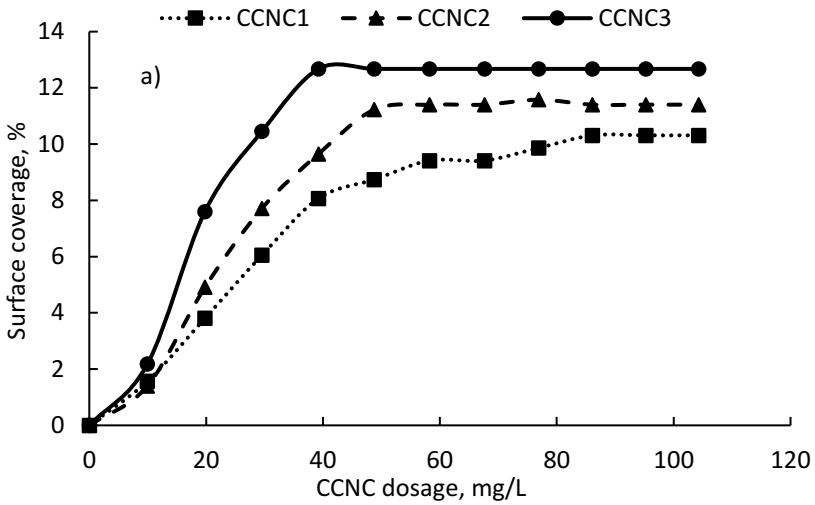
CCNC1
CCNC2
CCNC3
a)
Surface coverage, %
CCNC dosage, mg/L
0
2
4
6
8
10
12
14
0
20
40
60
80
100
120

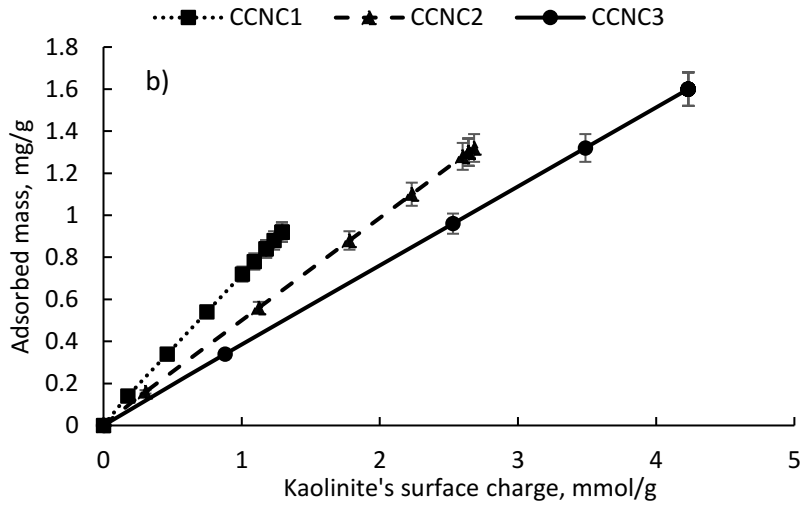
CCNC1
CCNC2
CCNC3
b)
Adsorbed mass, mg/g
Kaolinite's surface charge, mmol/g
0
0.2
0.4
0.6
0.8
1
1.2
1.4
1.6
1.8
0
1
2
3
4
5

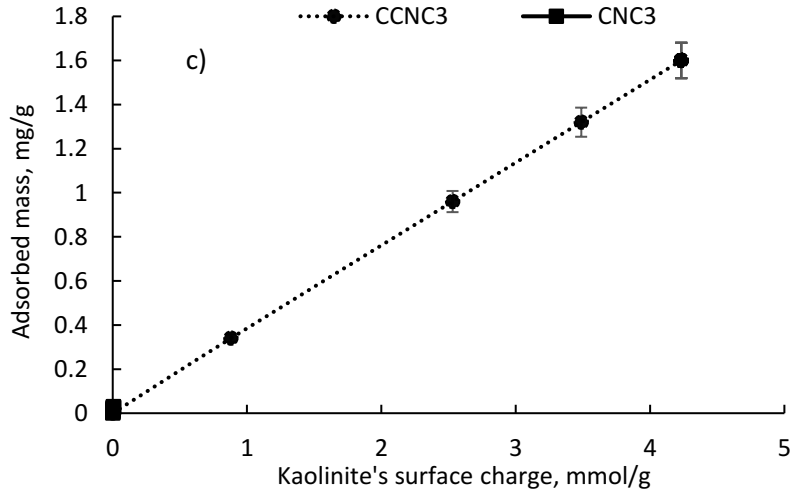
CCNC3
CNC3
c)
Adsorbed mass, mg/g
Kaolinite's surface charge, mmol/g
0
0.2
0.4
0.6
0.8
1
1.2
1.4
1.6
1.8
0
1
2
3
4
5

Figure 3.1. a) calculated kaolinite surface coverage upon CCNC adsorption versus CCNC dosage, b) calculated total negative charge density of kaolinite (original kaolinite charge density plus induced charge upon CCNC adsorption) and c) CNC and CCNC adsorption onto kaolinite surface versus the total charge density of kaolinite at pH 5.5.

3.4.3. Zeta potential analysis

Zeta potential of the particles is a critical factor affecting their stabilization/flocculation in a suspension system. The repulsion/attraction force of an adsorbed ionic particle in a particle/water interface is mainly classified based on the electrostatic interaction of the surrounded electric double layer and the steric effect of adsorbed particles. Figure 3.2a presents the suspension's zeta potential as a function of the total charges introduced to the suspension by CCNC addition. An increase in the total charges introduced to the suspension followed by the addition of CCNC samples altered significantly the suspension's zeta potential to around - 37, - 43 and - 52 mV for CCNC1, CCNC2, and CCNC3, respectively. At the same introduced charges, different values were obtained for zeta potential of the kaolinite particles, which further highlighted the role of CCNC size on the zeta potential of the suspension. Interestingly, the zeta potential of the suspension reached to approximately -37 to -50 mV via altering the surface charge of kaolinite (i.e., via adsorbing CCNC) regardless of the CCNC type (Figure 3.2a). As observed, the suspension's zeta potential continued to grow by adding more CCNCs, while a plateau in kaolinite's surface charge density was observed (Figure 3.2b) due to their limited adsorption. In other words, a greater change in the zeta potential was made via having more CCNC in the suspension system, and this change was more significant for CCNC3 due to its higher charge density. The results in Figure. 3.2a and b confirm that the impact of unadsorbed CCNC on the zeta potential is similar for all CCNCs (from -25 to -35 mV for CCNC1, from -35 to -45 mV for CCNC2 and from -40 to -50 mV for CCNC3). However, their difference in adsorption made a different initial alteration in the zeta potential that ultimately impacted the overall zeta potential of the suspension.

Figure 3.2c compares the effect of CNC and CCNC on kaolinite's surface charge density and zeta potential (results for CNC1/CCNC1 and CNC2/CCNC2 are depicted in Figure S3.8 in supplementary data). Although the addition of CNC had increased the surface charge density of kaolinite particles to around 5.3 μmol/g, this effect was less sensible for CNC than CCNC. The limited adsorption of CNC was probably the primary reason for its more limited impact on the zeta

potential of the system (i.e., changes to -26 mV). As seen, an alteration in the surface charge density of kaolinite particles via adsorption of CCNC3 improved the zeta potential of the system (-53 mV vs. -26 mV), but the amount of unadsorbed CCNC3 or CNC3 had a similar impact on the zeta potential of the system.

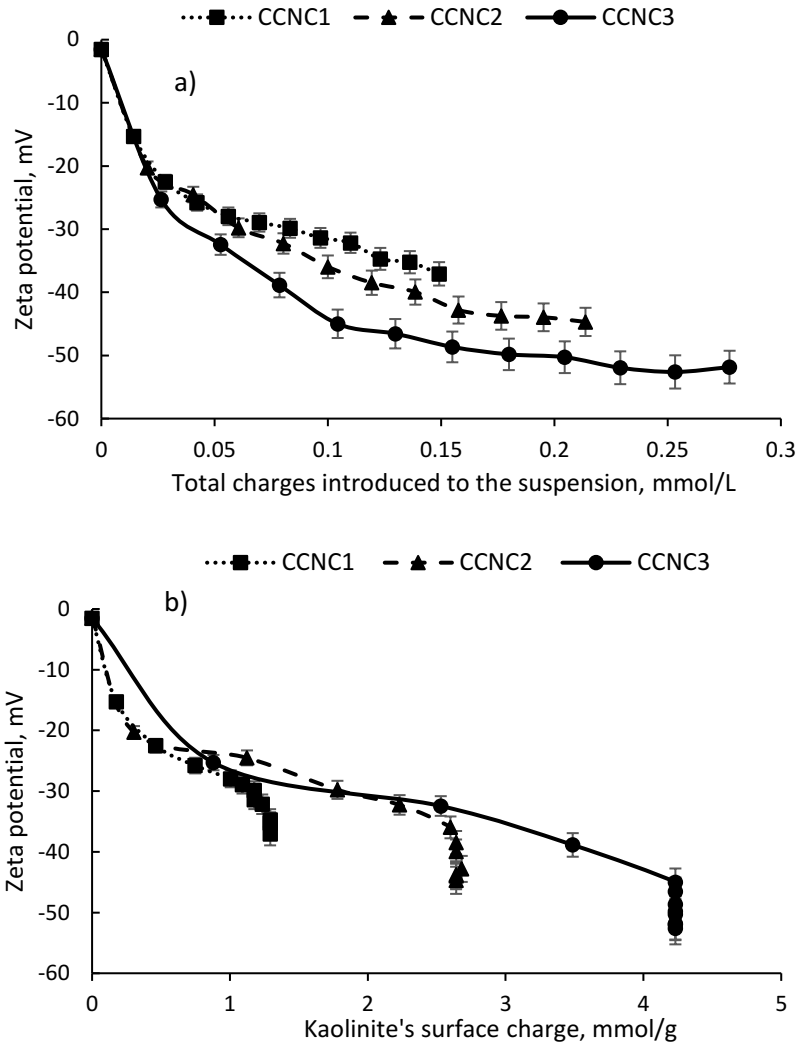

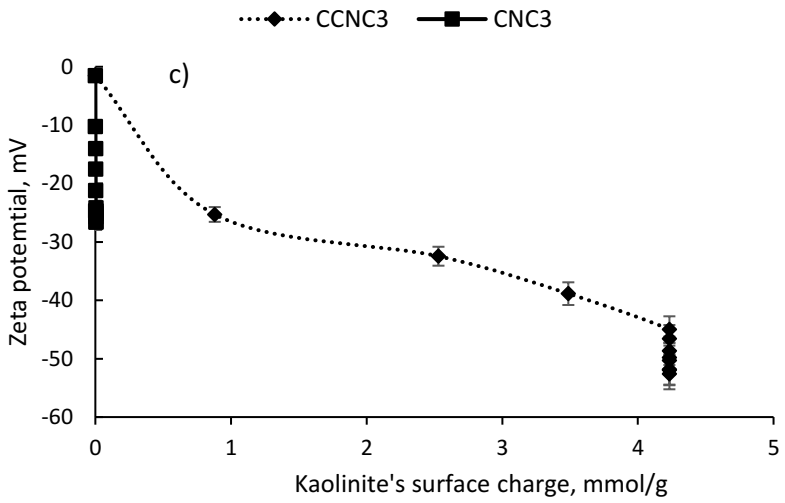

Figure 3.2. Changes in suspension's zeta potential concerning a) total charge induced to the suspension, b) kaolinite charge density for all CCNC samples, and c) kaolinite charge density for CNC and CCNC at pH 5.5

3.4.4. Stability analysis

A high TSI value is an indicator of system instability, while a low TSI value stands for the system stabilization (Kaombe et al., 2013). While the raw data of kaolinite suspension's stability in the presence and absence of the CNC/CCNC samples is presented in Figures S3.9, S3.10 and S3.11, Figure 3.3 depicts the improvement in kaolinite system's stability upon CCNC/CNC treatment. In Figure 3.3a, the effect of total charges introduced to the system on the stability of the system is depicted. It is observed that although CCNC3 could improve the suspension stability (TSI) at a much lower dosage than did CCNC1, it could enhance the stabilization of the system only by extra 17%. This reveals that doubling the CCNC size may contribute to attaining system stabilization at a lower dosage, but it may not have a considerable impact on the level of stabilization. However, it is not clear if the surface charge or overall charge of the system was more determinant on the stability of the system.

In Figure. 3.3b, the system stabilization (TSI) ameliorated up to 41, 54 and 58% when the kaolinite surface charge density increased to 1.2, 2.6 and 4.2 mmol/g, upon CCNC adsorption. The elevation in the surface charge density directly improved the stabilization, and this phenomenon was observed more dramatically for CCNC3. As the charges introduced by CCNC3 to kaolinite via adsorption was more dramatic, it impacted the TSI more significantly (Figure 3.3b). The results also depict that, at the same surface charge, the CCNCs behaved differently in stabilizing the

suspension: the smaller one (CCNC1) adsorbed more, and its adsorbed mass affected the TSI less significantly. In this case, the TSI changed more dramatically when more CCNC1 was available as unadsorbed material in the system. The introduction of more charges induced more dramatic repulsion (Yukselen & Kaya, 2003), while its larger size facilitated thicker repulsive layer around the particles and in the suspension altering the TSI more pronouncedly. In one study, the stabilization of kaolin suspension was revealed to be due to electrostatic repulsion promoted by the adsorption of sodium carboxymethylate cellulose on kaolin particles' surface (Sjöberg et al., 1999).

To differentiate the charge density from size effect, the stabilization performance of CNC3 and CCNC3 were compared in Figure 3.3c, and the performance of CNC1/CCNC1 and CNC2/CCNC2 were demonstrated in Figure S3.12. Generally, particle stabilization occurs through three different ways: (1) increase in particle's surface charge density, which leads to electrostatic repulsion, (2) non-DLVO-type interactions such as steric hindrance, and 3) hydrophobic/ hydrophilic interaction (Kamiya et al., 1999; Gan et al., 2013; Chen et al., 2018). In our case, CCNC has considerable charges on its surface developing the system stabilization through electrostatic repulsion in the kaolinite suspension. As the results in Figure S3.6a and S3.7 confirmed, hydrogen bonding development between CNC and kaolinite was weak. In this case, inducing carboxymethylate groups to CNC surface was advantageous since it provided CCNC with the ability to adsorb electrostatically and develop hydrogen bonds through the COO^- groups with kaolinite hydroxyl groups. However, the amount of sulfate half-ester groups on CNC is relatively low (Table 3.1), and it is unlikely to develop a strong electrostatic interaction for system stabilization through adsorption (Figure S3.6a). On the other hand, the hydrophobic/hydrophilic stabilization might play a role in case of CCNC since it is hydrophilic and by its adsorption to kaolinite surface, it may render the surface of kaolinite more hydrophilic developing more hydrogen bonds with the surrounded water (Konduri & Fatehi 2018b). Furthermore, a steric hindrance might also affect the stabilization performance of CNC and CCNC as they may remain between the kaolinite particles and avoid their agglomeration. This would be more pronounced for CNC than CCNC, considering its limited adsorption and thus contribution to altering the kaolinite's surface charge density (i.e., it improved the suspension stabilization up to around 25%). Although the surface coverage was less than 15%, up to 60% improvement in stabilization was achieved by CCNC3, which further proves the role of steric hindrance in CNC/CCNC dispersant performance.

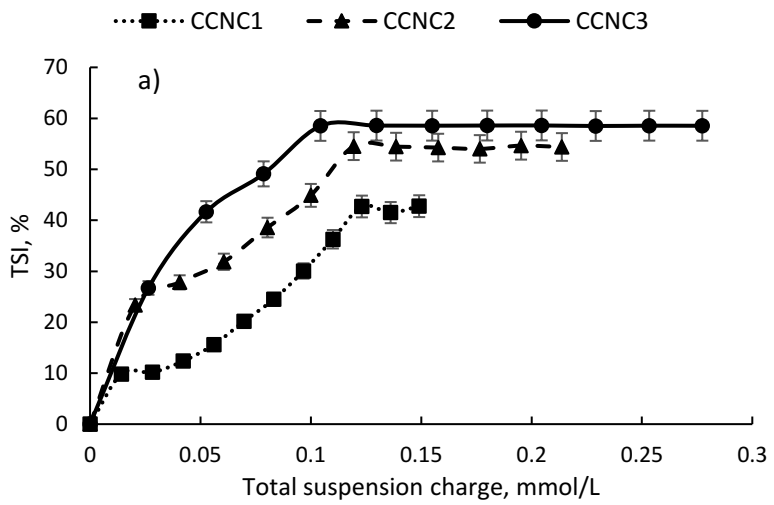
CCNC1
CCNC2
CCNC3
a)
TSI, %
Total suspension charge, mmol/L

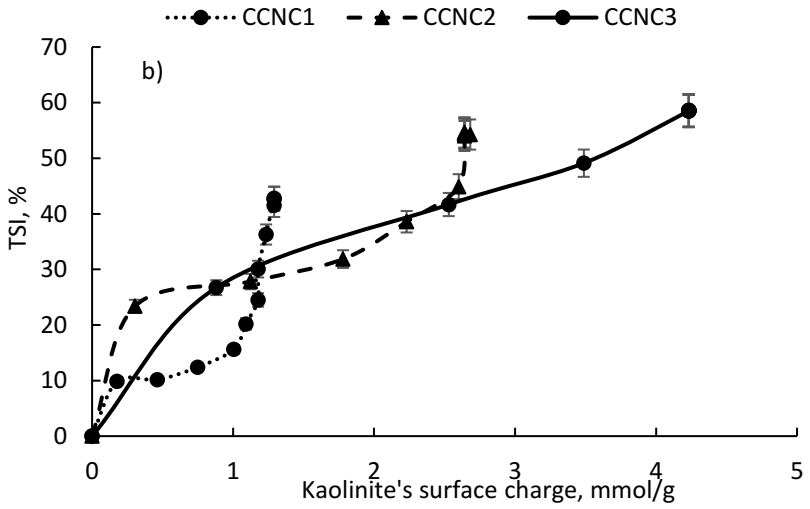
CCNC1
CCNC2
CCNC3
b)
TSI, %
Kaolinite's surface charge, mmol/g

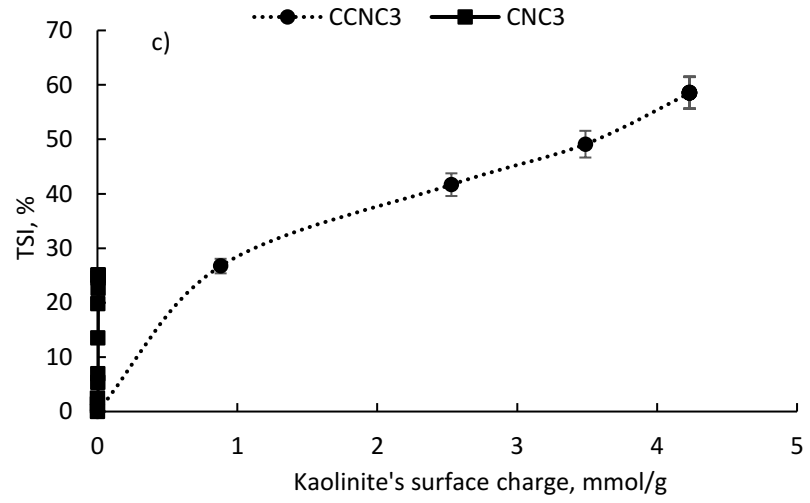
CCNC3
CNC3
c)
TSI, %
Kaolinite's surface charge, mmol/g

Figure 3.3. Improvement in kaolinite suspension stability (TSI, %) versus the calculated a) total charge induced to the system, and b) kaolinite surface charge for all CCNC samples and c) for CNC3/CCNC3 at pH 5.5

3.4.5. pH effect

The zeta potential analysis was performed to determine the isoelectric point (IEP) of the carboxymethylated CNC and CCNC samples as well as that of kaolinite. Figure S3.13 (supplementary information) presents the results for the zeta potential analysis of the particles. As seen, the zeta potential of kaolinite particles varied between 1.72 and - 20.55 mV when pH was changed from 3 to 11 (Moayedi et al., 2011a). As is well known, this pH dependency is due to the protonation and deprotonation of the Al-OH groups presented on the basal plane (O face) and edges of the particles. The zeta potential of kaolinite reached zero at pH 4-4.5, which implies that particles carry neutral charges at this pH (Palomino & Santamarina, 2005; Moayedi et al., 2011a, b). At pH 3, the zeta potential of CCNC1, CCNC2, and CCNC3 were -3.5, -2.5 and -1.6, respectively, which stems from the deprotonation of sulfate half-ester groups attached to CCNC (Table 3.1). By raising pH to 11, carboxymethylated groups on CCNC start to deprotonate and beget a more negative zeta potential of -38.45, -40.01 and -44.56 mV for samples, respectively. At this pH, both sulfate half-ester and carboxymethylate groups are responsible for the negative zeta potential of the suspension. The more negative zeta potential of CCNC3 compared to other CCNC suspensions coincides with its greater carboxymethylate group (Table 3.1).

Basically, pH is one of the most crucial factors in dispersing fine particles and system stabilization (Kamiya et al., 1999). Since a similar trend was observed for all CCNCs (Figure S3.6, S3.8-S3.11), CCNC3 was chosen to demonstrate the effect of pH on CCNC adsorption to kaolinite particle, as well as the stabilization (TSI, %) and zeta potential of the system. As seen in Figure 3.4a, the adsorption was higher for CCNC3 at pH 5.5 than pH 3 and 10, which is directly related to the functionality of CCNC3's carboxymethylated groups as well as kaolinite's surface charges. Although kaolinite particles possess a net positive charge (Figure S3.13) at pH 3, the carboxymethylate groups on CCNC3 are protonated and thus cannot facilitate the charge interaction and adsorption, while the sulfate half-ester groups are deprotonated at pH 3 (pKa of ~ 1.9) and thus play a marginal role in the adsorption. At pH 5.5, kaolinite particles possess sites with positive charges (on the O face and edges), and CCNC3 is negatively charged due to the

deprotonation of their carboxymethylate groups, facilitating the CCNC3 adsorption. The least amount of adsorption (0.1 mg/g) was observed at pH 10. At pH 10, functional groups on both kaolinite and CCNCs are deprotonated and carry high negative charges (the zeta potential for kaolinite was -21 mV at pH 10 (Figure S3.13)), which hampers the adsorption. This limited adsorption might be due to the development of hydrogen bonding between CCNC3 and kaolinite particles. In one study, 0.075 mg/m2 of sodium carboxymethylated cellulose was reported to adsorb on kaolin particles at pH 8.5 (Sjöberg et al. 1999).

Figure 3.4b and c correlate the improvement in suspension's stabilization and zeta potential for CCNC and CNC at different pH to better understand the role of carboxymethylate groups on system stability (the raw stability data for both CNC and CCNC in varied pH are presented in Figures S3.9, S3.10, and S3.11 in the supplementary information). As seen in Figure 3.4b and c a similar trend of increase in the zeta potential and stability of the suspension was observed at pH 3 for CCNC and CNC, which is related to the protonation of CCNC3's carboxymethylate groups. Slightly higher stability and zeta potential of CNC3 at pH 3 might also be because of its slightly higher sulfate half-ester group content (Table 3.1). Performance varied in higher pH values, especially at pH 5.5. At this pH, when the carboxymethylate groups on CCNC are deprotonated, the zeta potential of the suspension was dramatically altered with the addition of CCNC3 (Figure 3.4b) compared to CNC3 (Figure 3.4c). As seen, the enhancement in the system turbidity reached 29% for CNC3 at -26 mV, while both TSI and zeta potential increased to -52 mV and 58% with CCNC3 addition, respectively. This depicts that the carboxymethylate groups played a significant role and improved the system stability by almost 30% at pH 5.5. At pH 10, although the CCNC3 adsorption on kaolinite was limited, the CCNC3 addition led to more improvement in the negative zeta potential and stability of the system compared to CNC3 addition due to the carboxymethylate group content of CCNC3.

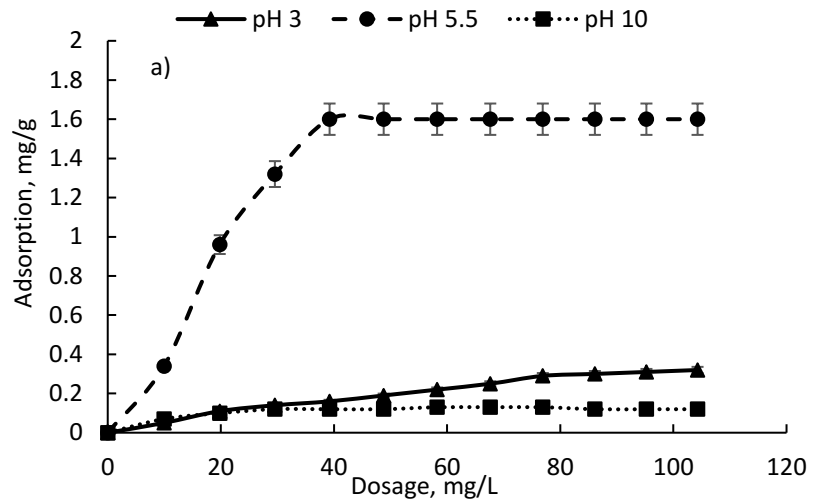
pH 3
pH 5.5
pH 10
a)
Adsorption, mg/g
Dosage, mg/L
0
0.2
0.4
0.6
0.8
1
1.2
1.4
1.6
1.8
2
0
20
40
60
80
100
120

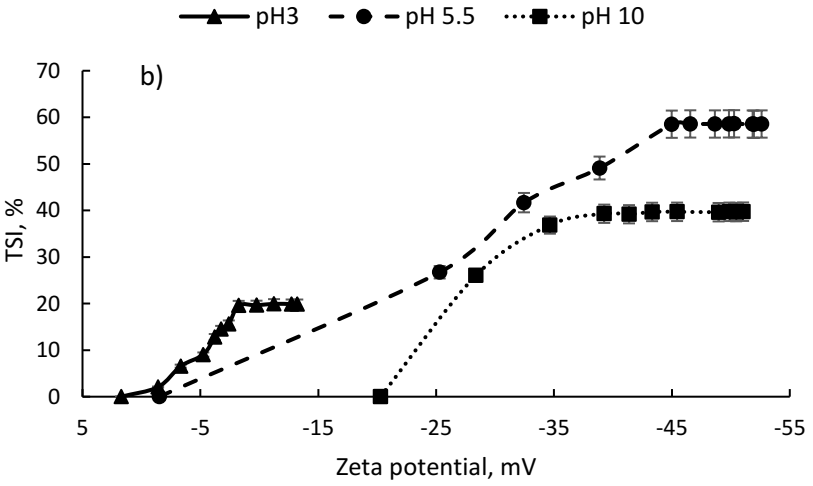
pH3
pH 5.5
pH 10
b)
TSI, %
Zeta potential, mV
0
10
20
30
40
50
60
70
5
-5
-15
-25
-35
-45
-55

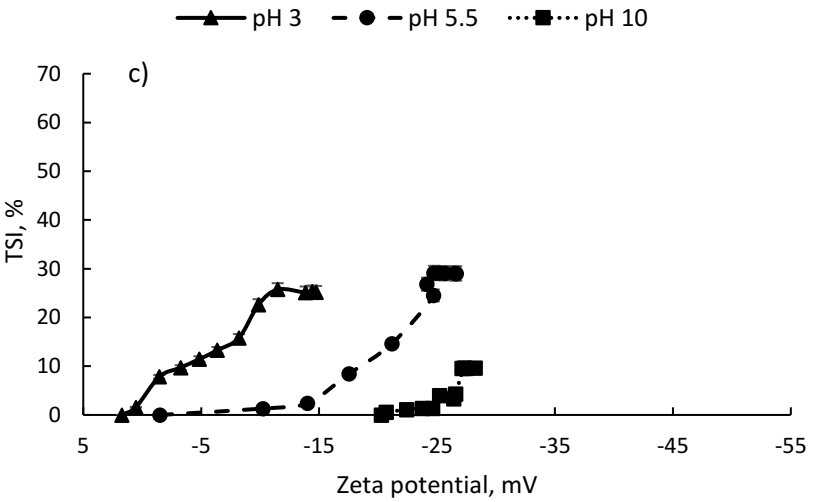
pH 3
pH 5.5
pH 10
c)
TSI, %
Zeta potential, mV
0
10
20
30
40
50
60
70
5
-5
-15
-25
-35
-45
-55

Figure 3.4. a) adsorption of CCNC3 as a function of its dosage, and system stability (TSI) as a function of the suspension's zeta potential for b) CCNC3, and c) CNC3 at three different pH of 3, 5.5 and 10.

3.4.6. Strength of stability

The stability of kaolinite suspension with and without CCNC was analyzed under different centrifugal forces by assessing the settling velocity of the particles. This analysis reveals the strength of stability by applying various centrifugal forces, which indirectly conveys the stability strength over time. As seen in Figure 3.5a, the settling velocity for kaolinite particles in the absence of CCNC in the alkaline condition is lower than in acidic condition in all applied centrifugal forces, which is due to the stronger repulsion force among highly negatively charged particles at alkaline pH (as seen in zeta potential analysis in Figure S3.13). In addition, the settling velocity of the kaolinite particles increased by increasing the RCF (Brunelli, et al., 2016). This was more pronounced for the suspension without CCNC (Figure 3.5a), as well as kaolinite suspension containing CCNC at pH 3 (Figure 3.5b). Figure 3.5b shows the sedimentation velocity of kaolinite particles as a function of CCNC3 addition at three different pH (results for CCNC1 and CCNC2 samples are demonstrated in Figure S3.14a in the supplementary information). As seen, although the addition of CCNC remarkably reduced the settling velocity of kaolinite particles at all pH, this reduction was more pronounced at pH 5.5 than other pH. As discussed above, the adsorbed and unadsorbed CCNC contributed significantly to the zeta potential and stability of the suspension, and this contribution was noticed more remarkably at a higher centrifugal force, which shows the strength of stability of the system in the presence of CCNC at pH 5.5. Since similar results were obtained for all CCNCs in specific pH (minimal difference would be related to a varied amount of carboxymethylated groups on CCNCs), it can be concluded that the size of CCNC has a marginal effect on its performance as a dispersant for kaolinite suspension in long time storage. Figure 3.5c shows the settling velocity of the kaolinite particles as a function of pH in the presence of CNC3 (results for CNC1 and CNC2 samples are demonstrated in Figure S3.14b in the supplementary information). It is seen that although the addition of CNC could reduce the kaolinite settling velocity (Figure 3.5a), it is less effective than CCNC, especially at pH 5.5, due to lack of its adsorption to kaolinite particles. Compared with the results in Figure 3.5b, it can be stated that the

carboxymethylate groups impacted the strength of system stability by 93% and 69% at pH 5.5 and 10, respectively.

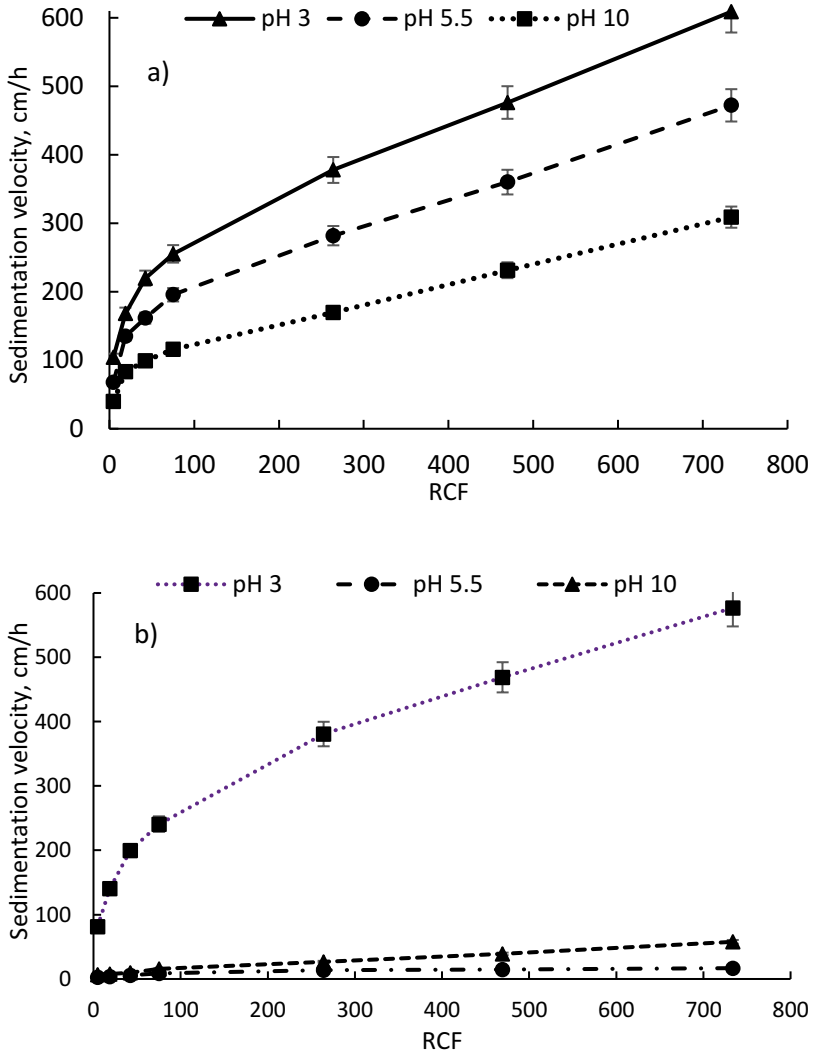

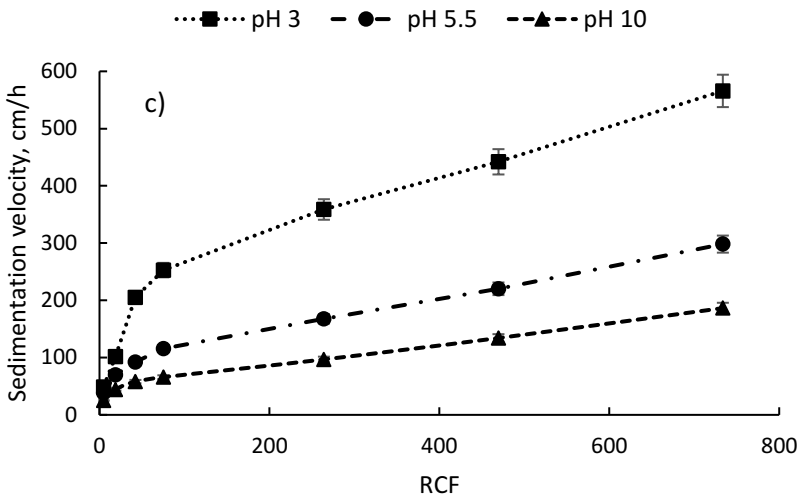

Figure 3.5. Settling velocity of kaolinite particles in the a) absence and b) presence of CCNC, and c) CNC, (50 mg/L) at pH 3, 5.5 and 10 as a function of RCF

3.5 Conclusions

In the present work, CNC with various sizes were carboxymethylated to increase their negative surface charges. With having more carboxymethylate groups, the CCNC3 could adsorb more (and at a lower dosage) onto kaolinite surface and cover more of kaolinite particles upon adsorption. Also, the zeta potential and system stability were improved by 30% when CCNC was used as a dispersant compared to CNC, which could clearly reveal the remarkable role of carboxymethylated groups in the process. The more dramatic adsorption of CCNC3 than other CCNCs imparted the surface charge of the kaolinite particles and hence the zeta potential of the suspension more pronouncedly. The impact of unadsorbed CCNCs on the zeta potential of the system was similar for all CCNCs. It was observed that doubling the size of CCNC begot a faster system stabilization, but it inconsiderably enhanced the level of stabilization. The surface charge density of kaolinite increased upon CCNC adsorption, which directly ameliorated the suspension stabilization. More importantly, the amount of functional groups on the CCNC-based dispersant was found to be a more critical factor than the size of CCNC in settling and strength of settling of the kaolinite particles. The adsorption of CCNC to kaolinite particles was the maximum at pH 5.5, which would be related to the deprotonation of CCNC's carboxymethylate groups, facilitating the charge interaction with kaolinite particles. Furthermore, the strength of suspension stability was observed to be higher at pH 5.5 due to the higher adsorption of CCNC on the particles. Comparing the results of CCNC3 and CNC3 reveals the impact of carboxymethylate group on the strength stability of

the system. To summarize, it was found that a larger CCNC that could be produced in milder hydrolysis condition could response to carboxymethylation more effective and make a more effective dispersant for kaolinite suspension.

3.6 References

Aras, A. (2004). The change of phase composition in kaolinite-and illite-rich clay-based ceramic bodies. *Applied Clay Science*, *24*(3-4), 257-269.

Beck-Candanedo, S., Roman, M., & Gray, D. G. (2005). Effect of reaction conditions on the properties and behavior of wood cellulose nanocrystal suspensions. *Biomacromolecules*, *6*(2), 1048-1054.

Bharti, B., Meissner, J., & Findenegg, G. H. (2011). Aggregation of silica nanoparticles directed by adsorption of lysozyme. *Langmuir*, *27*(16), 9823-9833.

Brunelli, A., Zabeo, A., Semenzin, E., Hristozov, D., & Marcomini, A. (2016). Extrapolated long-term stability of titanium dioxide nanoparticles and multi-walled carbon nanotubes in artificial freshwater. *Journal of Nanoparticle Research*, *18*(5), 113.

Cao, X., Habibi, Y., & Lucia, L. A. (2009). One-pot polymerization, surface grafting, and processing of waterborne polyurethane-cellulose nanocrystal nanocomposites. *Journal of Materials Chemistry*, *19*(38), 7137-7145.

Kong-Win Chang, J., Duret, X., Berberi, V., Zahedi-Niaki, H., & Lavoie, J. M. (2018). Two-step thermochemical cellulose hydrolysis with partial neutralization for glucose production. *Frontiers in chemistry*, *6*, 117.

Chen, D., & van de Ven, T. G. (2016). Flocculation kinetics of precipitated calcium carbonate (PCC) with sterically stabilized nanocrystalline cellulose (SNCC). *Colloids and Surfaces A: Physicochemical and Engineering Aspects*, *506*, 789-793.

Chen, J., Eraghi Kazzaz, A., AlipoorMazandarani, N., Hosseinpour Feizi, Z., & Fatehi, P. (2018). Production of flocculants, adsorbents, and dispersants from lignin. *Molecules*, *23*(4), 868.

Cheng, H., Liu, Q., Zhang, J., Yang, J., & Frost, R. L. (2010). Delamination of kaolinite–potassium acetate intercalates by ball-milling. *Journal of colloid and interface science*, *348*(2), 355-359.

Dodi, G., Hritcu, D., & Popa, M. I. (2011). Carboxymethylation of guar gum: synthesis and characterization. *Cellulose chemistry and Technology*, *45*(3), 171.

Feizi, Z. H., Kazzaz, A. E., Kong, F., & Fatehi, P. (2019). Evolving a flocculation process for isolating lignosulfonate from solution. *Separation and Purification Technology*, *222*, 254-263.

Ferek, R. J., Reid, J. S., Hobbs, P. V., Blake, D. R., & Liousse, C. (1998). Emission factors of hydrocarbons, halocarbons, trace gases and particles from biomass burning in Brazil. *Journal of Geophysical Research: Atmospheres*, *103*(D24), 32107-32118.

Gan, L., Zhou, M., Yang, D., & Qiu, X. (2013). Preparation and evaluation of carboxymethylated lignin as dispersant for aqueous graphite suspension using Turbiscan Lab analyzer. *Journal of dispersion science and technology*, *34*(5), 644-650.

Gharanjig, H., Gharanjig, K., & Khosravi, A. (2019). Effects of the side chain density of polycarboxylate dispersants on dye dispersion properties. *Coloration Technology*, *135*(2), 160-168.

Hamedi, M. M., Hajian, A., Fall, A. B., Hakansson, K., Salajkova, M., Lundell, F., ... & Berglund, L. A. (2014). Highly conducting, strong nanocomposites based on nanocellulose-assisted aqueous dispersions of single-wall carbon nanotubes. *ACS nano*, *8*(3), 2467-2476.

Hanif, Z., Ahmed, F. R., Shin, S. W., Kim, Y. K., & Um, S. H. (2014). Size-and dose-dependent toxicity of cellulose nanocrystals (CNC) on human fibroblasts and colon adenocarcinoma. *Colloids and Surfaces B: Biointerfaces*, *119*, 162-165.

He, W., Gao, W., & Fatehi, P. (2017). Oxidation of kraft lignin with hydrogen peroxide and its application as a dispersant for kaolin suspensions. *ACS Sustainable Chemistry & Engineering*, *5*(11), 10597-10605.

Kamiya, H., Fukuda, Y., Suzuki, Y., Tsukada, M., Kakui, T., & Naito, M. (1999). Effect of polymer dispersant structure on electrosteric interaction and dense alumina suspension behavior. *Journal of the American Ceramic Society*, *82*(12), 3407-3412.

Kaombe, D. D., Lenes, M., Toven, K., & Glomm, W. R. (2013). Turbiscan as a tool for studying the phase separation tendency of pyrolysis oil. *Energy & fuels*, *27*(3), 1446-1452.

Kazzaz, A. E., Feizi, Z. H., & Fatehi, P. (2018a). Interaction of sulfomethylated lignin and aluminum oxide. *Colloid and Polymer Science*, *296*(11), 1867-1878.

Kazzaz, A. E., Feizi, Z. H., Kong, F., & Fatehi, P. (2018b). Interaction of poly (acrylic acid) and aluminum oxide particles in suspension: particle size effect. *Colloids and Surfaces A: Physicochemical and Engineering Aspects*, *556*, 218-226.

Kłosek-Wawrzyn, E., Małolepszy, J., & Murzyn, P. (2013). Sintering behavior of kaolin with calcite. *Procedia Engineering*, *57*, 572-582.

Koci, K., Matějka, V., Kovář, P., Lacný, Z., & Obalová, L. (2011). Comparison of the pure TiO_2 and kaolinite/TiO_2 composite as catalyst for CO_2 photocatalytic reduction. *Catalysis Today*, *161*(1), 105-109.

Konduri, M. K., & Fatehi, P. (2016). Synthesis and characterization of carboxymethylated xylan and its application as a dispersant. *Carbohydrate polymers*, *146*, 26-35.

Konduri, M. K., & Fatehi, P. (2018a). Designing anionic lignin based dispersant for kaolin suspensions. *Colloids and Surfaces A: Physicochemical and Engineering Aspects*, *538*, 639-650.

Konduri, M. K., & Fatehi, P. (2018b). Adsorption and dispersion performance of oxidized sulfomethylated kraft lignin in coal water slurry. *Fuel Processing Technology*, *176*, 267-275.

Lee, H. J., Lee, H. S., Seo, J., Kang, Y. H., Kim, W., & Kang, T. H. K. (2019). State-of-the-art of cellulose nanocrystals and optimal method for their dispersion for construction-related applications. *Applied Sciences*, *9*(3), 426.

Lee, H. V., Hamid, S. B. A., & Zain, S. K. (2014). Conversion of lignocellulosic biomass to nanocellulose: structure and chemical process. *The Scientific World Journal*, *2014*, 1-20.

Ma, X., Cheng, Y., Qin, X., Guo, T., Deng, J., & Liu, X. (2017). Hydrophilic modification of cellulose nanocrystals improves the physicochemical properties of cassava starch-based nanocomposite films. *LWT*, *86*, 318-326.

Malaspina, D. C., & Faraudo, J. (2019). Molecular insight into the wetting behavior and amphiphilic character of cellulose nanocrystals. *Advances in colloid and interface science*, *267*, 15-25.

Mariano, M., El Kissi, N., & Dufresne, A. (2015). Melt processing of cellulose nanocrystal reinforced polycarbonate from a masterbatch process. *European Polymer Journal*, *69*, 208-223.

Ming, S., Chen, G., Wu, Z., Su, L., He, J., Kuang, Y., & Fang, Z. (2016). Effective dispersion of aqueous clay suspension using carboxylated nanofibrillated cellulose as dispersant. *Rsc Advances*, *6*(44), 37330-37336.

Moayedi, H., Huat, B. B., Kazemian, S., Daneshmand, S., Moazami, D., & Niroumand, H. (2011a). Electrophoresis of suspended kaolinite in multivalent electrolyte solution. *International Journal of Electrochemical Science*, *6*, 6514-6524.

Moayedi, H., Asadi, A., Moayedi, F., & Huat, B. B. (2011b). Zeta potential of tropical soil in presence of polyvinyl alcohol. *International Journal of Electrochemical Science*, *6*(5), 1294-1306.

Montanari, S., Roumani, M., Heux, L., & Vignon, M. R. (2005). Topochemistry of carboxylated cellulose nanocrystals resulting from TEMPO-mediated oxidation. *Macromolecules*, *38*(5), 1665-1671.

Murray H H, Lyons SC (1956) Correlation of paper-coating quality with degree of crystal perfection of kaolinite. *Clays and Clay Minerals* 4, 31-40.

Naderi, A., Lindström, T., & Sundström, J. (2014). Carboxymethylated nanofibrillated cellulose: rheological studies. *Cellulose*, *21*(3), 1561-1571.

Olivier, C., Moreau, C., Bertoncini, P., Bizot, H., Chauvet, O., & Cathala, B. (2012). Cellulose nanocrystal-assisted dispersion of luminescent single-walled carbon nanotubes for layer-by-layer assembled hybrid thin films. *Langmuir*, *28*(34), 12463-12471.

Ostolska, I., & Wiśniewska, M. (2014). Application of the zeta potential measurements to explanation of colloidal Cr 2 O 3 stability mechanism in the presence of the ionic polyamino acids. *Colloid and polymer science*, *292*(10), 2453-2464.

Palomino, A. M., & Santamarina, J. C. (2005). Fabric map for kaolinite: effects of pH and ionic concentration on behavior. *Clays and Clay minerals*, *53*(3), 211-223.

Qin, Y., Yu, L., Wu, R., Yang, D., Qiu, X., & Zhu, J. Y. (2016). Biorefinery lignosulfonates from sulfite-pretreated softwoods as dispersant for graphite. *ACS Sustainable Chemistry & Engineering*, *4*(4), 2200-2205.

Reid, M. S., Villalobos, M., & Cranston, E. D. (2017). The role of hydrogen bonding in non-ionic polymer adsorption to cellulose nanocrystals and silica colloids. *Current Opinion in Colloid & Interface Science*, *29*, 76-82.

Rubio-Hernández, F. J., Páez-Flor, N. M., Gómez-Merino, A. I., Sánchez-Luque, F. J., Delgado-García, R., & Goyos-Pérez, L. (2016). The influence of high-concentration Na hexametaphosphate dispersant on the rheological behavior of aqueous kaolin dispersions. *Clays and Clay Minerals*, *64*(3), 210-219.

Santi, C., Certini, G., & D'Acqui, L. P. (2006). Direct determination of organic carbon by dry combustion in soils with carbonates. *Communications in soil science and plant analysis*, *37*(1-2), 155-162.

Singh, B. P., Nayak, S., Samal, S., Bhattacharjee, S., & Besra, L. (2012). Characterization and dispersion of multiwalled carbon nanotubes (MWCNTs) in aqueous suspensions: surface chemistry aspects. *Journal of dispersion science and technology*, *33*(7), 1021-1029.

Sjöberg, M., Bergström, L., Larsson, A., & Sjöström, E. (1999). The effect of polymer and surfactant adsorption on the colloidal stability and rheology of kaolin dispersions. *Colloids and Surfaces A: Physicochemical and Engineering Aspects*, *159*(1), 197-208.

Tan, C., Peng, J., Lin, W., Xing, Y., Xu, K., Wu, J., & Chen, M. (2015). Role of surface modification and mechanical orientation on property enhancement of cellulose nanocrystals/polymer nanocomposites. *European Polymer Journal*, *62*, 186-197.

Tang, J., Sisler, J., Grishkewich, N., & Tam, K. C. (2017). Functionalization of cellulose nanocrystals for advanced applications. *Journal of colloid and interface science*, *494*, 397-409.

Tombacz, E., & Szekeres, M. (2006). Surface charge heterogeneity of kaolinite in aqueous suspension in comparison with montmorillonite. *Applied Clay Science*, *34*(1-4), 105-124.

Wågberg, L., Decher, G., Norgren, M., Lindström, T., Ankerfors, M., & Axnäs, K. (2008). The build-up of polyelectrolyte multilayers of microfibrillated cellulose and cationic polyelectrolytes. *Langmuir*, *24*(3), 784-795.

Wang, Q., Li, Y., & Wang, Y. (2011). Optimizing the weight loss-on-ignition methodology to quantify organic and carbonate carbon of sediments from diverse sources. *Environmental monitoring and assessment*, *174*(1-4), 241-257.

Wei, Z., & Gao, Y. (2016). Physicochemical properties of β-carotene emulsions stabilized by chitosan–chlorogenic acid complexes. *LWT-Food Science and Technology*, *71*, 295-301.

Yang, L., Lu, S., Li, J., Zhang, F., & Cha, R. (2016). Nanocrystalline cellulose-dispersed AKD emulsion for enhancing the mechanical and multiple barrier properties of surface-sized paper. *Carbohydrate polymers*, *136*, 1035-1040.

Yukselen, Y., & Kaya, A. (2003). Zeta potential of kaolinite in the presence of alkali, alkaline earth and hydrolyzable metal ions. *Water, Air, and Soil Pollution*, *145*(1-4), 155-168.

3.7 Appendix A. Supplementary material

Carboxymethylated Cellulose Nanocrystals as a Clay Suspension Dispersant: Effect of Size and Surface Functional Groups

Zahra Hosseinpour Feizi, Pedram Fatehi*
Chemical Engineering Department, Lakehead University, 955 Oliver Road, Thunder Bay, Ontario P7B 5E1, Canada
* Corresponding author, email: pfatehi@lakeheadu.ca; tel: 807-343-8697; fax: 807-346-7943

Supporting experimental section

Sulfate half-ester and carboxymethyl group content analysis

The sulfonate and carboxymethyl group contents were calculated by equation S3.1 and S3.2, respectively (Chen & van de Ven, 2016; Konduri & Fatehi, 2016).

Equation S3.1

$$Sulfate\ half\ ester\ group = \frac{V_i \times C_{NaOH}}{m_{CNC}}$$

Equation S3.2

$$Carboxymethyl\ group = \frac{(V_{ii} - V_i) \times C_{NaOH}}{m_{CNC}}$$

where V_i and V_{ii} are the volume (mL) of NaOH which neutralized strong and weak acidic groups, respectively, C_{NaOH} is the NaOH concentration (mmol/L) and m is the mass of dried weight (g) of CNC.

Charge density analysis

For analyzing the surface charge density of the kaolinite particles, 0.2 g of the sample was suspended in 20 mL of PDADMAC solution (0.005 M). The suspension was stirred at 150 rpm for 2 h at 30 °C and then filtered using nylon filters with a size of 0.45 μm. The filtrate was then titrated against PVSK solution (0.0055 M) using a particle charge detector, Mütek PCD 04 titrator (Herrsching, Germany). The titration analysis was carried out for PDADMAC solution before mixing with kaolinite as a control, and the difference was accounted for determining the surface charge density of the particles (Wang et al., 2017).

Thermogravimetric analysis (TGA)

The thermal analysis was performed on kaolinite and CNC samples prior to adsorption analysis to confirm the decomposition temperature range of the samples using a thermogravimetric analyzer, TGA, i-1000 series, Instrument Specialist Inc. For this experiment, samples which were left in 105 °C (for kaolinite) or 60 °C (for CNCs) for one or two days were submitted to the instrument and the analysis was performed under nitrogen with a stable flow rate of 35 mL/min. Each sample heated from 25 to 800 °C with the rate of 10 °C/min.

<u>Supporting information figures</u>

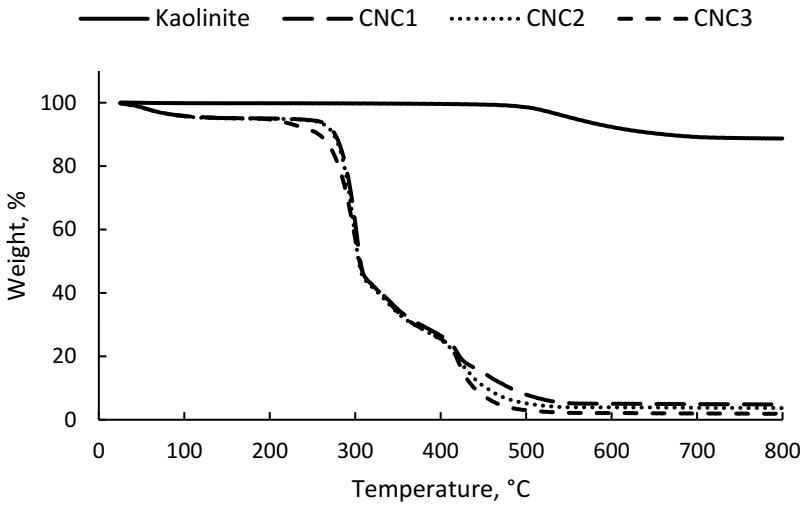

Figure S3.1. Decomposition trend of kaolinite and CNC samples obtained from TGA analysis

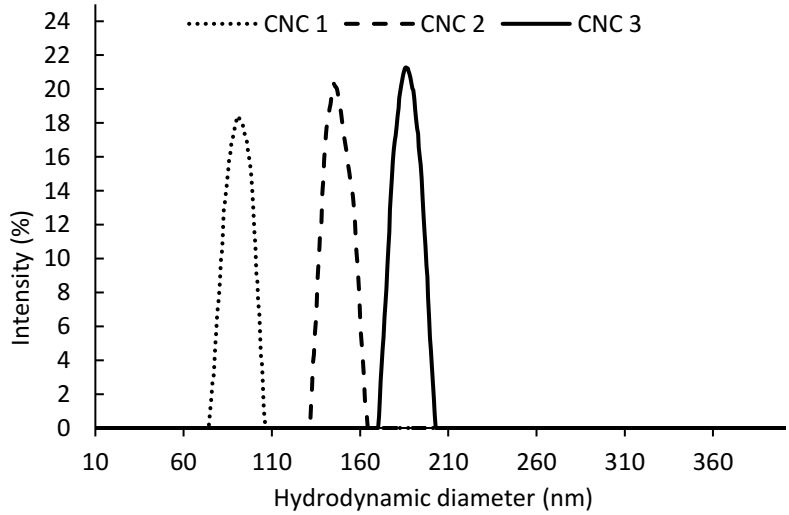

Figure S3.2. Hydrodynamic size of produced CNC samples centered at 90 (CNC1), 144 (CNC2), and 185 (CNC3) nm conducted at 25 °C.

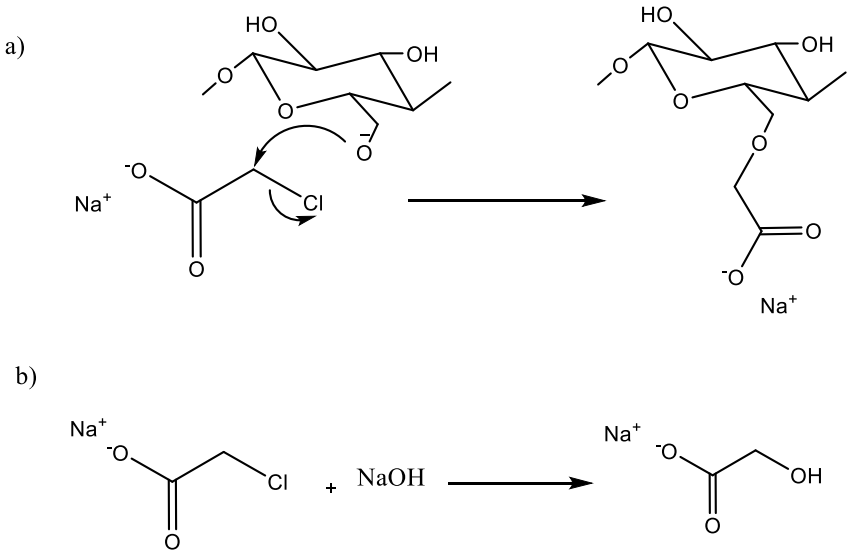

Figure S3.3. a) Carboxymethylation of CNC using SCA. The reaction proceeded at pH 12.5, at 55 °C for 3 h. R is either H or $C_2H_3O_2$. b) sodium glycolate production in the side reaction.

FTIR analysis for modification reaction

The FTIR analysis was carried out for CNC, and CCNC samples and the results are shown in Figures S4 and S5. The peak between 3267 and 3400 cm^{-1} is assigned to the O-H stretching, and the peak at 2897 and 1024 cm^{-1} corresponds to the C-H and C-O stretching of the pyranose ring skeletal, respectively (Rahman et al., 2017; Onyianta et al., 2018). As seen, the spectra for the CNC samples are similar, and there is no noticeable difference in their chemical structures. The appearance of the peak at 1595 cm^{-1} in Figure S5a, b corresponds to the C-O stretching of the attached carboxymethyl (CH_2COO-) group (Rahman et al., 2017; Onyianta et al., 2018), which confirms the success of CNC carboxymethylation. The CCNC adsorption on kaolinite particles through FTIR analysis is discussed in further sections in this paper.

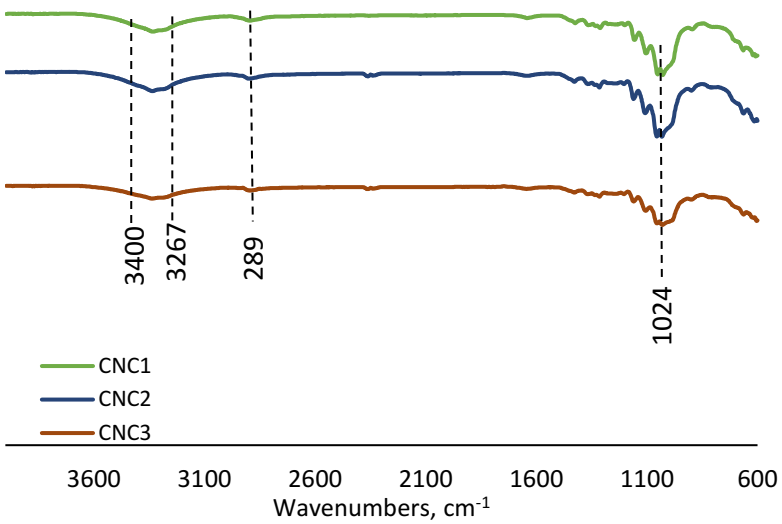

Figure S4. FTIR spectrum for unmodified CNC samples with varied sizes.

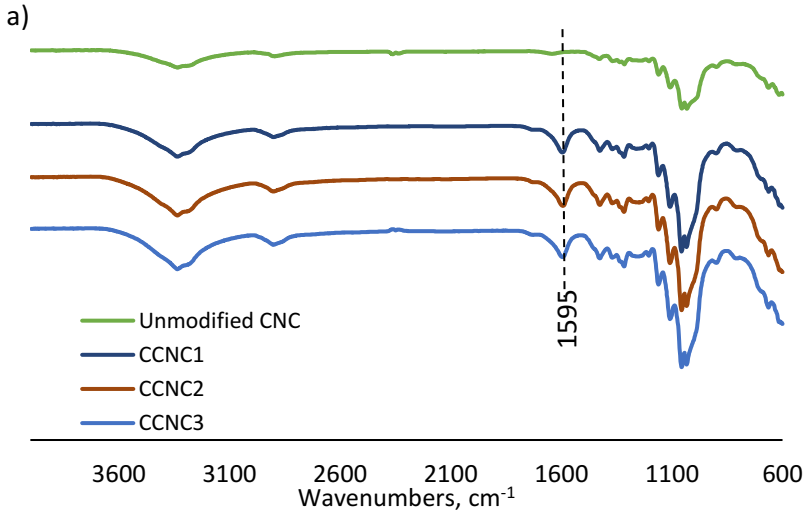

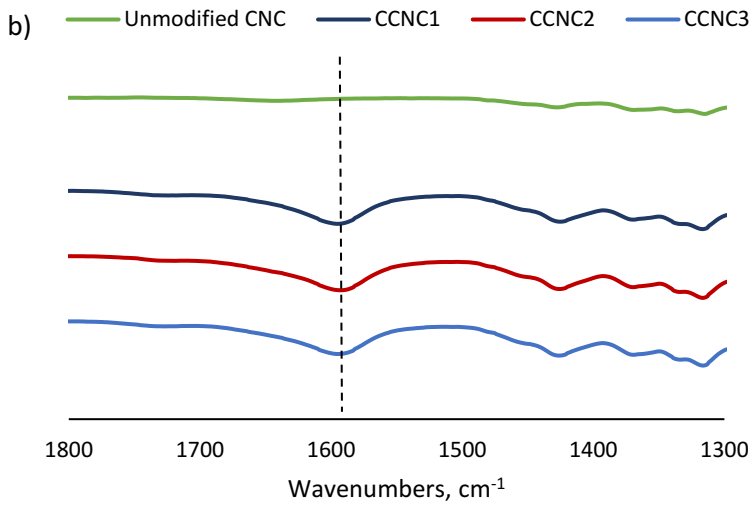

Figure S3.5. FTIR spectrum for carboxymethylated CNC samples in a) a broad range of 600-400 and b) a narrower range of 1300-1800 cm^{-1} for magnification

Physiochemistry of kaolinite particles

Kaolinite particles are composed of silicon-oxygen tetrahedra and aluminum -oxygen- hydroxyl octahedra, which further develop silica tetrahedral (T) and alumina octahedral (O) sheets (Kumar et al., 2016). These sheets layer in a lamella configuration by sharingoxygen atom. In other words, the hydroxyl groups of the O sheet develop hydrogen bonds with the oxygen of the T sheet, which makes kaolinite particle (Kumar et al., 2016). The basal planes and broken edges of the particle have different structures and surface charges. The T basal plane is negatively charged and supposed to be pH independent because of the isomorphous substitution of Al^{3+} for Si^{4+}. The charge on the O basal plane and edges is pH-dependent as they carry positive charges in acidic pH and negative charges in alkaline pH as a result of the protonation-deprotonation of exposed hydroxyl groups (Tombacz & Szekeres, 2006; Kumar et al., 2017).

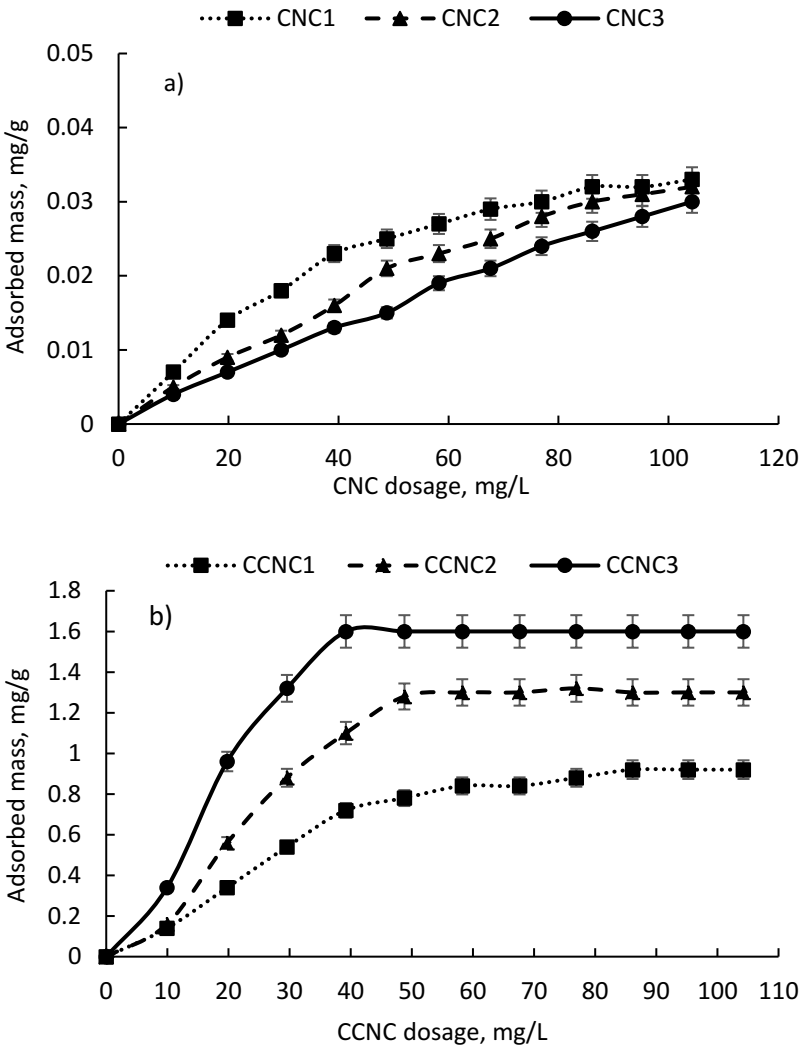

Figure S3.6. Adsorption isotherms of a) CNC, and b) CCNC nanoparticles on kaolinite particles at different dosages ranging from 9.95 to 104.27 mg/L at pH 5.5.

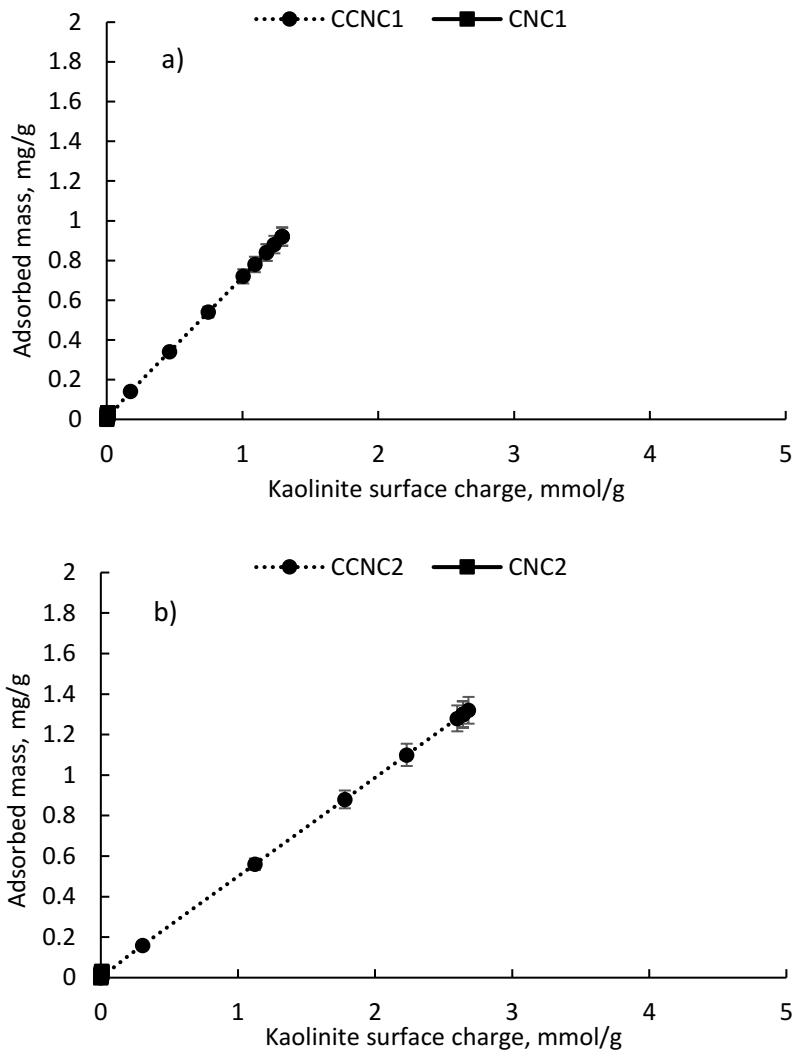

Figure S3.7. a) CNC1/CCNC1, and b) CNC2/CCNC2 adsorption onto kaolinite surface with respect to the total charge density of kaolinite, at pH 5.5.

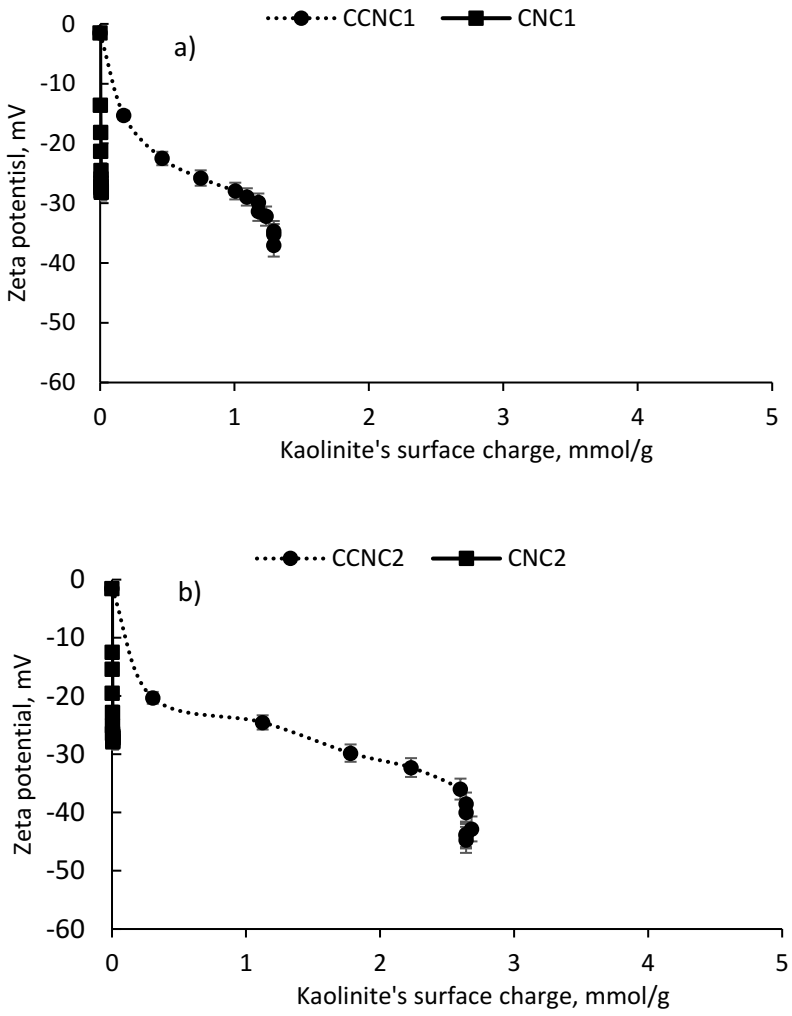

Figure S3.8. Changes in suspension zeta potential versus the calculated total negative charge density of kaolinite for a) CNC1/CCNC1, and b) CNC2/ CCNC2, at pH 5.5

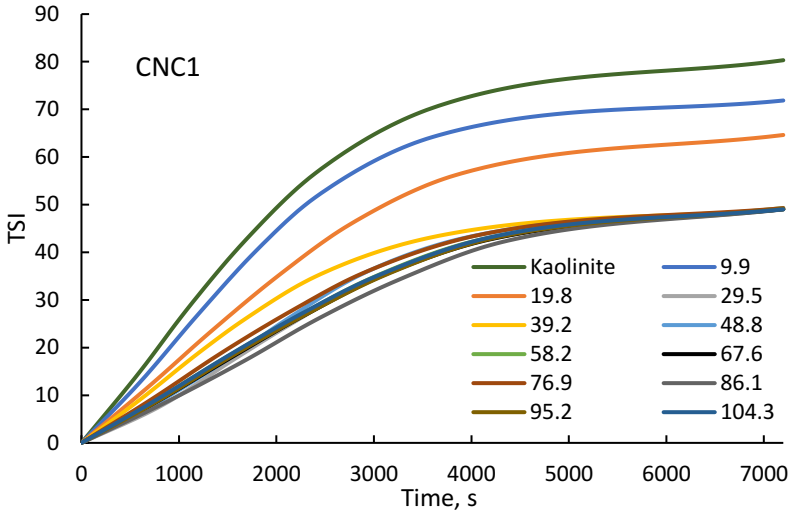
CNC1
TSI
Time, s
Kaolinite
9.9
19.8
29.5
39.2
48.8
58.2
67.6
76.9
86.1
95.2
104.3

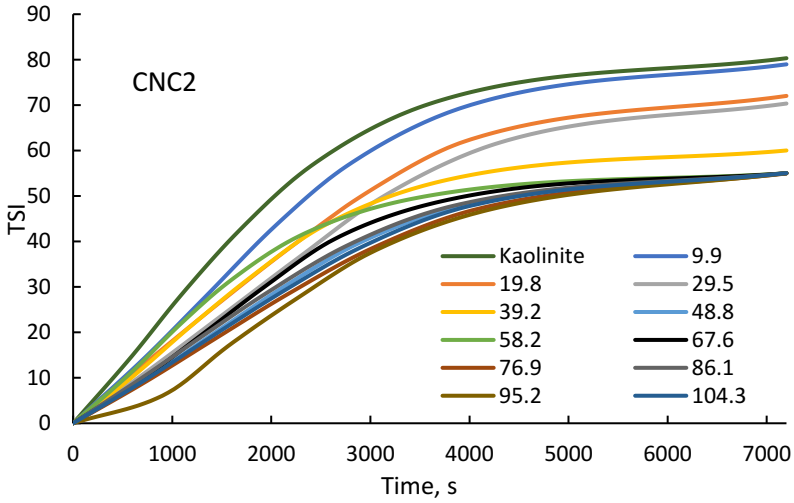
CNC2
TSI
Time, s
Kaolinite
9.9
19.8
29.5
39.2
48.8
58.2
67.6
76.9
86.1
95.2
104.3

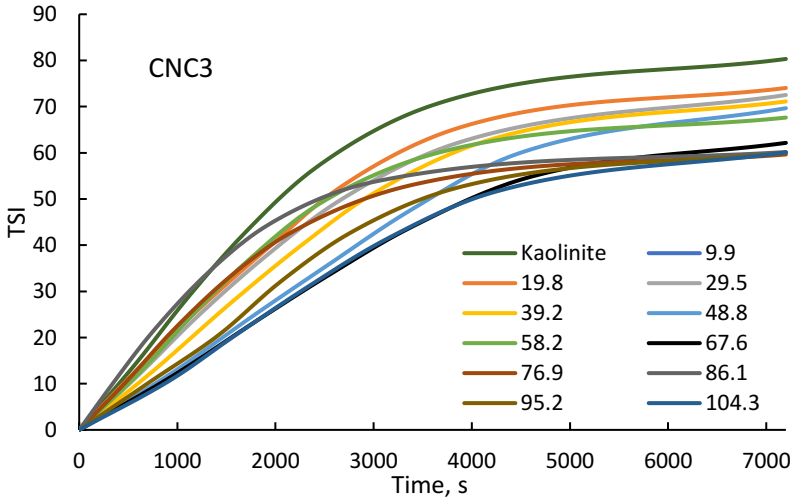
CNC3
TSI
Time, s
Kaolinite
9.9
19.8
29.5
39.2
48.8
58.2
67.6
76.9
86.1
95.2
104.3

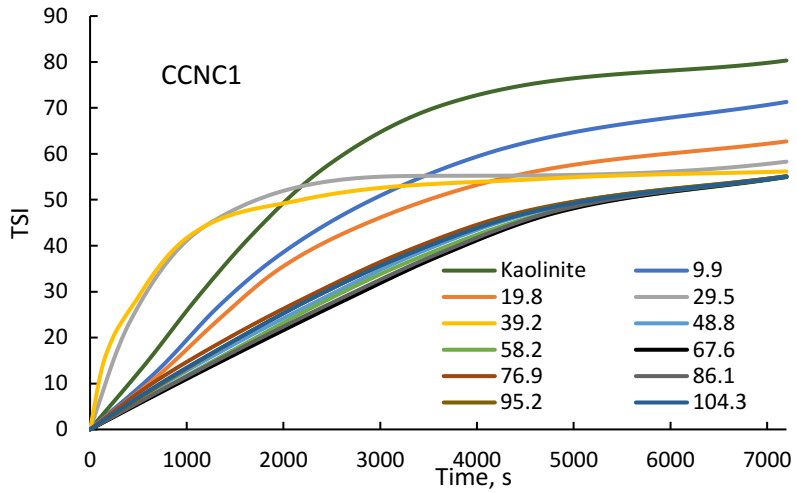
CCNC1
TSI
Time, s
Kaolinite
9.9
19.8
29.5
39.2
48.8
58.2
67.6
76.9
86.1
95.2
104.3

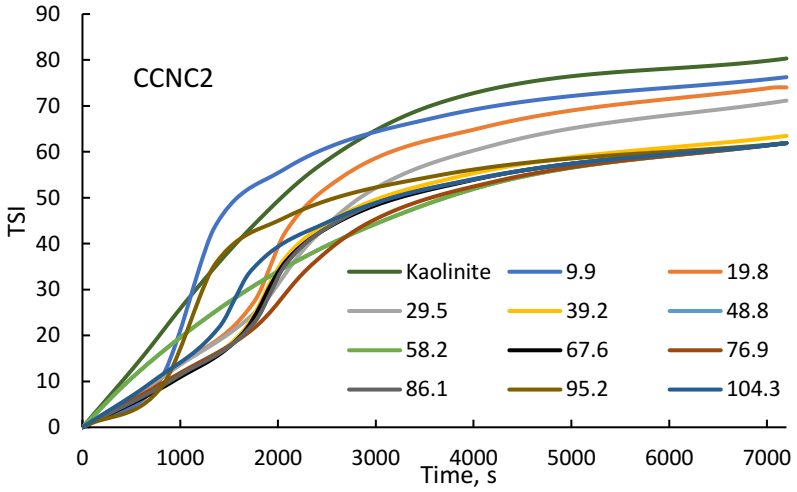
CCNC2
TSI
Time, s
Kaolinite
9.9
19.8
29.5
39.2
48.8
58.2
67.6
76.9
86.1
95.2
104.3

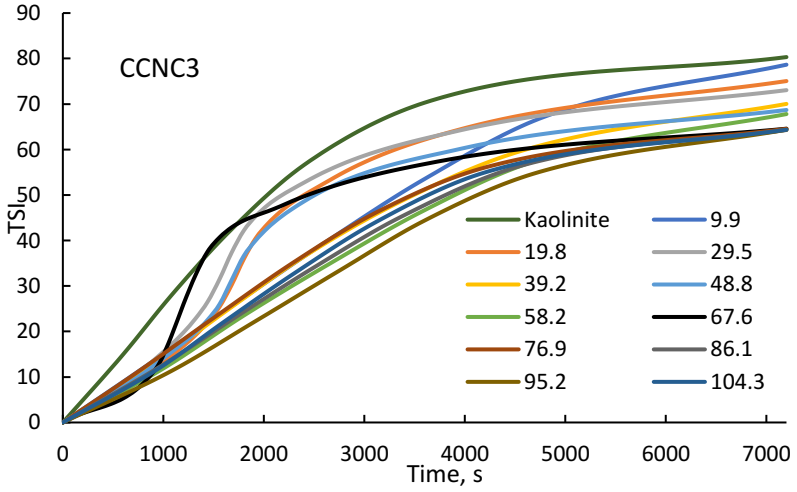
CCNC3
TSI
Time, s
Kaolinite
9.9
19.8
29.5
39.2
48.8
58.2
67.6
76.9
86.1
95.2
104.3

Figure S3.9. The TSI raw data of kaolinite suspension in the absence and presence of CNC/CCNC samples at pH 3. Legends are the CNC/CCNC dosages (mg//L).

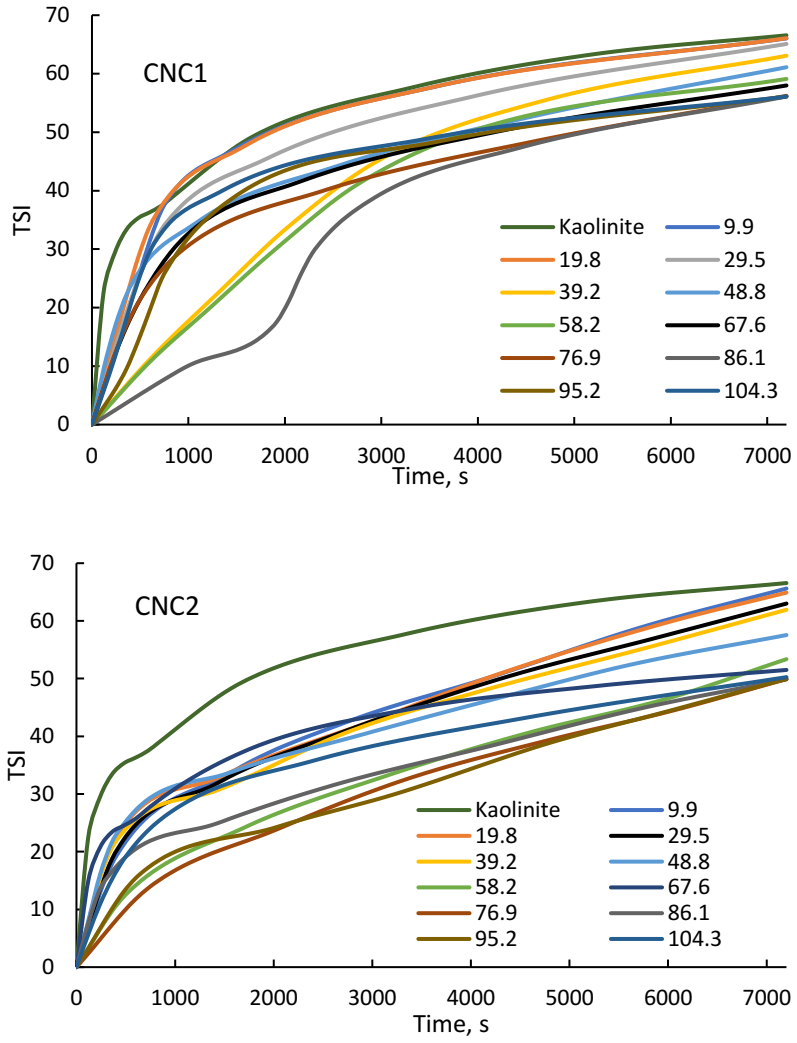

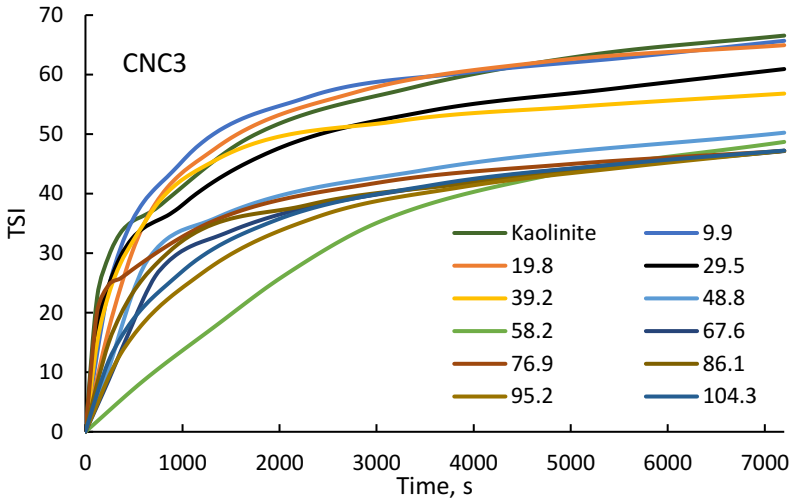
CNC3
TSI
Time, s
Kaolinite
9.9
19.8
29.5
39.2
48.8
58.2
67.6
76.9
86.1
95.2
104.3

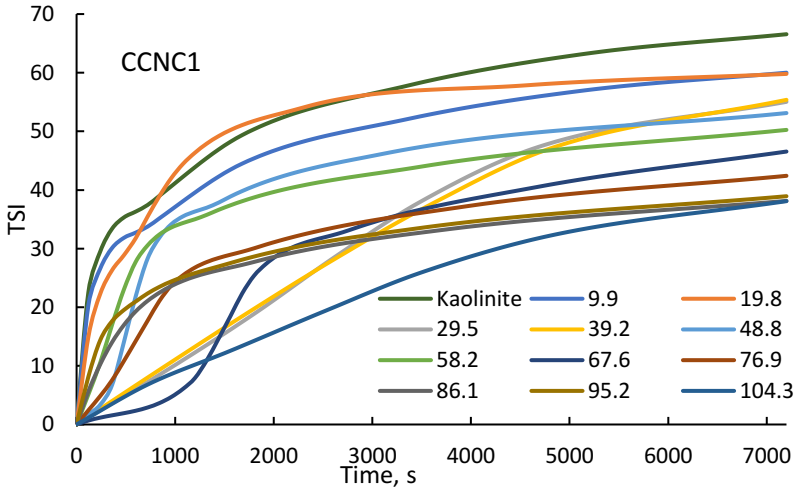
CCNC1
TSI
Time, s
Kaolinite
9.9
19.8
29.5
39.2
48.8
58.2
67.6
76.9
86.1
95.2
104.3

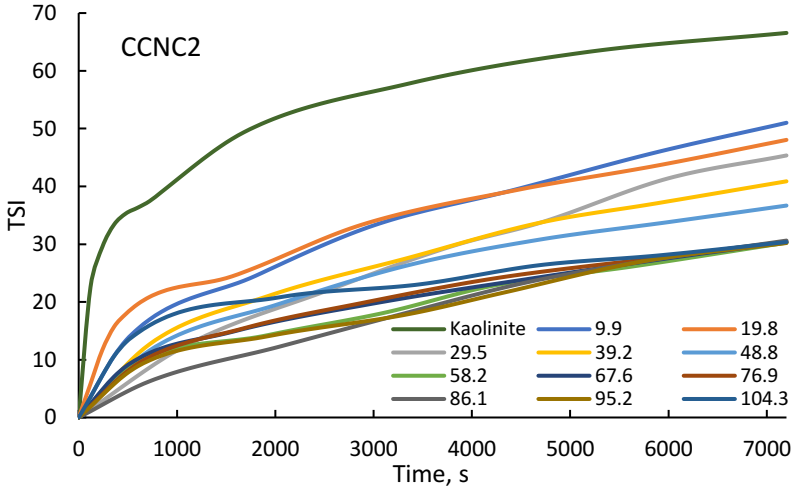
CCNC2
TSI
Time, s
Kaolinite
9.9
19.8
29.5
39.2
48.8
58.2
67.6
76.9
86.1
95.2
104.3

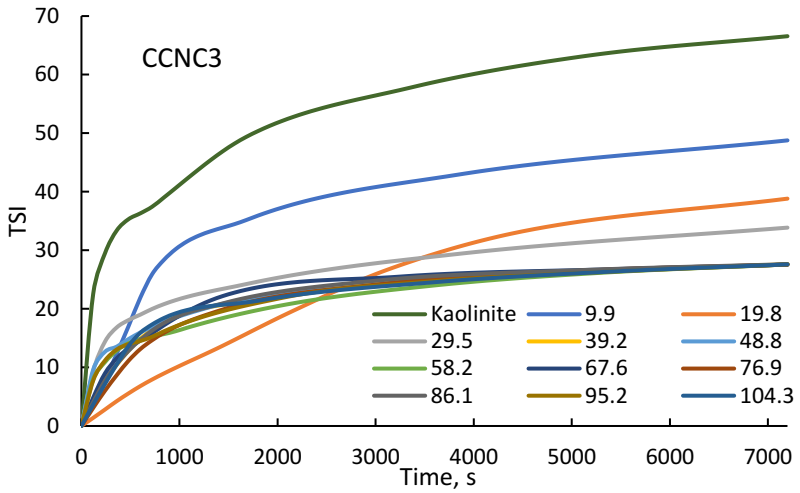

Figure S3.10. The TSI raw data of kaolinite suspension in the absence and presence of CNC/CCNC samples at pH 5.5. Legends are the CNC/CCNC dosages (mg//L).

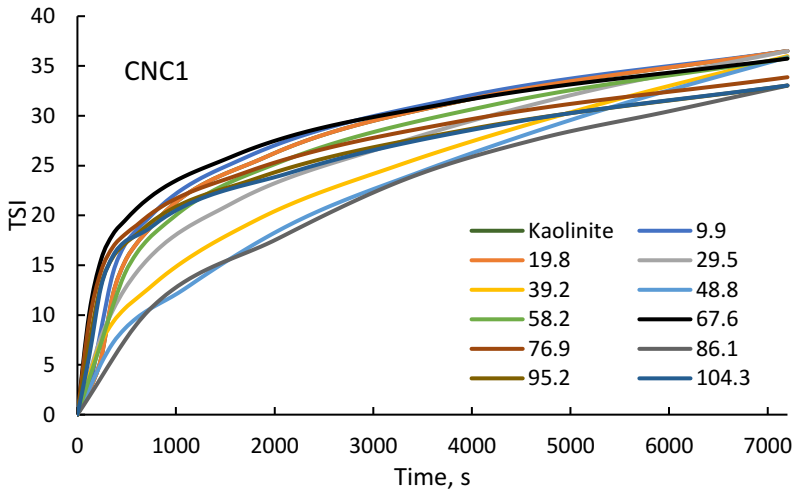

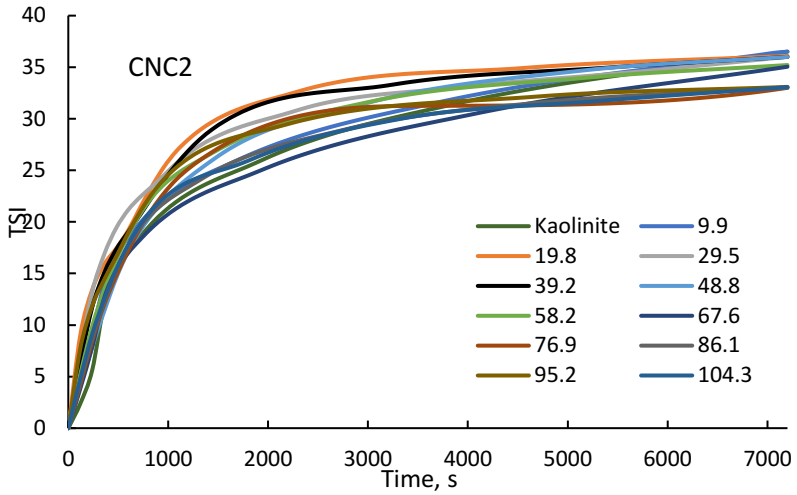
CNC2
TSI
Time, s
Kaolinite
9.9
19.8
29.5
39.2
48.8
58.2
67.6
76.9
86.1
95.2
104.3

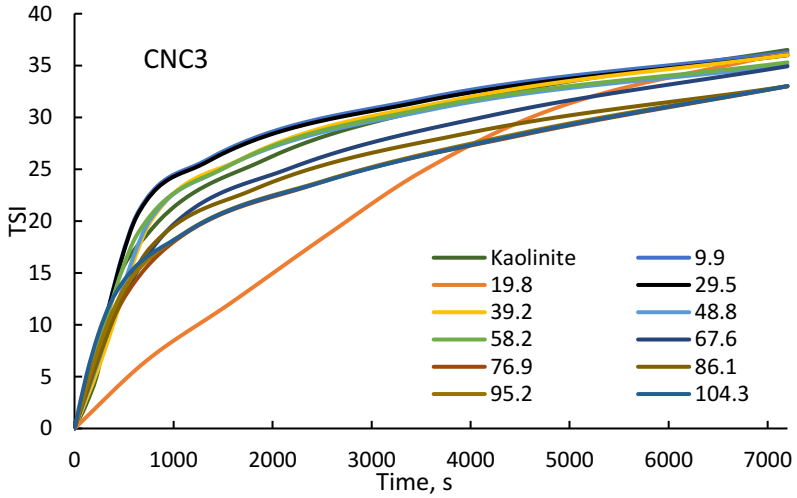
CNC3
TSI
Time, s
Kaolinite
9.9
19.8
29.5
39.2
48.8
58.2
67.6
76.9
86.1
95.2
104.3

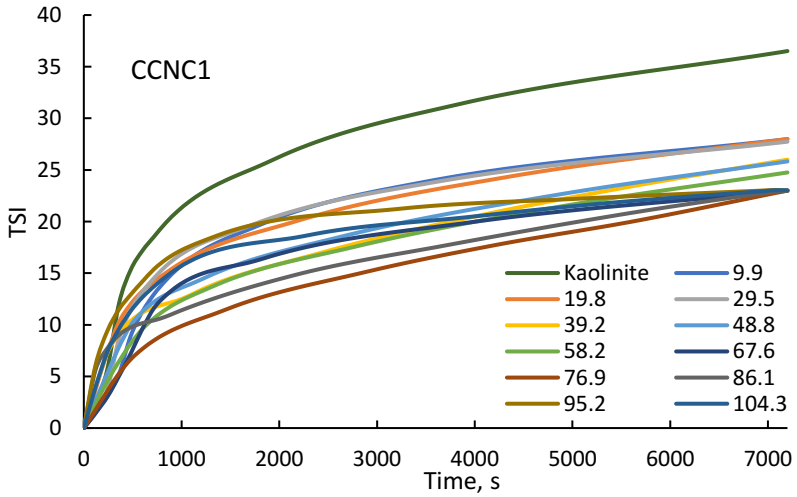
CCNC1
TSI
Time, s
Kaolinite
9.9
19.8
29.5
39.2
48.8
58.2
67.6
76.9
86.1
95.2
104.3

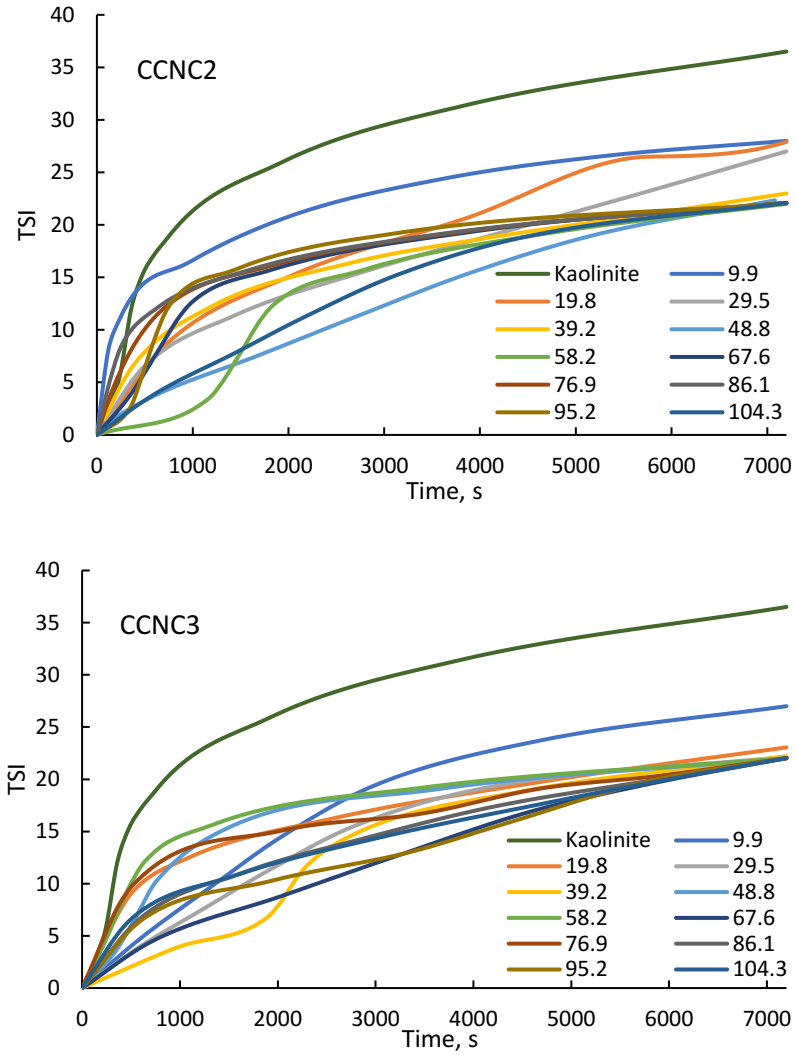

Figure S3.11. The TSI raw data of kaolinite suspension in the absence and presence of CNC/CCNC samples at pH 10. Legends are the CNC/CCNC dosages (mg//L).

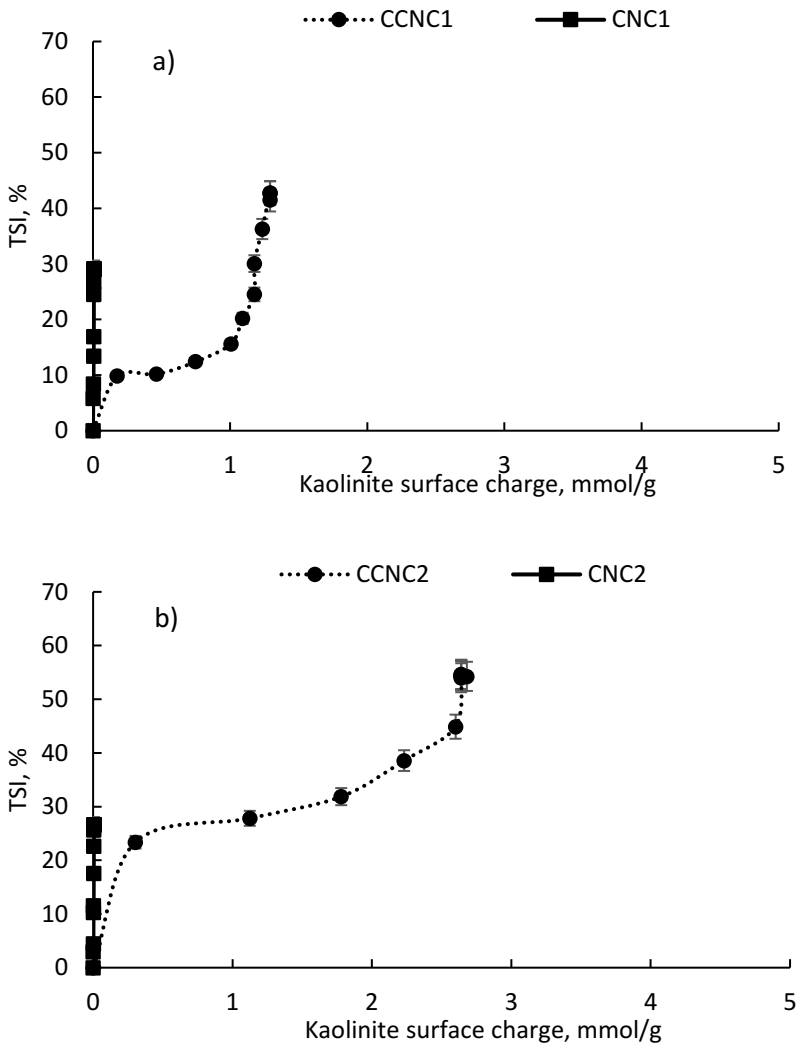

Figure S3.12. Improvement in kaolinite suspension stability (TSI, %) versus the calculated kaolinite particle surface charge for a) CNC1/CCNC1, and b) CNC2/CCNC2, at pH 5.5

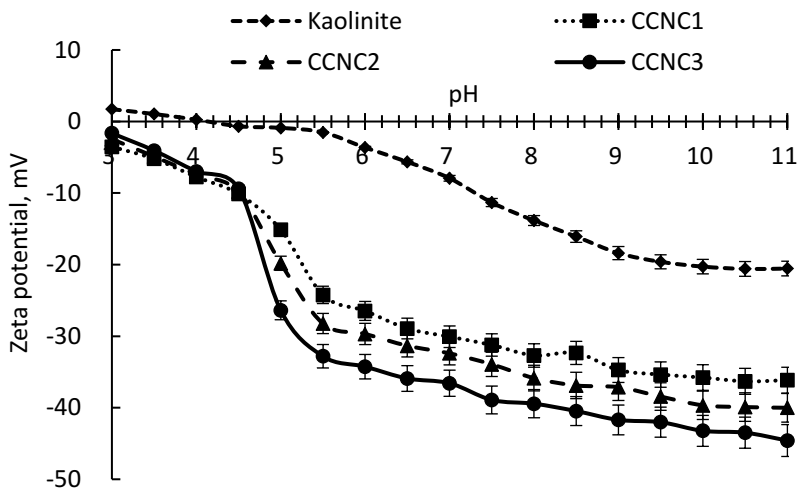

Figure S3.13. Zeta potential analysis of the CCNC samples and kaolinite conducted at different pH ranging from 3-11 at 25°C.

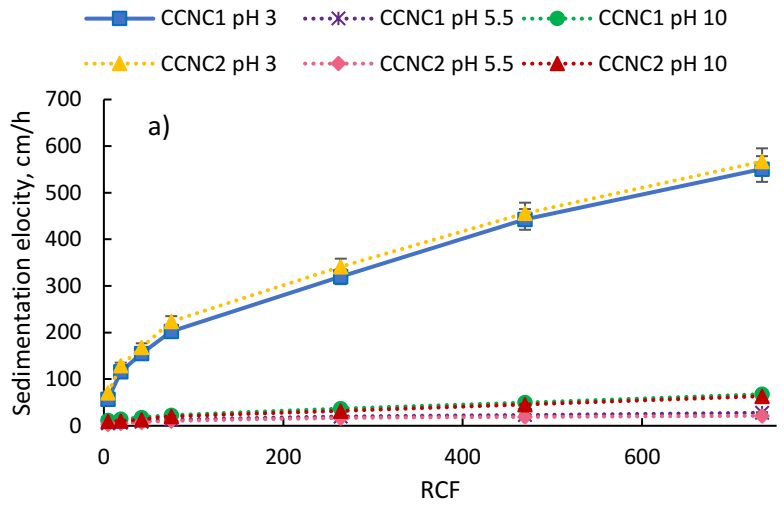

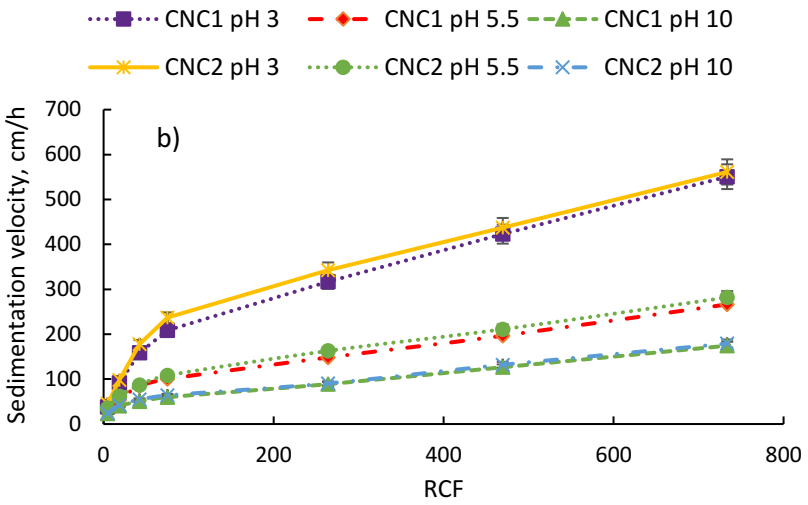

Figure S3.14. Settling velocity of kaolinite particles in the presence of qa) CCNC, and b) CNC, (50 mg/L) at pH 3, 5.5 and 10 as a function of RCF

References

Chen, D., & van de Ven, T. G. (2016). Flocculation kinetics of precipitated calcium carbonate (PCC) with sterically stabilized nanocrystalline cellulose (SNCC). *Colloids and Surfaces A: Physicochemical and Engineering Aspects*, *506*, 789-793.

Konduri, M. K., & Fatehi, P. (2016). Synthesis and characterization of carboxymethylated xylan and its application as a dispersant. *Carbohydrate polymers*, *146*, 26-35.

Kumar, N., Andersson, M. P., Van den Ende, D., Mugele, F., & Sîretanu, I. (2017). Probing the surface charge on the basal planes of kaolinite particles with high-resolution atomic force microscopy. *Langmuir*, *33*(50), 14226-14237.

Kumar, N., Zhao, C., Klaassen, A., van den Ende, D., Mugele, F., & Siretanu, I. (2016). Characterization of the surface charge distribution on kaolinite particles using high resolution atomic force microscopy. *Geochimica et cosmochimica acta*, *175*, 100-112.

Onyianta, A. J., Dorris, M., & Williams, R. L. (2018). Aqueous morpholine pre-treatment in cellulose nanofibril (CNF) production: comparison with carboxymethylation and TEMPO oxidisation pre-treatment methods. *Cellulose*, *25*(2), 1047-1064.

Abdul Rahman, N. H., Chieng, B. W., Ibrahim, N. A., & Abdul Rahman, N. (2017). Extraction and characterization of cellulose nanocrystals from tea leaf waste fibers. *Polymers*, *9*(11), 588.

Tombácz, E., & Szekeres, M. (2006). Surface charge heterogeneity of kaolinite in aqueous suspension in comparison with montmorillonite. *Applied Clay Science*, *34*(1-4), 105-124.

Wang, S., Konduri, M. K., Hou, Q., & Fatehi, P. (2016). Cationic xylan–METAC copolymer as a flocculant for clay suspensions. *RSC advances*, *6*(46), 40258-40269.

Chapter 4: Changes in the molecular structure of cellulose nanocrystals upon treating with solvents

Zahra Hosseinpour Feizi, Pedram Fatehi*[a]

Submitted to *Cellulose*

[a]Biorefining Research Institute, Green Processes Research Centre and Department of Chemical Engineering,
Lakehead University,
955 Oliver Road,
Thunder Bay, ON P7B 5E1, Canada

*Corresponding author

4.1 Abstract

The morphological properties of nano cellulosic materials affect their industrial applications significantly. Solvents are commonly used in treating cellulosic materials in altered applications. In this work, the treatment of cellulose nanocrystals (CNC) with dimethyl sulfoxide (DMSO) and 4-methyl morpholine N-oxide (NMMO) was investigated comprehensively under different conditions to evaluate the effect of solvent treatment on the properties of CNC. A polymorphism transition of cellulose I to II was observed when CNC was treated with the solvents, and the temperature of the treatment was more influential than the time of the treatment in altering the CNC properties. The XRD, light scattering, and wettability analyses confirmed that the partial dissolution of CNC in solvents reordered the cellulosic chains from parallel to semi-parallel. It also made more hydroxy groups accessible for hydrogen bonding, facilitating the CNC aggregation and instability in solutions. The XPS analysis revealed a remarkable alteration in the relative amounts of components in C 1s, reflecting transformation in the chemical bonds from C=O/O-C-O to C-O on the CNC surface. The increase in the hydroxy group of CNC also improved the water-uptake and hydrophilicity of CNC when it was treated with solvents. The results of this work would suggest that the alteration in the CNC characteristics should be considered when selecting solvents for developing industrial applications for CNC.

Keywords: Cellulose nanocrystal, solvent, crystal, dissolution, biorefining

4.2 Introduction

Cellulose, the most plentiful polymer on earth, is a significant source for many materials and biochemicals. This linear polysaccharide is composed of β-1,4 linked glucopyranose units. Cellulose fibers consist of highly ordered (i.e., crystalline) and less ordered (i.e., amorphous) regions. Recently, cellulose received attention as a nanostructured material in the forms of nano fibrillated cellulose (NFC) and cellulose nanocrystals (CNC). NFC, which consists of both crystalline and amorphous parts, is produced primarily by performing mechanical treatments of cellulose. Also, CNC, which consists of only the crystalline part of cellulose fibers, is produced mainly by treating cellulose fibers with concentrated acids (Habibi et al. 2010).

CNC has attracted tremendous attention for use in a wide variety of applications ranging from biomedical to composite (Lin and Dufresne 2014). The chemical modification has been the key in valorizing CNC. To confirm the valorization and adaptability of modified CNC in different applications, the chemical properties of CNC are generally assessed. Nuclear Magnetic Resonance (NMR) is a popular method to assess the properties of CNC. To prepare CNC for NMR analysis, dimethyl sulfoxide (DMSO) and 4-methyl morpholine N-oxide (NMMO) have been extensively used as effective CNC solvents (El-Wakil and Hassan 2008; Dankovich and Gray 2011; Hambardzumyan et al. 2012; Rabideau and Ismail 2015; Yang et al. 2017). Also, the cellulose/NMMO complex is effectively used in the commercial production of lyocell fibers (Krysztof et al. 2018). On the other hand, DMSO is known to be used along with other solvents, such as tetra(1-butyl) ammonium fluoride trihydrate, in synthesizing cellulose ethers (Casarano et al. 2014).

Although these solvents are used extensively for treating CNC, there is no report to discuss if these solvents alter the properties and thus the behavior of CNC. There are reports on the properties of the NMMO or alcohol regenerated cellulose fibers (Biganska and Navard 2009), where the phase separation and porosity of the cellulose fibers were evaluated. There have been several studies on the characteristics of DMSO/NMMO/ionic liquid-recovered cellulose fibers (El-Wakil & Hassan, 2008; Hauru et al. 2012; Medronho and Lindman, 2014, Li et al. 2018). However, studies on the effect of solvents on the CNC structure is limited. In this case, most studies have discussed the effect of solvents on the production of CNF (Man et al. 2011; Laitinen et al. 2017) or the generation of well-dispersed CNC suspension (Viet et al. 2007) without discussing how the structure of CNC is affected by such treatments. Despite their extensive uses, it is still unclear how exactly the treatment of CNC with NMMO and DMSO can chemically impact the structure of CNC. In this work, we aim to assess how the characteristics of CNC would be influenced by these solvents.

In this study, we analyzed solvent treatments under different conditions of temperature, time, and CNC concentration to analyze the manner and magnitude of changes in the cellulose structure. The wide treatment conditions analyzed in this study includes harsh treatment used in the industry (Zhao et al. 2007), as well as mild treatment followed for the sample preparation protocols of CNC analysis, e.g., H-NMR (King et al. 2018) or surface coatings application of CNC (Dankovich and Gray 2011; Hambardzumyan et al. 2012). Investigated CNC properties include changes in the crystallinity, molecular chemical composition and binding energies, thermal stability, dispersion

stability, self-assembly, hydrophilicity/hydrophobicity, and water-uptake affinity. The main novelty of this work was the assessment of the impact of solvent treatment on the characteristics of CNC at a molecular level.

4.3 Material and methods

4.3.1 Materials

Softwood bleached pulp was supplied by a kraft pulp mill located in Northern Ontario, Canada. Also, 4-Methylmorpholine N-oxide (NMMO) (40%), dimethyl sulfoxide (DMSO) (99.5%), sulfuric acid (98%), sodium hydroxide (98%), sodium chloride (99%), and hydrochloric acid (37 %) were obtained from Sigma Aldrich. Regenerated cellulose dialysis membrane with a 1000 g/mol molecular weight cut off was obtained from Spectrum Labs. Inc., USA.

4.3.2 CNC production

Cellulose nanocrystals (CNC) were produced according to the literature (Feizi and Fatehi 2020; Dong et al. 2016; Beck-Candanedo et al. 2005) with a minor modification. Softwood pulp was hydrolyzed with sulfuric acid (64 wt.%) and the pulp/acid ratio of 1/17 wt./wt. at 45 ºC for 60 min. Upon completion, the mixture was diluted tenfolds to cease the acid hydrolysis. The suspension was then centrifuged to remove the excess acid, washed with water, and centrifuged. This washing step was repeated twice. The pH was then adjusted to 7 using 0.1 M NaOH and the sample was dialyzed against deionized water for two days in a cellulosic dialysis membrane for further purification. Finally, CNC suspension was freeze-dried using a 1L benchtop freeze drier, Labconco Co., USA, and stored for further use.

4.3.3 CNC treatments

For CNC treatment under different conditions, freeze-dried CNC was mixed with different solutions/solvents of water, DMSO, and NMMO to make 0.5, 1, and 3% concentration of CNC in the samples. The mixtures were then treated for different times and temperatures. Upon completion, samples were diluted 10 folds with the addition of excess water and then purified using dialysis membrane against distilled deionized water for several days by changing the water every 6 h. Samples were then freeze-dried for further analyses.

4.3.4 X-ray Diffraction (XRD) Analysis

The diffraction patterns of the samples were obtained using a Pananalytical X'pert Pro diffractometer with Cu Kα radiation with a wavelength of 1.5419 Angstrom. Data were collected in the 2θ range of 6° to 40° at a rate of 2°/min. The measurement resolution for this analysis was 0.02°. Freeze-dried CNC samples were transferred onto clean silicon wafer pieces and submitted to the instrument. A blank run data was collected and subtracted from the experimental data of the CNC samples. Peak polarization and deconvolution were performed using the PeakFit software while using the Voit function for the crystalline peaks and the Fast Fourier transform (FFT) for the amorphous part (Yao et al. 2020; French 2020). The crystallinity index (CrI, %) was then calculated following equation 4.1 (Segal et al. 1959; Douard et al. 2020):

Equation 4.1

$$CrI = \frac{Area_{crystalline} - area_{amorphous}}{I_{crystalline}} \times 100$$

The crystallite size (τ) was calculated using the X-ray diffraction patterns through the Scherrer equation (equation 4.2):

Equation 4.2

$$\tau = \frac{K\lambda}{\beta cos\theta}$$

where K (0.94) is the Scherrer constant, λ (0.154 nm) is the X-ray radiation wavelength, β is the full width at half maximum of the (002) or (020) plane peak, and θ is the peak diffraction angle (Man et al. 2011). In addition, the plane spacing ($\frac{\Delta d}{d}$) fractional variation was calculated using equation 4.3, according to the literature (Aguayo et al. 2018):

Equation 4.3

$$\left|\frac{\Delta d}{d}\right| = \frac{\beta}{2tan\theta}$$

4.3.5 X-ray Photoelectron Spectroscopy (XPS)

X-ray photoelectron spectroscopy (XPS) measurements were performed on a Kratos Axis Supra (Shimadzu Group Company Japan), with a monochromatic Al Kα source and a charge neutralizer. Freeze-dried samples were transferred onto a double-sided carbon tape and submitted for analysis

under a high vacuum condition. The high-resolution XPS spectra of the samples were analyzed using ESCApe software.

4.3.6 Dynamic Light Scattering (DLS)

There The hydrodynamic radius of the produced CNC before and after solvent treatment was measured using a 90Plus PALS zeta analyzer (Nano Brook, Brookhaven, USA) at the scattering angle of 90° and the wavelength of 632 nm at 25 °C using 1 mM KCl after sonicating each sample for 30 seconds (Kazzaz et al. 2018a, 2018b; Feizi et al. 2019).

4.3.7 Sulfate half-ester and carboxylate group content analysis

The conductometric titration was used for measuring the sulfate half-ester group content of the produced CNC using an automatic conductometer (Metrohm 856 Titrado, Switzerland) according to Reid and coworkers (2017). Briefly, 0.03 g of freeze-dried CNC was mixed with 2 mL of NaCl (0.02 mol/L). Then, 150 mL of Milli-Q water was added, and samples were left for stirring until homogenized. Afterward, the pH of the suspension was set to 3.5 using 0.1 M HCl and titrated against 0.01 mol/L NaOH solution. The sulfate half-ester group content was calculated following the literature (Chen and van de Ven, 2016).

4.3.8 Thermogravimetric (TGA) Analysis

In this set of experiments, 5 mg of freeze-dried CNC samples were analyzed for their thermal decomposition process using the thermogravimetric analyzer, TGA, i-1000 series, Instrument Specialist Inc. This analysis was performed under nitrogen at a constant flow rate of 35 mL/min. Samples were heated from 25 °C up to 800 °C at a rate of 10 °C/min.

4.3.9 Differential Scanning Calorimetry (MDSC) Analysis

The thermal stability of CNC samples was determined using a differential scanning calorimeter (TA instrument, Q2000 DSC, Brossard, QC, Canada). In this analysis, 5-7 mg of the freeze-dried CNC samples were encapsulated in Tzero® aluminum pans. Calibration was carried out with Indium for enthalpy and heat capacity analysis. Thermograms were acquired with the ramp ranging from 20-250 °C at 3 °C/min in a modulation period of 40 s and an amplitude of 0.64 °C. The glass transition temperature was measured using a modulated DSC technique from the reversing signal of the second heating cycle of the heat/cool/heat cycles.

4.3.10 Powder wettability with Washburn method

The powder wettability analysis of the samples was performed following the Washburn method using the tensiometer Data Physics DCAT 21 system. In this method, 0.1 g of CNC samples were pressed inside the sample holder having small holes in its bottom and the holder was immersed into the milli-Q water. The amount of water absorbed into the CNC was then measured by the instrument.

4.3.11 Wettability analysis with contact angle

For wettability analysis, 1 mL of CNC suspension (10 g/L) was placed onto the Lamella microscope glasses and they were coated with CNC under vacuum with 60 Psi pressure using a spin-coater, WS-650 (Laurell) Technologies Corp, for 60 seconds at 1500 rpm. The glasses were then left for drying and used for contact angle analysis.

Theta Lite Contact Angle (Biolin Scientific, Finland) equipped with a camera was used for hydrophilicity/hydrophobicity analysis of the CNC samples. A water droplet (1.5 μL) was located onto blank or CNC-coated surfaces, and the hydrophilicity/hydrophobicity of the samples was measured for 20 seconds following the Young's Eq. (2) (Sriamornsak et al. 2008).

$$\gamma_{sg} - \gamma_{sl} = \gamma_{gl} \cos\theta \quad (2)$$

where γ_{sg}, γ_{sl}, and γ_{gl} are interfacial tensions (mN/m) of solid-gas, solid-liquid, and gas-liquid, respectively. The θ (°) is the angle of water droplet when it is placed on the CNC-coated surfaces.

4.3.12 Stability and self-assembly analyses

For analyzing the stability and self-assembly of CNC samples, LUMiSizer analytical photocentrifuge (LUM GmbH, Germany) was used. In this analysis, CNC samples were prepared in a 5 g/L concentration and stirred overnight for homogenization at ambient conditions and 150 rpm. Samples were sonicated for 30 seconds and then submitted to the instrument. A parallel NIR light with the λ= 865 nm was passed through cells, and the transmission signal was recorded with 2 s interval. Samples were subjected to different centrifugal forces in the range of 400 and 3000 rpm to generate different ratios of the centrifugal force to earth acceleration in this analysis (Feizi and Fathei 2020). The SEPView® software was used to calculate the instability index of the suspensions and particle size of CNC in the suspensions according to the literature (Zielińska et al. 2018).

4.4 Results and discussion

4.4.1 CNC treatment

The properties of CNC produced via acid hydrolysis is available in Table S4.1 in the supplementary materials. In this work, the CNC production yield of 38 % was achieved and the produced CNC had a sulfate half-ester group content of 0.21 mmol/g. The hydrodynamic diameter of CNC was also measured to be 144 nm.

To explore how the CNC treatment under various conditions would affect its properties, a total of 9 runs was performed on CNC considering treatment time, temperature, solvent type, and CNC concentration. The selected treatment conditions and CNC properties are demonstrated in Table 4.1. The treatments at 25 °C resemble conditions for laboratory analysis (El-Wakil & Hassan, 2008; Dankovich & Gray, 2011; Yang et al., 2017), and treatments at 100°C represent industrial conditions (Zhao et al., 2007; Jiang et al., 2019). As seen, treatments did not significantly affect the sulfate half-ester group content of the samples while no carboxylate groups were detected for the treated samples. Meanwhile, the hydrodynamic size analysis reflected variations when CNC was treated with solvents. As observed, the hydrodynamic size was increased for all solvent-treated CNC samples from approximately 140 nm to 220 nm and 260 nm for NMMO and DMSO treated samples, respectively. When harsher treatment conditions were applied, the hydrodynamic size enhanced more to approximately 360 and 420 nm for NMMO and DMSO treated CNC, respectively. The reason for the size change could be related to alterations in crystallographic properties as well as inter-and intramolecular bonds within the CNC structure led by the solvents.

Table 4.1. Solvent treatment conditions performed on CNC and the chemical and physical properties of generated CNC (the sulfate half-ester group contains SD values).

Sample No.	Control factors and their levels				Sulfate half-ester group, mmol/g	Carboxylate group, mmol/g	Hydrodynamic size, nm
	Solvent type	Temperature, °C	Time, h	CNC concentration, %			
1	Water	25	24	1	0.21± 0.02	<0.09[a]	146

2	NMMO	25	24	1	0.18 ± 0.04	±	<0.09[a]	225
3	DMSO	25	24	1	0.17 ± 0.02	±	<0.09[a]	262
4	Water	25	2	0.5	0.22 ± 0.03	±	<0.09[a]	139
5	NMMO	25	2	0.5	0.18 ± 0.05	±	<0.09[a]	207
6	DMSO	25	2	0.5	0.2 ± 0.02		<0.09[a]	239
7	Water	100	24	3	0.19 ± 0.05	±	<0.09[a]	143
8	NMMO	100	24	3	0.19 ± 0.02	±	<0.09[a]	361
9	DMSO	100	24	3	0.18 ± 0.04	±	<0.09[a]	427

[a] Method sensitivity < 0.09

4.4.2 X-Ray Diffraction (XRD) analysis

XRD analysis was performed to study the crystalline structure of CNC samples after each treatment. As seen in Figure 4.1a, a typical XRD pattern of CNC was obtained for samples 1, 4, and 7 with diffraction peaks at 15, 16.4, 20.2, 22.3, and 34.4°, which are assigned to planes (1 $\bar{1}$ 0), (1 1 0), (0 2 1), (2 0 0) and (0 0 4), respectively. These peaks agree with the characteristic peaks of cellulose type I diffraction pattern (French, 2014; Kaboorani & Riedl, 2015; Moriana et al., 2016), implying that produced CNC in this study was the cellulose type I. Figure 4.1a also reveals that treating CNC samples in water under different treatment times and temperatures did not affect the crystalline structure of CNC. Meanwhile, it is seen in Figure 4.1b that upon solvent treatment of CNC, the peak for (1 $\bar{1}$ 0) has shifted to around $2\theta = 12.2°$ and there is also an increased intensity at around $2\theta = 19.9°$ assigned to the plane (1 1 0). The results clearly state the polymorphism transition from cellulose type I to II in the solvent-treated samples (Yue et al., 2012; French, 2014; Sirviö, 2019).

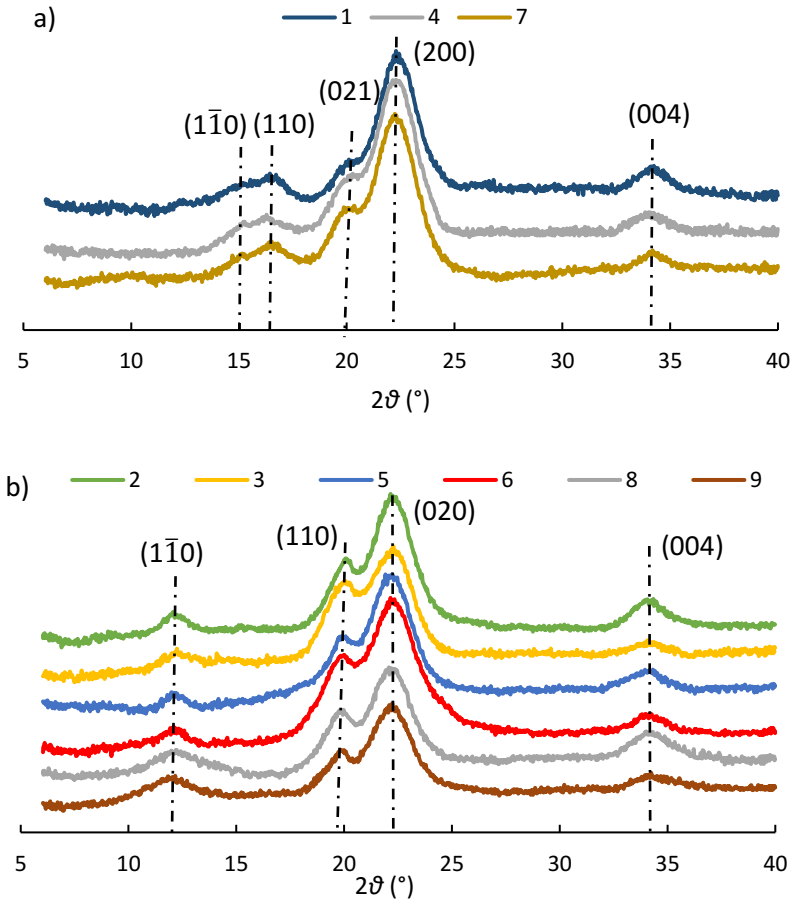

Figure 4.1. XRD pattern of CNC samples under various treatments in a) water (comprising cellulose type I patterns), and b) solvents (comprising cellulose type II patterns).

Table 4.2. Crystallographic analysis of CNC samples

CNC samples	CrI, %	τ, nm	$\frac{\Delta d}{d}$, Å
1	88.7	5.4	3.91
2	76.8	4.8	3.96
3	72.2	4.6	3.95
4	88.5	5.4	3.91
5	75.3	4.8	3.96
6	71.8	4.6	3.95
7	88.3	5.4	3.91
8	70.2	4.8	3.96

9	65.7	4.6	3.96

The crystallinity index (CrI), the apparent crystallite size (τ), and d-spacing ($\frac{\Delta d}{d}$) for CNC samples were also determined and listed in Table 4.2. As seen, treatments under altered conditions affected the crystallinity index (CrI) of the CNC samples. Considering the experimental conditions for sample 1 as a reference with 88.7 % crystallinity, it is seen that DMSO could affect the crystallinity slightly more than did NMMO, with 72.2, and 76.8 % of CrI, respectively, which could be attributed to the interaction of the glycosidic units of CNC with the solvents.

The reduction in the treatment period and CNC concentration did not affect the CrI (samples 4-6). Meanwhile, increasing the temperature slightly reduced the CrI in the presence of solvents, while NMMO had the least (70.2 % CrI) and DMSO had the most (65.7 % CrI) effects. The reason for this could be the swelling of CNC at 100 °C, which further facilitates solvent penetration into the crystalline structure of CNC (Samsudin et al., 2020). In addition, upon treatment with solvents, the crystalline size was reduced for samples while the d-spacing in (020) plane increased in all samples treated with solvents. These results convey that the partial dissolution mechanism affected the reordering of the cellulosic chains upon their precipitation and crystallization, which is discussed more comprehensively in the next section. Also, a minimal increase in the d-spacing for the solvent-treated samples might be yielded from the expansion of cellulose I lattice and changes in the hydrogen bonding network in the crystalline structure (Li et al., 2018).

4.4.3. XPS analysis

XPS analysis was performed to evaluate the chemical compositions of samples, atomic binding energy, and the location of atoms on the specimen. Figure S4.1 illustrates the wide-scan spectra of CNC samples. Table 4.3 also classifies the chemical compositions and bonds for all CNC samples in detail. As seen, CNC possesses different concentrations of O, C, and S, which is typical for an unmodified (sulfuric acid hydrolyzed) CNC (Kaboorani & Reidl, 2015). The sodium element, Na, in CNC samples is a counterion that is associated with the surface anionic groups (S) grafted onto the CNC surface (Kaboorani & Reidl, 2015; Fatona et al., 2018). In comparing the elements in CNC samples, it is observed that the CNC dissolution in NMMO and DMSO changes the relative amount of the elements. The concentration of carbon increased to approximately 5 % in the samples undergone varied treatment conditions. Also, the oxygen level slightly decreased

(approximately 1-2 %) in solvent-treated samples, which might be attributed to the decline in the sulfate half-ester group content in the dissolved samples. In this regard, the atomic ratio of O/C was decreased from 0.75 for untreated CNC (Fatona et al., 2018) to around 0.7 in solvent-treated samples. This observation further reveals the variations in the carbon atom of the samples.

Table 4.3. Elemental composition data and relative surface chemical bonds for CNC samples

Sample	Atomic concentration, %				C 1s Peak area, %			
	C	O	S	Na	C1 (C-C/C-H)	C2 (C-O)	C3 (C=O/O-C-O)	C4 (O-C=O)
1	54.52 ± 0.18	41.15 ± 0.17	1.42 ± 0.06	1.90 ± 0.10	2.55	28.33	52.45	16.67
2	58.30 ± 0.14	40.96 ± 0.14	0.42 ± 0.04	0.33 ± 0.04	6.47	61.51	27.24	4.78
3	58.14 ± 0.21	39.54 ± 0.20	0.47 ± 0.06	0.19 ± 0.09	14.29	60.36	21.75	3.60
4	55.11 ± 0.18	43.32 ± 0.20	1.47 ± 0.04	0.10 ± 0.08	3.24	31.88	50.02	14.86
5	59.34 ± 0.20	40.06 ± 0.19	0.49 ± 0.04	0.10 ± 0.03	9.72	60.46	25.26	4.56
6	59.81 ± 0.19	39.23 ± 0.22	0.54 ± 0.05	0.42 ± 0.07	13.12	62.96	20.47	3.46
7	56.63 ± 0.17	41.75 ± 0.19	1.51 ± 0.08	0.11 ± 0.06	3.61	29.87	50.94	15.58
8	59.22 ± 0.15	39.31 ± 0.14	0.73 ± 0.04	0.73 ± 0.06	10.96	60.62	24.21	4.21
9	60.97 ± 0.24	38.38 ± 0.22	0.44 ± 0.05	0.21 ± 0.03	13.47	64.39	18.93	3.20

The XPS spectra for C 1s were deconvolved to different carbon peaks in Figure 4.2 to better present their binding energy. The spectrum of sample 1 is shown in Figure 4.2, while Table 4.3 and Figure S4.2 includes the carbon peak area and the spectra for all samples, respectively. In general, the C

1s contains four categories of C1 (281.43 eV), C2 (283.42 eV), C3 (284.86 eV), and C4 (285.86 eV), which stand for C-C/C-H aliphatic linkages, C-O linkages in ethers and alcohols, O-C-O/C=O linkages in acetals, and O-C=O linkages in esters, respectively (Kaboorani & Reidl, 2015; Fatona et al., 2018). Interestingly, CNC treatment significantly changed the relative amounts of components in C 1s, reflecting alterations in the proportions of chemical bonds on the CNC surface. As seen, C3 (O-C-O/C=O) is a dominant component in water-treated CNC samples (numbers 1,4, and 7), with 51 %, while it decreased in solvent-treated samples to approximately 26 and 20 % for NMMO, and DMSO-treated samples, respectively. Meanwhile, the relative amount of C2 (C-O) increased drastically from approximately 30 in water-treated samples to roughly 61 % for the solvent-treated ones. In other words, the solvent treatment converted C3 on the surface to C2 groups. In addition, a more visible conversion of C3 to C2 was observed for samples 8 and 9, which would further exhibit the harsh effect of high temperature on the solvent-treated samples.

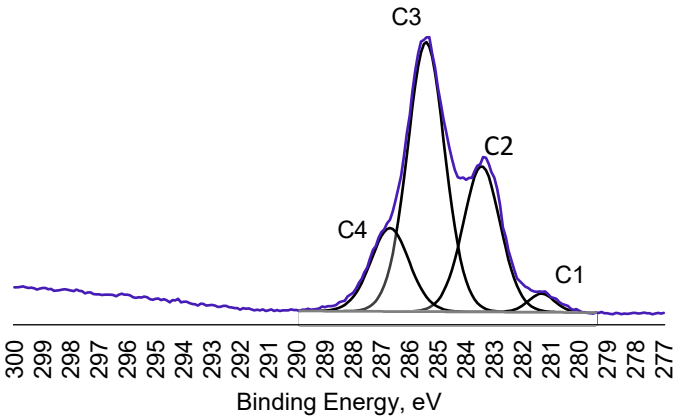

Figure 4.2. C1(s) high-resolution spectrum of CNC sample 1

4.4.4. Mechanisms of solvent treatment

Figure 4.3 shows the effect of solvents on CNC at molecular levels and explains the changes in carbon peaks. As is well known, DMSO is a polar molecule, possessing a strong polarized S-O bond. In treating CNC with solvents, the oxygen atom in the glycosidic bond (shown in red rectangle in Figure 4.3a) tends to develop bonds with S in DMSO due to its free lone pair of electrons (Figure 4.3b). When the solvent is removed, the glycosidic bond breaks, which reduces C3 (O-C-O) in a cellobiose unit. Following the purification of CNC samples with water, anhydroglucose units then form -OH bonds in the presence of water molecules, increasing C2 (C-

O) (Figure 4.3b). A similar trend occurs in the case of NMMO, in which N^+ interacts with O in the glycosidic bond (Figure 3c), the presence of water reduces the interaction levels of cellobiose unites with NMMO (Medronho & Lindman, 2014), resulting in less conversion of C3 to C2, compared to the DMSO treatment (the difference is showed in red rectangles in Figure 3b and 3c). This bond cleavage could also be the reason for smaller apparent crystallite size in solvent-treated samples compared to the water-treated ones based on the XRD analysis (Table 4.2). While C4 is attributed to impurities, such as carboxylic acid or ester groups existing in native cellulose, increment in C1 content could be mathematically proportional to changes in other carbon peaks, since data is reported in percentage.

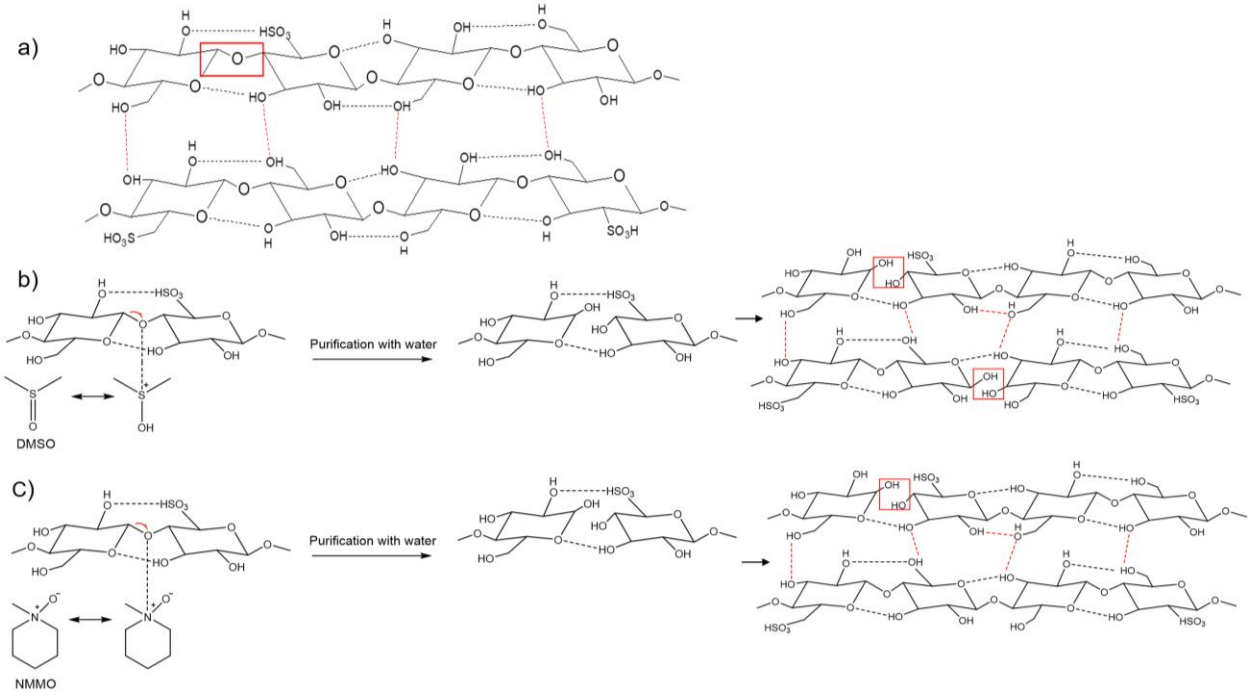

Figure 4.3. Effects of solvents on CNC a) CNC in cellulose type I, b) DMSO molecules developing a bond with O in a glycosidic unit of CNC, and bond cleavage upon purification and removing the solvent resulting in a CNC with a cellulose type II structure, and C) NMMO molecules generating a bond with O in the glycosidic bond and yielding a CNC with a cellulose type II structure upon solvent removal. Red rectangles reveal changes in the glycosidic bonds. The more cleavage is observable in CNC when using DMSO than NMMO.

4.4.5 TGA and DSC analyses

The thermal stability of CNC and regenerated CNC samples were analyzed to understand how the dissolution of CNC samples in DMSO and NMMO under different times, temperatures, and CNC

concentrations would affect its thermal resistance. For a better comparison, the TGA curves of samples 1, 2, and 3 are shown in Figure 4.4, while Figure S4.3 contains the TGA curves related to the rest of the samples. Moreover, Table 4.4 presents the pyrolysis onset of the CNC samples. The initial weight loss at 100 °C observed for all CNC samples is attributed to the moisture removal (Costa et al., 2015; Zainuddin et al., 2017). Sample 1 depicted a typical two-phase weight loss, in which the first phase started at 293 °C and the second one started at 423 °C. According to the literature (Costa et al., 2015; Zainuddin et al., 2017), sulfate half-ester groups replaced by hydroxy groups in the CNC production would reduce the activation energy of CNC degradation, which would yield the observed first stage thermal decomposition. The second step in the pyrolysis is attributed to the degradation of structural aromatized elements leading to an extremely crosslinked carbon skeleton (El-Wakil &Hassan, 2008).

Although similar decomposition patterns were observed for solvent-treated samples, they demonstrated a different thermal degradation pattern compared to the control samples (1, 4, and 7), indicating different depolymerization characteristics (Wan et al., 2017). Although these samples also showed a two-phase weight loss, the first phase started in lower temperatures, compared to CNC samples treated in water (samples 1, 4, and 7). This behavior reveals a reduction in the thermal resistance of the solvent-treated samples. Also, the decomposition for treated samples with solvents at 100 °C was initiated at a lower temperature (~ 200 °C for samples 8 and 9) (Figure 4.4, Table 4.4), which reveals the effect of temperature during treatments (Samsudin et al. 2020). In addition, since similar results were obtained for solvent-treated samples containing different CNC concentration, it could be revealed that this factor played a minimal role in affecting CNC samples.

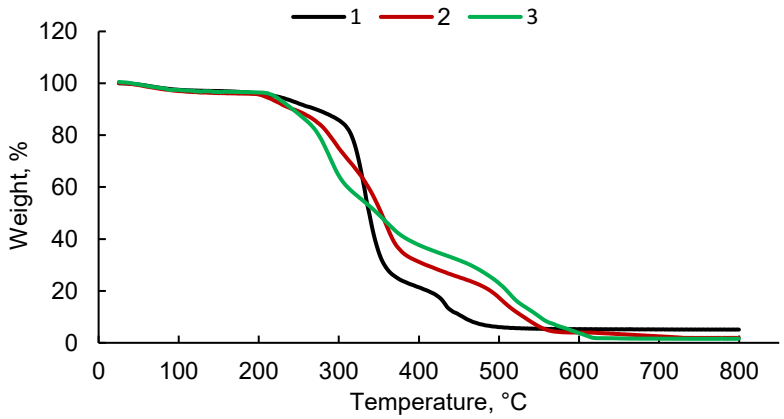

Figure 4.4. TGA graph of CNC samples 1, 2, and 3

Table 4.4 also contains the char yield (ash content) for the CNC samples. As seen, the char yield was reduced from 5 % for the water-treated samples (1, 4, and 7) to around 1.5 % for solvent-treated CNC samples. Considering the structure of CNC, the difference in thermal degradation processes and the reduction in the char yield might be due to the transition of cellulose I to cellulose II (Figure 4.1), in which the hydroxymethyl groups were rearranged in a non-parallel order, leading to a different inter and intramolecular hydrogen bonding (Wan et al., 2017). These results are consistent with the XRD results (Table 4.1) since a reduction in the crystallite size mostly lowers the thermal resistance of cellulosic materials (Poletto et al., 2013). Table 4.4 also includes the glass transition temperature (T_g) and heating capacity (C_p) of the CNC samples. As seen, the T_g and C_P for all samples is approximately 91 °C and 0.05 (J/g.°C), while no significant difference is observed between the samples. It is observed that small changes in the CrI of highly crystalline materials might not remarkably affect the T_g since the most proportion of the material is unable to participate in the molecular movements because of the high crystallinity of the samples (Maurer, 1965; Islam et al., 2010; Askadskii et al., 2014).

Table 4.4. TGA and DSC data of CNC samples

Sample	$T_{First\ phase}$, °C	$T_{Second\ phase}$, °C	Char yield at 800 °C, %	T_g point, °C	C_P, J/(g.°C)
1	293	423	5.0	92	0.06
2	210	477	1.8	92	0.048
3	217	457	1.5	91	0.045
4	271	422	5.2	91	0.063
5	234	430	1.9	91	0.044
6	220	456	1.5	91	0.041
7	269	418	5.0	91	0.048
8	212	473	1.6	91	0.045
9	199	482	1.3	91	0.03

4.4.6. Powder wettability with Washburn method

Powder wettability analysis was performed to measure the water uptake of CNC samples. As depicted in Figure 4.5, CNC samples treated in water (1, 4, and 7) absorbed around 13 g/g of water, while solvent-treated samples absorbed around 17 g/g of water (i.e., 25% increase in the water-uptake wettability of the treated CNC samples). Also, it is seen that samples treated with DMSO (3, 6, and 9) could absorb slightly more water than the NMMO-treated ones (2, 5, and 8) in all three different treatment conditions.

Generally, hydrogen bonds within cellulose crystals act in a regular pattern and link the OH-O structure within and between the cellulosic chains. This pattern makes the majority of -OH groups to be already occupied and unable to interact with their surroundings. As seen in Figures 4.4 and 4.6, treating CNC with solvents changed its crystalline structure in that more -OH groups would be available to develop inter and intra-molecular hydrogen bonds with water, begetting a higher water uptake (Hubbe et al., 2015). This variation in water uptake is in a good relationship with results obtained from XRD and XPS analyses (Figures 4.1 and 4.3), fortifying the polymorphism transition from cellulose type I to type II. Slightly higher water absorption by samples treated with DMSO than the ones treated with NMMO might also be ascribed to the lower CrI (Table 4.1) and higher glycosidic bond cleavage of the CNC samples treated with DMSO (Table 4.2 and Figure 4.4) (Medronho & Lindman, 2014).

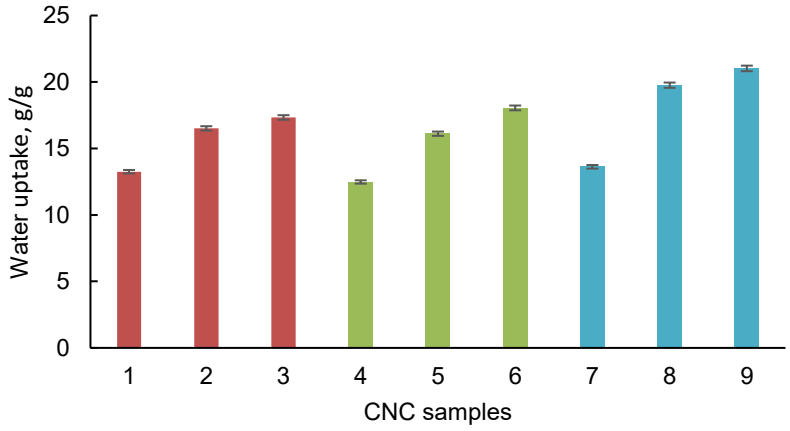

Figure 4.5 Water-uptake analysis for CNC samples

4.4.7. Hydrophilicity/hydrophobicity analysis

The contact angle analysis was carried out to illustrate how the solvent treatment affected the hydrophilicity/hydrophobicity of CNC samples. Figure 4.6 contains the contact angle of the CNC

samples while the images are depicted in Figure S4.4. As seen in Figure 4.6, the CNC is a very hydrophilic material before the treatment, which led to a contact angle of around 25°. The contact angle for solvent-treated samples was generally lower than the untreated CNC samples (blank), revealing an improvement in the hydrophilicity of the samples. According to Figures 4.2 and 4.3, treating CNC with solvents led to more OH group on CNC available for hydrogen bonding, which led to a smaller contact angle when a drop of water was placed on the CNC samples.

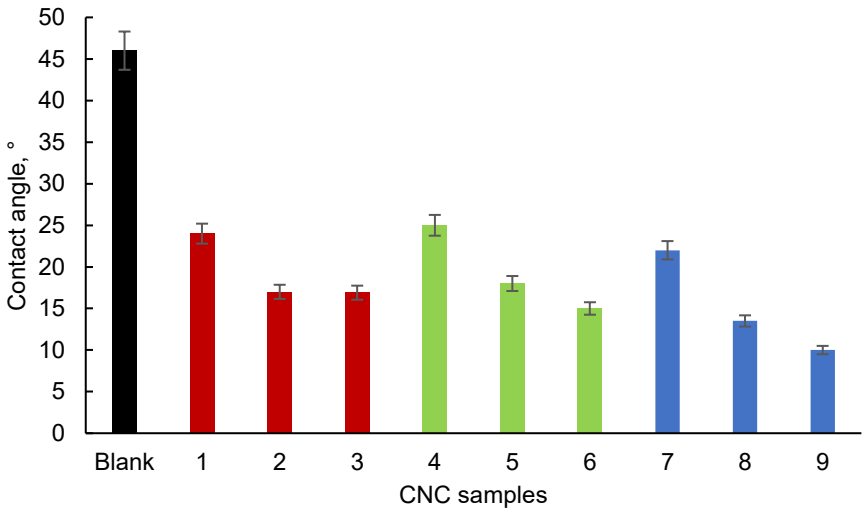

Figure 4.6. The contact angle of water on the CNC coated samples

4.4.8. Stability and self-assembly analyses

Generally, acid-hydrolyzed CNC repel each other in the suspension due to the presence of sulfate-half ester groups (Table 4.1) making the CNC suspension stable (Jia et al., 2013). Stability analysis was carried out under different relative centrifugal forces (RCF) to investigate if the solvent treatment would impact CNC stability in suspensions, and the results are depicted in Figures 4.7 and S4.6. As seen in Figures 4.7a and S4.6a, the instability index increased in the samples treated with solvents, implying that solvent treatment led to suspension instability (especially in a high RCF). As observed in Figure 4.7b and S4.6b, the particle size of the CNC samples also increased in solvent-treated samples, revealing CNC self-assembly under the examined RCF. The availability of more -OH groups on solvent-treated CNC samples (Figure 4.3) might have led to more hydrogen bonding between CNC samples, and thus more aggregation. Also, it was seen that the higher the CNC self-assembly, the higher the instability index, which would reveal a faster CNC sedimentation in solvent-treated CNC samples than the water-treated ones over time.

Overall, although all CNC solutions were found to be very stable (instability index < 1), solvent-treated samples faced stronger self-assemble characteristics than water-treated CNC.

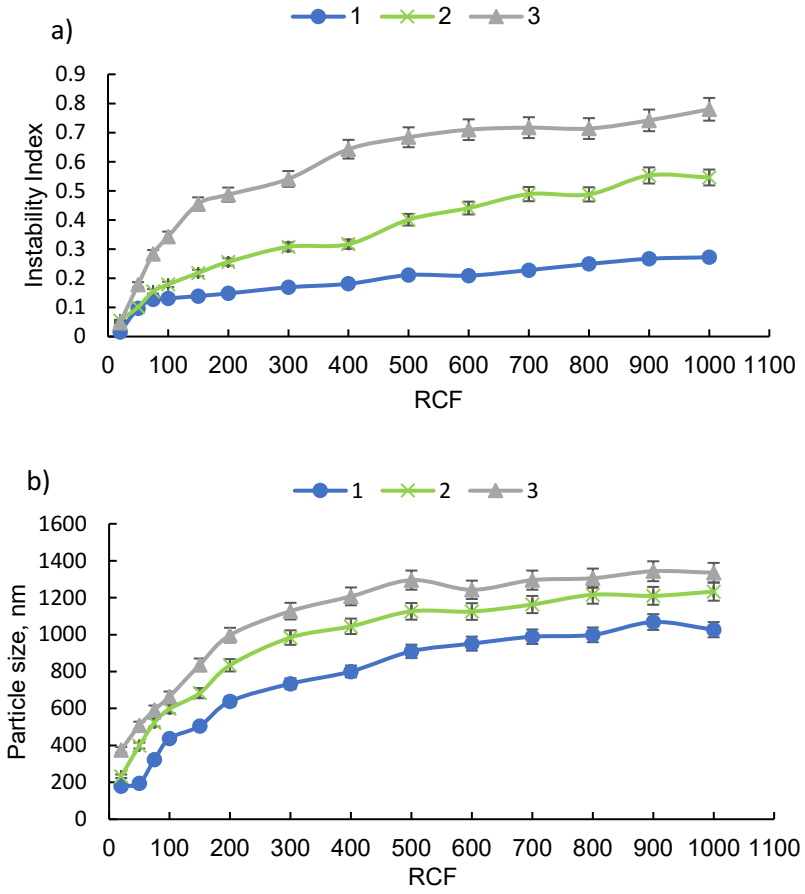

Figure 4.7. a) Instability index, and b) particle size of CNC samples

4.4.9. Application

In this work, CNC was treated with water as well as two different solvents of NMMO and DMSO for a different time duration, temperature, and CNC concentration to track how the structure of CNC would be affected by these factors in the CNC pretreatment. Since both cellulose types I and II have found tremendous applications in industry, it is critical to understand how intensive the structure and characteristics of CNC would be affected by the solvent treatment. Also, solvents, such as NMMO and DMSO, are very popular in laboratory analysis for dissolving cellulose for other analyses, e.g., H-NMR (King et al. ,2018), which would impact the ultimate results.

Although NMMO and DMSO are considered the most popular solvents for cellulose dissolution (Hambardzumyan et al., 2012; Casarano et al., 2014; Rabideau & Ismail, 2015; Krysztof et al.,

2018), they do affect the CNC structure in different levels by converting some glycosidic bonds to form -OH bonds (Figure 4.3, Tables 4.2 and 4.3). Our studies showed that, under the examined conditions, both cellulose types could coexist in the CNC structure. In this study, it was observed that treatment duration and CNC concentration affected the transition minimally while the treatment temperature affected the CNC more significantly. Meanwhile, DMSO was found to be more effective than NMMO in the conversion of cellulose type I to type II in CNC samples.

The polymorphism transition could be beneficial for some applications. DMSO treated CNC could be used in applications such as smart materials, e.g., sensors, due to its monoclinic crystal structure (Kim et al., 2016). NMMO-treated CNC could be more desirable for use in applications such as composites where less of the polymorphism transition is required (Jiang et al., 2019). However, the increased water-uptake of CNC with solvent treatment would limit the treated CNC's application in packaging and membrane, where more hydrophobicity is advantageous (Li et al., 2013; Zhang et al., 2018). Meanwhile, for composites where CNC is opted to be used as a reinforcing agent in which high thermal resistance and crystallinity are desired (Ng et al., 2015), CNC dissolution in NMMO or DMSO may not be the best option. In addition, although solvent-treated CNC samples were very stable, untreated CNC could still be the better candidate to be used as a dispersant in suspensions due to its limited affinity to self-assemble.

4.5 Conclusions

Dimethyl sulfoxide (DMSO) and 4-methyl morpholine N-oxide (NMMO) were separately used for treating cellulose nanocrystals to analyze the effect of solvent treatments on the characteristics of CNC. While treatment duration and CNC concentration had minimal effects, temperature led to a more transition in the crystalline structure of CNC. Treating CNC with NMMO and DMSO under conditions studied impacted the crystalline structure as well as its inter and intra-molecular hydrogen bonds of CNC, but a more transition was observed when DMSO was used. Under all conditions studied, the solvent treatment led to the polymorphism transition of cellulose I to II. A reduction in the crystallinity index and crystallite size followed by an increase in the d-spacing reveals the reordering of the cellulosic chains upon their precipitation and crystallization in solutions, leading to a change in the hydrogen bonding network of the crystalline structure of CNC. The XPS analysis also depicted a significant change in the relative amounts of components in C 1s upon CNC treatment with solvents, reflecting alterations in the proportions of chemical bonds on the CNC surface. The wettability (water-uptake and hydrophilicity) of the solvent-treated CNC

was observed to be higher than water-treated CNC, which is directly attributed to the development of more hydrogen bonds originating from more availability of -OH groups. This increment also led to more self-assembled CNC (and less stable suspension) in the suspensions. In conclusion, these effects are suggested to be taken into account for preparing CNC for industrial applications or laboratory analyses.

4.6 References

Aguayo, M., Fernández Pérez, A., Reyes, G., Oviedo, C., Gacitúa, W., Gonzalez, R., & Uyarte, O. (2018). Isolation and Characterization of Cellulose Nanocrystals from Rejected Fibers Originated in the Kraft Pulping Process. *Polymers*, *10*(10), 1145.

Askadskii, A., Popova, M., Matseevich, T., & Kurskaya, E. (2014). The Influence of the degree of crystallinity on the glass transition temperature of polymers. *Advanced Materials Research*, *864*, 751-754.

Beck-Candanedo, S., Roman, M., Gray, D.G. (2005). Effect of reaction conditions on the properties and behavior of wood cellulose nanocrystal suspensions. *Biomacromolecules,* 1048-1054.

Biganska, O., Navard, P. (2009). Morphology of cellulose objects regenerated from cellulose-N-methylmorpholine N-oxide-water solutions. *Cellulose*, 16(2):179-188.

Casarano. R., Pires, P.A., Borin, A.C., El Seoud, O.A. (2014). Novel solvents for cellulose: Use of dibenzyldimethylammonium fluoride/dimethyl sulfoxide (DMSO) as solvent for the etherification of the biopolymer and comparison with tetra (1-butyl) ammonium fluoride/DMSO. *Industrial Crops and Products*, *93*,185-191.

Chen, D., & van de Ven, T. G. (2016). Flocculation kinetics of precipitated calcium carbonate (PCC) with sterically stabilized nanocrystalline cellulose (SNCC). *Colloids and Surfaces A: Physicochemical and Engineering Aspects*, *506*, 789-793.

Costa, L. A., Fonseca, A. F., Pereira, F. V., & Druzian, J. I. (2015). Extraction and characterization of cellulose nanocrystals from corn stover. *Cellulose Chemistry & Technology*, *49*(2), 127-133.

Dankovich, T. A., & Gray, D. G. (2011). Contact angle measurements on smooth nanocrystalline cellulose (I) thin films. *Journal of adhesion science and technology*, *25*(6-7), 699-708.

Dong, S., Bortner, M. J., & Roman, M. (2016). Analysis of the sulfuric acid hydrolysis of wood pulp for cellulose nanocrystal production: A central composite design study. *Industrial Crops and Products*, *93*, 76-87.

Douard, L., Bras, J., Encinas, T., & Belgacem, M. N. (2020). Natural acidic deep eutectic solvent to obtain cellulose nanocrystals using the design of experience approach. *Carbohydrate Polymers*, *252*, 117136.

El-Wakil, N. A., & Hassan, M. L. (2008). Structural changes of regenerated cellulose dissolved in FeTNa, NaOH/thiourea, and NMMO systems. *Journal of Applied Polymer Science*, *109*(5), 2862-2871.

Fatona, A., Berry, R. M., Brook, M. A., & Moran-Mirabal, J. M. (2018). Versatile surface modification of cellulose fibers and cellulose nanocrystals through modular triazinyl chemistry. *Chemistry of Materials*, *30*(7), 2424-2435.

Feizi, Z.H., & Fatehi. P. (2020). Carboxymethylated cellulose nanocrystals as clay suspension dispersants: effect of size and surface functional groups. *Cellulose*, *27*, 3759-3772.

Feizi, Z. H., Kazzaz, A. E., Kong, F., & Fatehi, P. (2019). Evolving a flocculation process for isolating lignosulfonate from solution. *Separation and Purification Technology*, *222*, 254-263.

French, A. D. (2014). Idealized powder diffraction patterns for cellulose polymorphs. *Cellulose*, *21*(2), 885-896.

French, A.D. (2020). Increment in evolution of cellulose crystallinity analysis. *Cellulose*, *2*, 5445-5448.

Habibi, Y., Lucia, L. A., & Rojas, O. J. (2010). Cellulose nanocrystals: chemistry, self-assembly, and applications. *Chemical reviews*, *110*(6), 3479-3500.

Hambardzumyan, A., Foulon, L., Chabbert, B., & Aguié-Béghin, V. (2012). Natural organic UV-absorbent coatings based on cellulose and lignin: designed effects on spectroscopic properties. *Biomacromolecules*, *13*(12), 4081-4088.

Hauru, L. K., Hummel, M., King, A. W., Kilpelainen, I., & Sixta, H. (2012). Role of solvent parameters in the regeneration of cellulose from ionic liquid solutions. *Biomacromolecules*, *13*(9), 2896-2905.

Islam, M. I. U., Sherrell, R., & Langrish, T. A. G. (2010). An investigation of the relationship between glass transition temperatures and the crystallinity of spray-dried powders. *Drying technology*, *28*(3), 361-368.

Jia, X., Chen, Y., Shi, C., Ye, Y., Wang, P., Zeng, X., & Wu, T. (2013). Preparation and characterization of cellulose regenerated from phosphoric acid. *Journal of agricultural and food chemistry*, *61*(50), 12405-12414.

Jiang, Z., Tang, L., Gao, X., Zhang, W., Ma, J., & Zhang, L. (2019). Solvent regulation approach for preparing cellulose-nanocrystal-reinforced regenerated cellulose fibers and their properties. *ACS omega*, *4*(1), 2001-2008.

Jin, E., Guo, J., Yang, F., Zhu, Y., Song, J., Jin, Y., & Rojas, O. J. (2016). On the polymorphic and morphological changes of cellulose nanocrystals (CNC-I) upon mercerization and conversion to CNC-II. *Carbohydrate polymers*, *143*, 327-335.

Kaboorani, A., & Riedl, B. (2015). Surface modification of cellulose nanocrystals (CNC) by a cationic surfactant. *Industrial Crops and Products*, *65*, 45-55.

Kazzaz, A. E., Feizi, Z. H., & Fatehi, P. (2018). Interaction of sulfomethylated lignin and aluminum oxide. *Colloid and Polymer Science*, *296*(11), 1867-1878.

Kazzaz, A. E., Feizi, Z. H., Kong, F., & Fatehi, P. (2018). Interaction of poly (acrylic acid) and aluminum oxide particles in suspension: particle size effect. *Colloids and Surfaces A: Physicochemical and Engineering Aspects*, *556*, 218-226.

Kim, H. C., Mun, S., Ko, H. U., Zhai, L., Kafy, A., & Kim, J. (2016). Renewable smart materials. *Smart Materials and Structures*, *25*(7), 073001. https://doi.org/10.1088/0964-1726/25/7/073001

King, A. W., Mäkelä, V., Kedzior, S. A., Laaksonen, T., Partl, G. J., Heikkinen, S., ... & Kilpeläinen, I. (2018). Liquid-state nmr analysis of nanocelluloses. *Biomacromolecules*, *19*(7), 2708-2720.

Krysztof, M., Olejnik, K., Kulpinski, P., Stanislawska, A., & Khadzhynova, S. (2018). Regenerated cellulose from N-methylmorpholine N-oxide solutions as a coating agent for paper materials. *Cellulose*, *25*(6), 3595-3607.

Laitinen, O., Ojala, J., Sirviö, J. A., & Liimatainen, H. (2017). Sustainable stabilization of oil in water emulsions by cellulose nanocrystals synthesized from deep eutectic solvents. *Cellulose*, *24*(4), 1679-1689.

Li, F., Biagioni, P., Bollani, M., Maccagnan, A., & Piergiovanni, L. (2013). Multi-functional coating of cellulose nanocrystals for flexible packaging applications. *Cellulose*, *20*(5), 2491-2504.

Li, Y., Wang, J., Liu, X., & Zhang, S. (2018). Towards a molecular understanding of cellulose dissolution in ionic liquids: anion/cation effect, synergistic mechanism and physicochemical aspects. *Chemical science*, *9*(17), 4027-4043.

Lin, N., & Dufresne, A. (2014). Surface chemistry, morphological analysis and properties of cellulose nanocrystals with gradiented sulfation degrees. *Nanoscale*, *6*(10), 5384-5393.

Man, Z., Muhammad, N., Sarwono, A., Bustam, M. A., Kumar, M. V., & Rafiq, S. (2011). Preparation of cellulose nanocrystals using an ionic liquid. *Journal of Polymers and the Environment*, *19*(3), 726-731.

Maurer, J. J. (1965). Relation between glass transition temperature and composition of ethylene propylene copolymers. *Rubber Chemistry and Technology*, *38*(4), 979-990.

Medronho, B., & Lindman, B. (2014). Competing forces during cellulose dissolution: from solvents to mechanisms. *Current Opinion in Colloid & Interface Science*, *19*(1), 32-40.

Moriana, R., Vilaplana, F., & Ek, M. (2016). Cellulose nanocrystals from forest residues as reinforcing agents for composites: A study from macro-to nano-dimensions. *Carbohydrate polymers*, *139*, 139-149.

Ng, H. M., Sin, L. T., Tee, T. T., Bee, S. T., Hui, D., Low, C. Y., & Rahmat, A. R. (2015). Extraction of cellulose nanocrystals from plant sources for application as reinforcing agent in polymers. *Composites Part B: Engineering*, *75*, 176-200.

Poletto, M., Pistor. V., & Zattera, A.J. (2013). Structural characteristics and thermal properties of native cellulose. *Cellulose-fundamental aspects*, *2*,45-68.

Rabideau, B. D., & Ismail, A. E. (2015). Effect of water content in N-methylmorpholine N-oxide/cellulose solutions on thermodynamics, structure, and hydrogen bonding. *The Journal of Physical Chemistry B*, *119*(48), 15014-15022.

Reid, M. S., Villalobos, M., & Cranston, E. D. (2017). The role of hydrogen bonding in non-ionic polymer adsorption to cellulose nanocrystals and silica colloids. *Current Opinion in Colloid & Interface Science*, *29*, 76-82.

Samsudin, N. A., Low, F. W., Yusoff, Y., Shakeri, M., Tan, X. Y., Lai, C. W., ... & Amin, N. (2020). Effect of temperature on synthesis of cellulose nanoparticles via ionic liquid hydrolysis process. *Journal of Molecular Liquids*, 113030.

Segal, L. G. J. M. A., Creely, J. J., Martin Jr, A. E., & Conrad, C. M. (1959). An empirical method for estimating the degree of crystallinity of native cellulose using the X-ray diffractometer. *Textile research journal*, *29*(10), 786-794.

Sirviö, J. A. (2019). Fabrication of regenerated cellulose nanoparticles by mechanical disintegration of cellulose after dissolution and regeneration from a deep eutectic solvent. *Journal of Materials Chemistry A*, *7*(2), 755-763.

Sriamornsak, P., Wattanakorn, N., Nunthanid, J., & Puttipipatkhachorn, S. (2008). Mucoadhesion of pectin as evidence by wettability and chain interpenetration. *Carbohydrate Polymers*, *74*(3), 458-467.

Viet, D., Beck-Candanedo, S., & Gray, D. G. (2007). Dispersion of cellulose nanocrystals in polar organic solvents. *Cellulose*, *14*(2), 109-113.

Wan, Y., An, F., Zhou, P., Liu, Y., Lu, C., & Chen, H. (2017). Effect of the polymorphs of cellulose on its pyrolysis kinetic and char yield. *Journal of Analytical and Applied Pyrolysis*, *127*, 223-228.

Yang, X., Wang, X., Liu, H., Zhao, Y., Jiang, S., & Liu, L. (2017). Impact of dimethyl sulfoxide treatment on morphology and characteristics of nanofibrillated cellulose isolated from corn husks. *BioResources*, *12*(1), 95-106.

Yao, W., Weng, Y., Catchmark, J.M. (2020). Improved cellulose X-ray diffraction analysis using Fourier series modeling. *Cellulose*, 5563-5579.

Yue, Y., Zhou, C., French, A. D., Xia, G., Han, G., Wang, Q., & Wu, Q. (2012). Comparative properties of cellulose nano-crystals from native and mercerized cotton fibers. *Cellulose*, *19*(4), 1173-1187.

Zainuddin, N., Ahmad, I., Kargarzadeh, H., & Ramli, S. (2017). Hydrophobic kenaf nanocrystalline cellulose for the binding of curcumin. *Carbohydrate polymers*, *163*, 261-269.

Zhang, D., Karkooti, A., Liu, L., Sadrzadeh, M., Thundat, T., Liu, Y., & Narain, R. (2018). Fabrication of antifouling and antibacterial polyethersulfone (PES)/cellulose nanocrystals (CNC) nanocomposite membranes. *Journal of Membrane Science*, *549*, 350-356.

Zhao, H., Kwak, J. H., Wang, Y., Franz, J. A., White, J. M., & Holladay, J. E. (2007). Interactions between cellulose and N-methylmorpholine-N-oxide. *Carbohydrate Polymers*, *67*(1), 97-103.

Zielińska, A., Martins-Gomes, C., Ferreira, N. R., Silva, A. M., Nowak, I., & Souto, E. B. (2018). Anti-inflammatory and anti-cancer activity of citral: Optimization of citral-loaded solid lipid nanoparticles (SLN) using experimental factorial design and LUMiSizer®. *International journal of pharmaceutics*, *553*(1-2), 428-440.

4.7 Appendix A. Supplementary material

Changes in the molecular structure of cellulose nanocrystals upon treating with solvents

Zahra Hosseinpour Feizi, Pedram Fatehi*

Biorefining Research Institute, Green Processes Research Centre and Chemical Engineering Department, Lakehead University, 955 Oliver Road, Thunder Bay, Ontario P7B 5E1, Canada

* Corresponding author, email: pfatehi@lakeheadu.ca; tel: 807-343-8697; fax: 807-346-7943

Table S4.1. Properties of the produced CNC

Properties	CNC
Yield, %	38
Sulfate half-ester group content, mmol/g	0.21 ± 0.02
Hydrodynamic diameter, nm	144

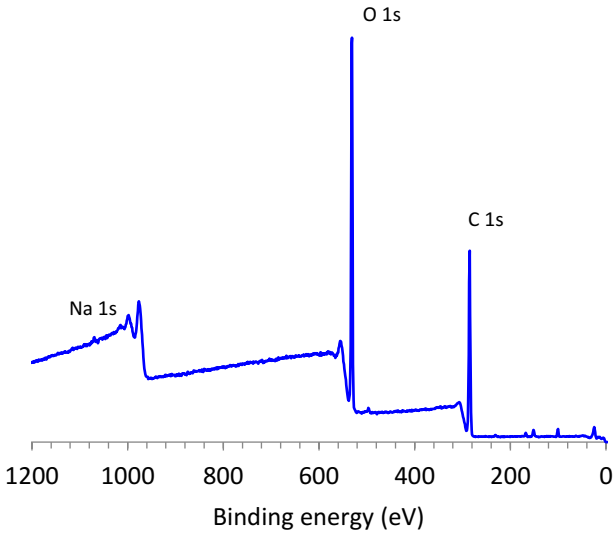

Figure S4.1. XPS survey spectra of CNC sample 1

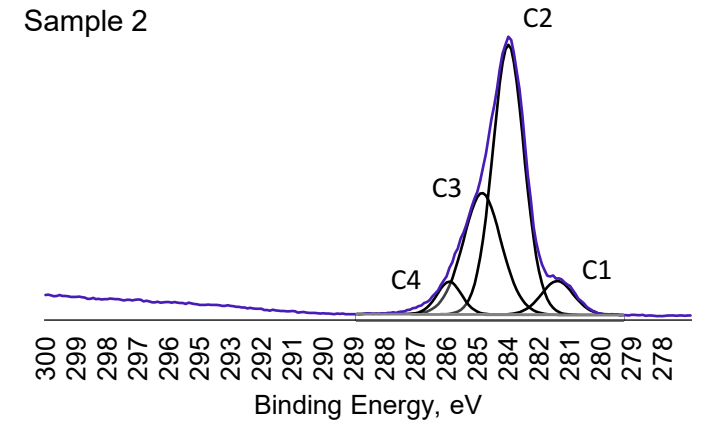
Sample 2
C2
C3
C4
C1
300 299 298 297 296 295 293 292 291 290 289 288 287 286 285 284 282 281 280 279 278
Binding Energy, eV

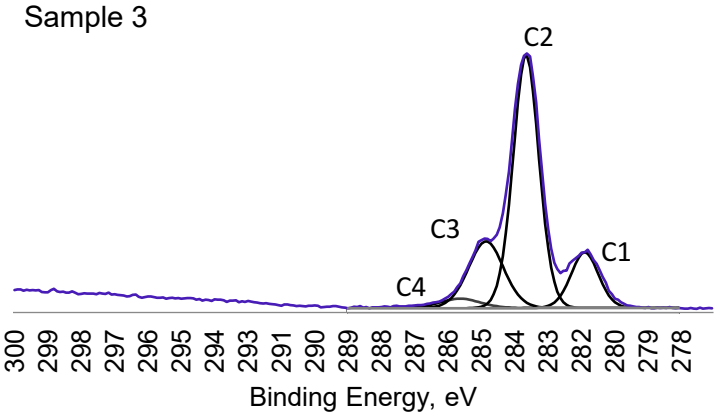
Sample 3
C2
C3
C1
C4
300 299 298 297 296 295 294 293 291 290 289 288 287 286 285 284 283 282 280 279 278
Binding Energy, eV

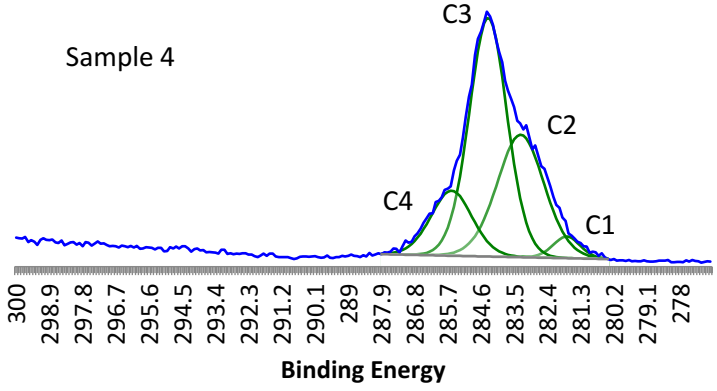
Sample 4
C3
C2
C4
C1
300 298.9 297.8 296.7 295.6 294.5 293.4 292.3 291.2 290.1 289 287.9 286.8 285.7 284.6 283.5 282.4 281.3 280.2 279.1 278
Binding Energy

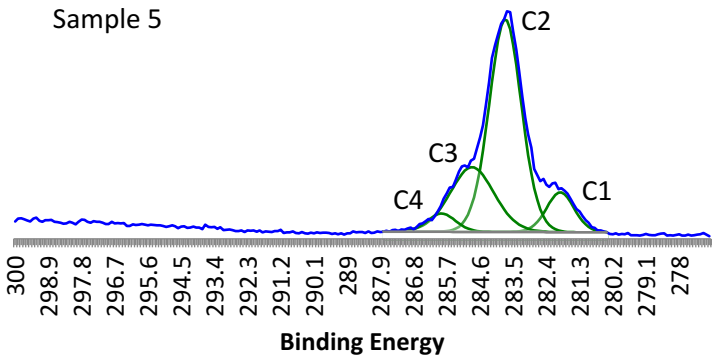
Sample 5
C2
C3
C4
C1
300
298.9
297.8
296.7
295.6
294.5
293.4
292.3
291.2
290.1
289
287.9
286.8
285.7
284.6
283.5
282.4
281.3
280.2
279.1
278
Binding Energy

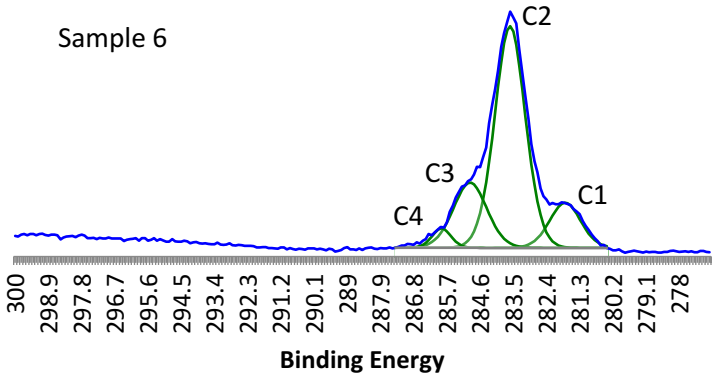
Sample 6
C2
C3
C4
C1
300
298.9
297.8
296.7
295.6
294.5
293.4
292.3
291.2
290.1
289
287.9
286.8
285.7
284.6
283.5
282.4
281.3
280.2
279.1
278
Binding Energy

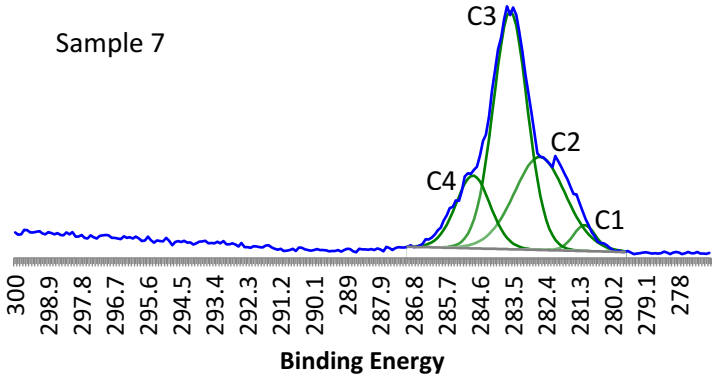
Sample 7
C3
C2
C4
C1
300
298.9
297.8
296.7
295.6
294.5
293.4
292.3
291.2
290.1
289
287.9
286.8
285.7
284.6
283.5
282.4
281.3
280.2
279.1
278
Binding Energy

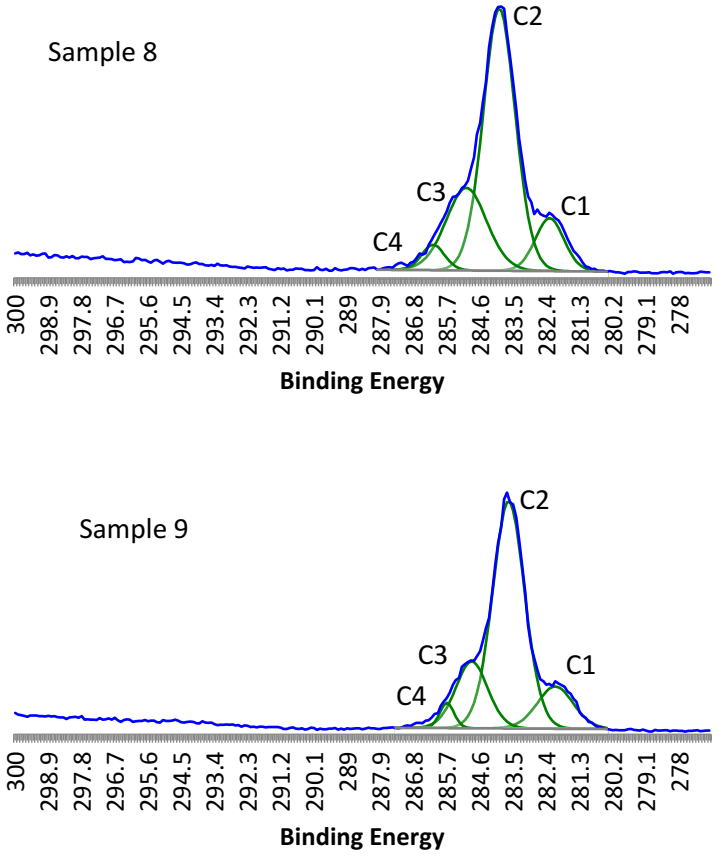

Figure S4.2. C1(s) high resolution spectra of CNC samples

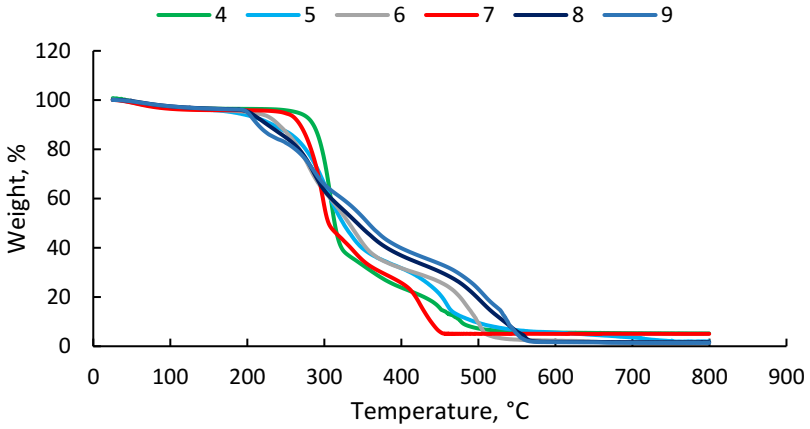

Figure S4.3. TGA graph of CNC samples

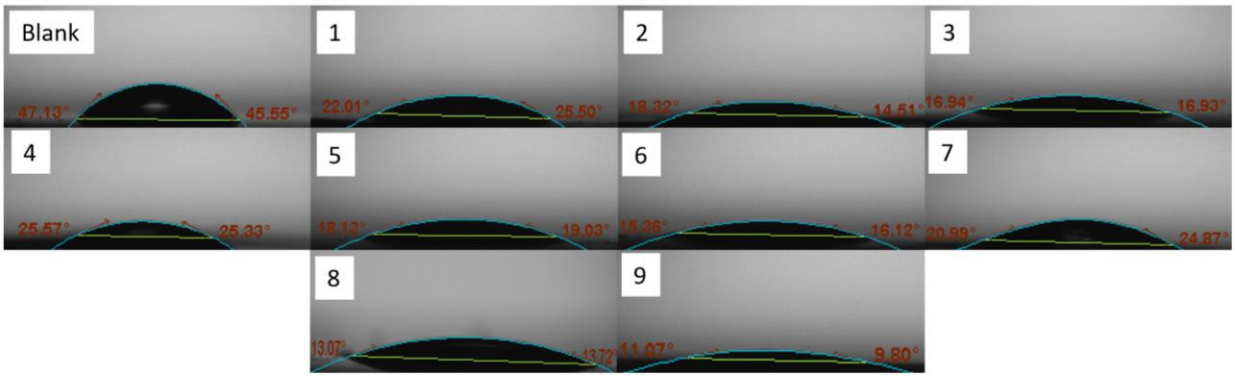

Figure S4.4. Contact angle analysis of CNC samples

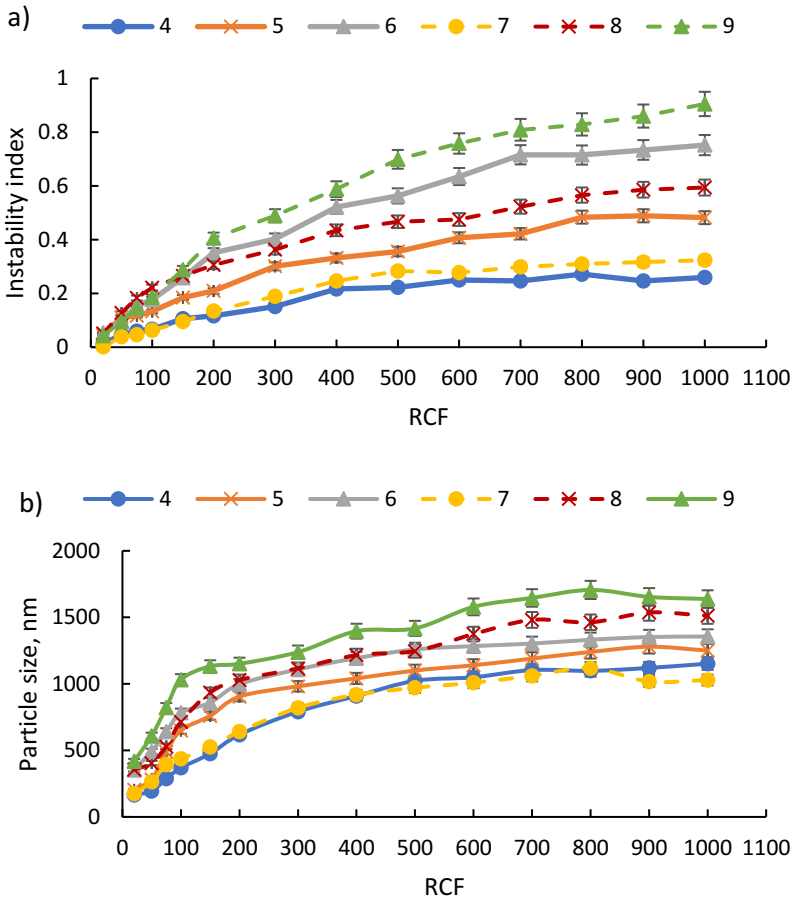

Figure S4.5. a) Instability index, and b) particle size of CNC samples

Chapter 5: Interaction of hairy carboxyalkyl cellulose nanocrystals with cationic surfactant: effect of carbon spacer

Adapted from: Zahra Hosseinpour Feizi, Pedram Fatehi*[a]

Carbohydrate Polymers, (2020), 117396.

[a] Biorefining Research Institute, Green Processes Research Centre and Department of Chemical Engineering,
Lakehead University,
955 Oliver Road,
Thunder Bay, ON P7B 5E1, Canada

*Corresponding author

5.1 Abstract

Tuning the surface chemistry of nanocellulose is essential for developing its end-use applications. Herein, different carboxyalkylated cellulose nanocrystals (CNC) with similar charge densities but with tunable hairy structures were produced. The effect of carbon spacer of the grafted groups on the interaction of the CNC and a cationic surfactant, myristyl trimethyl ammonium bromide (MTAB), at different pH and salinity was explored. The CNC with longer grafted chain length was more hydrophobic, adsorbed more MTAB, and formed a more compact MTAB adlayer than did CNC with the shorter chain length. Also, the adsorption was higher at neutral pH, implying a high electrostatic attraction and hydrophobic interaction between substrates. The hydrophobic interaction of MTAB and hairy CNC in saline systems improved its adsorption. Although MTAB adsorbed more when its concentration was higher than its critical micelle concentration (CMC), the adsorbed adlayer had a less compact structure on the CNC surfaces.

Keywords: carboxyalkylation, carboxybutylation, carboxyheptanation, carboxypantadecanation, cellulose nanocrystals, cationic surfactant

5.2 Introduction

Cellulose nanocrystal (CNC) is an appealing derivate of cellulose due to its prominent properties. This green and non-toxic material has been examined for many applications due to its high aspect ratio, large surface area and elastic modulus, and abundant surface hydroxyl groups (Feizi & Fatehi, 2020; Habibi et al., 2010).

To make CNC a more suitable material for a variety of high-value applications, such as biomedical engineering (Sunasee et al., 2016), wastewater treatment (Grishkewich et al., 2017), or food additives (Grishkewich et al., 2017); altered chemical modification pathways, such as esterification (Jasmani et al., 2013), etherification (Zaman et al., 2012) and oxidation (Eyley & Thielemans, 2014), have been carried out on the CNC to tune its surface properties.

Carboxymethylation is one of the versatile, straightforward, and green modifications (Kazzaz & Fatehi, 2020a; Kazzaz et al., 2019; Chen et al., 2018) conducted on cellulose to introduce carboxylate group charges to the CNC surface (Ma et al., 2017; Ming et al., 2016). In this context, other carboxyalkylation techniques can also introduce carboxylate groups to CNC, and these

reactions may alter the physicochemical characteristics of CNC differently. However, information on the impact of these carboxyalkylation reactions on CNC is unavailable. As the first objective of this work, various carboxyalkylation of CNC were conducted by which carboxyalkylate groups with different chain lengths (i.e., carbon spacers) were introduced onto the CNC to address this challenge.

Surfactants play a crucial role in the industry as emulsifying, cleaning, and dispersing agents (Tardy et al., 2017). Since surfactants containing trimethylammonium are widely used in the medical (Patel, 1983; Colomer et al., 2011) and textile (Tardy et al., 2017) industries, myristyl trimethyl ammonium bromide (MTAB) was selected as the cationic surfactant in our study. The CNC-MTAB interaction may result in colloidal systems with interesting properties applied in fields ranging from biomedical (Jackson et al., 2011) to food (Serpa et al., 2016) and personal care formulations (Dhar et al., 2012). While the interaction of cationic surfactants having different alkyl chain lengths has been studied with CNC (Brinatti et al., 2016), the impact of the physicochemical properties of CNC on its interaction with the surfactants has not been studied in detail. Tailoring the surfactant's chain length might limit its use in some applications since it significantly affects the water solubility and critical micelle concentration (CMC) of the surfactant (Sharma et al., 2016). Instead, tuning the surface characteristics of CNC would widen the application of CNC-surfactant formulations.

The addition of carboxylate functional groups with different hydrocarbon chain lengths (i.e., carbon spacer) could be a way to introduce charges and hairy structures to the CNC surface (Sheikhi & van de Ven, 2017). These alterations would provide CNC with both electrostatic and non-electrostatic affinity (Yang & van de Ven, 2016), and beget the possibility for generating different CNC-surfactant coating (He et al., 2019) and composite formulations (Sheikhi & van de Ven, 2017). The second objective of this work was to study the interaction of MTAB and CNC having different carboxyalkyl chain lengths (i.e., carbon spacers).

Undoubtedly, generating a functional CNC-surfactant complex for various fields is not possible without analyzing its behavior in varied salt and pH environments, which is the third objective of this work. Since electrostatic interaction is hindered under salinity and remarkably affected by pH, analyzing the impact of salt and pH becomes vital in understanding the interaction of charged CNC and surfactant (Curtis et al., 2016). This research would also help understand the interaction mechanisms (i.e., the electrostatic and non-electrostatic) of hairy CNC and MTAB. Also, since

surfactants adopt different configurations at different concentrations (Alila et al., 2005), the interaction analysis below and above CMC concentrations with CNC was performed to reveal the behavior of MTAB in interacting with CNC derivatives.

This study would verify the hypothesis that the carbon spacer of grafted carboxylate groups on CNC would alter the physicochemical properties and interaction of the CNC with cationic surfactants. Verifying this hypothesis would assist in designing CNC-surfactant complexes with desired properties adaptable to different environments (pH or salt). In this work, we produced CNC and modified it through carboxyalkylation. The samples with similar charge densities but with varying alkyl chain lengths were produced to examine the effect of alkyl chain length on the interaction of CNC and MTAB. Adsorption analysis was then carried out using a Quartz crystal microbalance with dissipation (QCM-D). Our findings would assist with understanding the fundamentals of the effect of the hairy surface structure of CNC when it interacts with a surfactant, e.g., MTAB, under various conditions of pH and saline. Also, the discussion was made on the possible applications of the produced carboxyalkylated CNC samples in surfactant-containing environments.

5.3 Material and methods

5.3.1 Materials

Bleached softwood kraft pulp was supplied by a pulp mill in northern Ontario, Canada. Sodium chloroacetate (SCA) (98%), 5-chlorovaleric acid (CVA) (98%), 8-bromooctanoic acid (BOA) (97%), 16-bromohexadecanoic acid (BHDA) (≥99%), isopropyl alcohol, polyethyleneimine (PEI) (50%) and myristyltrimethylammonium bromide (MTAB) (≥98.0%) with the critical micelle concentration (CMC) of 0.43 g/L were obtained from Sigma Aldrich. Sulfuric acid (98%), sodium hydroxide (≥97%), and hydrochloric acid were obtained from Sigma Aldrich company and diluted to 64 wt.%, 0.1 M, and 0.1 M, respectively, before use. Hydrogen peroxide, ammonium hydroxide, and KCl were obtained from Fisher scientific, Canada. Cellulosic dialysis membrane with a 1000 g/mol molecular weight cut off was obtained from Spectrum Labs.

5.3.2 CNC production

Cellulose nanocrystals (CNC) were produced in a laboratory-scale based on the method explained in the literature (Feizi, & Fatehi, 2020; Beck-Candanedo et al., 2005). Softwood pulp was segmented and hydrolyzed in a 64 wt.% sulfuric acid solution with the pulp/acid ratio of 1/17

wt./wt. at 45 ºC for one hour. Then, the sample was diluted ten folds to cease the acid hydrolysis. The suspension was then centrifuged to discard excess acid, washed with distilled water, and centrifuged at 2500 rpm for 10 min. This purification step was repeated twice. The pH of the samples was then adjusted to 7.0 by 0.1 M NaOH and dialyzed using membrane dialysis against deionized water for several days for further purification. Finally, the CNC suspension was freeze-dried using a 1L benchtop freeze drier (Labconco Co., USA) and stored for further use.

5.3.3 Carboxyalkylation of CNC

The carboxyalkylation of CNC was generated according to the carboxymethylation methodology of CNC reported in the literature (Feizi, & Fatehi, 2020; Ma et al., 2017). In this work, 0.5 g of CNC sample was added to 50 mL of isopropyl alcohol and stirred at 250 rpm and room temperature for 30 min. Then, the pH of the suspensions was adjusted to 12.0 using 0.1 M NaOH and stirred for another 20 min to deprotonate the hydroxy groups of CNC. Afterward, SCA (1-2 g) was added to the alkaline suspension to generate carboxymethylated CNC (MCNC), while CVA (1-2 g) was added to produce carboxybutylated CNC (BCNC). Also, BOA (1-2 g) was added to make carboxyheptanated CNC (HCNC) and BHDA (1-2 g) was added to generate carboxypantadecanated CNC (PCNC). These reagents were first dispersed in isopropyl alcohol and then added to the suspension dropwise over a 15 min period. The mixtures were then left to react at 55 ºC for 3 h under constant stirring (250 rpm). Afterward, the reaction mixtures were cooled to room temperature and left for the isopropyl alcohol and CNC phase separation. The alcohol was discarded from the top layer, and the modified CNC samples were dispersed in ethanol/water (80/20 vol/vol). The suspensions were then centrifuged at 3500 rpm for 10 min, and the produced modified CNC samples were collected from the bottom. The pH of the CNC suspensions was then adjusted to 7.0 while diluting with distilled water. The samples were then transferred to dialysis membranes and dialyzed for 48 h while changing the distilled water every 12 h. Then, the samples were freeze-dried and stored for further analyses.

5.3.4 Sulfate half-ester, carboxyalkylate group, and pK_a analyses

The conductometric titration was used for measuring the sulfate half-ester and carboxyalkylate group contents of CNC samples by using an automatic conductometer (Metrohm 856 Titrado, Switzerland), as described in the literature (Feizi, & Fatehi, 2020; Reid et al., 2017). In short, CNC derivatives (0.03 g) were mixed with 2 mL of 0.02 mol/L NaCl. Then, 150 mL of Milli-Q water

was added to the mixtures, and the samples were stirred at 250 rpm until homogenized. Afterward, the pH of the suspensions was adjusted to 3.5 using 0.1 M HCl and then titrated with NaOH solution (0.01 mol/L). The sulfate half-ester and carboxyalkylate group contents were then calculated as described in the supplementary information. The pK_a of the samples were also calculated according to the literature (Makino & Yamazaki, 1972).

The degree of substitution (DS) was then calculated following equation 5.1:

Equation 5.1

$$\text{Degree of Substitution (DS)} = \frac{M \times A}{1-(B \times A)} \quad (1)$$

where A is the total carboxyalkylate group content (mmol/g), B is the mass of attached carboxymethylate (0.059 g/mmol), carboxybutylate (0.101 g/mmol), carboxyheptanate (0.143 g/mmol), or carboxypantadecanate (0.255 g/mmol) group. M is the primary unit mass of CNC (anhydroglucose, 0.162 g/mmol).

5.3.5 Dynamic light scattering (DLS)

The hydrodynamic diameter of CNC samples (0.05 g/L) was measured by a 90Plus PALS zeta potential analyzer (Nano Brook, Brookhaven, USA) at the scattering angle of 90° and the wavelength of 632 nm at 25°C. This analysis was performed at three different pH of 3.0, 7.0, and 11.0 in the presence of KCl (1 mM) following the procedure explained in the literature (Kazzaz et al., 2018a). The experiment was also conducted at pH 7.0 in different concentrations of KCl and urea, separately.

5.3.6 Laser diffraction particle size analyzer

The size of CNC and PCNC samples was determined using a laser diffraction particle size analyzer (Malvern Mastersizer 3000, Worcestershire, UK) at 25 °C. The prepared CNC samples (9.05 g/L) were introduced to a chamber containing KCl solution (200 mM) under stirring. The reflective indices of CNC and water were 1.51 and 1.33, respectively (Niskanen et al., 2019). The rotational speed (i.e., level of turbulence) in the chamber of the instrument was increased from 700 to 3000 rpm to evaluate the impact of shear on the particle size of the CNC samples. The particle size analysis was setup to be measured once per two minutes. The conditions were kept constant for all measurements, and D_x (90) was utilized for expressing the particle diameter of the CNC samples that represents 90% of particle diameters lies bellow that value.

5.3.7 X-ray Diffraction (XRD) Analysis

The diffraction patterns of CNC derivatives were assessed using a Pananalytical X'pert Pro diffractometer with Cu Kα radiation with the wavelength of 1.5419 Angstrom. Data were collected in the 2θ range of 6° to 40° at a rate of 2°/min. The measurement resolution for this analysis was 0.02°. In this analysis, freeze-dried CNC samples were transferred onto the clean silicon wafer pieces and submitted to the instrument for analysis. A blank run data was collected and subtracted from the experimental data of the CNC samples. Peak polarization and deconvolution were then performed using the PeakFit software while using the Voit function for the crystalline peaks and the Fast Fourier transform (FFT) for the amorphous part (Yao, Weng, & Catchmark, 2020; French, 2020). The crystallinity index (CrI, %) was then calculated following equation.5.2 (Douard et al., 2020):

Equation 5.2

$$C = \frac{Area_{crystalline} - area_{amorphous}}{I_{crystalline}} \times 100 \quad (2)$$

5.3.8 ^{1}HNMR spectroscopy analysis

The structure of CNC samples was analyzed using ^{1}H NMR spectroscopy (Bruker Ascend^{TM} 400, US) with 128 scans. In this experiment, 40 mg of freeze-dried CNC samples were dissolved in 1 mL of DMSO[d_6] and stirred until fully dispersed (i.e., for 12 h). Samples were then transferred to 5 mm NMR tubes and immediately submitted to the instrument for the analysis (Kono, 2013; Kazzaz, & Fatehi, 2020c).

5.3.9 Zeta potential analysis

NanoBrook Zeta PALS (Brookhaven Instruments Corp, USA) was used to analyze the zeta potential of the CNC samples as well as the surfactant in altered pH. In this analysis, CNC-based suspensions and the MTAB solution were prepared in 5 g/L and 0.43 g/L concentrations, respectively, and left for stirring overnight, separately. The pH of the samples was set to 2.0-13.0, and the zeta potential was measured according to the procedure explained elsewhere (Feizi, et al., 2019; Kazzaz et al., 2018b). For zeta potential analysis under saline conditions, the same procedure was followed while samples were prepared in KCl with varying concentrations in the range of 0 and 360 mM. This analysis was repeated while mixing CNC suspensions and MTAB solutions

prepared in three different concentrations of 0.43, 1.34, and 2.25 g/L to identify the overall zeta potential of the suspensions after mixing.

5.3.10 Coating CNC derivatives on PEI-coated sensors of quartz crystal microbalance

In this analysis, gold-coated QCM-D sensors were cleaned by immersing into a freshly prepared and pre-heated (60°C) cleaning solution comprised of Mili-Q water/hydrogen peroxide/ammonium hydroxide (10:2:2 v/v/v ratio) for 5 min. Then, sensors were rinsed with Mili-Q water and dried with nitrogen gas. Afterward, they were placed in a UV/ozone oxidation cleaner (PSD Series, digital UV ozone system, NOVASCAN) for 15 min and then rinsed and dried before use.

Depositing QCM-D gold surfaces with polyethyleneimine (PEI) prior to coating with cellulose derivatives are known to increase the adhesion of CNC to the sensor (Zhang et al., 2018; Pirich et al., 2017; Bardet et al., 2015). For this reason, gold sensors were coated with PEI using a spin-coater, WS-650 (Laurell) Technologies Corp, for 30 seconds at 1500 rpm at 60 Psi (Zhang et al., 2018; Pirich et al., 2017; Bardet et al., 2015). PEI-coated sensors were subsequently spin-coated with 0.5% CNC suspensions for 30 seconds at 1500 rpm to create a homogenous surface (Pirich et al., 2017; Niinivaara et al., 2015). CNC-coated surfaces were then dried in an oven (60°C) for 30 min.

5.3.11 Wettability analysis

Theta Lite Contact Angle (Biolin Scientific, Finland) equipped with a camera was used for static hydrophilicity/hydrophobicity analysis of the CNC-coated surfaces. A water droplet (1.5 µL) was placed onto blank or CNC-coated QCM-D sensors, and the wettability of the sensors was measured for 20 seconds following Young's equation (5.3) (Sriamornsak et al., 2008).

Equation 5.3

$$\gamma_{sg} - \gamma_{sl} = \gamma_{gl}\cos\theta \quad (3)$$

where γ_{sg}, γ_{sl}, and γ_{gl} are interfacial tensions (mN/m) of solid-gas, solid-liquid, and gas-liquid, respectively. The θ (°) is the angle of the water droplet when it is placed on the CNC-coated surfaces. The same procedure was followed to analyze the contact angle of MTAB with different concentrations on the CNC-coated surfaces, while a surfactant droplet was placed onto the coated surfaces.

5.3.12 Scanning electron microscopy (SEM) analysis

FE-SEM (Hitachi SU-70) imaging was performed for the CNC-coated QCM-D sensors prior to the MTAB adsorption to provide the evidence of surface coverage of CNC derivatives on the PEI coated sensors. The images of the sensors were taken at the magnification of 1, and 2 μm and the voltage of 5 kV, and ImageJ program was used in calculating the CNC coverage of the sensors. In addition, by using the energy-dispersive X-ray spectroscopy (EDX) of the SEM instrument (Figure S5.1), the chemical compositions of the sensors before and after coating was analyzed. To determine the surface coverage, SEM images were converted to a 32-bit bichromatic image. The threshold was adjusted to include the nanoparticles covered the surface (Figure S5.2, white area) and exclude the uncovered area (Figure S5.2, black area). The surface coverage was then calculated by the software through dividing the covered area by the total area (Schram et al., 2015; Wilson et al., 2018). ImageJ also helped quantitatively with the calculation of the mean roughness of the topographical images by using the image as the input. The values of pixels in the images represent the distance (Van Pham & Vo, 2020).

5.3.13 Adsorption analysis of MTAB on CNC-coated surfaces

The adsorption analysis of MTAB on CNC-coated sensors was studied by a Quartz crystal microbalance with dissipation (QCM-D 401, E1, Q-Sense Inc. Gothenborg, Sweden) at pH of 3.0, 7.0, and 10.0 to evaluate the pH effect on the interaction and adsorption of the surfactant on the surfaces. This analysis was also performed under the saline condition (KCl) at pH 7.0. To evaluate the effect of micelle formation and concentration on the interaction of MTAB with functionalized CNC-coated surfaces, the adsorption analysis was conducted at three different MTAB concentrations of below CMC point (0.43 g/L), at the CMC point (1.34 g/L), and above CMC point (2.25 g/L) at pH 7.0. The detailed equations and fundamentals of QCM-D analysis were discussed in the literature (Niinivaara et al., 2015). The data analysis was conducted using Q-Tools software (Q-Sense, Gothenburg, Sweden). A thin adsorbed film with $\Delta D \leq 1 \times 10^{-6}$ with no spreading of overtones in Δf and ΔD graphs was considered as a rigid surface, and the Sauerbrey equation was used to quantitatively analyze the changes in the adsorbed mass (Jaafar et al., 2019; Niinivaara et al., 2015). The mass analysis of the surfaces depicting viscoelastic properties was conducted by fitting data into the Voigt model using harmonic overtones by Q-Tools software. In this model, the density and viscosity of the adsorbed MTAB layer were assumed to be 1090 kg/cm^3

and 1 mPa according to the literature (Wu et al., 2011). These models were used in QCM-D analysis to evaluate the adsorbed mass as well as the properties of the adsorbed layer. A baseline for adsorption analysis was generated using the Milli-Q water or the saline solution throughout the QCM analysis.

5.4 Results and discussion

5.4.1 CNC carboxyalkylation and characterization

The carboxyalkylation of CNC was carried out using varied reagent/CNC ratios at 55°C for three hours under an alkaline environment. According to the charge density analysis of the modified CNC samples (presented in Table S5.1 in the supplementary material), the following reagent ratios were selected for producing carboxyalkylated CNC due to their similar charge densities: carboxymethylated CNC (MCNC) with 1:2 weight ratio of CNC/SCA, carboxybutylated CNC (BCNC) with 1:2.5 weight ratio of CNC/CVA, carboxyheptanated CNC (HCNC) with 1:3 weight ratio of CNC/BOA, and carboxypantadecanated CNC (PCNC) with 1:4 weight ratio of CNC/BHDA. Figure S5.3 in the supplementary material shows the reaction routes for the CNC carboxyalkylation. Briefly, upon deprotonation of the hydroxy groups of CNC in alkaline pH, the substitution of the hydroxy groups with carboxyalkyl groups (SCA/CVA/BOA/BHDA) would occur. The properties of the CNC samples used in this study are presented in Table 5.1. The results confirmed that carboxyalkylated CNC possessed similar charge densities. As seen, CNC had a sulfate half-ester group content of 0.22 ± 0.04 mmol/g, the pK_a of 2.21, and the hydrodynamic diameter of approximately 154 nm. Also, the hydrodynamic diameters of MCNC, BCNC, HCNC, and PCNC were measured to be approximately 163, 170, 176, and 188 nm, respectively, while their monomodal size distributions are presented in Figure S5.4 in the supplementary material. It is also seen that increasing the carbon chain length of the carboxyalkyl donating groups has gradually enhanced the hydrodynamic diameter of the CNC derivatives. In the same vein, the hydrodynamic diameter distribution of the samples slightly widened when the carbon chain was enhanced. This behavior could be related to the different configurations of the chain length of the carboxyalkyl groups attached to the CNC surface. It is also seen in Table 5.1 that the carboxyalkylation lowered the sulfate half-ester group content of CNC due to treating CNC under an alkaline environment before carboxyalkylation (Jordan et al., 2019; Habibi et al., 2010), while introducing 2.61 ± 0.02, 2.45 ± 0.03, 2.42 ± 0.05 and 2.2 ± 0.03 mmol/g of carboxylate groups to

CNC. Using equation 1, a close degree of substitution of 0.49, 0.52, 0.59, and 0.66 mol/mol was obtained for MCNC, BCNC, HCNC, and PCNC samples, respectively. The existence of sulfate half-ester and introduction of carboxyalkyl groups increased the negative charge density of the samples from -0.2 mmol/g for CNC to approximately -2.0 mmol/g in the carboxyalkylated samples with the pK_a of around 4.7.

Table 5.1. Properties of CNC derivatives.

Properties	CNC	MCNC	BCNC	HCNC	PCNC
Sulfate half-ester group content, mmol/g	0.22 ± 0.04	0.15 ± 0.05	0.17 ± 0.02	0.15 ± 0.03	0.16 ± 0.05
Carboxylate group content, mmol/g	<0.09 [a]	2.61 ± 0.02	2.45 ± 0.03	2.42 ± 0.05	2.2 ± 0.03
Charge density, mmol/g	-0.20 ± 0.05	- 2.78 ± 0.06	- 2.65 ± 0.11	- 2.52 ± 0.15	- 2.1 ± 0.1
Degree of substitution, mol/mol		0.49	0.52	0.59	0.66
p*Ka*	2.21 ± 0.03	4.85 ± 0.05	4.72 ± 0.02	4.65 ± 0.03	4.74 ± 0.06
Hydrodynamic diameter, nm	154	163	170	176	188

[a] Method sensitivity < 0.09

Figure S5.5 presents the ^{1}H-NMR spectrum of the CNC samples. The protons of the CNC glucose unit appeared at 4.66, 3.77, 3.55 and 3.05 ppm belong to H1, H3, 6, 5, H2 and H4 in the anhydroglucose unit of CNC (Guo et al., 2013), respectively (Figure S5.5). The peak appeared at 4 ppm in MCNC is ascribed to the proton in the carboxymethylated functional group (Heinze et al., 1999; Mourya, Inamdar & Tiwari, 2010; Dodi et al., 2011; Konduri & Fatehi, 2016). As seen, increasing the chain length in the carboxyalkyl group led to the appearance of new peaks at 0.8-1.6 ppm, which is attributed to the internal and terminal methyl protons in the carboxyalkyl groups attached to CNC. The obtained results reveal the successful attachment of the carboxyalkyl groups to CNC.

To reveal the information related to the crystalline structure of the CNC samples, XRD analysis was performed, and the results are shown in Figure 5.1. As seen, a typical XRD pattern of CNC was attained with diffraction peaks at 15, 16.4, 20.2, 22.3, and 34.4°, which are assigned to planes

(1 $\bar{1}$ 0), (1 1 0), (0 2 1), (2 0 0) and (0 0 4) of CNC, respectively. The crystallinity index was calculated to be 85.99, 81.20, 77.29, 74.97, and 70.81 % for CNC, MCNC, BCNC, HCNC, and PCNC, respectively. As observed, an increase in the carbon chain length of the carboxylate functional group led to a reduction in the crystallinity index for the material.

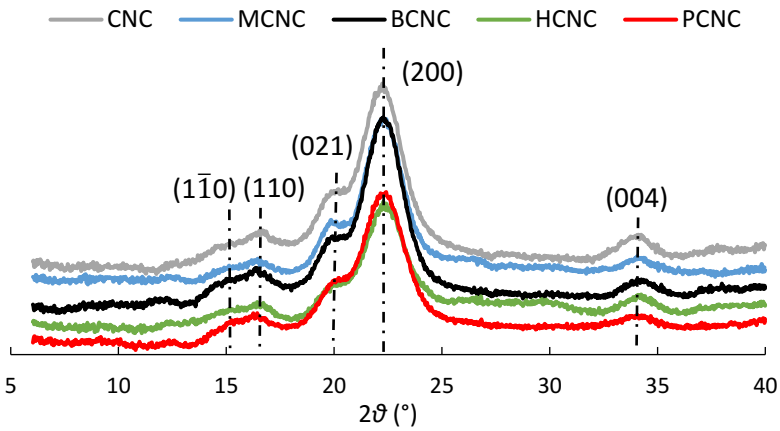

Figure 5.1. XRD patterns of CNC samples

5.4.2 Hairy morphology and particle size of CNC

The The hydrodynamic size of CNC samples was measured at different pH, and the values are depicted in Figure 5.2a. As seen, the hydrodynamic size of the samples was larger at pH 3.0 than other pH, which is ascribed to the protonation of carboxylate groups of the modified CNC samples at this pH, hampering their electrostatic repulsion and thus promoting their agglomeration in solution. Notably, larger difference in size was observed for PCNC than for other CNCs, which reveals that the longer carbon chain generated a larger size. This behavior might be attributed to intensified hydrophobic interaction between the carbon chains of CNC and formation of nanoparticle agglomeration when carboxylate groups were protonated.

However, increasing the pH mostly reduced the size, which was less pronounced for CNC, due to the deprotonation of the carboxylate functional groups and the increase in the surface charge density, yielding repulsion between individual CNC nanoparticles.

To confirm the hairy structure of CNC, the hydrodynamic size of CNC (i.e., smallest sample) and PCNC (i.e., largest sample) was measured under different salt and urea concentrations, and the results were depicted in Figures 5.2b, and 5.2c, respectively. As observed, an enhancement in the ionic strength increased the hydrodynamic size of CNC, especially that of PCNC. The addition of KCl to the CNC samples eliminates the charges located on the CNC particles. In the absence of

charges, the large size of PCNC could be attributed to the entanglement of the carbon chains of the PCNC. As larger size was obtained for PCNC, it can be claimed that the PCNC was agglomerated more intensely. These results would show that PCNC had more hairy structure than CNC. This method was also used by Safari and coworkers (2014) and Van De Ven and Sheikhi (2016) to prove the hairy structure of sterically and electrostatically stabilized CNC. Also, the addition of urea made larger hydrodynamic size for PCNC than for CNC (Figure 5.2c). CNC samples are known to develop intermolecular hydrogen bonding with water molecules. In the presence of urea, original hydrogen bonds developed between CNC and water molecules would break and new hydrogen bonds would form between CNC and urea (Alipoormazandarani & Fatehi, 2020). Thus, the drastic size increment for PCNC in urea could occur through the physical interaction of the alkyl chains of PCNC further confirming the hairy structure of PCNC.

To provide a solid evidence of the hairy structure of PCNC, the particle size of the CNC and PCNC were analyzed in saline system at two different rotational speeds, and the particle size of the material were presented as a function of time in Figure 5.2d. As the rotational speed increased, the particles of CNC and PCNC broke, and the breakage was more gradual for PCNC. This behavior conveys that PCNC nanoparticles have been physically/mechanically entangled that the elevated turbulency gradually reduced their sizes, which is the evidence of hairy structure of PCNC.

It should be stated that, as the particle size analysis by two different machines were conducted under different environments (e.g., shear rates and time), the coagulation tendency of the particles was different, and thus they generated different sizes in Figure 5.2.

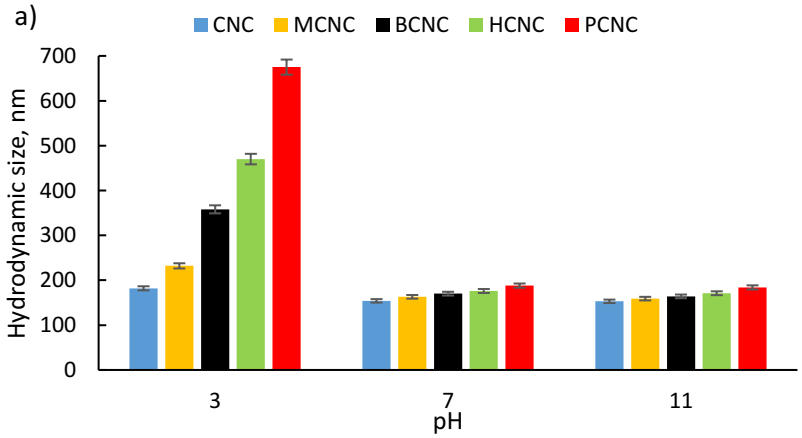

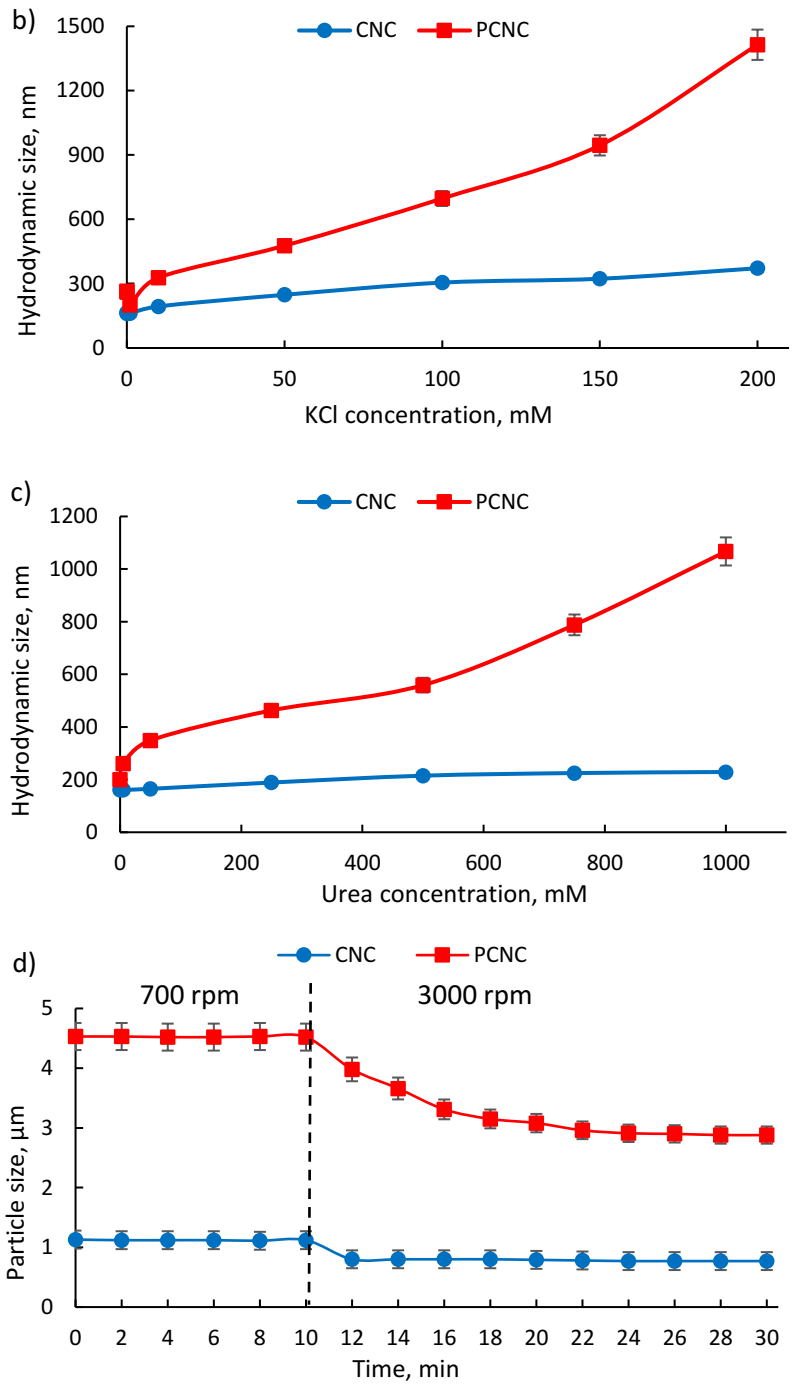

Figure 5.2. The hydrodynamic sizes of CNC and PCNC under different a) pH, b) salinity, and c) urea concentration at 25°C, which was conducted by DLS, and d) the particle sizes, D_x (90), of CNC and PCNC as a function of time conducted by the laser diffraction particle size analyzer at low rpm (700) and high rpm (3000) in 200 mM KCl.

5.4.3 CNC coated sensor evaluation

For coating golden sensors with CNC samples, PEI was first deposited on the sensors prior to CNC adsorption. The SEM images as well as the EDX-SEM images of the surfaces of the sensors are also provided in Figure S5.1a, and S5.1b, respectively, in the supplementary material. The needle-like CNC samples were observable on the surfaces in magnified SEM images. As seen in Figure S5.1b, the PEI coated sensors had larger C, N, and O peaks than untreated sensors in its EDX image. In addition, coating the PEI-coated sensors with CNC samples further increased the C and O peaks in these images while adding a peak for S (from sulfate-half ester groups of CNC), revealing the successful deposition of CNC samples on sensors. Figure 5.3 depicts the SEM images of dried CNC-coated surfaces with a 2 µm magnification. As seen, the uniform coverage of CNC derivatives was attained on the PEI-coated gold surfaces. These images were then analyzed using the ImageJ program to evaluate the coverage percentage and surface roughness of the CNC-covered sensors.

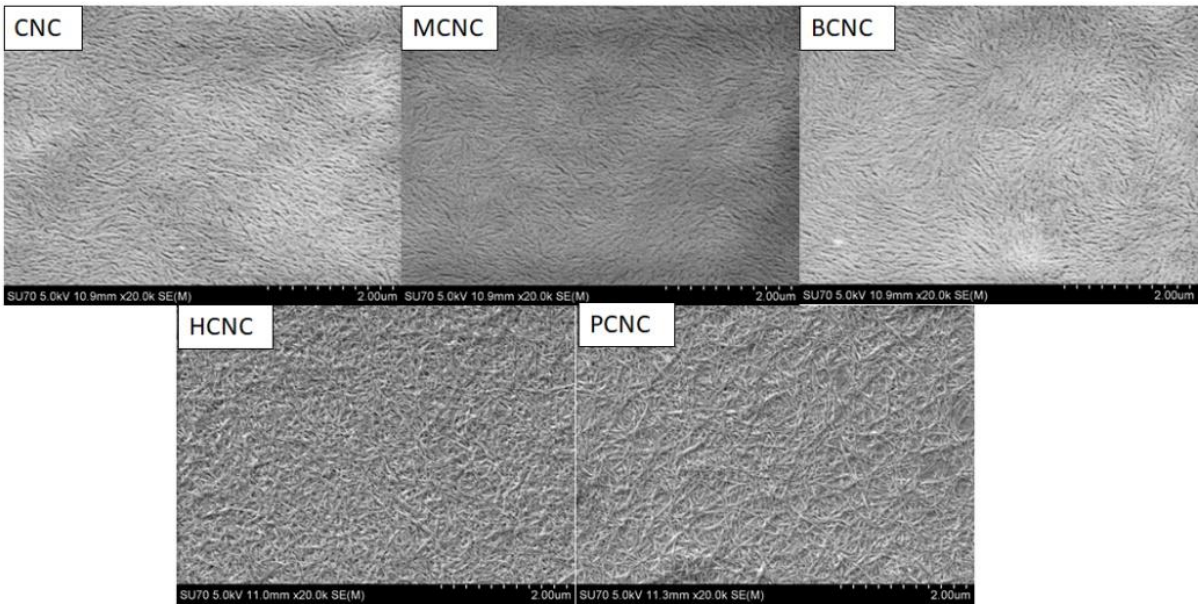

Figure 5.3. SEM images of the PEI-CNC-coated QCM-D sensors with 2 µm magnification.

As is observable in Figure S5.2 in the supplementary material and calculated by using ImageJ, up to 98% of the sensors were covered by CNC derivatives (Niinivaara et al., 2015; Villares, Moreau, Dammak, Capron, & Cathala, 2015). The coverage property of the blank and CNC-coated QCM-D sensors are also presented in Table 5.2. Grasped from Figure 5.3 and quantitative analysis using ImageJ, the surface of modified CNC coated sensors became rougher qualitatively in the order of PCNC>HCNC>BCNC>MCNC, as presented in Table 5.2.

Table 5.2. Properties of CNC-coated sensors.

	CNC	MCNC	BCNC	HCNC	PCNC
Surface coverage, %	98.74	98.58	98.49	98.78	98.75
Surface roughness, nm	20.56	16.58	22.51	28.44	34.18

5.4.4 pH effect

5.4.4.1 Zeta potential analysis

The zeta potential of the CNC samples and MTAB was analyzed at different pH to explore the effect of pH on the zeta potential of the samples. As seen in Figure S5.6 in the supplementary material, the zeta potential for the cationic surfactant was around +11 mV at pH 2.0-7.0, which was attributed to the protonation of its trimethylamine group. Increasing the pH to 11.0 reduced the zeta potential of the system to 0 mV gradually, which was related to the neutralization of the protonated nitrogen-containing group in the presence of excess OH. Meanwhile, the zeta potential for all CNC samples was close to 0 mV at pH 2.0. At pH 3.0, the sulfate half-ester groups on the CNC surface deprotonated, which would significantly reduce the zeta potential. This is aligned with the p*Ka* value of 2.21 obtained for unmodified CNC (Table 5.1). The zeta potential for carboxyalkylated CNC started to change more aggressively than unmodified CNC at higher pH than 4.0, which could be ascribed to the deprotonation of carboxyalkyl groups. According to this analysis, the pH values of 3.0, 7.0, and 11.0 were chosen to peruse the adsorption of MTAB on CNC-covered surfaces. At pH 3.0, the opposite charges of MTAB and CNC derivatives would promote charge interaction between MTAB and CNCs, while charge interaction would diminish at pH 11.0 as MTAB did not carry any charges at this pH. The largest charge interaction would probably occur at pH 7.0 as the maximum zeta potential gap exists between the charge of MTAB and CNCs at this pH.

5.4.4.2 Wettability analysis

Hydrophilicity/hydrophobicity properties of the CNC-coated surfaces were analyzed via the contact angle measurement at different pH of 3.0, 7.0, and 11.0, and the results are depicted in Figure 5.4, while the raw data is available in Figure S5.7 in the supplementary material. Examining the hydrophilicity/hydrophobicity of the coated surfaces prior to the adsorption analysis is very critical (Kazzaz & Fatehi, 2020b) and helps predict the interaction mechanism of the surfactant and the coated surfaces. As seen in Figure 5.4, coating the sensors with CNC derivatives reduced

the contact angle of water by 70% at all pH, which was ascribed to the hydrophilic nature of CNC. A lower contact angle with water was observed for MCNC and BCNC compared to CNC as these samples possessed hydrophilic carboxyalkyl groups on their surfaces. However, the contact angle for HCNC and PCNC was higher than that for the CNC, which could be directly related to the increase in the hydrocarbon chain of their carboxylate group. In other words, comparing the CNC surfaces, it is seen that the carboxylate groups improved the hydrophilicity of the surfaces, but the carbon chain extension improved the hydrophobicity and compensated for the contact angle drop (Song et al., 2006). In comparing the contact angle of the surfaces at different pH, the contact angles were similar (a slightly lower for pH 7.0 though). The obtained contact angle results were used to interpret the interacting behavior of the samples upon the MTAB adsorption to the CNC surface.

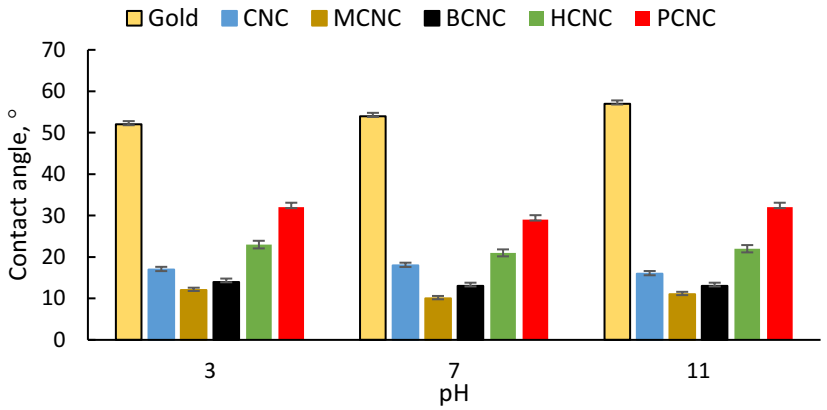

Figure 5.4. The contact angle of the water droplet on the CNC-coated gold surfaces conducted at different pH and 25°C.

5.4.4.2 Adsorption analysis

The adsorption of MTAB on CNC-based surfaces was analyzed using the QCM-D technique at different pH of 3.0, 7.0, and 11.0. Since surfactants have shown to be unable to penetrate the crystalline domain of cellulosic materials (Tardy et al., 2017), MTAB would be assumed to interact only with the surface of CNC and with the functional groups. As seen in Figure 5.5a, at pH 3.0, MTAB adsorbed more (around 50 mg/m^2) onto the PCNC covered surface, while it adsorbed the least on the MCNC coated surface (around 20.80 mg/m^2). The adsorption of MTAB on CNC at this pH would be due to a hydrophobic interaction of alkyl chains with the hydrocarbon tail of MTAB, as well as the charge interaction between sulfate half-esters on CNC (with the p*Ka* of 2.21

in Table 5.1) and the positively charged MTAB. As PCNC had a longer chain length and thus was more hydrophobic (Figure 5.4) than other CNC derivatives, the hydrophobic interaction between the alkyl chain of the carboxypantadecanyl group and the hydrocarbon tail of MTAB was more dominant. Also, the slightly lower sulfate half-ester groups of PCNC than other CNC derivatives should have played a minor role in interacting with MTAB (Tardy et al., 2017; Chotipang et al., 2007). The non-coulombic interaction of MTAB's alkyl chain with silica surfaces was also reported in the literature (Cocke et al., 2002). At this pH, MTAB is highly positive while the carboxyalkyl groups on CNC derivatives are protonated, considering their p*Ka* in the range of 4.6-4.8 (Table 5.1). Thus, the only electrostatic attraction, basically through an ion-exchange interaction, would be between MTAB and CNC's negatively charged sulfate half-ester groups (Hu et al., 2015). The slightly lower charge interaction and less hydrophobic interaction of MTAB and MCNC (Figure 5.4) might be the reasons for its lower adsorption on MCNC than CNC (Figure 5.5a).

The adsorption of MTAB almost doubled at pH 7.0 than pH 3.0 on CNC derivatives, which would be due to the deprotonation of CNC's carboxyalkyl groups (Table 5.1, Figure S5.6), begetting a strong electrostatic attraction between MTAB and CNC derivatives (Gangula et al., 2010). At this pH, the highest adsorption of MTAB occurred on the PCNC-covered surface (around 98.17 g/m^2), and the least occurred on the CNC (around 19 g/m^2). The higher hydrophobic interaction of PCNC than MCNC could still be the reason for its higher adsorption, while the general increase in the adsorption is due to the activation of the carboxylate group and its role (in addition to that of sulfate half-ester) (Figure S5.6 in the supplementary material) in the charge interaction with MTAB for adsorption. Electrostatic interaction was also reported as a driving force for the adsorption of cationic surfactants onto CNC (Brinatti et al., 2016; Abitbol et al., 2014). Overall, the electrostatic interaction between sulfate half-ester and carboxylate groups on CNC with MTAB, as well as the hydrophobic interaction are predicted to be the driving forces for the adsorption at this pH.

The adsorption of MTAB on the surfaces was lower at pH 11.0 due to the lack of electrostatic interactions resulting from the neutralization of MTAB (Figure S5.6), while the hydrophobic interaction between CNC derivatives and MTAB still played a role since higher adsorption was observed for PCNC than other CNC derivatives (Figure 5.5).

In addition, comparing the results obtained at all pH values, a faster surface saturation was observed for the adsorption at pH 7.0. As charge interaction was dominant at this pH, the results

in Figure 5.5 would imply that the charge interaction was developed more quickly than hydrophobic interaction, as hydrophobic interaction was dominant at pH 11.0 and the adsorption was slower at this pH (Gangula et al., 2010; Alila et al., 2005).

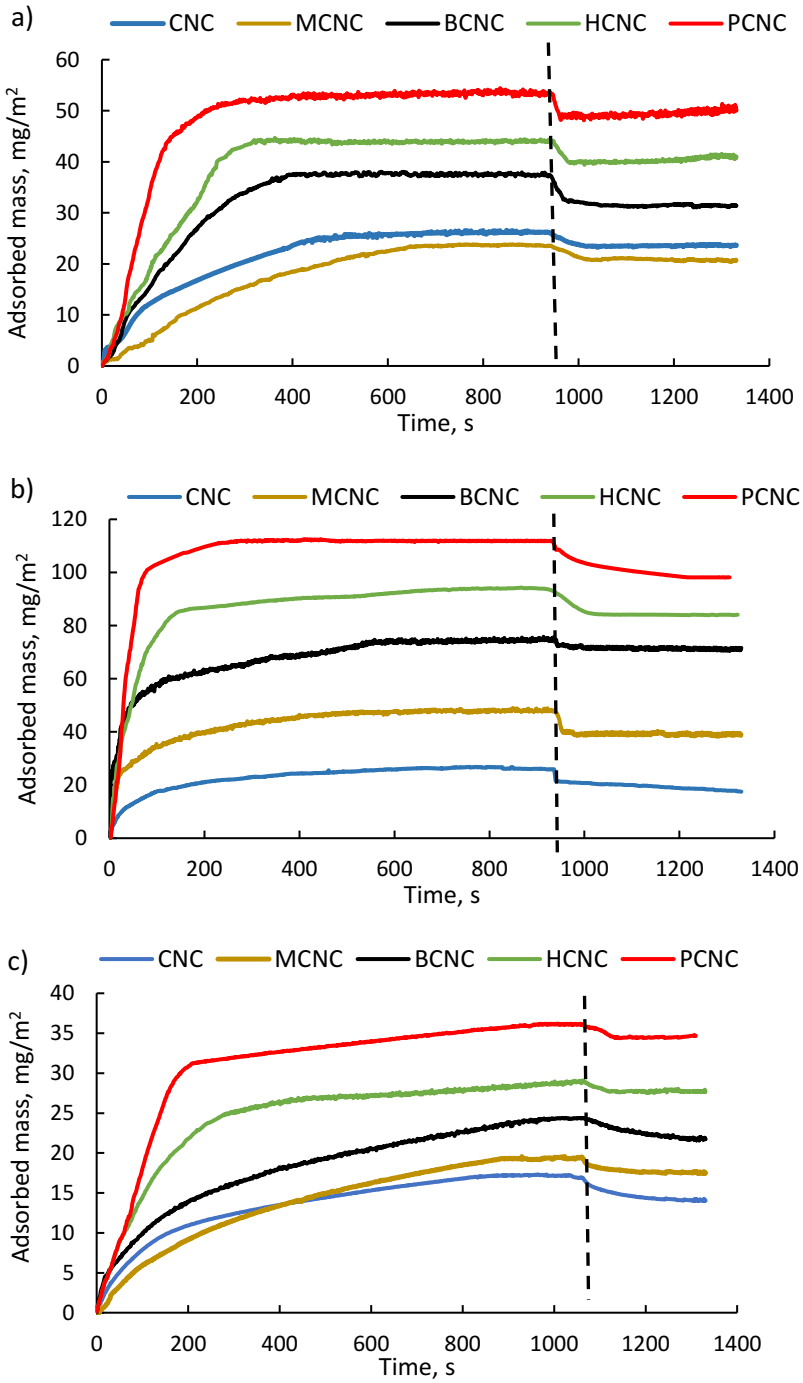

Figure 5.5. Adsorbed mass of MTAB on CNC-based surfaces at different pH values of a) 3.0, b) 7.0, and c) 11.0. The dashed line indicates buffer rinsing.

The thickness of the adlayer and surface viscoelasticity (pH 7.0) after the adsorption of MTAB on CNC surfaces were determined, and the results are depicted in Figure 5.6. Since a similar trend was observed for all CNC samples at pH 3.0 and 11.0, the related viscoelasticity graphs were presented in Figure S5.8 in the supplementary material. As seen in Figure 5.6a, the thickness of the unmodified CNC-coated surface was not significantly affected by the pH variation (approximately 15 nm). Furthermore, the increase in chain length reduced the thickness of the adlayer and this phenomenon was observed more dramatically at pH 7.0. In addition, it is seen in Figure 5.6b that the slope of changes in dissipation dropped as the alkyl chain length increased for CNC.

Generally, a higher $\Delta D/\Delta f$ is a sign of a looser surface, indicating a weak interaction between the adsorbed layer and the surface, whereas a lower $\Delta D/\Delta f$ depicts a more compact adsorbed layer resulting from a strong interaction between substrates (Saarinen et al., 2009; Tammelin et al., 2004). In our case (Figure 5.6b), the steep slope for CNC indicates a viscoelastic adlayer generated on the CNC surface, while the less steep slope observed for PCNC is an indication of a more compact and stronger adlayer formed on the surface. The higher adsorption (Figure 5.5) and smaller thickness on the CNC with a long chain length (Figure 5.6a) could be another indication of the formation of a more compact layer of MTAB on the CNC with a longer chain length (e.g., PCNC). Since the hydrocarbon tails of MTAB tend to minimize their contact with water molecules (Alila et al., 2005), the higher hydrophobicity of the CNC with longer alkyl chain (PCNC) might promote stronger interaction with MTAB and thus more diffusion of MTAB into the hairy structure of PCNC to generate a more compact structure. Alila et al. (2005) also reported that an increase in the interaction between cationic surfactants and cellulose fibers led to the formation of a denser layer on the surface.

As the hydrophobic interaction of MTAB and CNC was elevated by alkyl chain length extension of modified CNC, it may be concluded that the hydrophobic interaction tended to contribute more greatly to generate the compact structure, while charge neutralization tended to develop more viscoelastic adlayer of MTAB on the CNC surface.

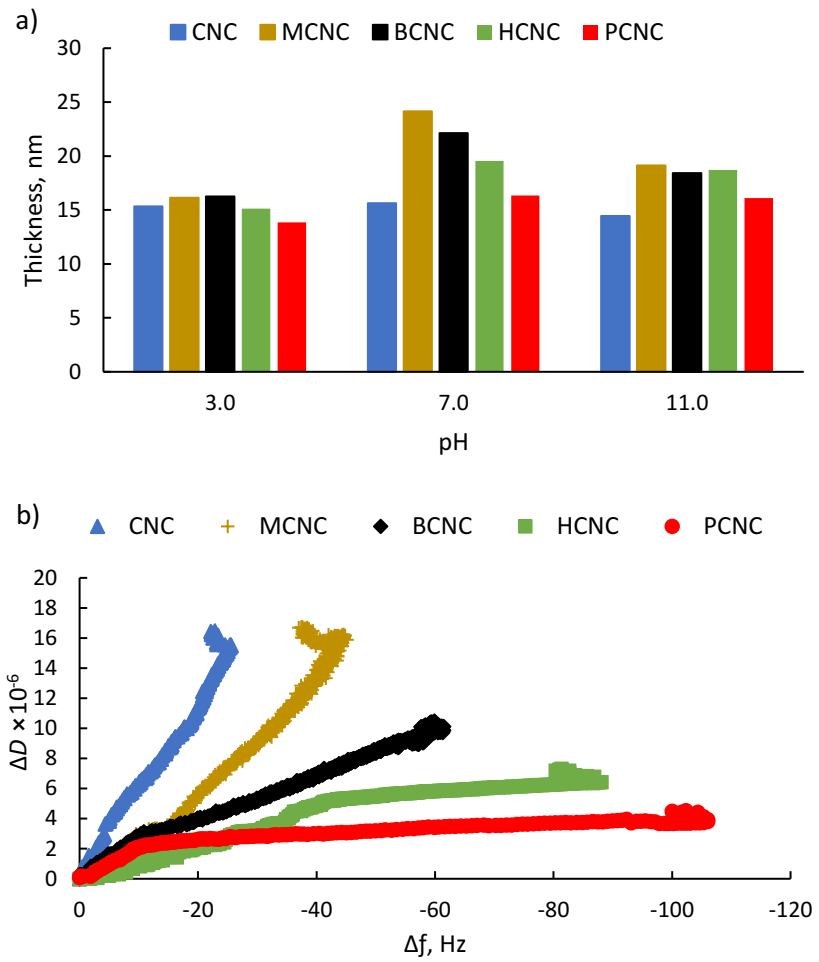

Figure 5.6. a) thickness of the layer after adsorption of MTAB on the CNC-based surfaces at different pH, and b) changes in the dissipation of adsorbed adlayer as a function of changes in the frequency of the third overtone of the CNC coated sensor for the adsorption of MTAB (at 0.43 g/L concentration) on the CNC surfaces at pH 7.0.

5.4.4.3 Interaction mechanism at different pH

As schematically presented in Figure 5.7, the highest MTAB-CNC interaction is observed at pH 7.0 while it decreased at pH 3.0 and 11.0, respectively. At pH 7.0, the electrostatic attraction between the hydrophilic part of MTAB and functional groups of CNC (carboxylate and sulfate half-ester) is dominant (Figure 5.4). Also, a hydrophobic interaction of carboxylate alkyl chains with the hydrocarbon tail of MTAB strengthens the adsorption at this pH, leading PCNC to have the highest MTAB adsorption. At pH 3.0, the charge interaction between MTAB and CNC surfaces is reduced dramatically due to the protonation of the carboxylate groups (Figure 5.4, Table 5.1), while sulfate half-esters are still deprotonated and contribute to the adsorption. The hydrophobic

interaction becomes dominant at this pH, resulting in PCNC capturing more MTAB monomers than other CNC surfaces. At pH 11.0, charge interaction disappears due to the protonation of MTAB's trimethylamine group while the hydrophobic interaction leads the adsorption.

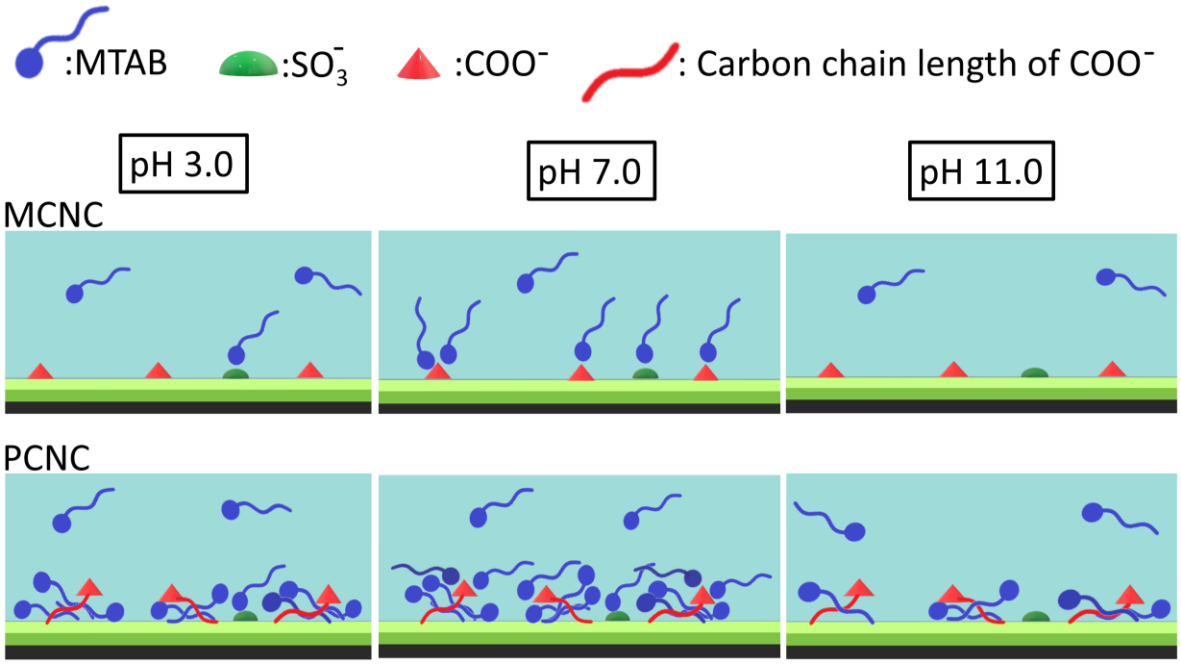

Figure 5.7. Schematic interaction mechanism of MTAB with the CNC-coated surfaces at different pH.

5.4.5 Salt effect

5.4.5.1 Zeta potential analysis

Zeta potential analysis was repeated in the presence of KCl (0-360 mM concentration) and the results are depicted in Figure S5.9 in the supplementary material. This analysis aimed to find the suitable concentration of KCl in which all charges on samples are eliminated. As seen, an increase in the KCl concentration to 240 mM led to the neutralization of all samples. The zeta potential is known to be affected significantly by the electrochemical double layer. In detail, an enhancement in the salt concentration yielded the electrochemical double layer to become compressed due to the decrease in the Debye length, which was caused by the increase in the Debye-Huckel screening strength at a higher salt concentration (Prathapan et al., 2016). The compression of the double layer would facilitate the adsorption of ions and ion pairs to the surface of CNC samples, leading to a minimal or zero zeta potential (Pashley, 1981; Breite et al., 2016). Although the CNC samples have varied carbon chain lengths, a close-to-zero zeta potential was achieved for all samples at

240 mM ionic strength due to their similar amount of charged groups on their CNC surfaces (Table 5.1, Figure S5.6).

5.4.5.2 Adsorption analysis

To further confirm the hydrophobic/hydrophobic interaction between MTAB and CNC surfaces, the adsorption analysis was repeated in the presence of 240 mM KCl at pH 7.0 (Figure S5.9). As seen in Figure 5.8a, MTAB followed a very similar adsorption pattern on the CNC and MCNC-coated surfaces with the adsorption of around 20 mg/m^2. However, the highest MTAB adsorption (around 33 g/m^2) was obtained on the PCNC-coated surface. As adding salt eliminates the effect of charge density, the higher adsorption of MTAB on the PCNC would be solely due to the hydrophobic interaction.

Figure 5.8b shows how hydrophobic interaction contributes to the adsorption of MTAB on CNC surfaces. As seen, the slope of the dissipation changes versus the frequency was reduced by the increase in the hydrocarbon chain length of the functional groups on the modified CNC. This indicates the more significant contribution of the hydrophobic interaction of PCNC than other CNC with MTAB. In comparing Figures 5.6b and 5.8b, it is seen that the slope of the lines was increased in saline systems, which might be due to the elimination of charge interaction, reducing the strength of interaction and adlayer compactness.

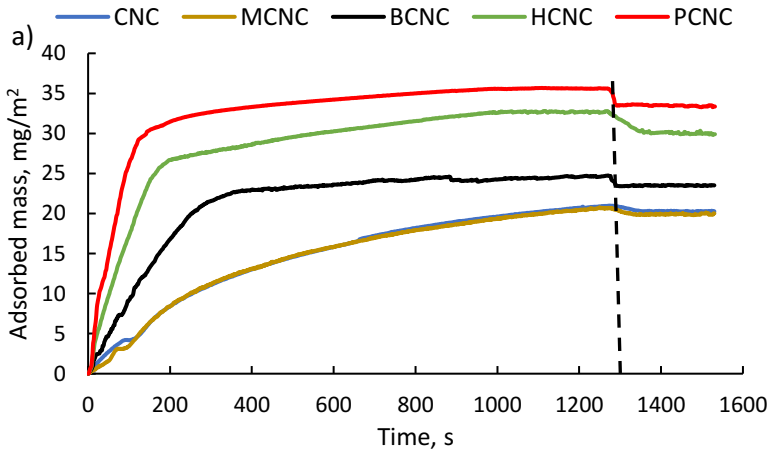

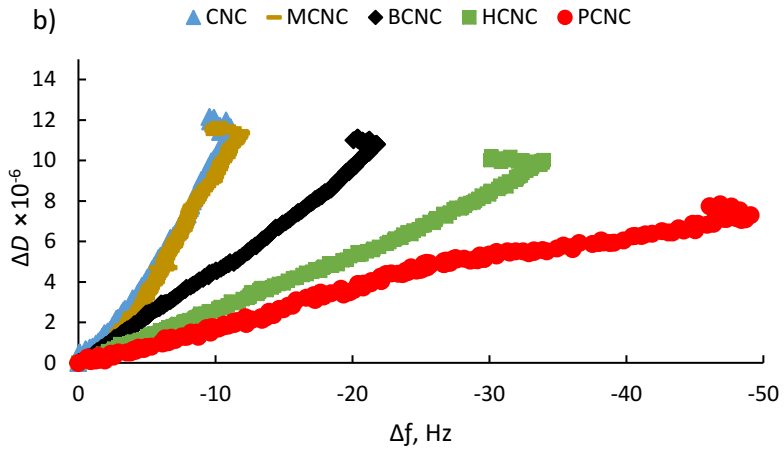

Figure 5.8. a) Adsorbed mass of MTAB on CNC-based surfaces (dashed line indicates buffer rinsing), and b) changes in the dissipation of adsorbed adlayer as a function of changes in the frequency of the third overtone of the CNC coated sensors for the adsorption of MTAB (at 0.43 g/L concentration) on the CNC surfaces at KCl concentration of 240 mM at pH 7.0.

5.4.6 MTAB dosage effect

5.4.6.1 Zeta potential and wettability

To The zeta potential of CNC suspensions having different dosages of MTAB is classified in Table 5.3. As seen, by increasing the concentration of MTAB, the zeta potential of the CNC suspension was reduced due to the partial neutralization of CNC charges. As the suspensions of modified CNC had higher zeta potential, relatively higher anionic zeta potential was achieved when MTAB was added.

Table 5.3 also includes the contact angle analysis for the surface of CNC-coated samples after adsorption of MTAB at different concentrations (wettability images are presented in Figure S5.10 in the supplementary material). As seen, the highest contact angle (approximately 50°) was observed when MTAB was used at a 0.43 g/L concentration. However, the contact angle decreased to around 30° and 20° when MTAB with 1.34 and 2.25 g/L concentrations were used, respectively. The reason for this change is due to the configuration of MTAB monomers, which is discussed comprehensively in the next section. Furthermore, the hydrophilicity/hydrophobicity of the CNC derivatives changed compared to the original values (Figure 5.4 and Table 5.3) due to the varied configuration and interaction of MTAB on and with the surfaces.

Table 5.3. Zeta potential and contact angle analyses conducted at three different MTAB concentration of below CMC point (0.43 g/L), at the CMC point (1.34 g/L), and above CMC point (2.25 g/L) at pH 7.0.

Samples	0.43 g/L MTAB		1.34 g/L MTAB		2.25 g/L MTAB	
	Zeta Potential, mV	Contact Angle, °	Zeta Potential, mV	Contact Angle, °	Zeta Potential, mV	Contact Angle, °
CNC	-20.26 ± 1.02	55 ± 2.3	-7.47 ± 0.47	43 ± 0.2	-5.96 ± 0.25	36 ± 0.7
MCNC	-27.09 ± 1.32	56 ± 2.2	-13.56 ± 0.8	38 ± 0.2	-8.29 ± 0.44	30 ± 0.03
BCNC	-26.71 ± 0.95	55 ± 0.5	-11.42 ± 0.35	37 ± 1.3	-8.43 ± 0.91	29 ± 1.5
HCNC	-26.03 ± 0.86	53 ± 1.1	-14.49 ± 1.08	37 ± 0.2	-7.24 ± 0.38	20 ± 0.2
PCNC	-25.46 ± 0.92	48 ± 0.9	-15.82 ± 1.2	35 ± 1.4	-9.76 ± 0.88	21 ± 1.3

5.4.6.2 Adsorption analysis

MTAB adsorption on CNC coated sensors was analyzed below CMC point (0.43 g/L), at the CMC point (1.34 g/L), and above CMC point (2.25 g/L) concentrations, and the results are depicted in Table 5.4. In general, a higher adsorption was observed at a higher MTAB concentration, and the adsorption was more pronounced for the PCNC than other CNCs, which would be due to its stronger hydrophobic interaction. The thickness of the formed layer upon the MTAB adsorption to CNC-coated surfaces is also reported in Table 5.4. An increase in the MTAB concentration enhanced the thickness of the adlayers for all surfaces, which could be related to the different surfactant configurations forming on the surface. According to the obtained results, it could be concluded that the interaction of CNC samples with MTAB is the strongest bellow the CMC point (Figure 5.6b).

Table 5.4. Adsorbed mass and thickness of MTAB on the CNC surface at three different MTAB concentrations of below CMC point (0.43 g/L), at the CMC point (1.34 g/L), and above CMC point (2.25 g/L) at pH 7.0.

Samples	0.43 g/L MTAB		1.34 g/L MTAB		2.25 g/L MTAB	
	Adsorbed mass, mg/m^2	Thickness, nm	Adsorbed mass, mg/m^2	Thickness, nm	Adsorbed mass, mg/m^2	Thickness, nm
CNC	17.515	15.64	19.547	26.56	19.767	27.42
MCNC	38.929	24.15	42.281	28.17	44.374	32.11

BCNC	71.197	22.12	84.522	26.61	86.438	33.24
HCNC	84.095	19.54	107.61	24.13	112.41	35.51
PCNC	98.174	16.35	130.67	23.28	134.05	35.88

Figure 5.9 depicts the adsorption kinetics of MTAB on the CNC samples at and above the CMC points while that of below CMC point is previously depicted in Figure 5.6b. Comparing Figures 5.6b and 5.9, it is seen that the slope of the adsorption was increased for almost all samples, which indicates a formation of a looser adlayer at or above CMC point compared to that of below the CMC point. The reason for this might be due to the micellar configuration of MTAB at and above the CMC point. When MTAB is in its micellar form, the hydrocarbon tails are located inside the micelle while the hydrophilic heads face outwards (Figure S5.11). This conformation hinders the hydrophobic interaction between MTAB hydrocarbon tails and CNC surfaces, leaving the electrostatic attraction to be the dominant adsorption force (Alila et al., 2005). Thus, it could be claimed that below the CMC point, charge neutralization along with the hydrophobic/hydrophobic interaction play important roles in the adsorption (leading to a more compact adlayer). At and above the CMC concentration, the charge neutralization plays a more dominant role over the hydrophobic interaction in the adsorption (resulting in the generation of a looser adlayer).

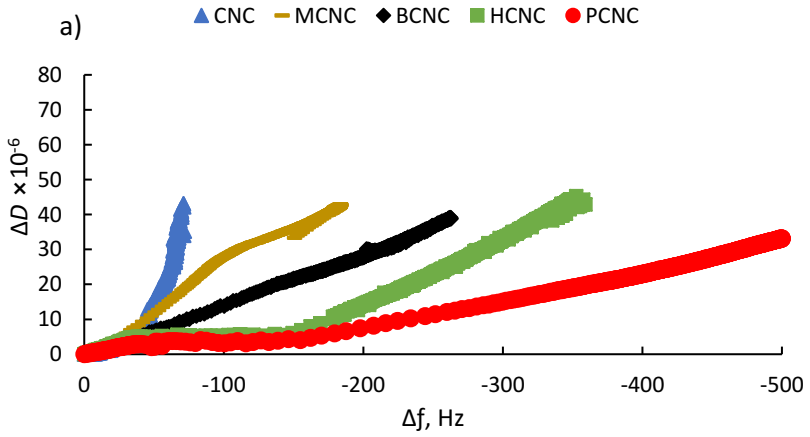

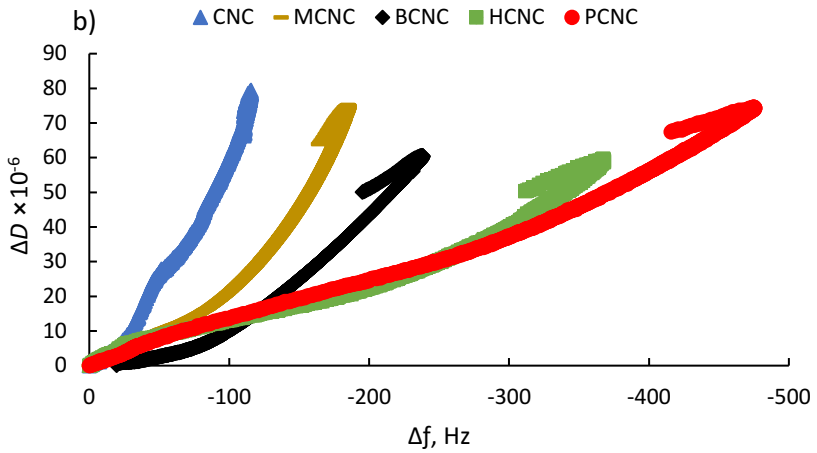

Figure 5.9. Changes in the dissipation of adsorbed adlayer as a function of changes in the frequency of the 3rd overtone of the CNC coated sensors for the adsorption of MTAB at a) 1.34 g/L, and b) 2.25 g/L concentration on CNC surfaces at pH 7.0.

5.4.6.3 Interaction mechanism at different MTAB dosages

Figure S5.11 in the supplementary material provides a schematic demonstration of MTAB interaction with CNC surfaces in different MTAB concentrations. When MTAB is used below its CMC concentration, it adsorbs onto the CNC-coated surfaces through the ion exchange mechanism, while there is no interaction among MTAB molecules. In this case, the hydrophobic tails of the adsorbed surfactants are faced upward. The higher contact angle of MTAB adsorbed surfaces than CNC surfaces provide evidence for the hydrophobicity improvement of the surface and thus charge interaction mechanism (Figure 5.4). By increasing the concentration of MTAB in the CNC system to the CMC point, MTAB molecules begin to associate through a lateral interaction involving hemimicelle (monolayered) and micelle (bilayered) aggregates (Alila et al., 2005). This configuration allows the hydrophilic headgroups of some MTAB monomers to be in contact with the water/air interface (Figure S5.11), leading to a reduction in the contact angle. When MTAB was mixed with CNC at higher than the CMC concentration, the MTAB monomers mostly form micellar conformations on the CNC-coated surfaces, further lowering the contact angle (Alila et al., 2005).

5.4.7 Application

The Carboxyalkylated CNC samples were produced using different reagents of SCA, CVA, BOA, BHDA as carboxyalkyl group donors. These chemical donors have the same charged group, but

they have different carbon chain lengths (Figure S5.3). This study aimed to produce carboxyalkylated samples with a very similar charge density but varied hydrocarbon chain lengths to interact with a cationic surfactant. The results confirmed that CNC with different hairy properties can be produced following similar reaction chemistry but with using different reagents. Also, the results of this work confirmed that by selecting different chemical reagents, it is possible to tailor the surface of CNC for potentially different applications.

Generally, the compactness and/or viscoelasticity of CNC surfaces could be very critical in many applications. A more viscoelastic surface could be beneficial in the production of polarized or polyethylene oxide films (Kadar et al., 2020; Fernandes et al., 2019; Surov et al., 2018). On the other hand, a more hydrophobic and compact surface might be beneficial in coating applications, such as paint and ink (He et al., 2019; Haramagatti et al., 2018). Therefore, the use of MCNC would generate a more viscoelastic layer and the use of PCNC would make a more compact surface for coating applications, e.g., painting.

Interestingly, the anchoring effect of surfactants on hydrophobic surfaces would be enhanced by an increase in the hydrocarbon chain length (Mahmudov et al., 2015; Lin et al., 2013). In the case of such applications as latex, ink, paper coating, adhesive, surfactant-templated silicate, biomedical and polymer nanocomposite productions, HCNC and PCNC samples could be suitable candidates since they would have higher interaction with the medium containing surfactants and the surrounded particles, leading to a more uniform colloidal stability and distribution of the particles (Mekki et al., 2010).

Also, our results showed the strong interaction of modified CNC samples with the surfactant under different pH and saline conditions. This behavior depicts that in applications where variation in pH and salt could occur, such as in coating foams and composites (Micheau et al., 2013) and coating membranes (Bueno & Moraes, 2011), the compact interaction of PCNC and the surfactant could still be achieved.

5.5 Conclusions

In this work, carboxyalkyl cellulose nanocrystals (CNC) with similar charge densities but different alkyl chain lengths were generated. The contact angle analysis confirmed that the longer the alkyl chain, the more hydrophobic the modified CNC. The adsorption analysis of the cationic surfactant, MTAB, with CNC samples at different pH revealed that the charge interaction developed more

quickly than hydrophobic interaction. Also, our hypothesis was verified since MTAB was adsorbed more onto the surface covered with CNC with the longest chain length (PCNC) at all pH, implying a hydrophobic/hydrophobic interaction between the alkyl chain in carboxypantadecanyl functional group, facilitating more adsorption. Also, a more compact and rigid adlayer of MTAB was obtained on the PCNC than MCNC, implying the role of hydrocarbon tail in generating more compact and stronger layers. In the absence of electrostatic interaction in saline systems, the higher MTAB adsorption on the PCNC was a sign of significant hydrophobic/hydrophobic interaction between the MTAB and CNC. The MTAB-CNC interaction was stronger below the CMC point of MTAB, while it was weak at and above the CMC concentrations due to the micellar configuration of MTAB, hindering the hydrophobic interaction. Overall, our results depicted that MTAB-CNC surfaces with tailored viscoelastic characteristics could be produced for various applications.

5.6 References

Abitbol, T., Marway, H., & Cranston, E. D. (2014). Surface modification of cellulose nanocrystals with cetyltrimethylammonium bromide. *Nordic Pulp & Paper Research Journal*, *29*(1), 46-57.

Alila, S., Boufi, S., Belgacem, M. N., & Beneventi, D. (2005). Adsorption of a cationic surfactant onto cellulosic fibers I. Surface charge effects. *Langmuir*, *21*(18), 8106-8113.

Alipoormazandarani, N., & Fatehi, P. (2020). Interaction Mechanism of Anionic Lignin and Cationic Soft Surface in Saline Systems. *The Journal of Physical Chemistry B*, *124*, 8678-8689.

Bardet, R. A. P. H. A. E. L., Sillard, C. É. C. I. L. E., Belgacem, N., & Bras, J. U. L. I. E. N. (2015). Self-assembly of cellulose nanocrystals with fluorescent agent in iridescent films. *Cellulose Chem. Technol*, *49*(7-8), 587-595.

Beck-Candanedo, S., Roman, M., & Gray, D. G. (2005). Effect of reaction conditions on the properties and behavior of wood cellulose nanocrystal suspensions. *Biomacromolecules*, *6*(2), 1048-1054.

Breite, D., Went, M., Prager, A., & Schulze, A. (2016). The critical zeta potential of polymer membranes: how electrolytes impact membrane fouling. *RSC Advances*, *6*(100), 98180-98189.

Brinatti, C., Huang, J., Berry, R. M., Tam, K. C., & Loh, W. (2016). Structural and energetic studies on the interaction of cationic surfactants and cellulose nanocrystals. *Langmuir, 32*(3), 689-698.

Chen, J., Eraghi Kazzaz, A., AlipoorMazandarani, N., Hosseinpour Feizi, Z., & Fatehi, P. (2018). Production of flocculants, adsorbents, and dispersants from lignin. *Molecules*, *23*(4), 868.

Chen, Q., Kang, M., Xie, Q., & Wang, J. (2020). Effect of melamine modified cellulose nanocrystals on the performance of oil-immersed transformer insulation paper. *Cellulose*, *27*(13), 7621-7636.

Chotipong, A., Scamehorn, J. F., Rirksomboon, T., Chavadej, S., & Supaphol, P. (2007). Removal of solvent-based ink from printed surface of high-density polyethylene bottles by alkyltrimethylammonium bromides: Effects of pH, temperature, and salinity. *Colloids and Surfaces A: Physicochemical and Engineering Aspects*, *297*(1-3), 163-171.

Cocke, D. L., Schennach, R., & Yu, Z. (2002). The surface properties of tetradecyltrimethylammonium bromide observed by capillary electrophoresis. *Journal of Chromatographic Science*, *40*(4), 187-190.

Colomer, A., Pinazo, A., Manresa, M. A., Vinardell, M. P., Mitjans, M., Infante, M. R., & Pérez, L. (2011). Cationic surfactants derived from lysine: effects of their structure and charge type on antimicrobial and hemolytic activities. *Journal of medicinal chemistry, 54*(4), 989-1002.

Curtis, K. A., Miller, D., Millard, P., Basu, S., Horkay, F., & Chandran, P. L. (2016). Unusual salt and pH induced changes in polyethylenimine solutions. *PLoS One*, *11*(9), e0158147.

Dhar, N., Au, D., Berry, R. C., & Tam, K. C. (2012). Interactions of nanocrystalline cellulose with an oppositely charged surfactant in aqueous medium. *Colloids and Surfaces A: Physicochemical and Engineering Aspects*, *415*, 310-319.

Dodi, G., Hritcu, D., & Popa, M. I. (2011). Carboxymethylation of guar gum: synthesis and characterization. *Cellulose chemistry and Technology*, *45*(3), 171.

Douard, L., Bras, J., Encinas, T., & Belgacem, N. (2020). Natural acidic deep eutectic solvent to obtain cellulose nanocrystals using the design of experience approach. *Carbohydrate Polymers*, 117136.

Eyley, S., & Thielemans, W. (2014). Surface modification of cellulose nanocrystals. *Nanoscale*, *6*(14), 7764-7779.

Feizi, Z. H., & Fatehi, P. (2020). Carboxymethylated cellulose nanocrystals as clay suspension dispersants: effect of size and surface functional groups. *Cellulose*, *27*, 3759-3772.

Feizi, Z. H., Kazzaz, A. E., Kong, F., & Fatehi, P. (2019). Evolving a flocculation process for isolating lignosulfonate from solution. *Separation and Purification Technology*, *222*, 254-263.

Fernandes, S. N., Lopes, L. F., & Godinho, M. H. (2019). Recent advances in the manipulation of circularly polarised light with cellulose nanocrystal films. *Current Opinion in Solid State and Materials Science, 23*(2), 63-73.

French, A. D. (2020). Increment in evolution of cellulose crystallinity analysis. *Cellulose*, 27:5445-5448.

Gangula, S., Suen, S. Y., & Conte, E. D. (2010). Analytical applications of admicelle and hemimicelle solid phase extraction of organic analytes. *Microchemical Journal*, *95*(1), 2-4.

Grishkewich, N., Mohammed, N., Tang, J., & Tam, K. C. (2017). Recent advances in the application of cellulose nanocrystals. *Current Opinion in Colloid & Interface Science*, *29*, 32-45.

Guo, Y., Liu, Q., Chen, H., Wang, X., Shen, Z., Shu, X., & Sun, R. (2013). Direct grafting modification of pulp in ionic liquids and self-assembly behavior of the graft copolymers. *Cellulose*, *20*(2), 873-884.

Habibi, Y., Lucia, L. A., & Rojas, O. J. (2010). Cellulose nanocrystals: chemistry, self-assembly, and applications. *Chemical reviews*, *110*(6), 3479-3500.

Haramagatti, C. R., Dhande, P., Bhavsar, R., Umbarkar, A., & Joshi, A. (2018). Role of surfactants on stability of iron oxide yellow pigment dispersions. *Progress in Organic Coatings*, *120*, 260-265.

He, Y., Boluk, Y., Pan, J., Ahniyaz, A., Deltin, T., & Claesson, P. M. (2019). Comparative study of CNC and CNF as additives in waterborne acrylate-based anti-corrosion coatings. *Journal of Dispersion Science and Technology*, doi.org/10.1080/01932691.2019.1647229.

Heinze, T., Liebert, T. I. M., Klüfers, P., & Meister, F. (1999). Carboxymethylation of cellulose in unconventional media. *Cellulose*, *6*(2), 153-165.

Hu, Z., Ballinger, S., Pelton, R., & Cranston, E. D. (2015). Surfactant-enhanced cellulose nanocrystal Pickering emulsions. *Journal of Colloid and Interface Science, 439*, 139-148.

Jaafar, Z., Mazeau, K., Boissière, A., Le Gall, S., Villares, A., Vigouroux, J., & Cathala, B. (2019). Meaning of xylan acetylation on xylan-cellulose interactions: A quartz crystal microbalance with dissipation (QCM-D) and molecular dynamic study. *Carbohydrate Polymers*, *226*, 115315.

Jackson, J. K., Letchford, K., Wasserman, B. Z., Ye, L., Hamad, W. Y., & Burt, H. M. (2011). The use of nanocrystalline cellulose for the binding and controlled release of drugs. *International Journal of Nanomedicine*, *6*, 321.

Jasmani, L., Eyley, S., Wallbridge, R., & Thielemans, W. (2013). A facile one-pot route to cationic cellulose nanocrystals. *Nanoscale*, *5*(21), 10207-10211.

Jin, E., Guo, J., Yang, F., Zhu, Y., Song, J., Jin, Y., & Rojas, O. J. (2016). On the polymorphic and morphological changes of cellulose nanocrystals (CNC-I) upon mercerization and conversion to CNC-II. *Carbohydrate Polymers*, *143*, 327-335.

Jordan, J. H., Easson, M. W., & Condon, B. D. (2019). Alkali hydrolysis of sulfated cellulose nanocrystals: optimization of reaction conditions and tailored surface charge. *Nanomaterials*, *9*(9), 1232.

Kadar, R., Fazilati, M., & Nypelo, T. (2020). Unexpected microphase transitions in flow towards nematic order of cellulose nanocrystals. *Cellulose*, *27*(4), 2003-2014.

Kazzaz, A. E., & Fatehi, P. (2020a). Technical lignin and its potential modification routes: A mini-review. *Industrial Crops and Products*, *154*, 112732.

Kazzaz, A. E., & Fatehi, P. (2020b). Fabrication of amphoteric lignin and its hydrophilicity/oleophilicity at oil/water interface. *Journal of Colloid and Interface Science*, *561*, 231-243.

Kazzaz, A. E., & Fatehi, P. (2020c). Interaction of synthetic and lignin-based sulfonated polymers with hydrophilic, hydrophobic, and charged self-assembled monolayers. *RSC Advances*, *10*(60), 36778-36793.

Kazzaz, A. E., Feizi, Z. H., & Fatehi, P. (2018). Interaction of sulfomethylated lignin and aluminum oxide. *Colloid and Polymer Science*, *296*(11), 1867-1878.

Kazzaz, A. E., Feizi, Z. H., & Fatehi, P. (2019). Grafting strategies for hydroxy groups of lignin for producing materials. *Green Chemistry*, *21*(21), 5714-5752.

Kazzaz, A. E., Feizi, Z. H., Kong, F., & Fatehi, P. (2018a). Interaction of poly (acrylic acid) and aluminum oxide particles in suspension: particle size effect. *Colloids and Surfaces A: Physicochemical and Engineering Aspects, 556*, 218-226.

Konduri, M. K., & Fatehi, P. (2016). Synthesis and characterization of carboxymethylated xylan and its application as a dispersant. *Carbohydrate Polymers*, *146*, 26-35.

Kono, H. (2013). 1H and 13C chemical shift assignment of the monomers that comprise carboxymethyl cellulose. *Carbohydrate Polymers*, *97*(2), 384-390.

Lin, N. J., Yang, H. S., Chang, Y., Tung, K. L., Chen, W. H., Cheng, H. W., & Lai, J. Y. (2013). Surface self-assembled PEGylation of fluoro-based PVDF membranes via hydrophobic-driven copolymer anchoring for ultra-stable biofouling resistance. *Langmuir*, *29*(32), 10183-10193.

Ma, X., Cheng, Y., Qin, X., Guo, T., Deng, J., & Liu, X. (2017). Hydrophilic modification of cellulose nanocrystals improves the physicochemical properties of cassava starch-based nanocomposite films. *LWT*, *86*, 318-326.

Mahmudov, R., Chen, C., & Huang, C. P. (2015). Functionalized activated carbon for the adsorptive removal of perchlorate from water solutions. *Frontiers of Chemical Science and Engineering*, *9*(2), 194-208.

Makino, R., & Yamazaki, I. (1972). Effects of 2, 4-Substituents of Deuterobemin upon Peroxidase Functions: 1. Preparation and Some Properties of Artificial Enzymes. *The Journal of Biochemistry*, *72*(3), 655-664.

Mekki, S., Saïdi-Besbes, S., Elaissari, A., Valour, J. P., & Derdour, A. (2010). Novel polymerizable surfactants: synthesis and application in the emulsion polymerization of styrene. *Polymer Journal*, *42*(5), 401-405.

Micheau, C., Bauduin, P., Diat, O., & Faure, S. (2013). Specific salt and pH effects on foam film of a pH sensitive surfactant. *Langmuir*, *29*(27), 8472-8481.

Ming, S., Chen, G., Wu, Z., Su, L., He, J., Kuang, Y., & Fang, Z. (2016). Effective dispersion of aqueous clay suspension using carboxylated nanofibrillated cellulose as dispersant. *RSC Advances*, *6*(44), 37330-37336.

Mourya, V. K., Inamdar, N. N., & Tiwari, A. (2010). Carboxymethyl chitosan and its applications. *Advanced Materials Letters*, *1*(1), 11-33.

Niinivaara, E., Faustini, M., Tammelin, T., & Kontturi, E. (2015). Water vapor uptake of ultrathin films of biologically derived nanocrystals: quantitative assessment with quartz crystal microbalance and spectroscopic ellipsometry. *Langmuir, 31*(44), 12170-12176.

Niskanen, I., Suopajärvi, T., Liimatainen, H., Fabritius, T., Heikkilä, R., & Thungström, G. (2019). Determining the complex refractive index of cellulose nanocrystals by combination of Beer-Lambert and immersion matching methods. *Journal of Quantitative Spectroscopy and Radiative Transfer*, *235*, 1-6.

Pashley, R. M. (1981). Hydration forces between mica surfaces in aqueous electrolyte solutions. *Journal of Colloid and Interface Science*, *80*(1), 153-162.

Patel, C. U. (1983). Anti-static properties of some cationic polymers used in hair care products. *International Journal of Cosmetic Science*, *5*(5), 181-188.

Pirich, C. L., de Freitas, R. A., Torresi, R. M., Picheth, G. F., & Sierakowski, M. R. (2017). Piezoelectric immunochip coated with thin films of bacterial cellulose nanocrystals for dengue detection. *Biosensors and Bioelectronics, 92*, 47-53.

Prathapan, R., Thapa, R., Garnier, G., & Tabor, R. F. (2016). Modulating the zeta potential of cellulose nanocrystals using salts and surfactants. *Colloids and Surfaces A: Physicochemical and Engineering Aspects*, *509*, 11-18.

Reid, M. S., Villalobos, M., & Cranston, E. D. (2017). The role of hydrogen bonding in non-ionic polymer adsorption to cellulose nanocrystals and silica colloids. *Current Opinion in Colloid & Interface Science*, *29*, 76-82.

Saarinen, T., Orelma, H., Grönqvist, S., Andberg, M., Holappa, S., & Laine, J. (2009). Adsorption of different laccases on cellulose and lignin surfaces. *BioResources, 4*(1), 94-110.

Safari, S., Sheikhi, A., & van de Ven, T. G. (2014). Electroacoustic characterization of conventional and electrosterically stabilized nanocrystalline celluloses. *Journal of Colloid and Interface Science*, *432*, 151-157.

Schram, C. J., Taylor, L. S., & Beaudoin, S. P. (2015). Influence of polymers on the crystal growth rate of felodipine: correlating adsorbed polymer surface coverage to solution crystal growth inhibition. *Langmuir*, *31*(41), 11279-11287.

Serpa, A., Velásquez-Cock, J., Gañán, P., Castro, C., Vélez, L., & Zuluaga, R. (2016). Vegetable nanocellulose in food science: A review. *Food Hydrocolloids*, *57*, 178-186.

Sharma, N. K., Singh, M., & Bhattarai, A. (2016). Hydrophobic study of increasing alkyl chain length of platinum surfactant complexes: synthesis, characterization, micellization, thermodynamics, thermogravimetrics and surface morphology. *RSC Advances*, *6*(93), 90607-90623.

Sheikhi, A., & van de Ven, T. G. (2017). Colloidal aspects of Janus-like hairy cellulose nanocrystalloids. *Current Opinion in Colloid & Interface Science*, *29*, 21-31.

Song, X., Zhai, J., Wang, Y., & Jiang, L. (2006). Self-assembly of amino-functionalized monolayers on silicon surfaces and preparation of superhydrophobic surfaces based on alkanoic acid dual layers and surface roughening. *Journal of Colloid and Interface Science, 298*(1), 267-273.

Sriamornsak, P., Wattanakorn, N., Nunthanid, J., & Puttipipatkhachorn, S. (2008). Mucoadhesion of pectin as evidence by wettability and chain interpenetration. *Carbohydrate Polymers*, *74*(3), 458-467.

Sunasee, R., Hemraz, U. D., & Ckless, K. (2016). Cellulose nanocrystals: a versatile nanoplatform for emerging biomedical applications. *Expert Opinion on Drug Delivery*, *13*(9), 1243-1256.

Surov, O. V., Voronova, M. I., Afineevskii, A. V., & Zakharov, A. G. (2018). Polyethylene oxide films reinforced by cellulose nanocrystals: Microstructure-properties relationship. *Carbohydrate Polymers*, *181*, 489-498.

Tammelin, T., Merta, J., Johansson, L. S., & Stenius, P. (2004). Viscoelastic properties of cationic starch adsorbed on quartz studied by QCM-D. *Langmuir, 20*(25), 10900-10909.

Tardy, B. L., Yokota, S., Ago, M., Xiang, W., Kondo, T., Bordes, R., & Rojas, O. J. (2017). Nanocellulose–surfactant interactions. *Current Opinion in Colloid & Interface Science*, *29*, 57-67.

Van De Ven, T. G., & Sheikhi, A. (2016). Hairy cellulose nanocrystalloids: a novel class of nanocellulose. *Nanoscale*, *8*(33), 15101-15114.

Van Pham, K., & Vo, C. Q. (2020). A new method for assessment of nickel-titanium endodontic instrument surface roughness using field emission scanning electronic microscope. *BMC Oral Health*, *20*(1), 1-7.

Villares, A., Moreau, C., Dammak, A., Capron, I., & Cathala, B. (2015). Kinetic aspects of the adsorption of xyloglucan onto cellulose nanocrystals. *Soft Matter*, *11*(32), 6472-6481.

Wilson, C., Brigham, B., Sandoval, J., Sabatka, D., Wilson, E., Sebest, C., Schofield, B. J., Holmes, A. E., & Sutlief, A. L. (2018). The Quantitative Assessment of Pseudomonas aeruginosa (PA) 14 Biofilm Surface Coverage on Slippery Liquid Infused Polymer Surfaces (SLIPS). *International Journal of Nanotechnology in Medicine & Engineering*, *3*(3), 35-42.

Wu, S., Shi, L., Garfield, L. B., Tabor, R. F., Striolo, A., & Grady, B. P. (2011). Influence of surface roughness on cetyltrimethylammonium bromide adsorption from aqueous solution. *Langmuir, 27*(10), 6091-6098.

Yang, H., & van de Ven, T. G. (2016). Preparation of hairy cationic nanocrystalline cellulose. *Cellulose*, *23*(3), 1791-1801.

Yao, W., Weng, Y., & Catchmark, J. M. (2020). Improved cellulose X-ray diffraction analysis using Fourier series modeling. *Cellulose*, 5563-5579.

Zaman, M., Xiao, H., Chibante, F., & Ni, Y. (2012). Synthesis and characterization of cationically modified nanocrystalline cellulose. *Carbohydrate Polymers*, *89*(1), 163-170.

Zhang, Y., Yang, F., Hu, F., Song, J., Wu, S., & Jin, Y. (2018). Binding preference of family 1 carbohydrate binding module on nanocrystalline cellulose and nanofibrillar cellulose films assessed by quartz crystal microbalance. *Cellulose*, *25*(6), 3327-3337.

Zorzi Bueno, C., & Maria Moraes, Â. (2011). Development of porous lamellar chitosan-alginate membranes: Effect of different surfactants on biomaterial properties. *Journal of Applied Polymer Science*, *122*(1), 624-631.

5.7 Appendix A. Supplementary material

Interaction of hairy carboxyalkyl cellulose nanocrystals with cationic surfactant: effect of carbon spacer

Zahra Hosseinpour Feizi, Pedram Fatehi*

Biorefining Research Institute, Green Processes Research Centre and Chemical Engineering Department, Lakehead University, 955 Oliver Road, Thunder Bay, Ontario P7B 5E1, Canada

* Corresponding author, email: pfatehi@lakeheadu.ca; tel: 807-343-8697; fax: 807-346-7943

Supporting experimental section

Sulfonate and carboxymethyl group content analysis

The sulfonate and carboxymethyl group contents of the CNC samples were calculated by equationS1 and S2, respectively (Chen & van de Ven, 2016; Konduri & Fatehi, 2016).

Equation S1

$$\text{Sulfate half ester group} = \frac{V_i \times C_{NaOH}}{m_{CNC}}$$

Equation S2

$$\text{Carboxyalkyl group} = \frac{(V_{ii} - V_i) \times C_{NaOH}}{m_{CNC}}$$

where V_i and V_{ii} are the volume (mL) of NaOH which had neutralized strong and weak acidic groups, respectively, C_{NaOH} is the NaOH concentration (mol/L) and m is the mass of dried weight (g) of CNC.

a)

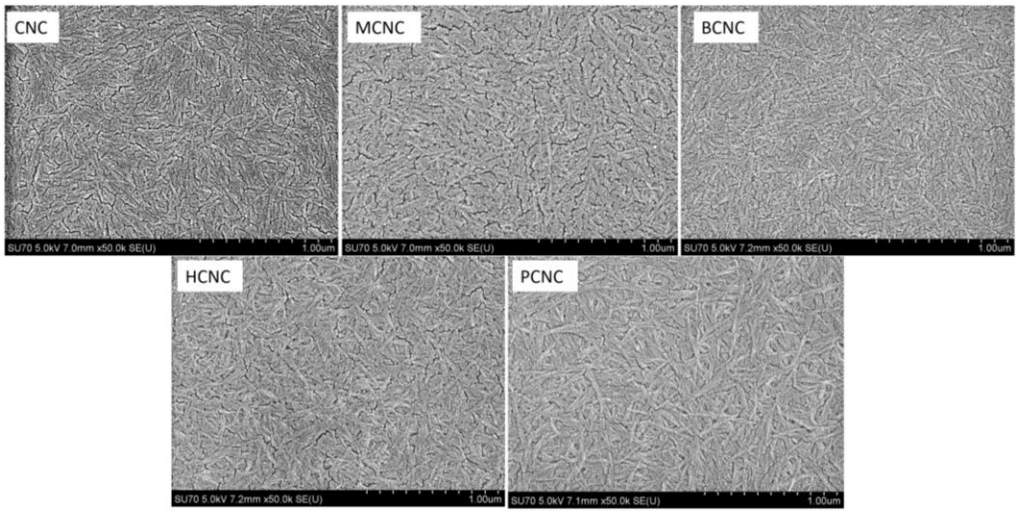

b)

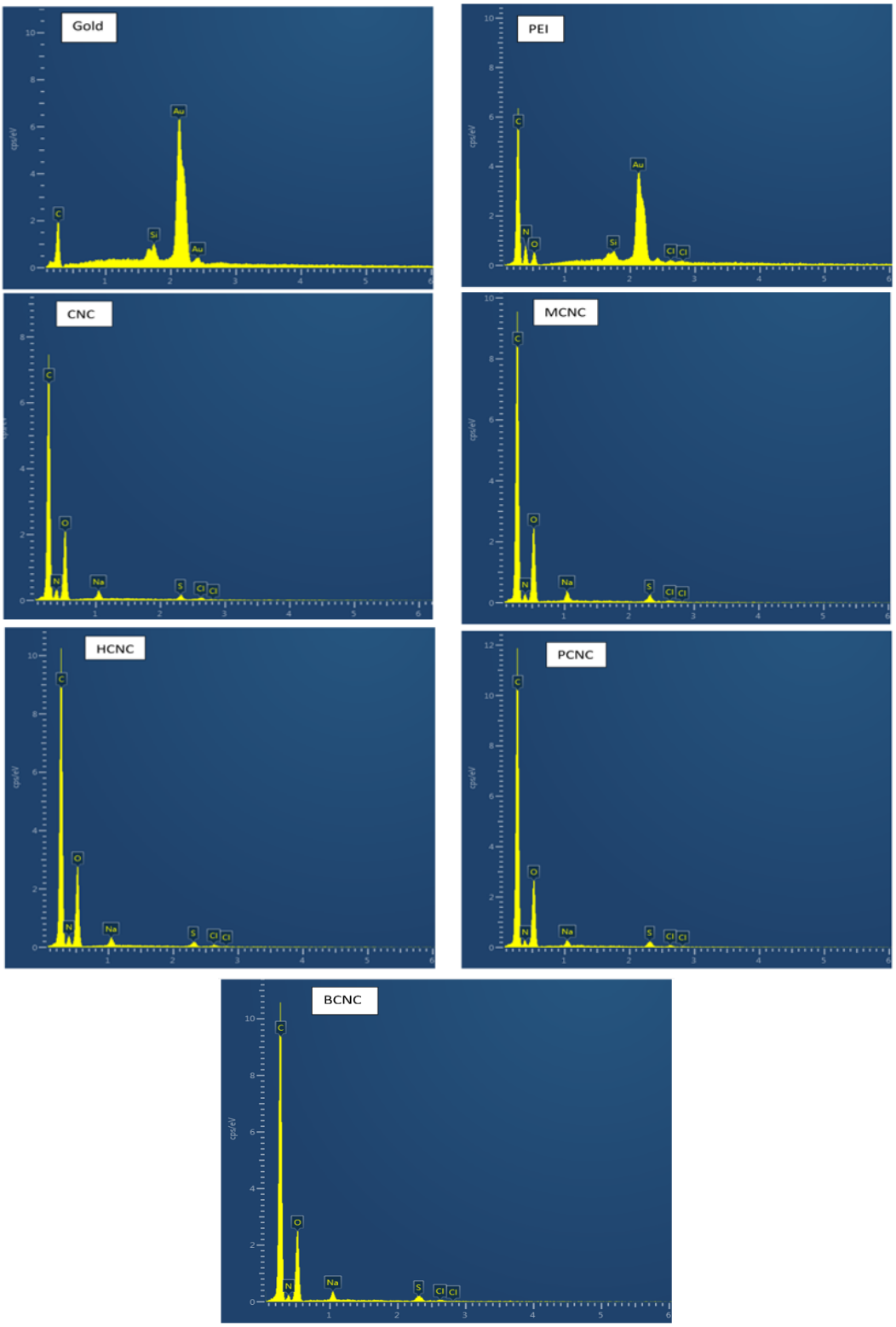

Figure S5.1. a) magnified view of SEM images, and b) EDX-SEM images of the bare gold sensor, PEI-coated, and PEI-CNC coated sensors.

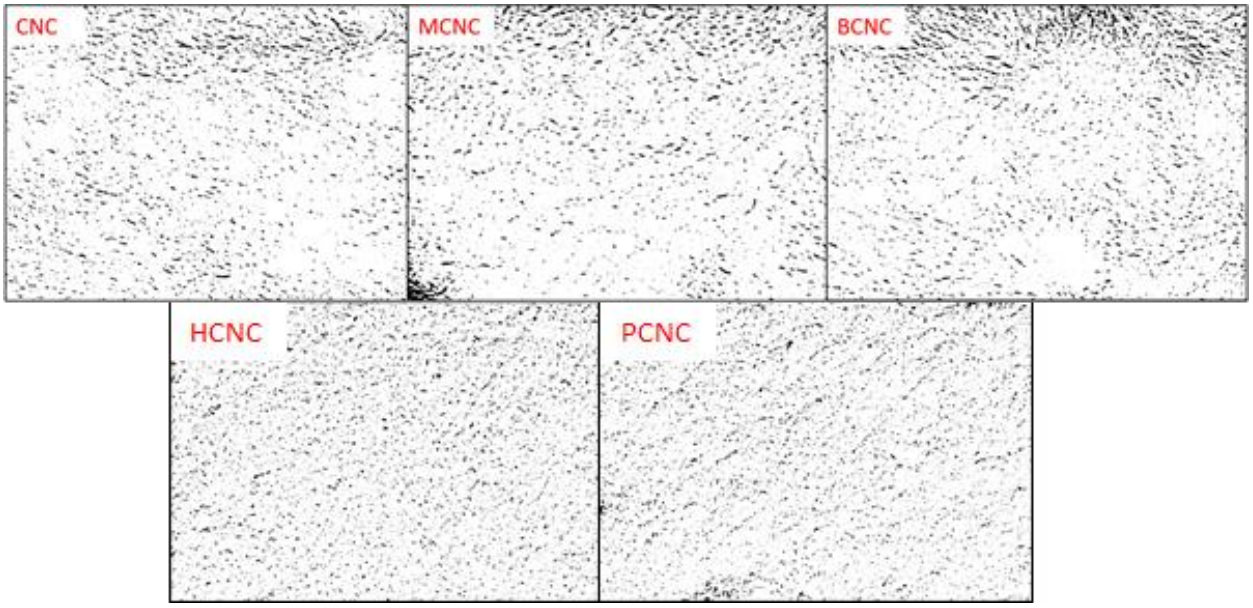

Figure S5.2. Processed images using ImageJ program for analyzing the coverage percentage of the PEI-CNC-covered QCM-D sensors.

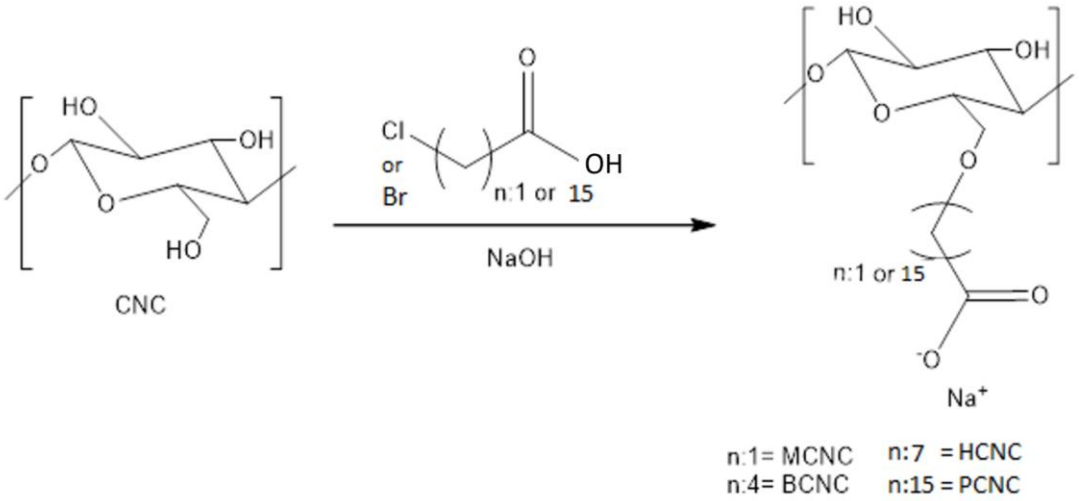

Figure S5.3. Carboxyalkylation of CNC was conducted at 55°C for three hours.

Table S5.1. The charge density of the carboxyalkylated CNC samples in various reagent/CNC ratio at 55°C for three hours.

Reagent/CNC ratio, wt.%	MCNC	BCNC	HCNC	PCNC
1:2	- 2.78 ± 0.06	-1.72 ± 0.05	-0.84 ± 0.1	-0.41 ± 0.08

1:2.5	-3.06 ± 0.1	-2.65 ± 0.11	-1.78 ± 0.05	-0.76 ± 0.14
1:3	-3.55 ± 0.09	-2.98 ± 0.09	-2.52 ± 0.15	-1.2 ± 0.12
1:3.5	-3.91 ± 0.14	-3.34 ± 0.24	-3.08 ± 0.18	-1.78 ± 0.06
1:4	-4.2 ± 0.26	-3.61 ± 0.15	-3.22 ± 0.07	-2.3 ± 0.1

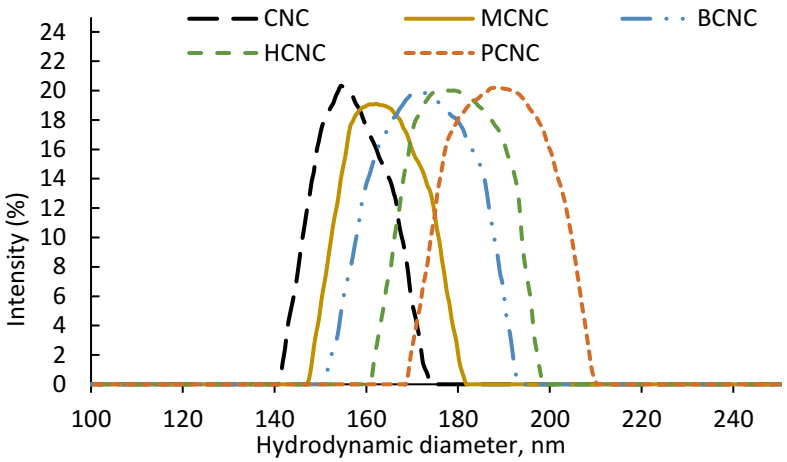

Figure S5.4. Hydrodynamic diameter of CNC samples conducted at pH 7.0.

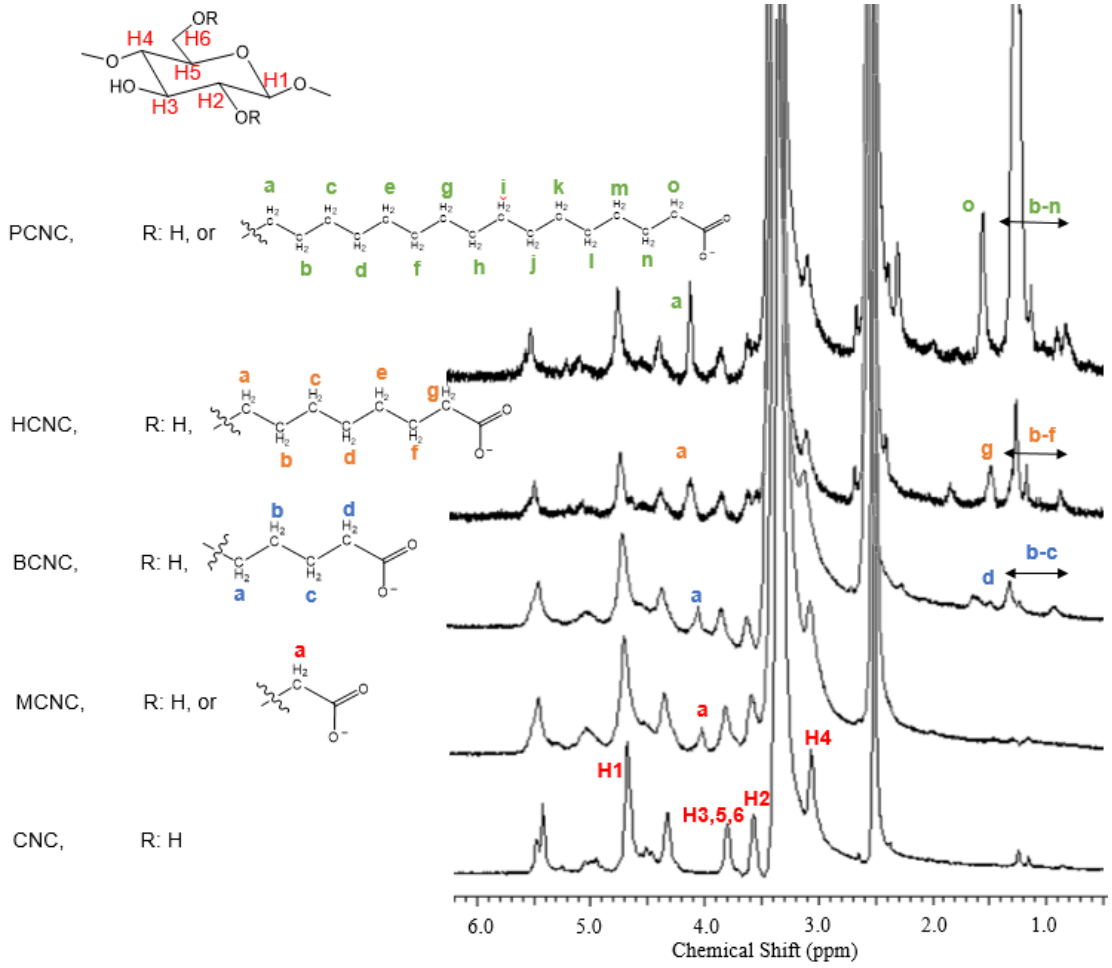

Figure S5.5. ^{1}H NMR spectra of CNC samples

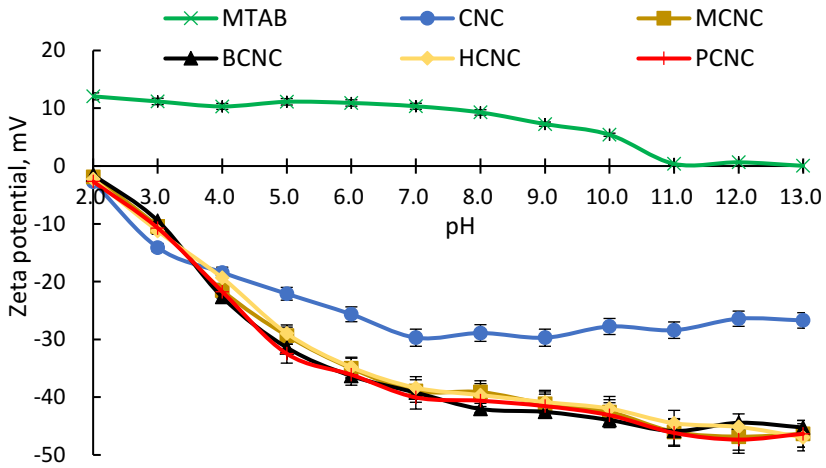

Figure S5.6. Zeta potential analysis of MTAB (0.43 g/L) and CNC derivatives performed without mixing the two at different pH at 25°C.

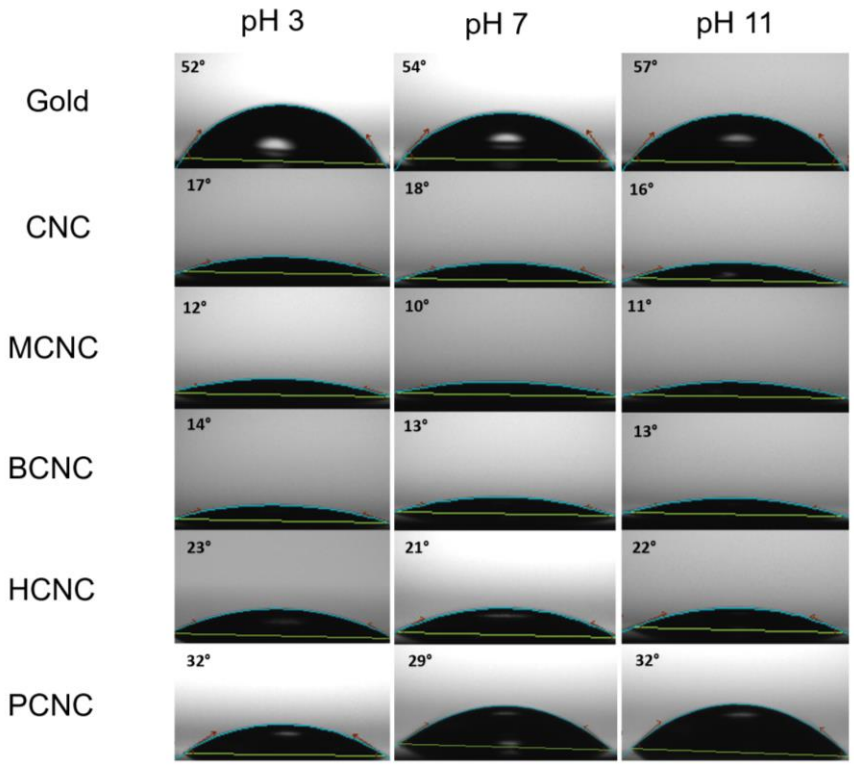

Figure S5.7. Contact angle analysis of uncoated, and CNC-coated surfaces of the gold sensors performed at three different pH of 3.0, 7.0, and 11.0.

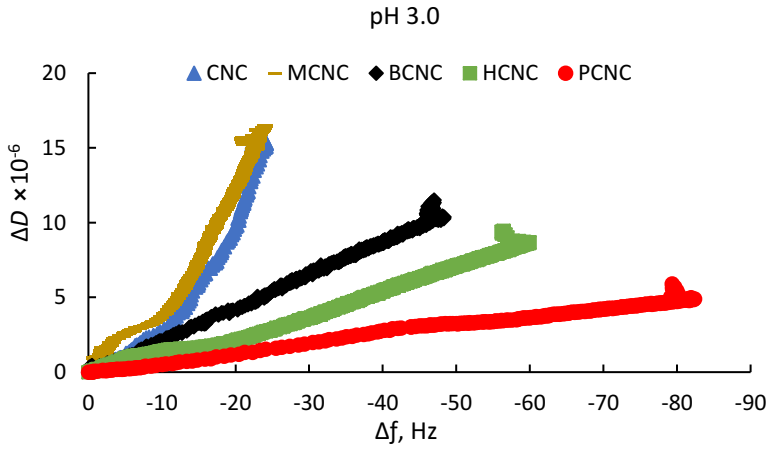

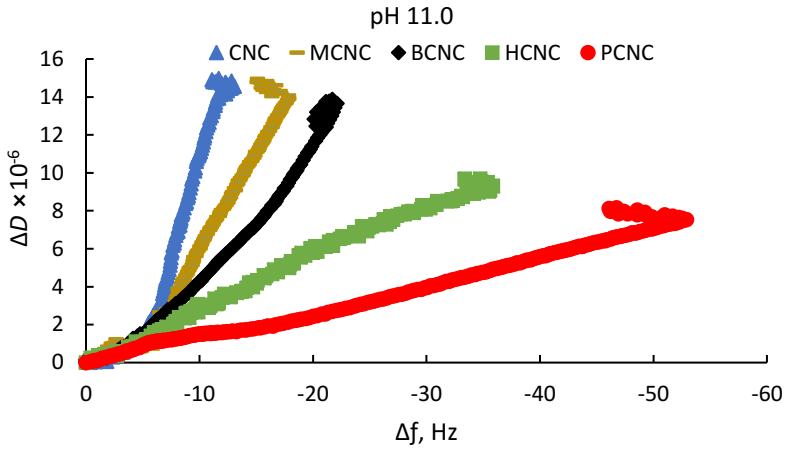

Figure S5.8. Changes in the dissipation of adsorbed adlayer as a function of changes in the frequency of the third overtone of the CNC coated sensor for the adsorption of MTAB (in 0.43 g/mol concentration) on CNC surfaces.

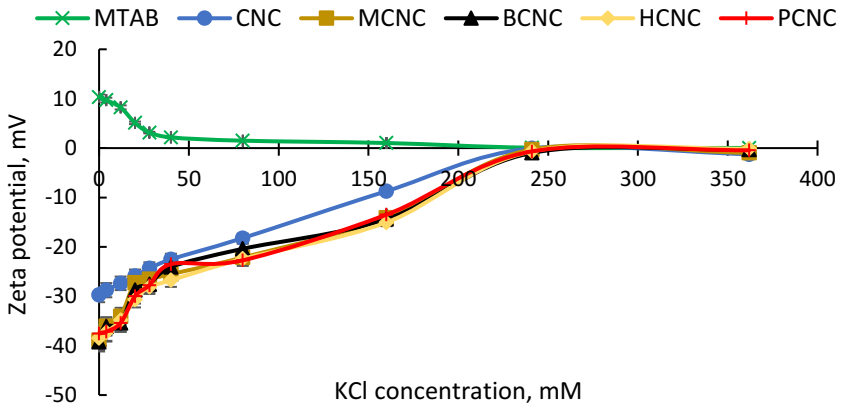

Figure S5.9. Zeta potential of MTAB and unmodified/modified CNC at different KCl concentrations conducted at pH 7 at 25°C.

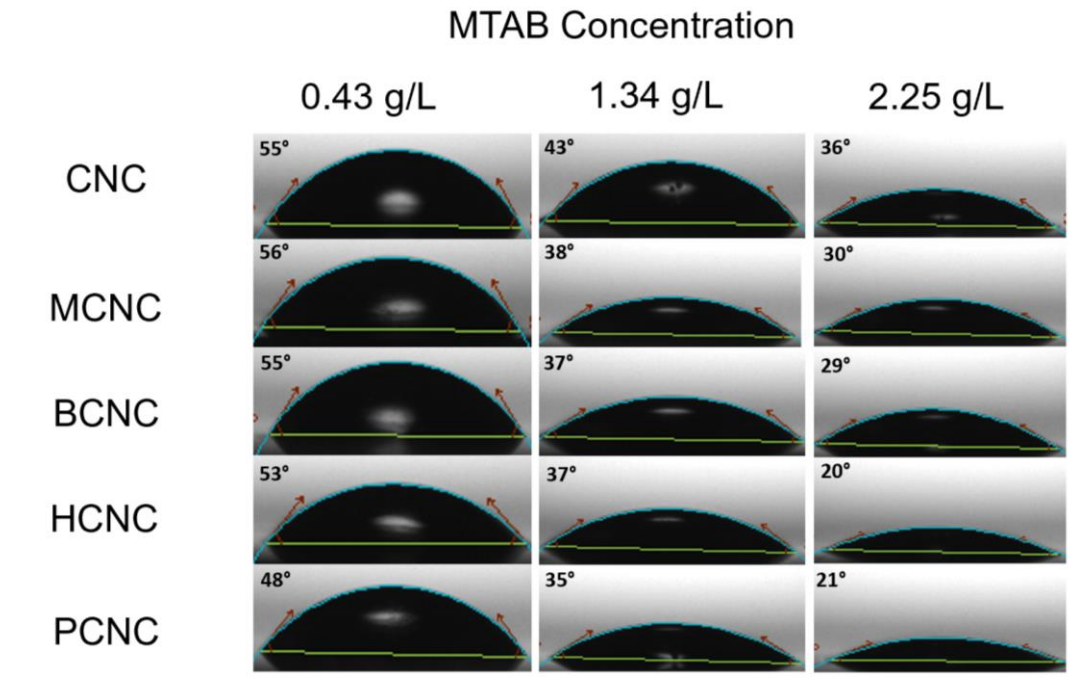

Figure S5.10. Contact angle of MTAB droplet with different concentrations on CNC-coated surfaces.

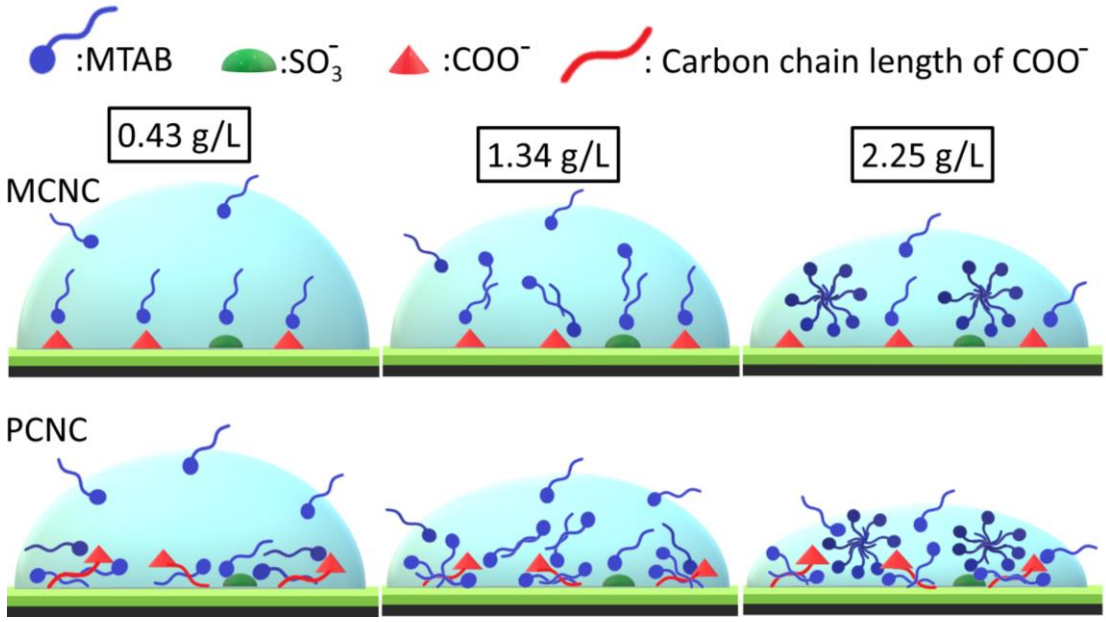

Figure S5.11. Schematic interaction mechanism of MTAB with the CNC-coated surfaces in three different MTAB dosages of 0.43, 1.34, and 2.25 g/L.

References

Chen, D., & van de Ven, T. G. (2016). Flocculation kinetics of precipitated calcium carbonate induced by electrosterically stabilized nanocrystalline cellulose. *Colloids and Surfaces A: Physicochemical and Engineering Aspects*, *504*, 11-17.

Konduri, M. K., & Fatehi, P. (2016). Synthesis and characterization of carboxymethylated xylan and its application as a dispersant. *Carbohydrate Polymers*, *146*, 26-35.

Chapter 6: Anionic cellulose nanocrystals as antibiotic adsorbents

Zahra Hosseinpour Feizi, Pedram Fatehi*

Under submission

Department of Chemical Engineering,
Lakehead University,
955 Oliver Road,
Thunder Bay, ON P7B 5E1, Canada

* Corresponding author

6.1 Abstract

While antibiotics are beneficial for dealing with infections, their release into the environment has raised global concerns. In this work, the interaction of cellulose nanocrystal (CNC) derivatives was studied as an adsorbent for sulfamethoxazole (SMX), ciprofloxacin (CIP), and doxycycline (DOX) antibiotics. CNC was carboxyalkylated to bear different carbon chain lengths and negative charges on its surface. Among antibiotics, DOX was observed to have higher and faster adsorption to the carboxyalkylated CNC derivatives. In the pH range of 3 to 10, the highest adsorption of DOX on the CNC with a longer carbon chain (PCNC) occurred at pH 6.0, which was due to the electrostatic and π interactions along with hydrogen bonding. The contact angle and Quartz crystal microbalance (QCM) adsorption analyses revealed a faster interaction and adsorption of DOX on PCNC. The results also revealed the diffusion of DOX into the porous structure of CNC derivatives, especially that of PCNC. Also, a more compact adsorbed layer of DOX was formed on PCNC than other CNC surfaces. Carboxyalkylation was observed to slightly reduce the surface area of CNC, while the antibiotic adsorption drastically increased the surface area of CNC due to their adsorption on the surface. XPS analysis revealed that carboxyalkylation significantly enhanced the C-C/C-H, while antibiotic adsorption to PCNC enhanced C-C/C-H and C-N/C-O contents in the antibiotic-loaded CNC samples. Overall, carboxyalkylated CNC was observed to have an outstanding affinity to antibiotics, especially DOX, which could pave the way for the use of CNC in such applications that surface/antibiotic interactions are essential.

Keywords: carboxyalkylation, carboxyheptanation, carboxypantadecanation, cellulose nanocrystals, antibiotics

6.2 Introduction

Cellulose nanocrystal (CNC) is a derivate of cellulose, which has attracted attention in recent years. This non-toxic and renewable material has been analyzed to be used in many applications due to its prominent properties, such as abundant surface hydroxyl groups, large surface area, and high aspect ratio (Hu et al., 2015). These properties have made CNC a good candidate to be used with antibiotics in many applications, such as an adsorbent for removing antibiotics from the water and wastewater, or drug delivery, and drug generation (Salimi et al., 2019).

CNC with hydrophilic sugar-based nature does not trigger an immune system response in the human body and has become an interesting material to carry bioactive molecules in biomedical applications. Many researchers have studied CNC as a drug carrier in recent years following different strategies (Salimi et al., 2019). The surface alteration of CNC has been considered as a means to improve its biocompatibility with hydrophilic or hydrophobic drugs (Lam et al., 2012; Wang et al., 2015; Tang et al., 2018).

Antibiotics have been widely used in different sectors, such as medicine and agriculture, for decades. Although they are beneficial to mammalian health, their extensive use has led to their accumulation in wastewater, sludge, underground, and surface water in high concentrations (Yu et al., 2019). Since antibiotics pass the body generally unchanged and are not degraded in the wastewater treatment plants (Lange et al., 2006), they release to the environment, which may have devastating effects including the generation of antibiotic-resistant bacteria and genes. This problem could subsequently impose a potential risk to the environment and human health (Suda et al., 2012; Yu et al., 2019; Hou et al., 2019). To cease this phenomenon, antibiotics need to be separated from water and wastewater. Adsorption technology is an efficient, fast, and economically practical method used in the wastewater treatment process (Yu et al., 2016). Adsorbents such as thermal-responsive magnetic polymers (Xu et al., 2012), sewage/waste oil sludge-derived materials (Seredych & Bandosz, 2007), functionalized silica (Zhang et al., 2015), activated persulfate (Kang et al., 2016), activated carbon/graphene (Yu et al., 2016), or functionalized carbon nanotubes (Xiong et al., 2018) have been developed as antibiotic adsorbents. However, these adsorbents either suffer from complicated production pathways or may result in toxicity and secondary pollution (Kakavandi et al., 2014).

Cellulose and its derivatives have been used as antibiotic adsorbents in the last decade. In one study ciprofloxacin was adsorbed onto anionic and cationic cellulose (Hu & Wang, 2016). In another study, a graphene oxide/cellulose nanofibril aerogel was used to adsorb antibiotics from aqueous media (Wang et al., 2017). A starch-based hydrogel has also been studied to adsorb Fluvastatin from water (Mohamed & Mahmoud, 2020). However, CNC by having abundant surface hydroxyl groups (i.e., an anchor for chemical modification) as well as a nano size (which contributes to a larger surface area) would be a better candidate for adsorbing antibiotics. In another study, a composite of cellulose nanocrystals/graphene oxide was used as levofloxacin hydrochloride adsorbent (Tao et al., 2020). However, graphene oxide is not an eco-friendly

material and could lead to cytotoxicity (Liao et al., 2011), which limits its applications in biomedical fields.

To propose CNC as a candidate for the above-mentioned applications, the interaction of CNC with antibiotics needs to be studied extensively. In this study, the interaction of CNC with some most commonly used antibiotics, namely doxycycline, ciprofloxacin, and sulfamethoxazole has been studied for the first time, as the main objective. Also, due to their poor metabolization, these antibiotics are amongst the least biodegradable antibiotics and the most frequently detected ones in the aquatic environment (Carabineiro et al., 2011; Chen et al., 2014).

Although CNC possesses abundant hydroxyl groups on its surface, its interaction with different materials is limited (Kaboorani & Reidl, 2015). The surface modification of CNC is beneficial to increase its selectivity and adsorption capacity. Herein, carboxyalkylation was carried out to not only introduce charged groups onto the CNC surface but also add additional non-electrostatic properties to the surface of CNC. It is reported that the surface properties of CNC are influenced by the carbon chain length of the attached functional group (Gårdebjer et al., 2015). Considering this, we hypothesized that the carboxylate groups having different carbon chain lengths could impact the adsorption of antibiotics onto the CNC surface differently. To validate this hypothesis, two carboxyalkylation reactions of carboxyheptanation and carboxypantadecanation have been carried out on CNC samples and their interaction with antibiotics was studied comprehensively as the second objective of this work. While other carboxyalkylation reactions could also be carried out on CNC, as conducted in the previous chapter, carboxyheptanation and carboxypantadecanation were chosen to be performed to have medium and long chain lengths on CNC for comparison. In this work, the adsorption of antibiotics on CNC was extensively studied using a Quartz crystal microbalance with dissipation (QCM-D) and UV-vis spectrophotometer. Also, the zeta potential of CNC suspensions, hydrophilicity/hydrophobicity of CNC and antibiotic samples, as well as antibiotic diffusion into CNC, were analyzed to exploit the interaction of antibiotics with CNC derivatives.

6.3 Experimental section

6.3.1 Materials

Softwood bleached pulp was supplied by a pulp mill in northern Ontario, Canada. Doxycycline (DOC), ciprofloxacin (CIP), sulfamethoxazole (SMX), 8-bromooctanoic acid (BOA) (97%), 16-bromohexadecanoic acid (BHDA) isopropyl alcohol, and polyethyleneimine (50%) (PEI) were

obtained from Sigma Aldrich and used as received. Sulfuric acid (98%), sodium hydroxide (≥97%), and hydrochloric acid were obtained from Sigma Aldrich and diluted to 64 wt.%, 0.1 M and 0.1 M, respectively, prior to use. KCl was obtained from Fisher scientific, Canada. Cellulosic dialysis membrane (with 1000 g/mol molecular weight cut off) was obtained from Spectrum Labs.

6.3.2 CNC production and carboxyalkylation

Information related to the production and carboxyalkylation of CNC is provided in the supplementary information.

6.3.3 Functional group content analysis

Conductometric titration was used to measure the sulfate half-ester and carboxyalkyl group contents of CNC samples using an automatic conductometer (Metrohm 856 Titrado, Switzerland), as stated in the literature (Reid et al., 2017; Feizi, & Fatehi, 2020a). Briefly, 0.03 g of CNC samples were mixed with 2 mL of NaCl (0.02 mol/L). Then, 150 mL of Milli-Q water was added to the suspensions, and samples were left for stirring at 250 rpm until homogenized. Then, the pH of the mixtures was adjusted to 3.5 using HCl (0.1 M) and titrated with 0.01 mol/L NaOH solution. The sulfate half-ester and carboxyalkylate groups were then calculated following the steps available in the supplementary information.

Degree of substitution (DS) was calculated following equation 6.1:

Equation 6.1

$$\text{Degree of Substitution (DS)} = \frac{M \times A}{1-(B \times A)} \quad (1)$$

where A is the total carboxyalkylate group content (mmol/g), B is the mass of either attached carboxyheptanate (0.143 g/mmol), or carboxypantadecanate (0.255 g/mmol) group. M is the CNC primary unit mass (anhydroglucose, 0.162 g/mmol).

Conductometric titration was also used to measure the functional group content of the antibiotics following the literature (Kralj et al., 2011) while potentiometric titration (Metrohm 905 Titrado, Switzerland) was used to analyze the phenolic hydroxyl groups of DOX following the literature (Kong et al., 2015).

6.3.4 Dynamic light scattering

A 90Plus PALS Zeta Analyzer (Nano Brook, Brookhaven, USA) was used to measure the hydrodynamic size of CNC and antibiotic samples at the scattering angle and wavelength of 90°

of 632 nm, respectively, at 25 °C and natural pH. For this analysis, samples were dispersed/dissolved in water (5 g/L and 100 mg/L concentration of CNC and antibiotic samples, respectively) overnight at pH 7.0. Then, samples were sonicated for three minutes and 100 µL of them was transferred into 10 mL of previously filtered KCl (1 mM) and submitted to the instrument for further analysis (Kazzaz et al., 2018).

6.3.5 Zeta potential analysis

NanoBrook Zeta PALS (Brookhaven Instruments Corp, USA) was used to evaluate the zeta potential of the antibiotics and CNC samples at various pH. For this set of experiments, CNC (5 g/L) and antibiotic samples (100 mg/L) were prepared as stock solutions and left for homogenization overnight. Then, the pH of the samples was adjusted to 2.0 -13.0 and dispersed using ultrasonication for one minute at 25°C. Afterward, 100 µL of the samples was added to 10 mL of a filtered KCl solution (1 mM) before analysis. In a separate set of experiments, CNC samples (5 g/L) were dosed into antibiotic (100 mg/L) solutions to generate the CNC concentration of 10-200 mg/L. Samples were then incubated at 25 °C for two hours at 150 rpm, and the zeta potential was measured as explained. Measurements were carried out three times for each sample, and the average values were revealed in this study (Feizi et al., 2019).

6.3.6 Antibiotic adsorption analysis

The adsorption of antibiotics on the CNC samples was evaluated using a UV-Vis spectrophotometer (Genesys 10S UV-Vis, Thermo Scientific) with the aid of a calibration curve. The wavelength used for DOC, CIP, and SMX was 325, 278, and 257 nm, respectively (Givianrad et al., 2011; Naveed & Waheed, 2014; Ma et al., 2018). In this experiment, CNC (5 g/L) and antibiotic (100 mg/L) suspensions were prepared, and their pH was set to 3.0, 6.0, and 10.0. CNC samples were then dosed into antibiotic samples to form the CNC concentration in the range of 10-200 mg/L. Then, samples were incubated at 25 °C for two hours at 150 rpm in a water bath shaker. Upon completion, suspensions were centrifuged at 2500 rpm for 10 min and then samples were collected from the top part of the glass vials. The concentration of antibiotics in the suspensions were evaluated using equation 6.2:

Equation 6.2

$$\text{Adsorption} = \frac{(C_0 - C)}{C} \quad (2)$$

where C_0 is the antibiotic concentration before CNC addition, and C is the antibiotic concentration after treating with CNC samples.

6.3.7 Contact angle analysis

Theta Lite Contact Angle analyzer (Biolin Scientific, Finland) that had a camera was used for static hydrophilicity/hydrophobicity analysis of the antibiotic- and CNC-coated surfaces. A water droplet of 1.5 µL having varied pH was placed onto the plain glass slide or antibiotic/CNC-coated surfaces, and the wettability of the CNC samples was measured for about 20 seconds following Young's equation (Equation 6.3):

Equation 6.3

$$\gamma_{sg} - \gamma_{sl} = \gamma_{gl} \cos\theta \quad (3)$$

where γ_{sg}, γ_{sl}, and γ_{gl} are interfacial tension (mN/m) of solid-gas, solid-liquid, and gas-liquid, respectively. θ (°) is the angle of the water droplet on the CNC surfaces.

For diffusion analysis, a drop of each antibiotic (100 mg/L) was placed onto CNC-coated surfaces in a confined glass chamber and the diffusivity analysis was performed for about five minutes while the contact angle was livelily measured. This analysis was performed triple for each sample and the mean value is reported in this study.

6.3.8 Coating CNC derivatives on the PEI-coated Sensors

The coating gold sensors of Quartz crystal microbalance with dissipation (QCM-D) with polyethyleneimine (PEI) before coating with cellulose derivatives is known to enhance the CNC adhesion to the sensor (Bardet et al., 2015; Pirich et al., 2017). For this reason, the gold sensors were coated with PEI polymer, which was prepared at 5 g/L concentration and pH 6, under vacuum with 60 Psi pressure using a spin-coater, WS-650 (Laurell) Technologies Corp, for 30 seconds at 1500 rpm (Bardet et al., 2015; Pirich et al., 2017). The PEI-coated sensors were spin-coated with CNC suspensions (5 g/L, pH 6.0) for 30 seconds at 1500 rpm (Niinivaara et al., 2015; Pirich et al., 2017). Then, CNC-coated surfaces were dried in an oven (60°C) for 30 min. The evidence of this coating is provided in the supplementary information in Figure S1.

6.3.9 Scanning electron microscopy (SEM) analysis

FE-SEM (Hitachi SU-70) imaging was conducted for the CNC-coated QCM-D sensors before and after the antibiotic adsorption to reveal the evidence of surface coverage of CNC derivatives on

the PEI coated sensors. The images were taken at the magnification of 1, and 2 μm and the voltage of 5 kV. Also, the energy-dispersive X-ray spectroscopy (EDX) of the SEM instrument was used to reveal the chemical compositions of the sensors before and after coating was analyzed.

6.3.10 Adsorption analysis of antibiotics on CNC-coated Surfaces

The adsorption analysis of antibiotics on CNC-coated sensors was analyzed with a Quartz crystal microbalance with dissipation (QCM-D 401, E1, Q-Sense Inc. Gothenborg, Sweden) at varied pH of 3.0, 6.0, and 10.0. Milli-Q water was used to form the baseline for this analysis. Then, sensors were exposed to antibiotic solutions (100 g/L) at a 0.15 mL/min flow rate and 22 °C temperature. When the equilibrium was reached, the samples were rinsed with the buffer solution (Milli-Q water) for about 2 min. The fundamentals of this analysis were included in the supplementary information. The data analysis was performed using the Q-Tools software (Q-Sense, Gothenburg, Sweden). Briefly, a thin film with $\Delta D \leq 1 \times 10^{-6}$ and no spreading of the overtones in ΔD and Δf graphs is considered as a rigid surface, while an adsorbed layer with $\Delta D \geq 1 \times 10^{-6}$ and spread overtones reflect a viscoelastic layer formed on the surface (Niinivaara et al., 2015). The QCM-D data was used to evaluate the properties of the adsorbed layer. The mass analysis was performed by fitting data into the Voigt model using the harmonic overtones by Q-Tools software according to the literature (Feizi & Fatehi, 2020b).

6.3.11 Surface area analysis

The specific surface area (S_{BET}) of the plain and antibiotic-loaded CNC samples were determined following the Brunauer-Emmett-Teller (BET) method by NOVA 2200e (Quantachrome Instruments) in the N_2 adsorption isotherm relative pressure range of $p/p_0 = 0.01$-0.99. The average pore size (d_p) of the samples was determined ($d_p = 4V_p/S_{BET}$). The total pore volume (V_p) was also measured at $p/p_0 = 0.99$. The samples were degassed in a vacuum at 373 K for 12 h before performing the measurement (Kazzaz et al., 2018). To prepare the antibiotic-loaded CNC samples, CNC suspensions (5 g/L) and antibiotics (100 mg/L) were prepared at neutral pH. CNC samples were then dosed into antibiotic samples to form the CNC concentration of 150 mg/L. Samples were then incubated at 25 °C for two hours at 150 rpm in a water bath shaker. Suspensions were then centrifuged at 2500 rpm for 10 min and then samples were collected from the bottom part of the glass vials and freeze-dried.

6.3.12 X-ray Photoelectron Spectroscopy (XPS)

X-ray photoelectron spectroscopy (XPS) analysis was performed using a Kratos Axis Supra (Shimadzu Group Company Japan), with a monochromatic Al Kα source and a charge neutralizer. For this experiment, plain and antibiotic-loaded CNC samples (prepared as explained before) were transferred onto a double-sided carbon tape and submitted for analysis under a high vacuum condition. The high-resolution XPS spectra of the samples were analyzed using ESCApe software.

6.4 Results and discussion

6.4.1 CNC carboxyalkylation

CNC carboxyalkylation was performed using different CNC/reagent ratios for three hours at 55°C in an alkaline condition. The details of these reactions and full characterization of the samples are provided in our previous work (Feizi & Fatehi, 2020b). Table 6.1 presents the properties of the CNC samples used in this work. Carboxyalkylated CNC samples had a similar carboxyalkyl group content but with different carbon chain lengths (Figure S6.2). As identified, unmodified CNC (UCNC) possessed a sulfate half-ester group content of 0.22 ± 0.04 mmol/g, and the hydrodynamic diameter of 154 nm. The hydrodynamic diameter of carboxyheptanated CNC (HCNC) and carboxypantadecanated CNC (PCNC) was furthermore measured to be around 176, and 188 nm, respectively (Figure S3). It is also seen in Table 6.1 that carboxyalkylation introduced 2.42 ± 0.05 and 2.2 ± 0.03 mmol/g of carboxylate groups to CNC. Also, a close degree of substitution of 0.59 and 0.66 mol/mol was obtained for HCNC and PCNC samples, respectively. Table 6.1 also includes the properties of the antibiotic samples. As seen, SMX contained 0.66 ± 0.05 mmol/g of sulfonamide group, while CIP possessed 2.7 mmol/g of the carboxylate group. The phenolic hydroxyl groups of DOX was also measured to be 1.81 ± 0.06 mmol/g. The amine group content of the antibiotics is also 0.92 ± 0.07, 0.86 ± 0.05, and 0.73 ± 0.03 for SMX, CIP, and DOX, respectively. All of these functional groups contribute to varying the developed adsorption mechanisms between antibiotics and CNC samples at different pH. The hydrodynamic diameter of SMX, CIP, and DOX was also measured to be 6, 7, and 10 nm, respectively.

Table 6.1. The properties of CNC derivatives and antibiotics

Properties	UCNC	HCNC	PCNC	SMX	CIP	DOX

Sulfate half-ester group content, mmol/g	0.22 ± 0.04	0.15 ± 0.03	0.16 ± 0.05	-	-	-
Sulfonamid group content, mmol/g	-	-	-	0.66 ± 0.05	-	-
Carboxylate group content, mmol/g	>0.09 [a]	2.42 ± 0.05	2.2 ± 0.03	>0.09 [a]	2.7 ± 0.04	>0.09 [a]
Phenolic hydroxyl group content, mmol/g	-	-	-	>0.09 [a]	>0.09 [a]	1.81 ± 0.06
Amine group content, mmol/g	-	-	-	0.92 ± 0.07	0.86 ± 0.05	0.73 ± 0.03
Degree of substitution, mol/mol		0.59	0.66	-	-	-
Hydrodynamic diameter, nm	154	176	188	6	7	10

[a] Method sensitivity < 0.09

6.4.2 Zeta potential and adsorption analyses

The Figure 6.1 depicts the zeta potential of the antibiotics and CNC samples at a pH range of 2.0 and 13.0. As seen, all antibiotics possessed a positive zeta potential at pH 2.0 and 3.0, while they gradually become zwitterionic as the pH increases to around 7.0. The reason for this behavior could be the amine groups present on the antibiotics that would protonate in acidic pH and render the zeta potential positive (Table 6.1, Figure S6.4). By pH increment to neutral and basic, the sulfonamide group on SMX, carboxylic acid groups on CIP, and hydroxyl groups on DOX deprotonate and lead to a reversal in the zeta potential values. In the meantime, the zeta potential of CNC samples is close to 0 at pH 2.0, while it increases to around -14 mV at pH 3.0. At this pH, only the sulfate half-ester groups on CNC samples are deprotonated while the carboxyl groups on HCNC and PCNC samples are still protonated. Above pH 4.0, the carboxyl groups become negatively charged and lead to a more negative zeta potential for the carboxyalkylated samples. Considering the results, pH 3.0, 6.0, and 10.0 were selected to peruse further analyses and reveal the pH effect on the interaction of CNC with the antibiotics.

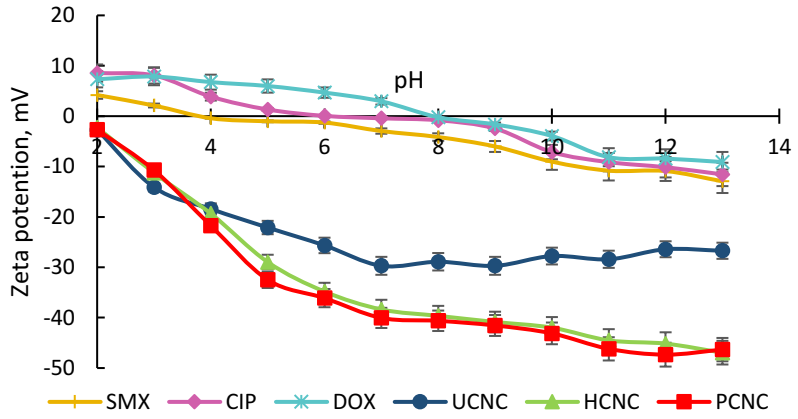

Figure 6.1. Zeta potential of antibiotics and CNC samples at different pH

Figure 6.2 depicts the adsorption of DOX using different CNC samples conducted at pH 6.0. At this pH, DOX possessed a positive zeta potential since its phenolic diketone groups are protonated (Figure S6.4), while the carboxyalkylated samples became negatively charged. This matter leads to an instant and high level of DOX adsorption due to the electrostatic attraction between the substrates, specially HCNC and PCNC. In addition, the following phenomena might have occurred for the better adsorption performance of HCNC and PCNC samples over UCNC; 1) a hydrogen bonding developed between CNC carboxyl groups and phenolic hydroxyl and diketone groups of DOX (Hunt et al., 2015; Oberoi et al., 2019), 2) π interaction, which will be discussed further in the next sessions.

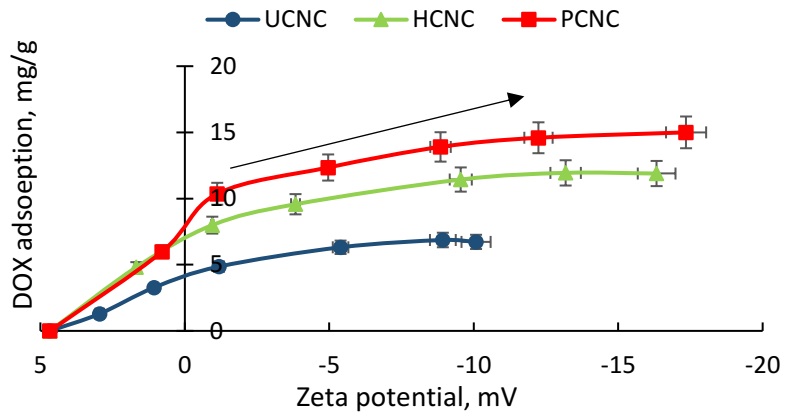

Figure 6.2. DOX adsorption on CNC samples as a function of zeta potential at pH 6.0 and 25 °C. The arrow shows the CNC dosage increase.

Figures S6.5 to S6.10 show the zeta potential, and the adsorption of the antibiotics on CNC samples as a function of CNC concentration at different pH of 3.0, 6.0, and 10.0. Since the adsorption of DOX was the highest among all antibiotics, and PCNC performed the best in adsorbing antibiotics, further analyses were focused more on these two substrates.

The adsorption of all antibiotics on PCNC is shown as a function of zeta potential in Figure 6.3. As seen, the highest adsorption was observed for DOX compared to CIP and SMX, which is raised by the functional groups present on DOX (Table 6.1, Figure S6.4). At pH 6.0, CIP exists in its zwitterionic form due to its deprotonated carboxyl groups co-existing with the positively charged amine groups (Figure S6.4). This fact has led the zeta potential of CIP to be close to 0 mV at this pH (Figure 6.1). Continuous CIP adsorption (up to around 7 mg/g) would be a sign of additional interaction via 1) charge-assisted hydrogen bonding ((-)CAHB) between the carboxyl groups of CIP and carboxyalkyl groups of CNC (this hydrogen bonding occurs between two acids with similar proton affinity) (Hunt et al., 2015; Ni & Pignatello, 2018), 2) anion-π interaction between negatively charged functional groups of CNC and phenolic rings of CIP (Zhu et al., 2015; Lucas et al., 2016), 3) hydrogen bonding and 4) hydrophobic CH-π interaction between the HCNC and PCNC hydrocarbon with CIP aromatic rings, respectively (Tsuzuki et al., 2000; Hunt et al., 2015; Maresca et al., 2008). Also, a minimal SMX adsorption (4 mg/g) was observed by PCNC, which could be due to the sulfonamide and amine groups of SMX forming hydrogen bonding and π interaction (through p-amino sulfonamide ring) with PCNC (Chen et al., 2014; Hunt et al., 2015; Lucas et al., 2016; Oberoi et al., 2019).

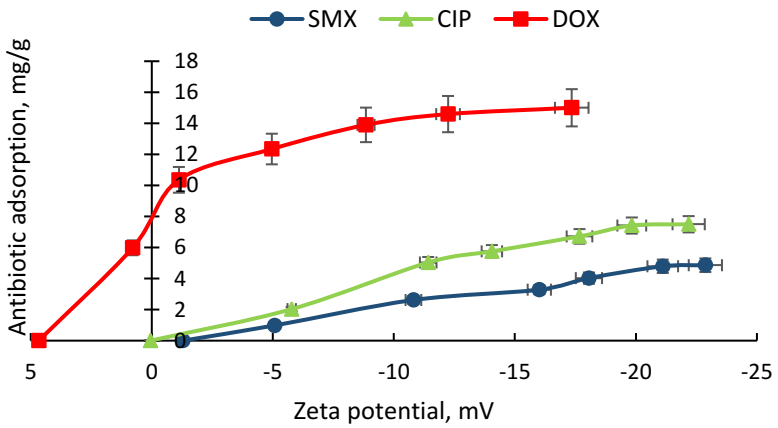

Figure 6.3. Adsorption of antibiotics by PCNC versus the zeta potential at pH 6.0 and 25 °C

Figure 6.4 reveals the adsorption of DOX by PCNC at different pH. The highest adsorption was attained at pH 6.0, which is due to the development of adsorption mechanisms stated earlier. At

pH 3.0, the DOX adsorption increased with a decrease in the zeta potential of the suspension, revealing the important role of charge neutralization in the DOX adsorption. At pH 10.0, the phenolic diketones of DOX deprotonated and generated negative charges on DOX leading to the overall charge repulsion between the substrates and thus suppression of the adsorption.

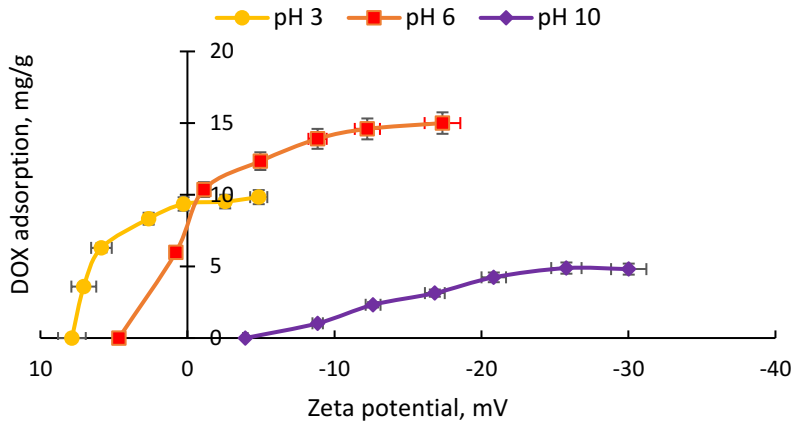

Figure 6.4. DOX adsorption by PCNC versus the zeta potential of the system conducted at 25 °C

6.4.3 Contact angle analysis

The hydrophilic/hydrophobic properties of the antibiotics and CNC-coated surfaces were analyzed at different pH of 3.0, 6.0, and 10.0 as depicted in Figure 6.5, while the images are presented in Figure S6.11. Analyzing this property is very crucial since it would help recognize the interaction mechanism of the antibiotics and CNC-coated surfaces. As seen in Figure 6.5, the water contact angle values of 15, 20, and 30° were obtained for UCNC, HCNC, and PCNC coated surfaces, respectively, at pH 6.0. An increase in the hydrocarbon chain length of the grafting group on the CNC surface decreased the hydrophilicity of the modified samples (Song et al., 2006). Also, the variation in pH was observed to affect the UCNC sample minimally, while it influenced the contact angle of modified CNC more greatly due to the deprotonation of their carboxylate group, promoting the hydrophilicity of the samples (Kim & Mitani, 2006). In the meantime, the water droplet contact angle of 35, 21, and 23° were measured for SMX, CIP, and DOX- coated surfaces, respectively at pH 6.0. This reveals that both CIP and DOX were more hydrophilic than SMX, which might be due to their hydrophilic functional groups, i.e., carboxylate on CIP and hydroxy groups on DOX (Table 6.1, Figure S6.4). Also, while the pH variation affected SMX insignificantly, it affected CIP and DOX more significantly, which might also be related to the deprotonation of their functional groups.

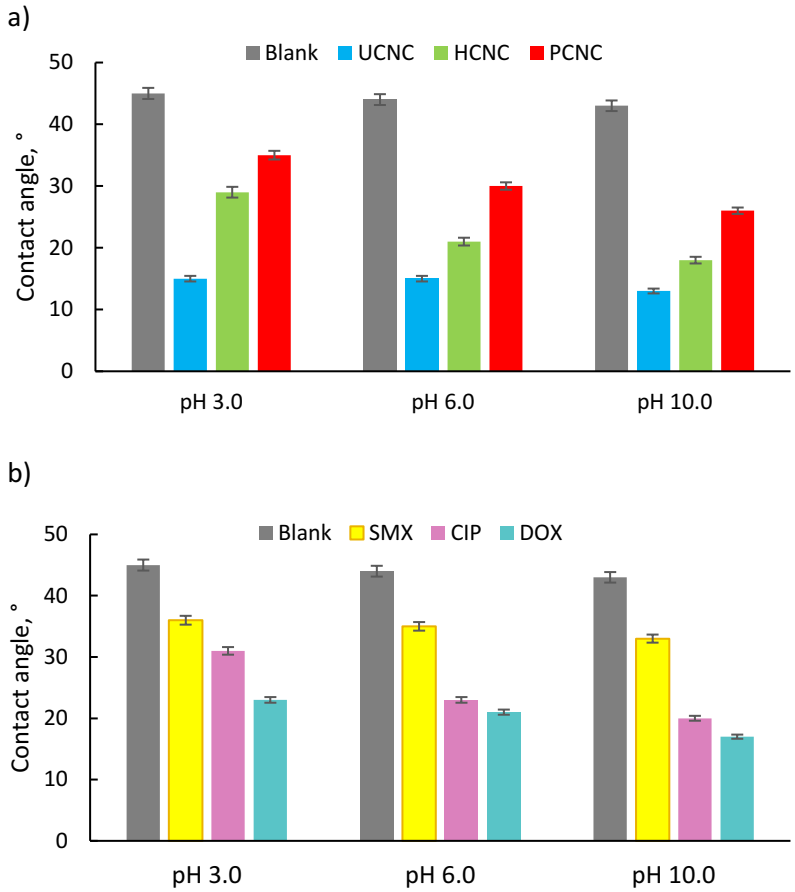

Figure 6.5. Contact angle analysis of antibiotics and CNC samples conducted at different pH and 25 °C, a) CNC samples, and b) antibiotics

The kinetic studies of the contact angle of a water droplet containing antibiotics on different CNC-coated surfaces would provide evidence for their interaction with different CNC samples. The changes in the contact angle of the droplet would then reveal whether the antibiotics would adsorb on the CNC surface or they diffuse into the CNC adlayer. Figure 6.6 depicts the contact angle of droplets containing antibiotics on the CNC surfaces. DOX was chosen to be analyzed on all CNC surfaces due to its higher adsorption (Figures 6.3, and S6.7-S6.9). Also, this analysis was repeated for all antibiotics on the PCNC-coated surface in Figures S6.8-S6.10. As seen in Figure 6.6a, a droplet of DOX solution showed a more rapid initial decline on the PCNC surface than on the other two surfaces, which shows the fast interaction and adsorption of DOX on PCNC. In the meantime, all CNC surfaces experienced a diffusion of DOX droplet into the coated adlayer. However, the diffusion was shorter for UCNC and longer for PCNC. The contact angle results

reveal that the chain length of the grafted CNC affected the structure of the coated adlayer (made it more porous) so that DOX diffused into the CNC with longer carbon chain length (i.e., PCNC) more greatly.

Figure 6.6b depicts the contact angle of droplets containing different antibiotics on PCNC. As seen, the $\Delta\theta$ of the samples is 5, 8, and 12 ° for SMX, CIP, and DOX, respectively. When comparing the interaction of all three antibiotics on the PCNC surface, it is seen that DOX had a slightly faster initial decline compared to CIP and SMX, which reveals the more adsorption affinity of this antibiotic onto PCNC. Also, the diffusion period was shorter for DOX than the other two antibiotics, which reveals its faster diffusion and higher interaction affinity (larger $\Delta\theta$) with PCNC. Such behavior might be due to more hydrogen bonding and π interactions development between the two substrates.

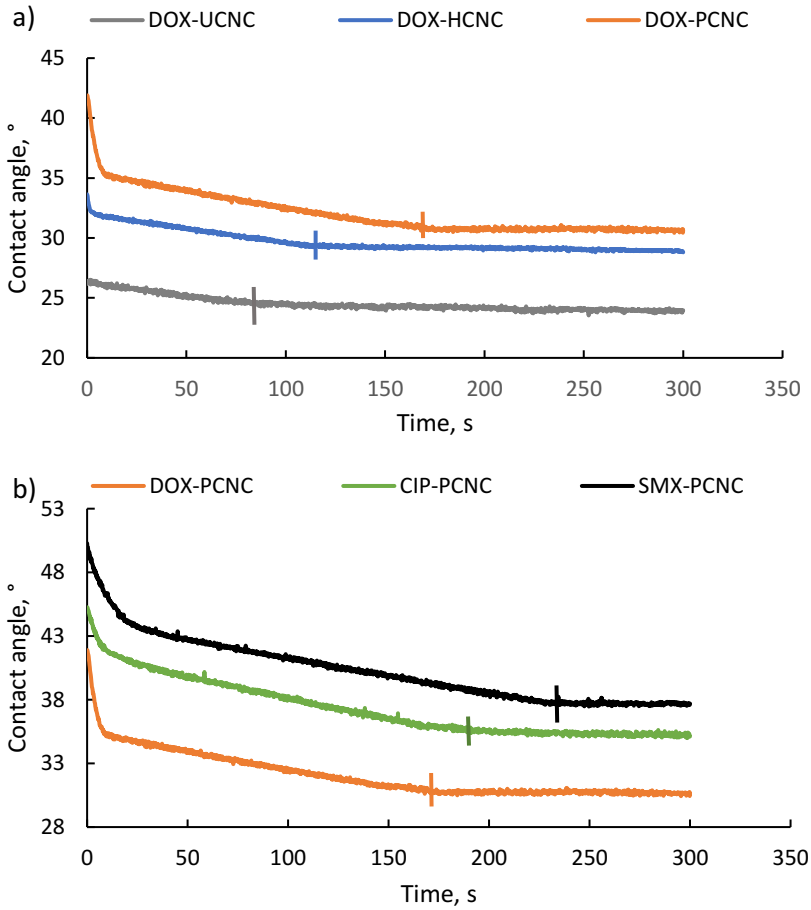

Figure 6.6. Contact angle analysis versus time for a) DOX on different CNC-coated surfaces, and b) antibiotics on the PCNC-coated surface at pH 6.0 and 25 °C. Vertical lines depict the end of the diffusion period.

6.4.4 Adsorption analysis

The adsorption of antibiotics on CNC-coated surfaces was analyzed using a QCM-D. Figure 6.7 demonstrates the adsorption of DOX on CNC-coated surfaces performed at pH 6.0. As seen, DOX was adsorbed the most on the PCNC while it adsorbed the least on the UCNC surface. The reason for this could be due to electrostatic attraction as well as the hydrogen bonding and π interactions developed between DOX and PCNC. Perhaps, CH-π interaction between the alkyl tails of CNC and the phenolic rings of DOX took place, leading to a slightly higher DOX adsorption on PCNC. In addition, the least steep slope ($\Delta D/\Delta f$) of the DOX adsorption on the PCNC surface, along with the highest adsorbed mass, reveals the creation of a more compact structure of DOX/PCNC than DOX and other CNC derivatives. In Figure 6.7b, the adsorbed mass of DOX is depicted as a function of time to depict the kinetics of adsorption. As seen, the initial adsorption on the carboxyalkylated CNC surfaces happened more quickly than UCNC while the saturation also took longer to be achieved for these surfaces, which conveys the role of carboxyalkylation on the adsorption of DOX. These results are in a good correlation with the contact angle kinetic studies shown in Figure 6.6.

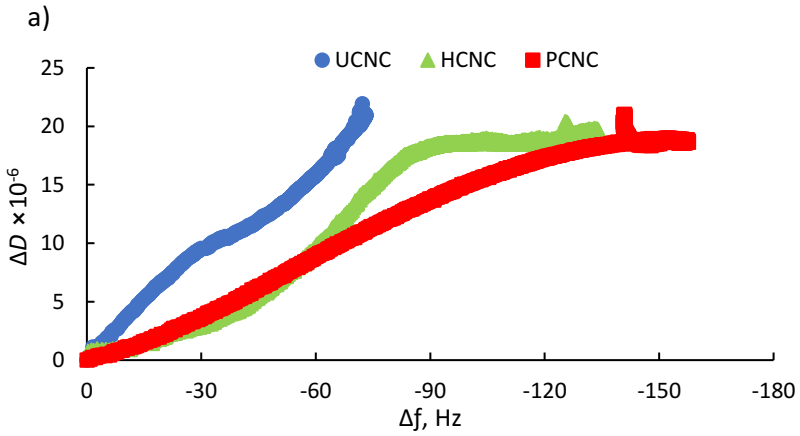

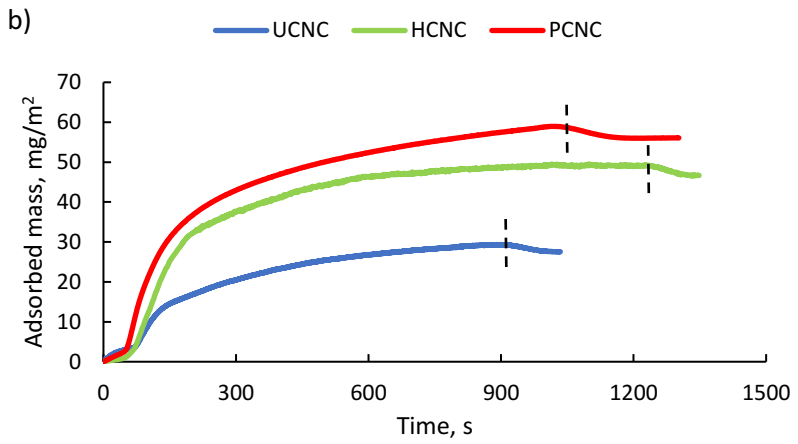

Figure 6.7. Adsorption of DOX on CNC-coated surfaces performed at pH 6 and 25 °C. a) $\Delta D/\Delta f$ data of adsorption, and b) adsorbed mass of DOX on CNC-coated samples with respect to time. Dashed lines indicate rinsing.

The adsorption of antibiotics on the PCNC-coated surface is shown in Figure 6.8a through $\Delta D/\Delta f$ data, while the adsorbed mass of antibiotics concerning the time is depicted in Figure 6.8b. The highest adsorption achieved for DOX on this surface could be attributed to the more electrostatic attraction (Figure 6.1) along with more hydrogen bonding and π interactions of DOX and PCNC. Also, the initial adsorption of DOX was higher than other antibiotics on PCNC, while the surface saturation (stability of the line) took longer to be attained. These results are in harmony with the contact angle-kinetic studies since a slightly faster initial decline was observed for DOX (Figure 6.6).

Figure 8c includes the adsorption of DOX on the PCNC surface at varied pH. As seen, the least adsorption was achieved at pH 10, while the most occurred at pH 6.0. At pH 10.0, where DOX becomes negatively charged (Figure 6.2), the overall adsorption is suppressed by electrostatic repulsion. While more adsorption at pH 3.0 than pH 10.0 could reveal the domination of electrostatic attraction between positively charged DOX and PCNC along with hydrogen bonding and π interactions. The deprotonation of carboxyalkyl groups on PCNC at pH 6.0 might have paved the way for more hydrogen bonding ((-)CAHB) and π interactions (anion-π), which all contributed to the improved adsorption at this pH.

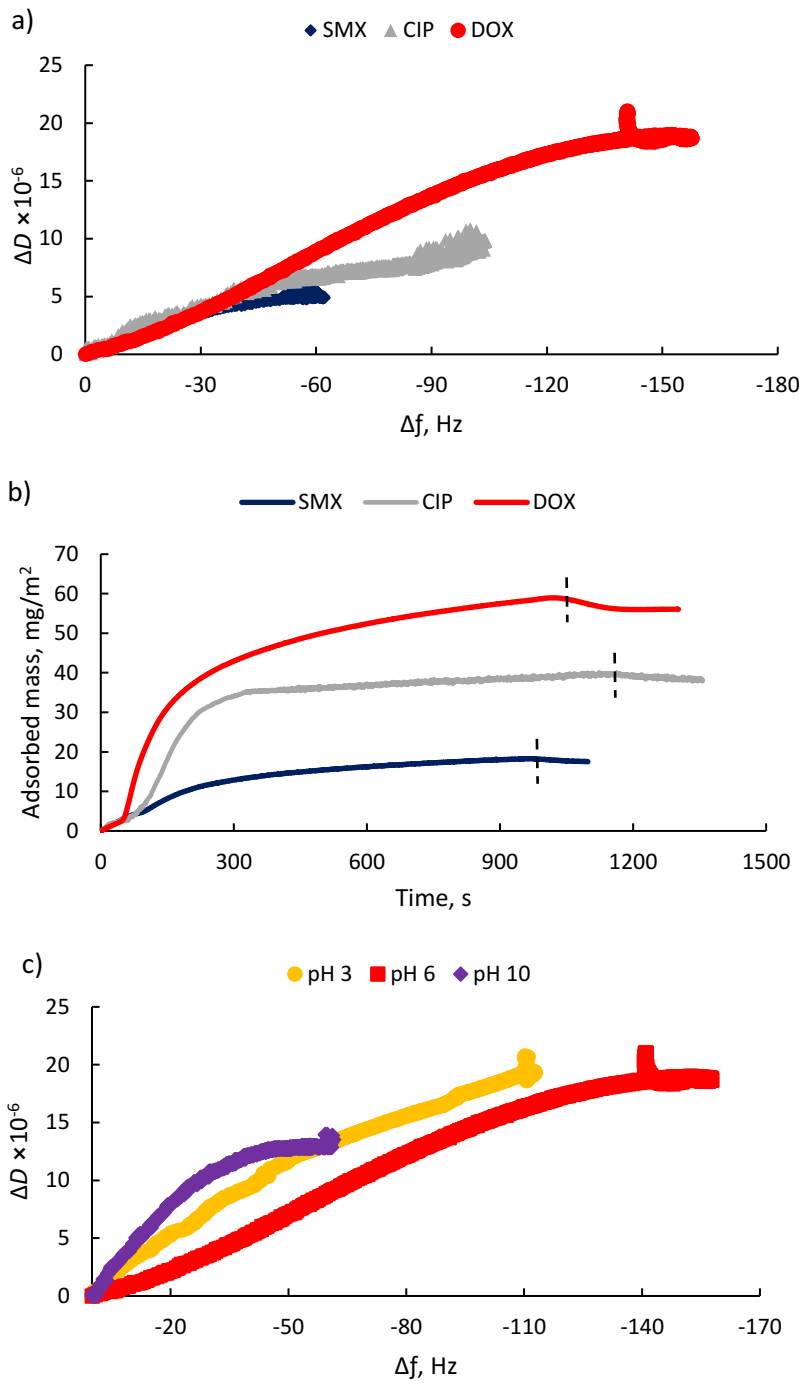
a)
SMX
CIP
DOX
25
20
15
10
5
0
ΔD ×10-6
0
-30
-60
-90
-120
-150
-180
Δf, Hz
b)
SMX
CIP
DOX
70
60
50
40
30
20
10
0
Adsorbed mass, mg/m2
0
300
600
900
1200
1500
Time, s
c)
pH 3
pH 6
pH 10
25
20
15
10
5
0
ΔD ×10-6
-20
-50
-80
-110
-140
-170
Δf, Hz

Figure 6.8. adsorption of antibiotics on the PCNC-coated surface performed at pH 6.0 and 25 °C. a) $\Delta D/\Delta f$ data of adsorption, b) adsorbed mass of antibiotics on PCNC concerning time, and c) the adsorption of DOX on the PCNC-coated surface conducted at different pH and 25 °C. Dashed lines indicate rinsing.

6.4.5 BET analysis

Table 6.2 includes the surface area as well as pore size and pore volume of CNC samples before and after loading with antibiotics. As seen, carboxyalkylation slightly reduced the surface area and total pore volume in the CNC samples while it lightly increased the average pore size. As the reaction was conducted under alkaline conditions, CNC might have gone through mild hydrolysis, which increased the pore size and pore volume of CNC and thus reducing its surface area. Also, the longer carboxyalkylated group might have coated the surface of CNC more significantly and reduced its porous structure. Moreover, the antibiotic adsorption drastically increased the surface area in all CNC samples, specifically that of PCNC. Also, the larger impact of DOX and CIP than SMX on the surface area might be attributed to their higher adsorption to CNC samples (Figure 6.8). These results reveal successful adsorption of antibiotics since the surface area of antibiotics had contributed to the overall surface area increment (Wang et al., 2016). Also, the adsorption of antibiotics led to a slight reduction and increment in the average pore size and total pore volume of the PCNC samples, respectively, which reveals that antibiotics were adsorbed and filled the pores in CNC samples (Yurduşen et al., 2020). This phenomenon is further exhibited in Figure 9b.

Table 6.2. Surface area, pore size, and pore volume analyses of CNC samples

Samples	Surface area, m^2/g	Average pore size, nm	Total pore volume, cm^3/g
UCNC	41.0	2.1	0.04
HCNC	38.9	2.9	0.09
PCNC	38.2	3.1	0.12
DOX-UCNC	68.8	2.1	0.07
DOX-HCNC	170.8	2.2	0.28
DOX-PCNC	178.5	2.1	0.35
SMX-PCNC	136.4	2.0	0.18
CIP-PCNC	177	2.0	0.18

6.4.6 Mechanism of antibiotic adsorption

The adsorption mechanisms of DOX on CNC surfaces are depicted in Figure 6.9. Figure 6.9a reveals the developed interactions at different pH. At pH 3.0, charge neutralization (shown in green dashed line), and π interactions (shown in red dashed lines) including 1) anion-π interaction between PCNC sulfate-half ester groups and phenolic rings of DOX (Lucas et al., 2016); and 2) π interaction between PCNC alkyl tails and the phenolic rings in DOX (Tsuzuki et al., 2000; Chen et al., 2014) would have been the driven forces for adsorption. At pH 6.0, aside from a strong charge neutralization, extensive hydrogen bonding between the negatively charged carboxyl groups of PCNC and hydroxyl groups of DOX would have occurred leading to much higher adsorption of DOX to PCNC at pH 6.0 than 3.0. At pH 6, more π interactions (specially anion-π) might have been developed due to the deprotonation of PCNC carboxyl groups (Hunt et al., 2015; Oberoi et al., 2019). The pH increment would further suppress the development of various interactions due to the domination of a negative charge between DOX and PCNC generating from the repulsion force (Figure 6.1). The adsorption at pH 11.0 might be due to the π interactions that could still happen (Figures 6.4 and 6.8c).

Figure 6.9b depicts the physical adsorption of DOX on all CNC surfaces while the least and most adsorption is schematically depicted on UCNC and PCNC, respectively. Carboxyalkylation has been shown to increase the CNC porosity due to the addition of alkyl chains as confirmed by the BET analysis. As implied in the figure, DOX adsorption contributed to an increase in the surface area (Table 2) of PCNC. While the adsorption led to a reduced pore size on CNC, the overall pore volume is shown to be increased. In other words, DOX had occupied the pores upon its adsorption while this occupation further led to an increased total pore volume as observed by the BET analysis. SEM images of CNC samples after antibiotic adsorption were also taken and exhibited in Figure S12. Considering the surface of the samples upon antibiotic adsorption, no significant alteration in the morphology of the samples were detected by SEM when compared to the pristine CNC samples (Figure S6.1a, b). Thus, the XPS analysis was carried out to depict the chemical alteration of the CNC samples before and after the antibiotic adsorption, which is revealed in the following section.

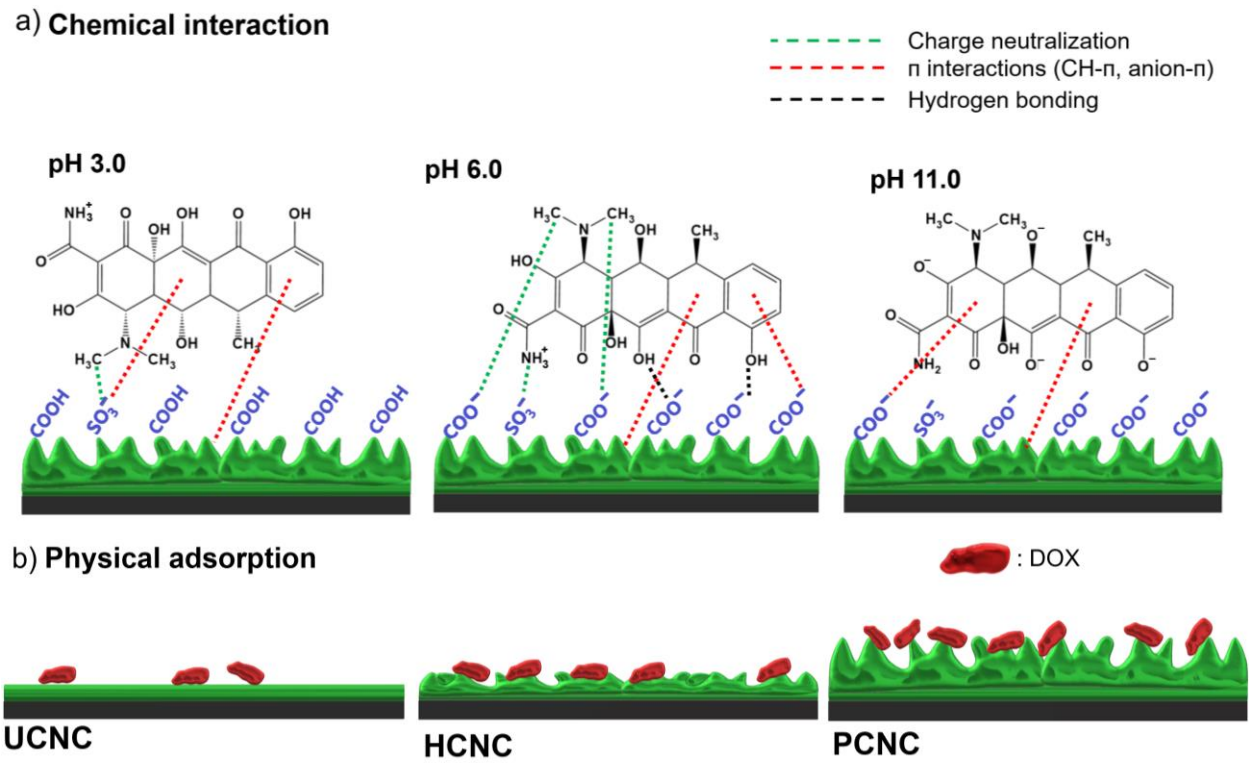

Figure 6.9. a) the chemical interaction of DOX with PCNC ant different pH, and b) the physical adsorption of DOX on CNC samples. The depicted porosity of HCNC and PCNC surfaces are raised from the short and long alkyl chains of carboxyl groups, respectively.

6.4.7 XPS analysis

XPS analysis reveals useful information with respect to the surface elemental composition as well as the functional groups of the samples. Figure 6.10 demonstrates the wide-scan spectra of CNC samples before and after loading with antibiotics. As seen in Figure 6.10a, the survey spectra of UCNC, HCNC, and PCNC shows typical patterns mostly consisting of carbon and oxygen. The spectra for antibiotic-adsorbed CNC samples contain other elements, e.g., nitrogen, implying the adsorption of antibiotics to CNC samples. In detail, the DOX-CNC spectra contain a peak at 400 ev raised from the nitrogen atom of DOX, while the spectrum for CIP-PCNC shows peaks at the binding energy of 687.7 and 400 ev, which are related to the fluorine and nitrogen of CIP on the PCNC (Figure S6.4) (Chang et al., 2015). Elevated peaks at 164.2 and 400 ev in the SMX-PCNC spectrum is also ascribed to sulfur and nitrogen contents of SMX, further revealing its adsorption on PCNC.

Figure 6.10b demonstrates the related peak spectra, which were deconvoluted to different carbon and oxygen peaks, while Table 6.3 contains the C 1s and O 1s peak area of the samples. Generally, the C 1s includes four categories of C1 (281.43 eV), C2 (283.42 eV), C3 (284.86 eV), and C4 (285.86 eV), standing for C-C/C-H aliphatic linkages, C-N/C-O linkages in ethers and alcohols, O-C-O/C=O linkages in acetals, and O-C=O linkages in esters, respectively, which are detectable in UCNC C1 spectrum (Kaboorani & Reidl, 2015; Fatona et al., 2018). The carboxyalkylation of CNC altered the relative amounts of components in the C 1s spectra, in which the C1 (C-C/C-H) peak increased from 3 % in UCNC to around 12 and 37% in the HCNC and PCNC samples, respectively, which would be due to an increase in the aliphatic hydrocarbons of HCNC and PCNC (Li et al., 2018), further revealing the successful carboxyheptanation and carboxypantadecanation of CNC.

Comparing the C spectra of DOX adsorption to CNC derivatives, an increase in the C1 and C2 peaks related to C-C/C-H and C-N/C-O groups, respectively, reveals the more adsorption of DOX onto HCNC and PCNC than UCNC. In the case of the antibiotic-loaded PCNC samples, a larger peak of C3 in SMX, CIP, and DOX-loaded PCNC than the unloaded PCNC could be ascribed to the interaction of C=O/O-C-O groups of PCNC and N-H groups in the antibiotics (Li et al., 2018). As seen in the O1 spectra of samples, unmodified CNC contains a C-O bond at 532 ev (Wang et al., 2016). Through carboxyalkylation, a bond related to $C=O/COO^{-}$ appeared at 533.2 ev (Chang et al., 2015; Wang et al., 2016). Further increase in the latter bond in CIP and DOX-loaded CNC samples reveals the adsorption of these antibiotics onto CNC samples (HCNC, and PCNC).

Table 6.3. Relative surface chemical bonds for CNC samples

Sample	C 1s Peak area, %			
	C1 (C-C/C-H)	C2 (C-N/C-O)	C3 (C=O/O-C-O)	C4 (O-C=O)
UCNC	2.78	21.88	57.55	17.78
HCNC	11.59	47.5	26.92	13.99
PCNC	37.06	35.32	18.74	8.88

DOX-UCNC	2.06	14.71	62.84	1.5
DOC-HCNC	35.79	38.79	21.74	3.68
DOX-PCNC	23.42	47.58	22.82	6.18
SMX-PCNC	36.64	39.03	17.63	6.7
CIP-PCNC	36.11	35.25	20.66	7.96

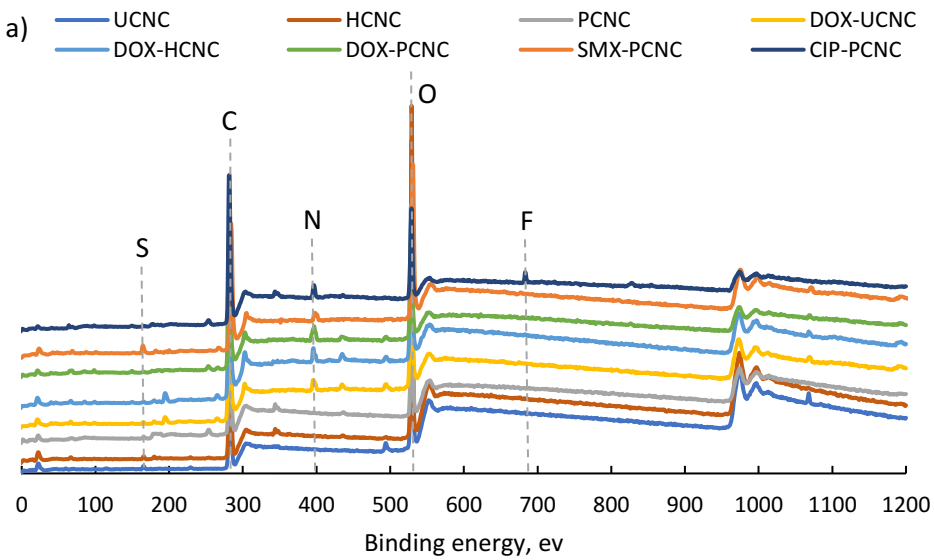

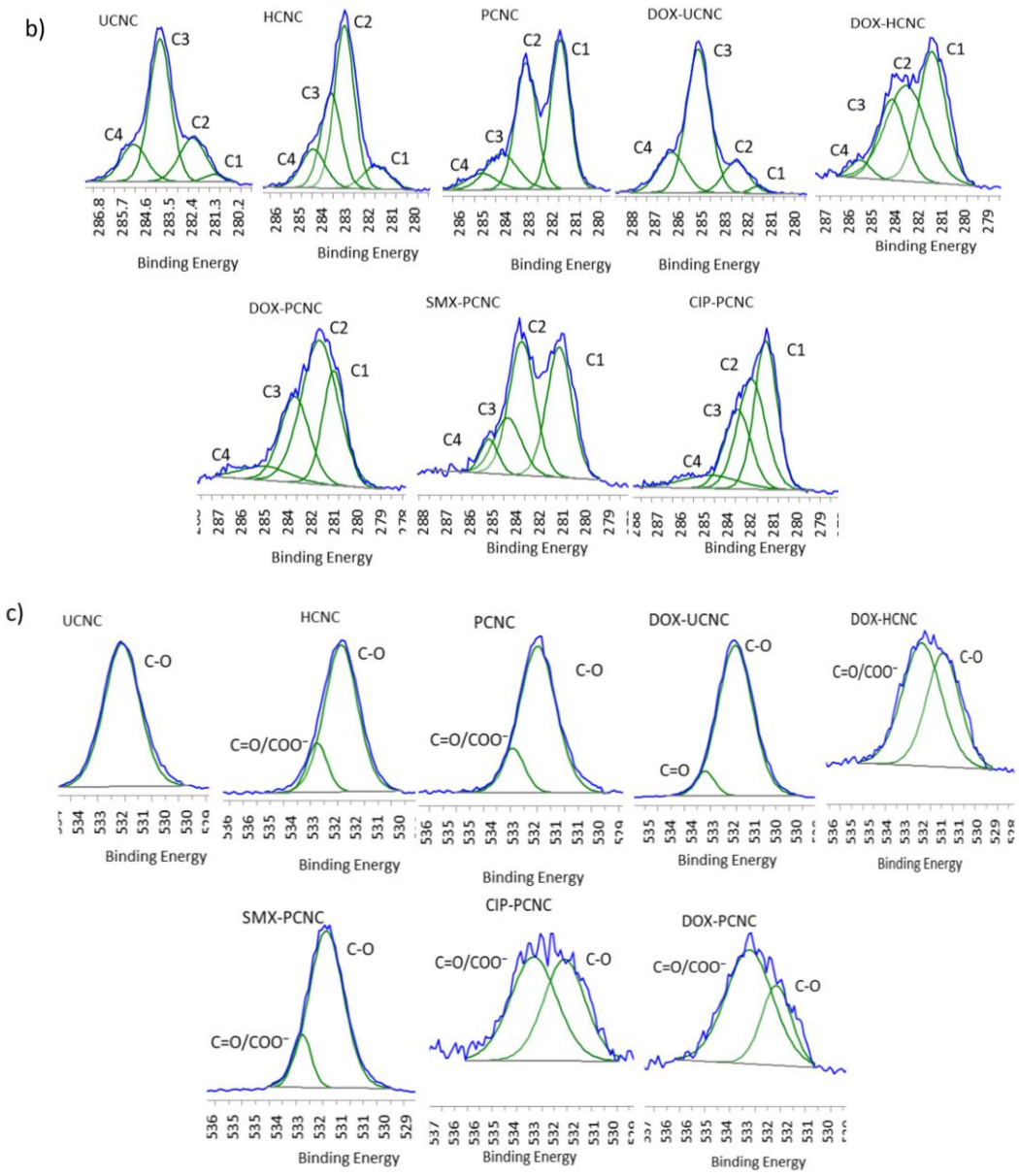

Figure 6.10. a) XPS survey spectra, b) C1(s) and c) O1 high-resolution spectra of CNC samples

6.5 Conclusions

In this study, the produced carboxyalkyl cellulose nanocrystals (CNC), as well as unmodified CNC, were used as antibiotic adsorbents. The highest antibiotic adsorption was observed for DOX at pH 6.0, due to a strong electrostatic attraction, π interactions, and hydrogen bonding developed among carboxyalkylated CNC and DOX which had also been analyzed through zeta potential analysis. The least DOX adsorption happened at pH 10.0, which is probably due to the electrostatic repulsion force hampering the adsorption. Also, carboxyalkylated CNC samples worked better in

antibiotic adsorption than the unmodified CNC did, which reveals the role of these functional groups in the adsorption. An increase in the hydrocarbon chain length of the carboxylate groups decreased the hydrophilicity of the modified samples. Also, carboxyalkylated CNC samples were more sensitive to pH alteration than the unmodified CNC, slightly promoting the hydrophilicity of the samples at higher pH promoting the deprotonation of the functional groups of CNC derivatives. CIP and DOX were more hydrophilic than SMX, due to their hydrophilic functional groups while they were more sensitive than SMX to pH variation. The contact angle analysis of DOX on CNC derivatives also depicted that the CNC with the highest carbon chain length was more porous and that DOX diffused more into the PCNC. In comparing the contact angle and QCM adsorption analyses of three antibiotics on PCNC, DOX depicted faster interaction due to the more hydrogen bonding and π interactions developed between the two substrates. The adsorption of DOX was higher at pH 6.0 on PCNC because the carboxylate groups of PCNC can be deprotonated at this pH, promoting more hydrogen bonding ((-)CAHB) and π interactions (anion-π). Carboxyalkylation reactions were both observed to slightly reduce the CNC surface area due to the mild hydrolysis of CNC under the alkaline reaction required for carboxyalkylation. In the meantime, the antibiotic adsorption remarkably increased the surface area in CNC as their adsorption increased the overall surface area of the material. The surface area change was more pronounced for DOX-PCNC complex due to the more interaction and adsorption of DOX on PCNC. XPS analysis also conveyed that carboxyalkylation drastically increased the C-C/C-H component, while antibiotic adsorption to PCNC augmented the C-C/C-H and C-N/C-O components.

6.6 References

Bardet, R., Sillard, C., Belgacem, N., & Bras, J. (2015). Self-assembly of cellulose nanocrystals with fluorescent agent in iridescent films. *Cellulose Chem. Technol*, *49*(7-8), 587-595.

Carabineiro, S. A. C., Thavorn-Amornsri, T., Pereira, M. F. R., & Figueiredo, J. L. (2011). Adsorption of ciprofloxacin on surface-modified carbon materials. *Water Research*, *45*(15), 4583-4591.

Chang, J., Chen, Y., Zhao, S., Guan, X., & Fan, H. (2015). Poly (N-acryloyl ciprofloxacin-co-acrylic acid) grafted magnetite nanoparticles for microbial decontamination of collagen solution: have we conquered the problem of antimicrobial residues? *Polymer Chemistry*, *6*(47), 8150-8160.

Chen, H., Gao, B., & Li, H. (2014). Functionalization, pH, and ionic strength influenced sorption of sulfamethoxazole on graphene. Journal of Environmental Chemical Engineering, 2(1), 310-315.

Fatona, A., Berry, R. M., Brook, M. A., & Moran-Mirabal, J. M. (2018). Versatile surface modification of cellulose fibers and cellulose nanocrystals through modular triazinyl chemistry. *Chemistry of Materials*, *30*(7), 2424-2435.

Feizi, Z. H., & Fatehi, P. (2020a). Carboxymethylated cellulose nanocrystals as clay suspension dispersants: effect of size and surface functional groups. *Cellulose*, *27*, 3759-3772.

Feizi, Z. H., & Fatehi, P. (2020b). Interaction of hairy carboxyalkyl cellulose nanocrystals with cationic surfactant: Effect of carbon spacer. *Cabohydrate Polymers*, 117396.

Feizi, Z. H., Kazzaz, A. E., Kong, F., & Fatehi, P. (2019). Evolving a flocculation process for isolating lignosulfonate from solution. *Separation and Purification Technology*, *222*, 254-263.

Givianrad, M. H., Saber-Tehrani, M., Aberoomand-Azar, P., & Mohagheghian, M. (2011). H-point standard additions method for simultaneous determination of sulfamethoxazole and trimethoprim in pharmaceutical formulations and biological fluids with simultaneous addition of two analytes. *Spectrochimica Acta Part A: Molecular and Biomolecular Spectroscopy*, *78*(3), 1196-1200.

Hou, T., Du, H., Yang, Z., Tian, Z., Shen, S., Shi, Y., ... & Zhang, L. (2019). Flocculation of different types of combined contaminants of antibiotics and heavy metals by thermo-responsive flocculants with various architectures. Separation and Purification Technology, 223, 123-132.

Hu, D., & Wang, L. (2016). Adsorption of ciprofloxacin from aqueous solutions onto cationic and anionic flax noil cellulose. *Desalination and Water Treatment*, *57*(58), 28436-28449.

Hu, Z., Ballinger, S., Pelton, R., & Cranston, E. D. (2015). Surfactant-enhanced cellulose nanocrystal Pickering emulsions. *Journal of colloid and interface science*, *439*, 139-148.

Hunt, P. A., Ashworth, C. R., & Matthews, R. P. (2015). Hydrogen bonding in ionic liquids. *Chemical Society Reviews*, *44*(5), 1257-1288.

Kaboorani, A., and Riedl, B. (2015). Surface modification of cellulose nanocrystals (CNC) by a cationic surfactant. *Industrial Crops and Products*, 65, 45-55.

Kang, J., Duan, X., Zhou, L., Sun, H., Tadé, M. O., & Wang, S. (2016). Carbocatalytic activation of persulfate for removal of antibiotics in water solutions. Chemical Engineering Journal, 288, 399-405.

Kazzaz, A. E., Feizi, Z. H., & Fatehi, P. (2018). Interaction of sulfomethylated lignin and aluminum oxide. *Colloid and Polymer Science*, *296*(11), 1867-1878.

Kong, F., Wang, S., Price, J. T., Konduri, M. K., & Fatehi, P. (2015). Water soluble kraft lignin–acrylic acid copolymer: Synthesis and characterization. *Green Chemistry*, *17*(8), 4355-4366.

Kralj, S., Drofenik, M., & Makovec, D. (2011). Controlled surface functionalization of silica-coated magnetic nanoparticles with terminal amino and carboxyl groups. *Journal of Nanoparticle Research*, *13*(7), 2829-2841.

Kim, Y. T., & Mitani, T. (2006). Competitive effect of carbon nanotubes oxidation on aqueous EDLC performance: Balancing hydrophilicity and conductivity. *Journal of power sources*, *158*(2), 1517-1522.

Lam, E., Male, K. B., Chong, J. H., Leung, A. C., & Luong, J. H. (2012). Applications of functionalized and nanoparticle-modified nanocrystalline cellulose. *Trends in biotechnology*, *30*(5), 283-290.

Lange, F., Cornelissen, S., Kubac, D., Sein, M. M., Von Sonntag, J., Hannich, C. B., ... & Von Sonntag, C. (2006). Degradation of macrolide antibiotics by ozone: a mechanistic case study with clarithromycin. Chemosphere, 65(1), 17-23.

Li, J., Yu, G., Pan, L., Li, C., You, F., Xie, S., ... & Shang, X. (2018). Study of ciprofloxacin removal by biochar obtained from used tea leaves. *Journal of Environmental Sciences*, *73*, 20-30.

Liao, K. H., Lin, Y. S., Macosko, C. W., & Haynes, C. L. (2011). Cytotoxicity of graphene oxide and graphene in human erythrocytes and skin fibroblasts. *ACS applied materials & interfaces*, *3*(7), 2607-2615.

Lucas, X., Bauzá, A., Frontera, A., & Quinonero, D. (2016). A thorough anion–π interaction study in biomolecules: on the importance of cooperativity effects. *Chemical science*, *7*(2), 1038-1050.

Ma, J., Li, B., Zhou, L., Zhu, Y., Li, J., & Qiu, Y. (2018). Simple Urea Immersion Enhanced Removal of Tetracycline from Water by Polystyrene Microspheres. *International journal of environmental research and public health*, *15*(7), 1524.

Maresca, M., Derghal, A., Carravagna, C., Dudin, S., & Fantini, J. (2008). Controlled aggregation of adenine by sugars: physicochemical studies, molecular modelling simulations of sugar–aromatic CH–π stacking interactions, and biological significance. *Physical Chemistry Chemical Physics*, *10*(19), 2792-2800.

Mohamed, A. K., & Mahmoud, M. E. (2020). Encapsulation of Starch Hydrogel and Doping Nanomagnetite onto Metal-Organic Frameworks for Efficient Removal of Fluvastatin Antibiotic from Water. *Carbohydrate Polymers*, 116438.

Naveed, S., & Waheed, N. (2014). Simple UV spectrophotometric assay of ciprofloxacin. *Mintage J Pharm Med Sci*, *3*(4), 10-13.

Ni, J., & Pignatello, J. J. (2018). Charge-assisted hydrogen bonding as a cohesive force in soil organic matter: water solubility enhancement by addition of simple carboxylic acids. *Environmental Science: Processes & Impacts*, *20*(9), 1225-1233.

Niinivaara, E., Faustini, M., Tammelin, T., & Kontturi, E. (2015). Water vapor uptake of ultrathin films of biologically derived nanocrystals: quantitative assessment with quartz crystal microbalance and spectroscopic ellipsometry. *Langmuir, 31*(44), 12170-12176.

Oberoi, A. S., Jia, Y., Zhang, H., Khanal, S. K., & Lu, H. (2019). Insights into the fate and removal of antibiotics in engineered biological treatment systems: a critical review. *Environmental science & technology*, *53*(13), 7234-7264.

Pirich, C. L., de Freitas, R. A., Torresi, R. M., Picheth, G. F., & Sierakowski, M. R. (2017). Piezoelectric immunochip coated with thin films of bacterial cellulose nanocrystals for dengue detection. *Biosensors and Bioelectronics*, *92*, 47-53.

Reid, M. S., Villalobos, M., & Cranston, E. D. (2017). The role of hydrogen bonding in non-ionic polymer adsorption to cellulose nanocrystals and silica colloids. *Current Opinion in Colloid & Interface Science*, *29*, 76-82.

Salimi, S., Sotudeh-Gharebagh, R., Zarghami, R., Chan, S. Y., & Yuen, K. H. (2019). Production of nanocellulose and its applications in drug delivery: A critical review. *ACS Sustainable Chemistry & Engineering*, *7*(19), 15800-15827.

Kakavandi, B., Esrafili, A., Mohseni-Bandpi, A., Jonidi Jafari, A., & Rezaei Kalantary, R. (2014). Magnetic Fe3O4@ C nanoparticles as adsorbents for removal of amoxicillin from aqueous solution. *Water science and technology*, *69*(1), 147-155.

Seredych, M., & Bandosz, T. J. (2007). Removal of cationic and ionic dyes on industrial−municipal sludge based composite adsorbents. *Industrial & engineering chemistry research*, *46*(6), 1786-1793.

Song, X., Zhai, J., Wang, Y., & Jiang, L. (2006). Self-assembly of amino-functionalized monolayers on silicon surfaces and preparation of superhydrophobic surfaces based on alkanoic acid dual layers and surface roughening. *Journal of Colloid and Interface Science, 298*(1), 267-273.

Suda, T., Hata, T., Kawai, S., Okamura, H., & Nishida, T. (2012). Treatment of tetracycline antibiotics by laccase in the presence of 1-hydroxybenzotriazole. Bioresource technology, 103(1), 498-501.

Tang, L., Lin, F., Li, T., Cai, Z., Hong, B., & Huang, B. (2018). Design and synthesis of functionalized cellulose nanocrystals-based drug conjugates for colon-targeted drug delivery. *Cellulose*, *25*(8), 4525-4536.

Tao, J., Yang, J., Ma, C., Li, J., Du, K., Wei, Z., ... & Deng, X. (2020). Cellulose nanocrystals/graphene oxide composite for the adsorption and removal of levofloxacin hydrochloride antibiotic from aqueous solution. *Royal Society Open Science*, *7*(10), 200857.

Tsuzuki, S., Honda, K., Uchimaru, T., Mikami, M., & Tanabe, K. (2000). The magnitude of the CH/π interaction between benzene and some model hydrocarbons. *Journal of the American Chemical Society*, *122*(15), 3746-3753.

Wang, B., Lv, X. L., Feng, D., Xie, L. H., Zhang, J., Li, M., ... & Zhou, H. C. (2016). Highly stable Zr (IV)-based metal–organic frameworks for the detection and removal of antibiotics and organic explosives in water. *Journal of the American Chemical Society*, *138*(19), 6204-6216.

Wang, H., He, J., Zhang, M., Tam, K. C., & Ni, P. (2015). A new pathway towards polymer modified cellulose nanocrystals via a “grafting onto” process for drug delivery. *Polymer Chemistry*, *6*(23), 4206-4209.

Wang, J., Yao, Q., Sheng, C., Jin, C., & Sun, Q. (2017). One-step preparation of graphene oxide/cellulose nanofibril hybrid aerogel for adsorptive removal of four kinds of antibiotics. *Journal of Nanomaterials*, *2017*. https://doi.org/10.1155/2017/5150613

Wijaya, C. J., Saputra, S. N., Soetaredjo, F. E., Putro, J. N., Lin, C. X., Kurniawan, A., ... & Ismadji, S. (2017). Cellulose nanocrystals from passion fruit peels waste as antibiotic drug carrier. *Carbohydrate polymers*, *175*, 370-376.

Xiong, W., Zeng, Z., Li, X., Zeng, G., Xiao, R., Yang, Z., ... & Zhou, C. (2018). Multi-walled carbon nanotube/amino-functionalized MIL-53 (Fe) composites: remarkable adsorptive removal of antibiotics from aqueous solutions. *Chemosphere*, *210*, 1061-1069.

Xu, L., Pan, J., Dai, J., Li, X., Hang, H., Cao, Z., & Yan, Y. (2012). Preparation of thermal-responsive magnetic molecularly imprinted polymers for selective removal of antibiotics from aqueous solution. *Journal of hazardous materials*, *233*, 48-56.

Yu, F., Li, Y., Han, S., & Ma, J. (2016). Adsorptive removal of antibiotics from aqueous solution using carbon materials. *Chemosphere*, *153*, 365-385.

Yu, K., Sun, C., Zhang, B., Hassan, M., & He, Y. (2019). Size-dependent adsorption of antibiotics onto nanoparticles in a field-scale wastewater treatment plant. Environmental Pollution, 248, 1079-1087.

Zhang, Z., Lan, H., Liu, H., & Qu, J. (2015). Removal of tetracycline antibiotics from aqueous solution by amino-Fe (III) functionalized SBA15. *Colloids and Surfaces A: Physicochemical and Engineering Aspects*, *471*, 133-138.

Zhu, X., Tsang, D. C., Chen, F., Li, S., & Yang, X. (2015). Ciprofloxacin adsorption on graphene and granular activated carbon: kinetics, isotherms, and effects of solution chemistry. *Environmental technology*, *36*(24), 3094-3102.

Gårdebjer, S., Bergstrand, A., Idström, A., Börstell, C., Naana, S., Nordstierna, L., & Larsson, A. (2015). Solid-state NMR to quantify surface coverage and chain length of lactic acid modified cellulose nanocrystals, used as fillers in biodegradable composites. *Composites Science and Technology*, *107*, 1-9.

Yurduşen, A., Yürüm, A., & Yürüm, Y. (2020). A remarkable increase in the adsorbed H_2 amount: Influence of pore size distribution on the H2 adsorption capacity of Fe-BTC. *International Journal of Hydrogen Energy*.

6.7 Appendix A. Supplementary material

Interaction of hairy carboxyalkyl cellulose nanocrystals with cationic surfactant: effect of carbon spacer

Zahra Hosseinpour Feizi, Pedram Fatehi*

Biorefining Research Institute, Green Processes Research Centre and Chemical Engineering Department, Lakehead University, 955 Oliver Road, Thunder Bay, Ontario P7B 5E1, Canada

* Corresponding author, email: pfatehi@lakeheadu.ca; tel: 807-343-8697; fax: 807-346-7943

Supporting experimental section

CNC production

Cellulose nanocrystals (CNC) was produced according to the method described in the literature (Feizi & Fathei, 2020). Softwood pulp was segmented and hydrolyzed by sulfuric acid solution (64 wt.%) with the pulp/acid ratio of 1/17 wt./wt. for one hour at 45 ºC. Then, the acid hydrolysis was stopped by diluting the samples ten folds. The suspension was then centrifuged at 2500 rpm for 10 min to collect the product and the spent acid was discarded. The suspension was then washed with distilled water, and recentrifuged. This step was repeated twice. The pH of the sample was then adjusted to 7.0 and dialyzed against deionized water for further purification for several days using cellulosic dialysis membranes. Afterward, the CNC suspension was freeze-dried using a 1L benchtop freeze-drier, Labconco Co., USA) and stored.

Carboxyalkylation of CNC

CNC carboxyalkylation was simulated according to the literature (Ma et al., 2017; Feizi, & Fatehi, 2020). Briefly, a CNC sample (0.5 g) was added to isopropyl alcohol (50 mL) and stirred (250 rpm) at room temperature for 30 min for each carboxyalkyl reaction mixture. The pH of the suspensions was then adjusted to 12 by NaOH (0.1 M) and stirred for 20 min for the deprotonation of the CNC hydroxy groups. Afterward, BOA (1-2 g) was gradually added to the alkaline suspension to generate carboxyheptanated CNC (HCNC), and BHDA was added to generate carboxypantadecanated CNC (PCNC). The reaction mixtures were then left to react at 55 ºC for 3 h while stirring at 250 rpm. Upon completion, the mixtures were cooled to room temperature, the alcohol was discarded from the top layer, and the modified CNC samples were dispersed in ethanol/water (80/20 vol/vol) mixture. The mixtures were centrifuged, and the modified CNC

samples were collected from the bottom. The samples were then dialyzed in membranes for 48 h with the water changing every 12 h. Samples were then freeze-dried and stored.

Sulfonate and carboxymethyl group content analysis

The sulfonate and carboxymethyl group contents of the CNC samples were calculated by equation 6S1 and 2, respectively (Chen and & de Ven 2016; Konduri & Fatehi 2016).

Equation 6.1

$$Sulfate\ half\ ester\ group = \frac{V_i \times C_{NaOH}}{m_{CNC}}$$

Equation 6.2

$$Carboxyalkyl\ group = \frac{(V_{ii} - V_i) \times C_{NaOH}}{m_{CNC}}$$

where V_i and V_{ii} are the volume (mL) of NaOH which had neutralized strong and weak acidic groups, respectively, C_{NaOH} is the NaOH concentration (mol/L) and m is the mass of dried weight (g) of CNC.

Evaluation of CNC-coated sensors

PEI was deposited on the sensors prior to CNC adsorption. SEM images as well as the EDX-SEM images of the sensor surfaces are provided in Figure S6.1a-c. Needle-like CNC samples were observed on the surfaces in magnified SEM images. Also, the PEI coated sensors were observed to have larger C, N, and O peaks than untreated sensors in its EDX image (Figure S6.1c). Coating the PEI-coated sensors with CNC derivatives further enhanced the C and O peaks while a peak for S (from sulfate-half ester groups of CNC) was also added, implying the successful deposition of CNC samples on sensors. As seen in Figure S1a, and b, the uniform coverage of CNC derivatives was attained on the PEI-coated gold surfaces.

a)

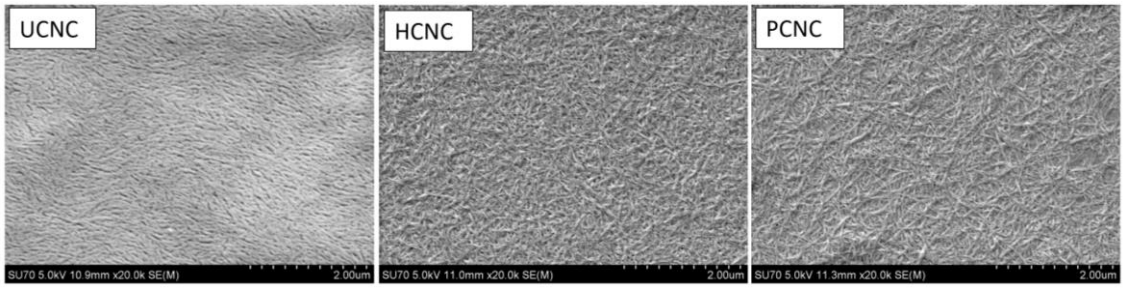

b)

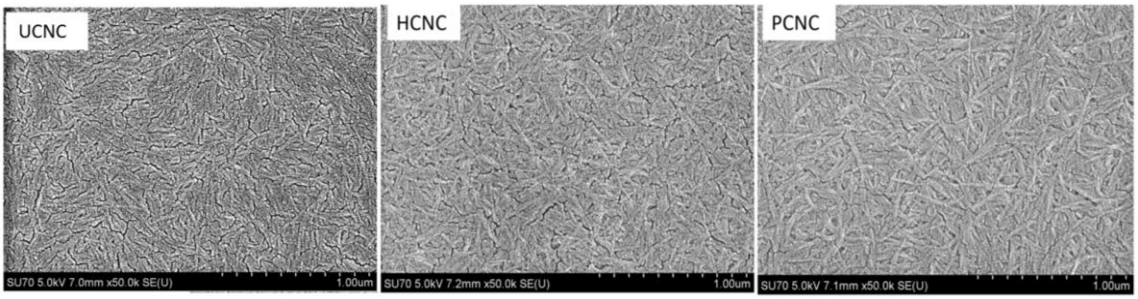

c)

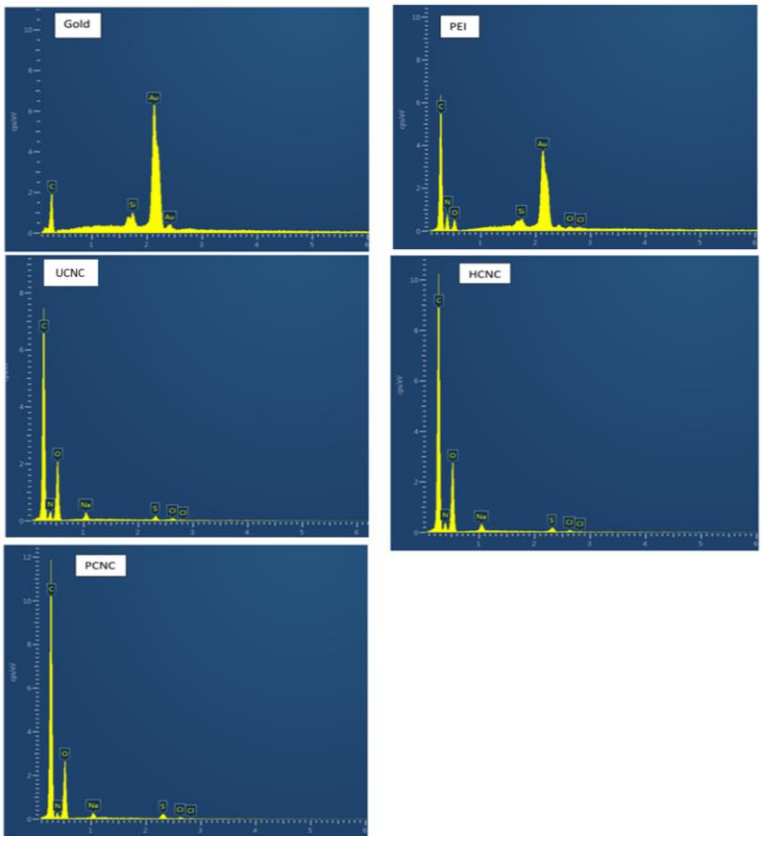

Figure S6.1. a) SEM images of CNC-coated surfaces at a) 2, and b) 1 µm magnification, and c) EDX-SEM images of the bare gold sensor, PEI-coated, and PEI-CNC coated sensors.

Evaluation of CNC-coated sensors

PEI was deposited on the sensors prior to CNC adsorption. SEM images as well as the EDX-SEM images of the sensor surfaces are provided in Figure S1a-c. Needle-like CNC samples were observed on the surfaces in magnified SEM images. Also, the PEI coated sensors were observed to have larger C, N, and O peaks than untreated sensors in its EDX image (Figure S1c). Coating the PEI-coated sensors with CNC derivatives further enhanced the C and O peaks while a peak for

S (from sulfate-half ester groups of CNC) was also added, implying the successful deposition of CNC samples on sensors. As seen in Figure S1a, and b, the uniform coverage of CNC derivatives was attained on the PEI-coated gold surfaces.

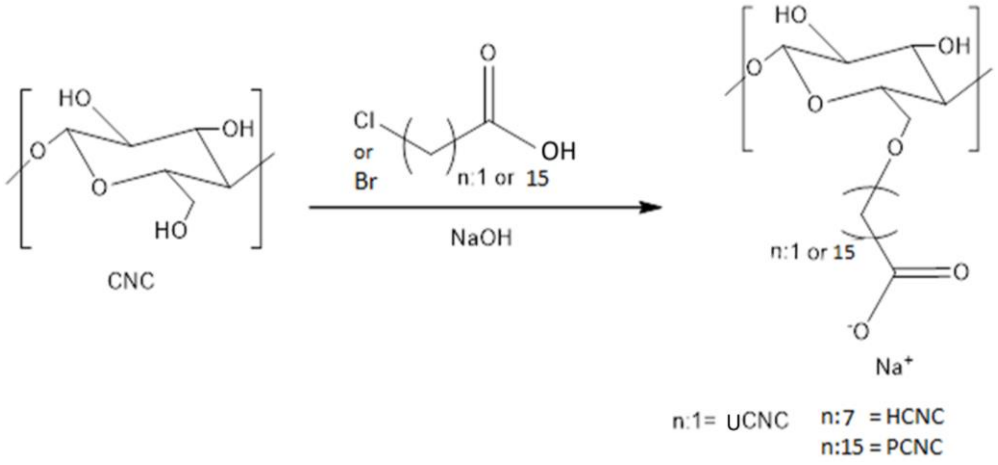

Figure S6.2. Carboxyalkylation of CNC

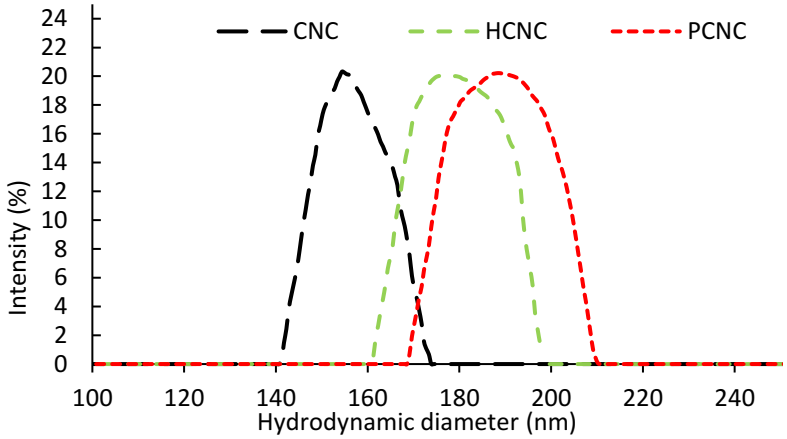

Figure S6.3. Hydrodynamic size of CNC samples

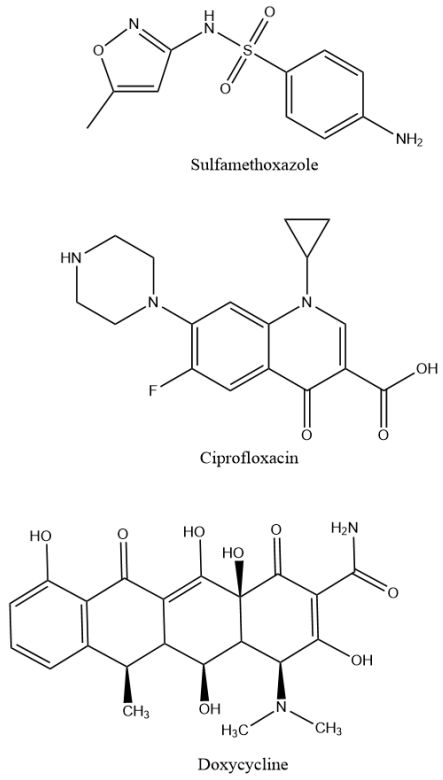

Figure S6.4. Chemical structure of antibiotics

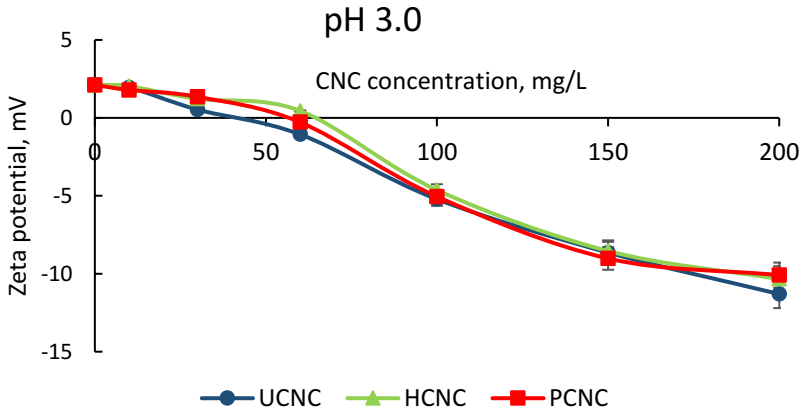

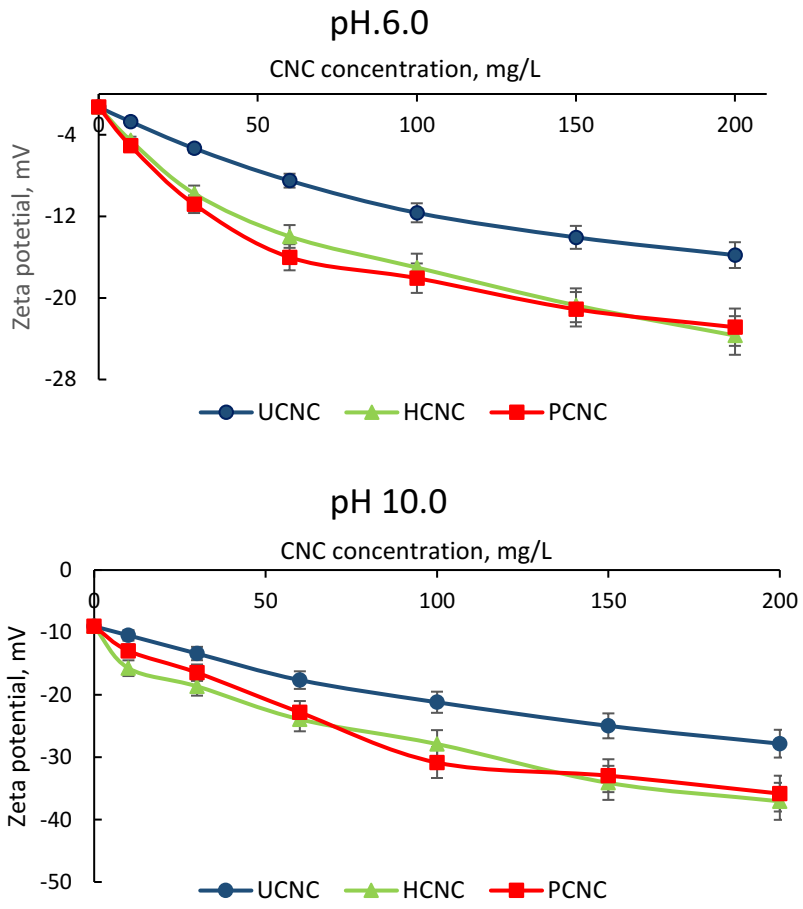

Figure S6.5. Zeta potential of SMX with respect to CNC concentration conducted at different pH

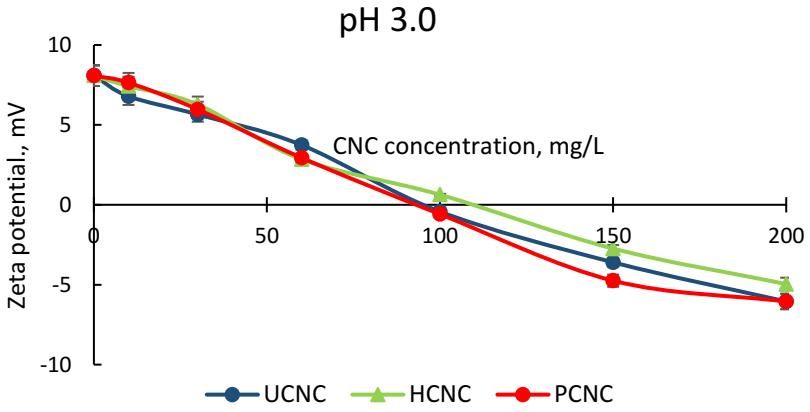

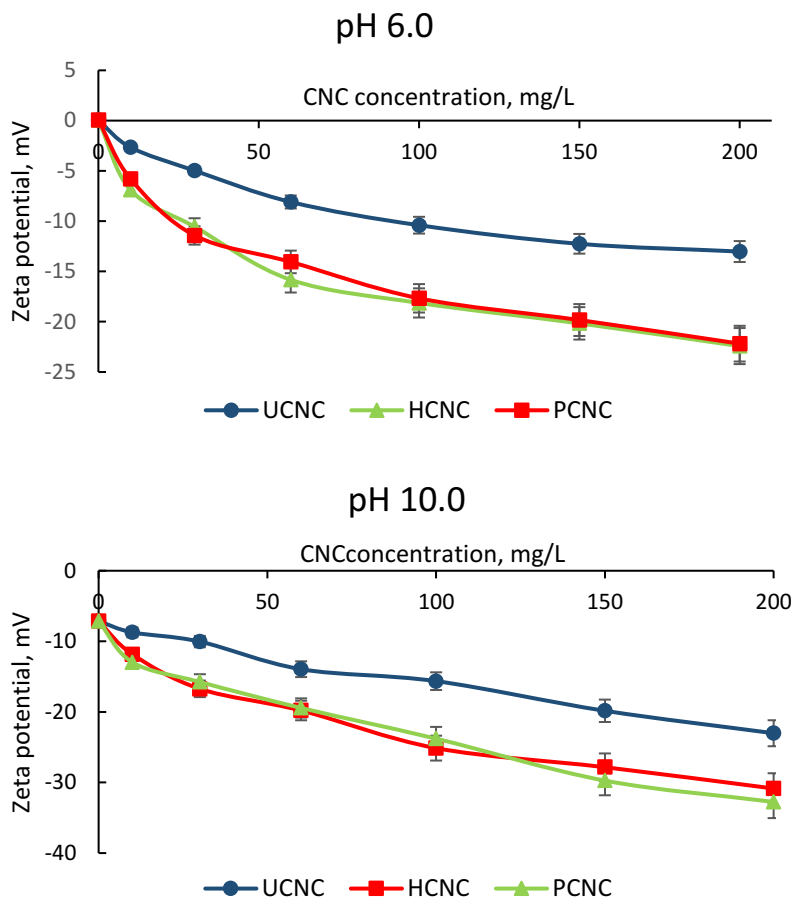

Figure S6.6. Zeta potential of CIP with respect to CNC concentration conducted at different pH

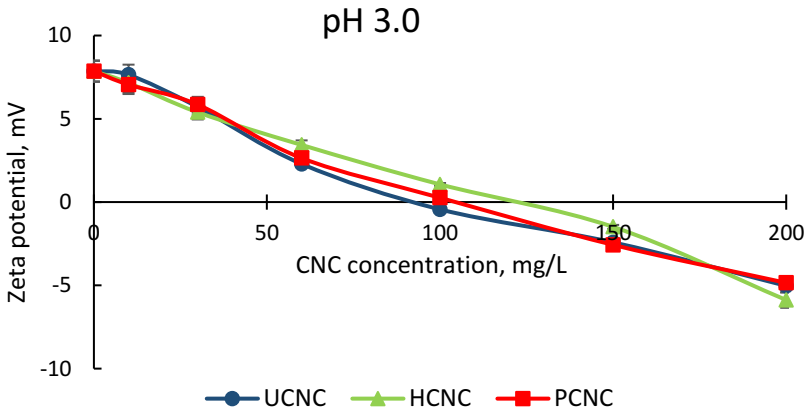

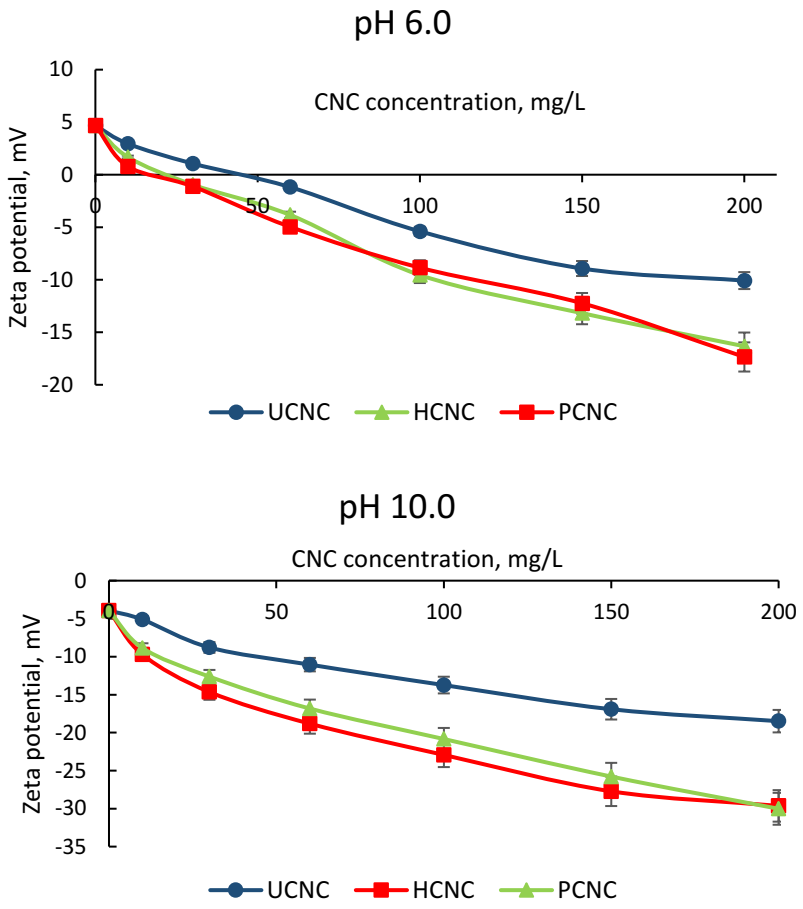

Figure S6.7. Zeta potential of DOX with respect to CNC concentration conducted at different pH

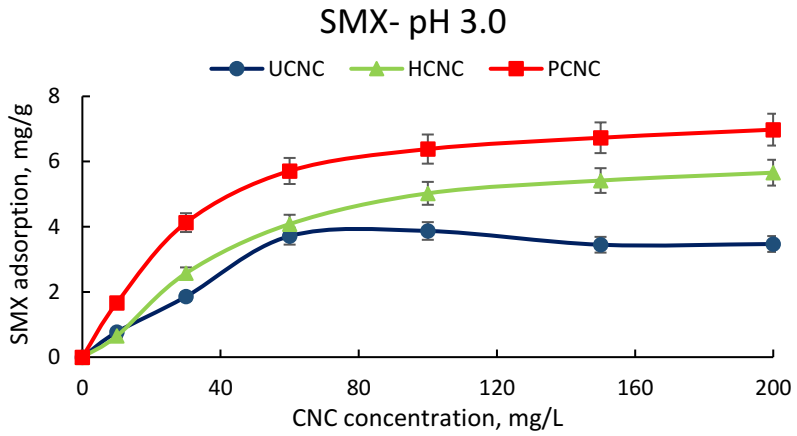

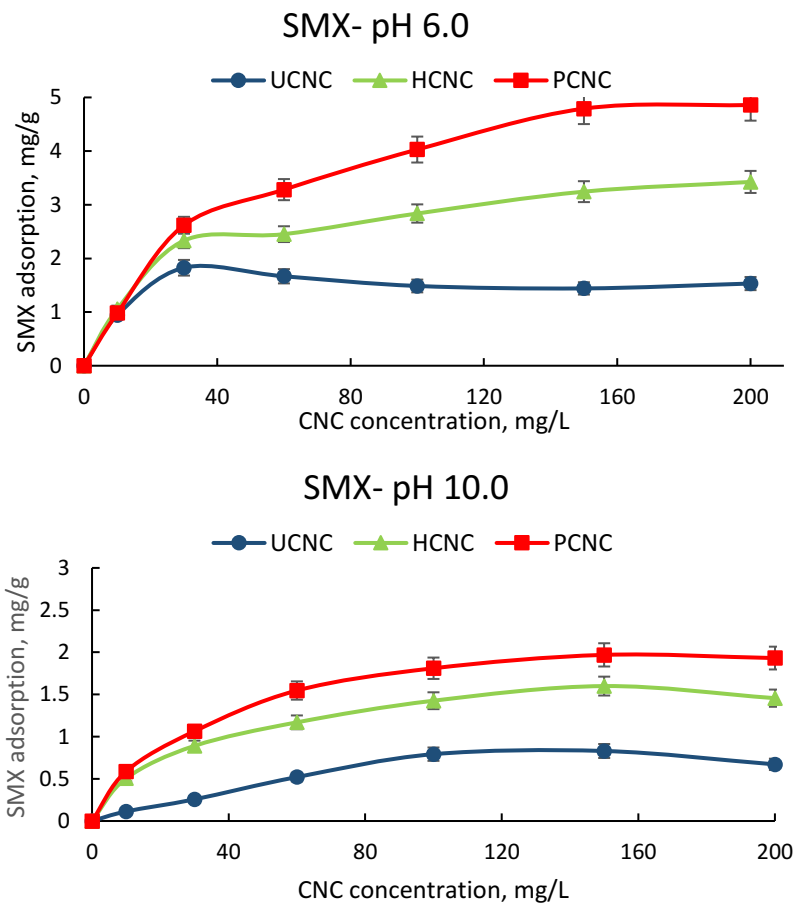

Figure S6.8. SMX adsorption versus the added CNC concentration carried out at different pH

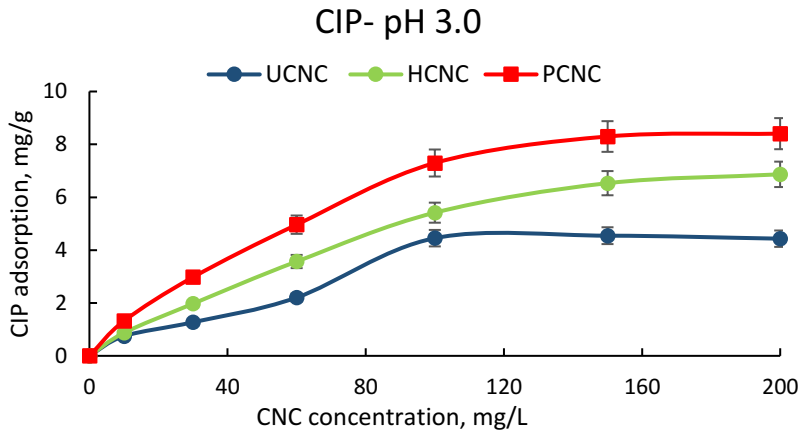

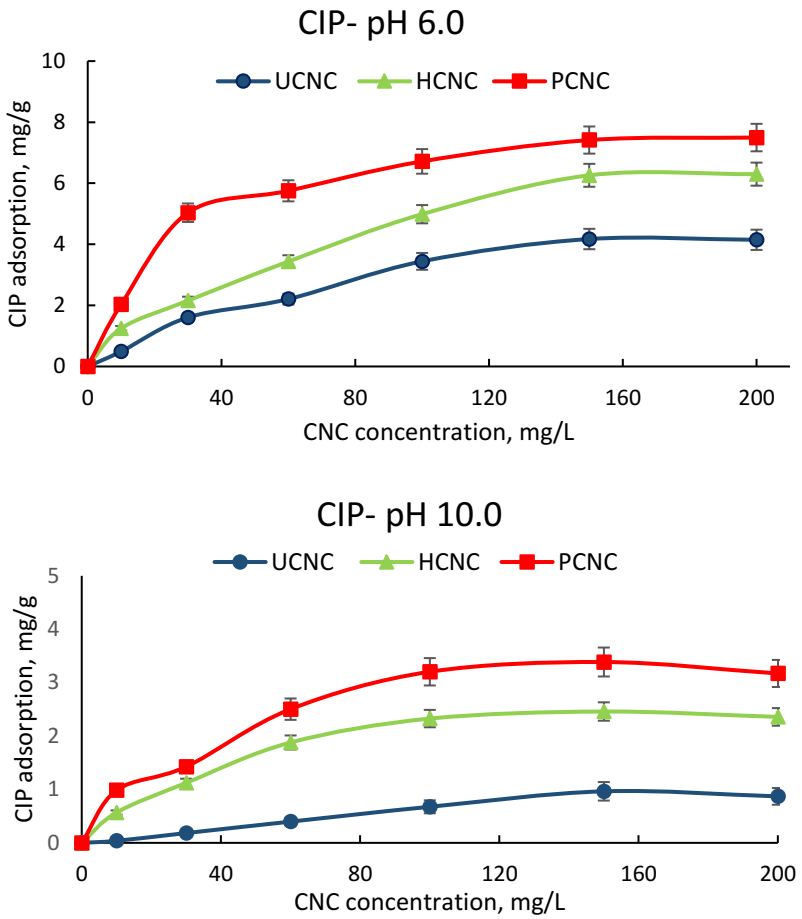

Figure S6.9. CIP adsorption versus added CNC dosage performed at different pH

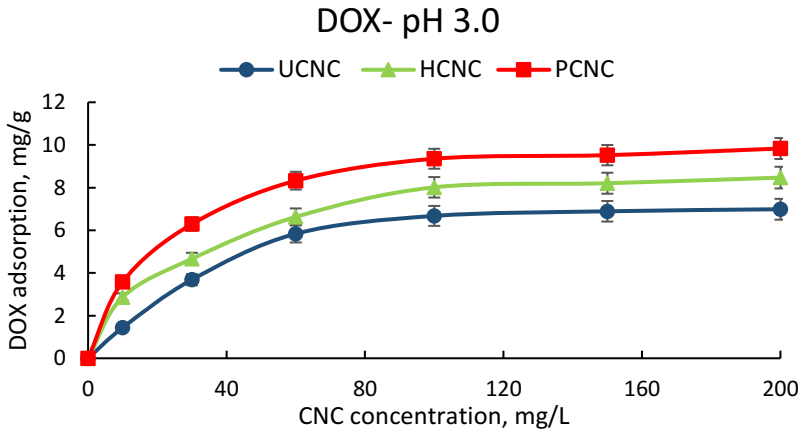

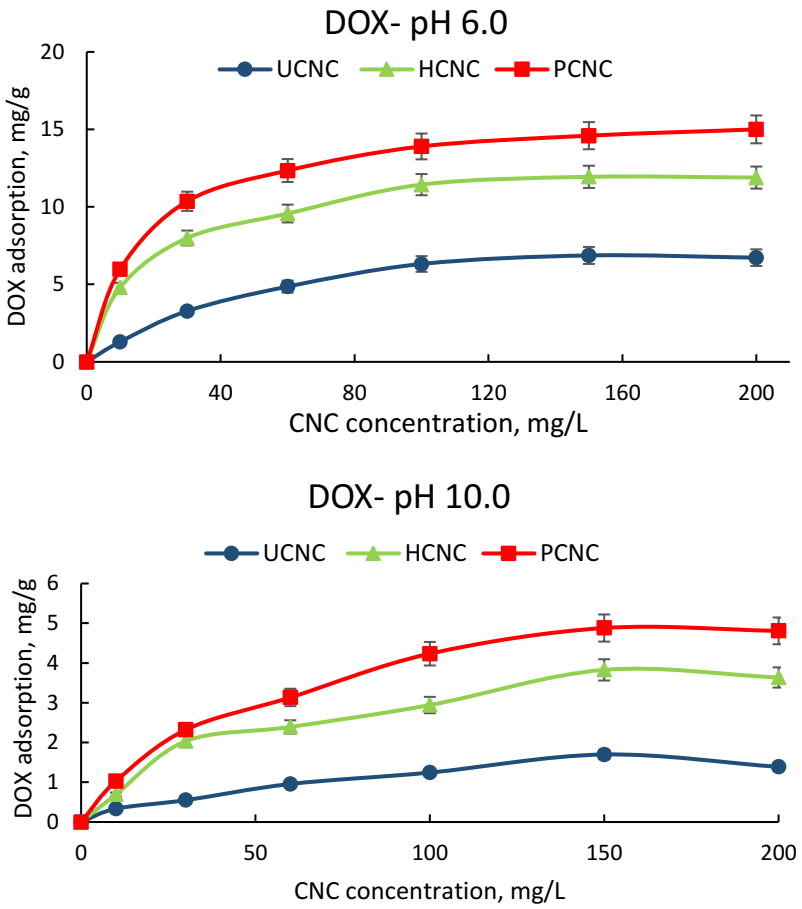

Figure S6.10. DOX adsorption versus added CNC dosage performed at different pH

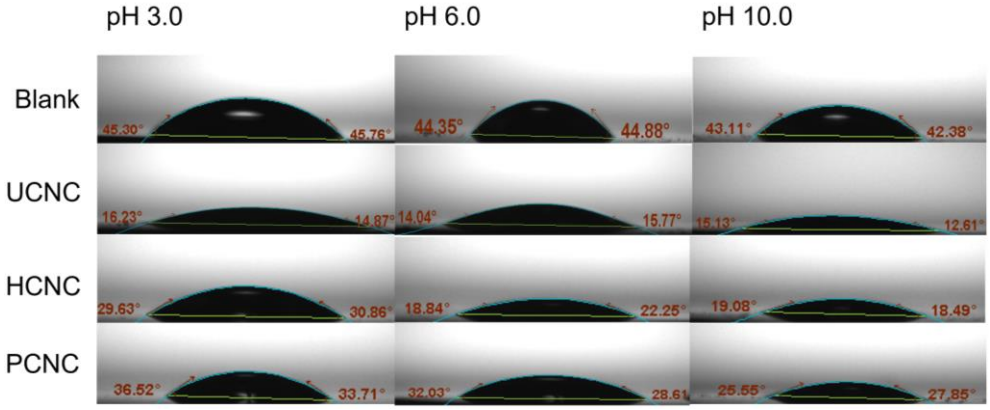

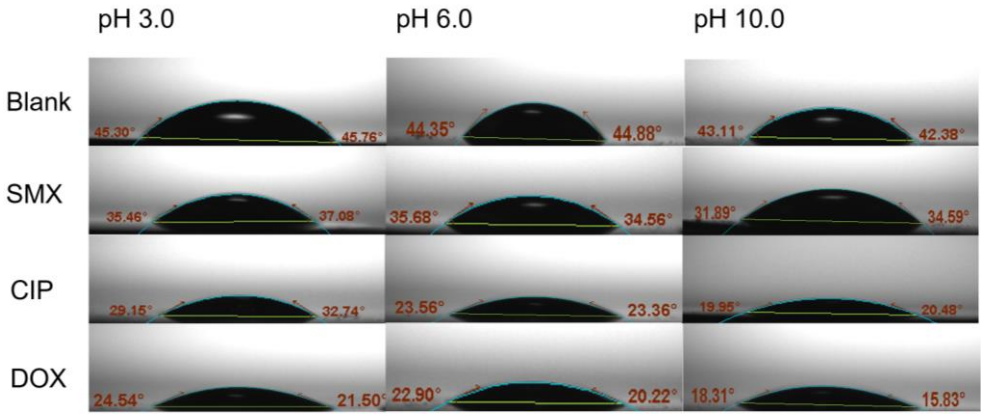

Figure S6.11. Contact angle analysis of CNC and antibiotic-coated surfaces performed at different pH

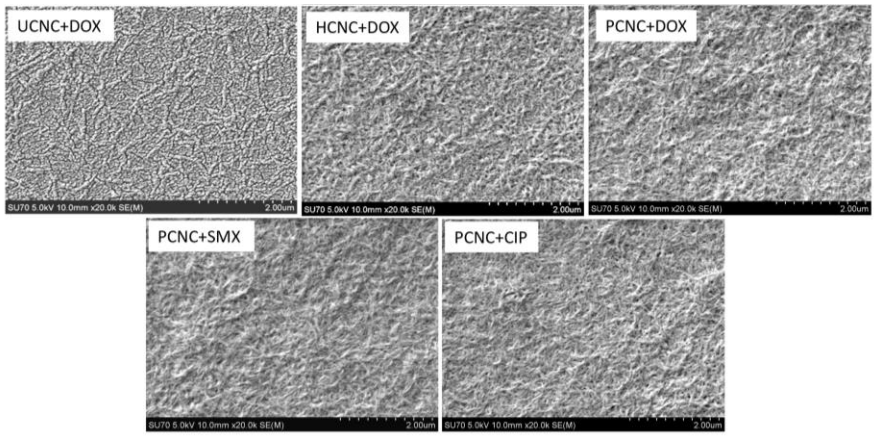

Figure S6.12. SEM images of CNC samples before and after antibiotic adsorption

References

Feizi, Z. H., & Fatehi, P. (2020). Carboxymethylated cellulose nanocrystals as clay suspension dispersants: effect of size and surface functional groups. *Cellulose*, *27*, 3759-3772.

Ma, X., Cheng, Y., Qin, X., Guo, T., Deng, J., & Liu, X. (2017). Hydrophilic modification of cellulose nanocrystals improves the physicochemical properties of cassava starch-based nanocomposite films. *LWT*, *86*, 318-326.

Konduri, M. K., & Fatehi, P. (2016). Synthesis and characterization of carboxymethylated xylan and its application as a dispersant. *Carbohydrate Polymers*, *146*, 26-35.

Chen, D., & van de Ven, T. G. (2016). Flocculation kinetics of precipitated calcium carbonate (PCC) with sterically stabilized nanocrystalline cellulose (SNCC). *Colloids and Surfaces A: Physicochemical and Engineering Aspects*, *506*, 789-793.

Chapter 7: Conclusion and Future directions

7.1 Summary of conclusions

Throughout this thesis, the interaction of anionic CNC with different materials of mineral particles, surfactants, and antibiotics, was investigated to reveal the novel applications of CNC a dispersant and adsorbent for aqueous systems. This interaction was analyzed under different conditions of varied times, temperatures, pH, salinity, and dosages.

For using CNC as a dispersant, CNC was produced in different sizes and was then carboxymethylated to enhance its surface negativity. The largest modified CNC was able to cover kaolinite particles more significantly than the smallest modified CNC in a lower dosage. The zeta potential and thus the stability of the system were increased by 30% when carboxymethylated CNC was used as a dispersant in comparison with unmodified CNC, which would define the critical role of carboxylate groups played in the increment of CNC capacity as a dispersant. Although doubling the CNC size yielded a faster system stabilization, it insignificantly improved the obtained level of stabilization. The functional groups on the carboxymethylated CNC were found to be more important than CNC size on the settling and strength of settling. The modified CNC adsorption, as well as the strength of suspension stability, were the highest at pH 5.5, which could be due to the deprotonation of carboxylate groups on CNC, facilitating the electrostatic adsorption onto kaolinite particles and leading to a better dispersion. Overall, an increase in the CNC size led to a more intense degree of substitution for carboxymethylation, which made CNC a more effective dispersant for the kaolinite suspension.

Since CNC is treated with solvents for different laboratory analyses or industrial applications, the effect of solvent treatment was analyzed on the characteristics of CNC. For this reason, dimethyl sulfoxide (DMSO) and 4-Methylmorpholine N-oxide (NMMO), were separately utilized for CNC treatment under various conditions of different times, temperatures, and CNC concentrations. Upon treatment, a polymorphism transition of cellulose I to II was observed for CNC under all conditions. A diminish in the CNC crystallinity index and crystallite size following enhancement in the *d-spacing* of the (200) plane disclosed the reordering of the cellulosic chains after their precipitation and crystallization, which begot a change in the hydrogen bond network in the crystalline structure. Also, XPS analysis demonstrated a remarkable change in the relative amounts of components in the C 1s upon solvent treatment in CNC. Developing more hydrogen bonds were

observed by an increase in the water-uptake and hydrophilicity of CNC, which is originated from an enhancement in the -OH groups' availability. Enhancement in this feature also yielded more self-assembly in the solvent-treated CNC and hence, less CNC suspension stability. Treatment temperature was observed to be more effective in the transition than treatment duration and CNC concentration. In comparing the effect of DMSO and NMMO on CNC, a more transition was occurred in DMSO treated CNC. Overall, CNC treatment with NMMO and DMSO affected the crystalline structure as well as inter and intra-molecular hydrogen bonds under all conditions studied. Based on this study, changes in the CNC structure and properties need to be considered in the analytical laboratory and industrial end-use of solvent-treated CNC.

Surfactants are important materials in day-to-day lives, and their interaction with different polymers is critical for different industries. In chapter 5 of this thesis, carboxyalkylated CNC with similar charge densities, but varied alkyl chain lengths were produced and interacted with a cationic surfactant (MTAB) under different pH, salinity, and surfactant concentration. It was confirmed through the contact angle analysis that the longer the alkyl chain, the more hydrophobic the modified CNC would be. The adsorption analysis of modified CNC with MTAB at different pH disclosed that the electrostatic interaction was developed more quickly than the hydrophobic interaction. Also, MTAB was adsorbed more onto the surface covered with CNC with the longest hydrocarbon chain length (PCNC) than CNC with the shortest chain length (MCNC) at all pH. This reveals a hydrophobic/hydrophobic interaction developed among the alkyl chain in the carboxypantadecanyl functional group with the MTAB hydrophobic tail, resulting in more adsorption onto this surface. Moreover, a more compact and rigid layer of MTAB was achieved on PCNC than MCNC, revealing the role of the hydrocarbon tail in producing more compact and stronger layers. In salinity, by eliminating the electrostatic interaction, a higher MTAB adsorption was still observed on PCNC, which was another sign of remarkable hydrophobic/hydrophobic interaction between the two substrates. The MTAB-CNC interaction was the strongest below the CMC point of MTAB, while it weakened at and above the CMC point due to the micellar configuration of MTAB, suppressing the hydrophobic interaction. To conclude, our results demonstrated that the CNC-MTAB complex with desired features could be generated for various applications.

In the last research study presented in this thesis, the generated carboxyalkyl cellulose nanocrystals (CNC), as well as the unmodified CNC, were used as adsorbents for sulfamethoxazole (SMX),

ciprofloxacin (CIP), and doxycycline (DOX) antibiotic adsorbents. The highest antibiotic adsorption was obtained for DOX at pH 6.0, due to the strong electrostatic attraction, π interactions, and hydrogen bonding developed between carboxyalkylated CNC and DOX. The least DOX adsorption occurred at pH 10.0, which probably would be due to the electrostatic repulsion force limiting the adsorption. Also, carboxyalkylated CNC samples worked better than the unmodified CNC in antibiotic adsorption, which implies the critical role of these functional groups on the adsorption. Elongation in the hydrocarbon chain length of the induced carboxylate groups diminished the hydrophilicity of the modified CNC samples. Carboxyalkylated CNC samples depicted more sensitivity to pH variation than the unmodified CNC did, slightly improving the hydrophilicity by increasing the pH, which was resulted from the protonation of the carboxyl groups. CIP and DOX were more hydrophilic than SMX, due to their hydrophilic functional groups while they also were more sensitive than SMX to pH changes. The contact angle analysis of DOX on CNC-covered surfaces also demonstrated that the CNC with the highest carbon chain length was more porous and that DOX diffused more into the PCNC. The adsorption of DOX was higher at pH 6.0 on PCNC because the carboxylate groups of PCNC were deprotonated at this pH, promoting more hydrogen bonding ((-)CAHB) and π interactions (anion-π). Carboxyalkylation reactions were both observed to slightly reduce the CNC surface area due to the mild hydrolysis that CNC might have gone under in an alkaline reaction condition. While the antibiotic adsorption significantly increased the surface area of CNC due to the antibiotic surface area contributing to that of CNC upon the adsorption. This difference was more pronounced for DOX-PCNC complex due to the more interaction and adsorption. XPS analysis also showed a drastic increment in the C-C/C-H component resulting from the carboxyalkylation, while antibiotic adsorption to PCNC enhanced the C-C/C-H and C-N/C-O components.

7.2 Recommendation for future work

Although carboxyalkylated CNC performed efficiently as a dispersant for kaolinite suspension, other mineral suspensions, such as coal, could also be used to evaluate their dispersion with CNC and reveal the efficiency of CNC as a dispersant in a wider range of mineral suspensions. Although DMSO and NMMO are the two most used solvents, the impact of other common solvents, such as ionic liquids, could also be studied at the molecular level on CNC characteristics. While anionic CNC interacted strongly with a cationic surfactant, studies could be carried out on CNC interaction

with anionic, and/or non-ionic surfactants. Also, modified CNC, either cationic or amphoteric, could be used as an adsorbent for a broader range of antibiotics. Eventually, although unmodified CNC is a bio-based and non-toxic nanomaterial, toxicity studies need to be carried on carboxyalkylated CNC to disclose its toxicity and safety to be used in various industries.

Publication list

1) Feizi, Z. H., & Fatehi, P. (2020). Interaction of hairy carboxyalkyl cellulose nanocrystals with cationic surfactant: Effect of carbon spacer. *Carbohydrate Polymers*, 117396.
2) Feizi, Z. H., & Fatehi, P. (2020). Carboxymethylated cellulose nanocrystals as clay suspension dispersants: effect of size and surface functional groups. *Cellulose*, 1-14.
3) Feizi, Z. H., Kazzaz, A. E., Kong, F., & Fatehi, P. (2019). Evolving a flocculation process for isolating lignosulfonate from solution. *Separation and Purification Technology*, *222*, 254-263.
4) Feizi, Z. H., & Fatehi, P. (2020). Changes in the molecular structure of cellulose nanocrystals upon treating with solvents. Submitted to *Cellulose*.
5) Feizi, Z. H., & Fatehi, P. (2020). Anionic cellulose nanocrystals as antibiotic adsorbents**.** Under submission.
6) Kazzaz, A. E., Feizi, Z. H., & Fatehi, P. (2019). Grafting strategies for hydroxy groups of lignin for producing materials. *Green Chemistry*, *21*(21), 5714-5752.
7) Kazzaz, A. E., Feizi, Z. H., Kong, F., & Fatehi, P. (2018). Interaction of poly (acrylic acid) and aluminum oxide particles in suspension: particle size effect. *Colloids and Surfaces A: Physicochemical and Engineering Aspects*, *556*, 218-226.
8) Kazzaz, A. E., Feizi, Z. H., & Fatehi, P. (2018). Interaction of sulfomethylated lignin and aluminum oxide. *Colloid and Polymer Science*, *296*(11), 1867-1878.
9) Chen, J., Eraghi Kazzaz, A., AlipoorMazandarani, N., Hosseinpour Feizi, Z., & Fatehi, P. (2018). Production of flocculants, adsorbents, and dispersants from lignin. *Molecules*, *23*(4), 868.